Copy No. 6

DEFENCE R&D DÉFENSE

AN EXPERIMENTAL AND NUMERICAL INVESTIGATION INTO FATIGUE CRACK PROPAGATION OF 350 WT STEEL SUBJECTED TO SEMI-RANDOM CYCLIC LOADING

Philip A. Rushton

Department of Civil Engineering
Dalhousie University
PO Box 1000
Halifax
Nova Scotia
Canada
B3J 2X4

Contract # W7707-8-5687/001/HAL

Defence R&D Canada

DEFENCE RESEARCH ESTABLISHMENT ATLANTIC

Contractor Report
DREA CR 2000-154
March 2001

National Defence Défense nationale

Canada

104-06933/

National Defence **Défense nationale**
Research and Development Branch Bureau de recherche et développement

DREA CR 2000-154

AN EXPERIMENTAL AND NUMERICAL INVESTIGATION INTO FATIGUE CRACK PROPAGATION OF 350WT STEEL SUBJECTED TO SEMI-RANDOM CYCLIC LOADING

By
Philip A. Rushton

Department of Civil Engineering
Dalhousie University
PO Box 1000, Halifax, Nova Scotia, Canada, B3J 2X4

The scientific or technical validity of this Contract Report is entirely the responsibility of the contractor and the contents do not necessarily have the approval or endorsement of Defence R&D Canada

Scientific Authority D C Stredulinsky

W7707-8-5687/001/HAL
Contract Number

March 2001

CONTRACTOR REPORT

Prepared for

Defence Research Establishment Atlantic **Centre de Recherches pour la Défense Atlantique**

Canada

Contract Scientific Authority

David C. Stredulinsky

Approved by

J.L. Kennedy

Head, Warship Signatures & Safety

Approved for release by

Kirk Foster

Chair/DRP

© Her Majesty the Queen as represented by the Minister of National Defence, 2001

© Sa majesté la reine, représentée par le ministre de la Défense nationale, 2001

Abstract

A variety of aspects in the fields of fracture mechanics, fatigue, and fatigue crack propagation are reviewed in the first five chapters of this report, as well as a number of concepts and methodologies employed in fracture control and repair. The information provided in these chapters will not only educate the reader, but also provide him or her with the tools necessary to perform a variety of fatigue- and fracture-related analyses.

Chapter 4 contains a comprehensive review of a number of constant amplitude and variable amplitude fatigue crack growth models. There is inherently great variation amongst these models, with respect to modeling approach, parameters considered, the number of calibration parameters required (empirical or otherwise), relative ease of use, and the level of computational effort required. Unfortunately, few of these models bear any physical or practical significance and many will see only limited use due to their inherent complexity. Moreover, an all-encompassing fatigue crack growth model has yet to be developed, despite the enormous number of models currently available.

Chapters 6 and 7 focus on the experimental testing program employed to investigate the fatigue crack growth of center-cracked 350WT steel specimens subjected to semi- random loading comprised of various combinations of intermittent tensile overloads and compressive underloads. A significant amount of information is presented regarding post-overload and post-underload crack growth behavior.

Modifications to the commonly used Wheeler model have been proposed, which allow the effects of compressive loading to be considered. The modified Wheeler model appears to provide reasonably accurate fatigue life predictions by using an 'effective' plastic zone to incorporate sequence effects. While the modified Wheeler model does not significantly improve the predictive accuracy of the original Wheeler model, it does give some physical significance to an otherwise empirical approach to modeling such sequence effects. In addition, it is shown that the Wheeler shaping exponent may potentially be expressed as a function of the overload ratio and the overload/underload ratio for a given stress ratio.

A finite element investigation (using the NISA finite element package) was performed on a typical specimen, the results of which appear to validate the proposed existence of a crack tip 'compressive plastic zone' under compressive loading. The size of this plastic zone is typically smaller than that produced by an equivalent tensile overload. The nonlinear finite element analysis also predicts a zone of tensile yielding at the crack tip upon removal of this compressive underload, further substantiating the observed phenomenon of crack growth acceleration. The size of these compression-induced 'yield zones' were found to depend not only on the relative magnitude of the compressive underload and preceding tensile overload, but also on the assumed crack face separation.

The exponential delay model proposed by Trask (1998) has been revised to include the effects of not only overload ratio, but also stress ratio and overload/underload ratio. Although seemingly complex, the resulting delay model may be easily incorporated into any existing crack growth model for constant amplitude loading, and has been shown to yield fatigue life predictions which are in good agreement with the experimental data.

Fatigue crack growth threshold behavior of 350WT steel was also examined. The resulting K_{th} was similar to that suggested by Barsom et al (1987), but yielded poor life predictions when used in conjunction with the Zheng and Hirt model.

Sommaire

Les cinq premiers chapitres du présent rapport examinent divers aspects de la mécanique des ruptures, de la fatigue, de la propagation des fissures par fatigue, de même qu'un certain nombre de concepts et de méthodologies servant à la prévention et à la réparation des ruptures. Les renseignements contenus dans ces chapitres instruiront le lecteur et lui donneront aussi les outils nécessaires pour effectuer diverses analyses de fatigue et de ruptures par fatigue.

Le chapitre 4 contient un examen approfondi d'un certain nombre de modèles de propagation de fissures de fatigue à amplitude constante et à amplitude variable. Un grand écart fondamental existe entre ces modèles en ce qui concerne la méthode de modélisation, les paramètres pris en compte, le nombre de paramètres d'étalonnage requis (empiriques ou autres), la facilité relative d'utilisation et la complexité des calculs requis. Malheureusement, peu de ces modèles ont une portée physique ou pratique et la plupart d'entre eux ne servent que de façon limitée en raison de leur complexité fondamentale. De plus, il n'existe toujours pas de modèle universel de propagation des fissures de fatigue, malgré l'énorme nombre de modèles existants.

Les chapitres 6 et 7 traitent du programme expérimental d'essais servant à étudier la propagation des fissures de fatigue au moyen d'éprouvettes d'acier 350WT fissurées au centre et soumis à des charges semi-aléatoires comprenant diverses combinaisons de surcharges de traction intermittentes et de sous-charges de compression. Une quantité importante de renseignements est présentée sur le comportement des propagations des fissures avant une surcharge et après une sous-charge.

On a proposé des modifications au modèle Wheeler, fréquemment utilisé. Ces modifications permettent de tenir compte des effets des charges de compression. Le modèle de Wheeler modifié semble fournir des prédictions raisonnablement précises sur la résistance à la fatigue en utilisant une zone de déformation plastique effective pour incorporer les effets séquentiels. Bien que le modèle de Wheeler modifié n'améliore pas sensiblement la précision des prévisions du modèle original, il donne néanmoins une certaine portée physique à une méthode autrement empirique pour la modélisation de ces effets séquentiels. De plus, il est démontré que l'exposant de forme peut être exprimé comme une fonction du taux de surcharge et du rapport surcharge/sous-charge pour un rapport de contrainte donné.

Une étude par éléments finis (à l'aide du programme de calcul par éléments finis NISA) a été faite sur un spécimen représentatif et les résultats semblent confirmer l'existence proposée d'une zone d'extrémité de fissure par déformation plastique sous une charge de compression. La dimension de cette zone de déformation plastique est typiquement plus petite que celle produite par une surcharge de tension. L'analyse non linéaire paréléments finis prédit également une zone de rupture par traction à l'extrémité de la fissure lorsque la sous-charge de compression est dissipée. Ceci prouve bien le phénomène observé de l'accélération de la propagation des fissures. On a constaté que les dimensions de ces zones élastiques par compression provoquées dépendent non seulement de l'importance relative de la sous-charge de compression et de la surcharge de traction qui précède, mais aussi de la séparation de la surface supposée des fissures.

Le modèle de retard exponentiel proposé par Trask (1998) a été modifié pour inclure non seulement les effets du taux de surcharge, mais aussi ceux du facteur de contrainte et du facteur de surcharge/sous-charge. Bien qu'apparemment complexe, le modèle de retard qui en résulte peut être incorporé facilement dans tout modèle de propagation des fissures pour toute charge à amplitude constante et a démontré des prédictions d'endurance qui concordent bien avec les données expérimentales.

Le comportement de l'acier 350WT à la limite de propagation des fissures de fatigue a aussi été examiné. Le K_{th} résultant était semblable à celui suggéré par Barsom et autres (1987), mais donnait des prédictions d'endurance médiocres lorsqu'il était utilisé avec le modèle de Zheng et Hirt.

DREA Contract Report CR 2000-154

An Experimental and Numerical Investigation into Fatigue Crack Propagation of 350WT Steel Subjected to Semi-Random Cyclic Loading

by

Philip A. Rushton

Executive Summary

Background: The Warship Signatures and Safety (WSS) Section at DREA has been developing and testing methods for application of realistic sea loads to finite element models to predict hull structural performance. Much of this work has been incorporated into a Defence Research and Development Canada major project entitled "Improved Ship Structural Maintenance Management" (ISSMM) One component of this work is the assessment of the behavior of fatigue cracks in ship structures. There are several fatigue crack propagation models available, each taking a different approach to model fatigue loading and the associated propagation. Selection of the most suitable model for the assessment of ship fatigue crack propagation (FCP) is still challenging and can be quite complex, partly because wave loading is semi-random. Since most FCP models are based on constant amplitude loading, they often fall short of predicting the FCP in such applications, and therefore, they are deemed inadequate. Contracted work to Dalhousie University has provided an in depth survey of available FCP models and fatigue test methods, and has examined in detail nineteen FCP models. The work has also included an experimental fatigue crack propagation testing program, subjecting several center-cracked specimens of 350 WT steel (used in the Halifax class frigates) to both constant amplitude loading and semi-random loading. It has also included the measurement of the threshold stress intensity factor K_{th}, since some of the FCP models are sensitive to this parameter. Finally, a nonlinear finite element investigation was conducted to examine the stress state (i e , the plastic zone) and the associated residual stress, thereby complementing the experimental findings.

Principal Results: The experimental program has provided valuable data for 350WT crack propagation on the effects of compressive underloads (UL), tensile overloads (OL), an UL immediately followed an OL, and the effect of varying stress ratio (R) in conjunction with varying the overload ratio (OLR). A modified Wheeler model has been developed which can satisfactorily predict the crack propagation observed in the experimental variable amplitude load sequences considered.

Significance of Results: The work has resulted in identification and development of suitable models and model parameters for fatigue crack propagation in 350WT steel under variable amplitude loading. These results should help provide better crack propagation prediction tools in the ISSMM software.

Future Plans: The research has identified several areas for future work. Most fatigue crack propagation models contain a number of empirical parameters that must be calibrated for specific materials through expensive and time consuming testing. A model proposed by Zheng and Hirt is attractive because it uses physically significant parameters such as the threshold stress intensity and Young's modulus. This model will be considered further and improved measurement of the threshold stress intensity obtained. Additional testing is also needed to verify the proposed modifications of the Wheeler retardation model with both overload/underload and underload-only loading sequences. Other more realistic random loading sequences will also be considered.

Rapport sur le contrat 2000-154 du CRDA

Étude expérimentale et numérique de la propagation des fissures de fatigue de l'acier 350WT soumis à des charges cycliques semi-aléatoires

par
Philip A. Rushton

Résumé

Explication : La section des signatures et de la sécurité des navires du CRDA développe et met à l'épreuve des méthodes d'essais pour l'application de modèles à éléments finis des charges exercées par la mer pour prédire le rendement de la structure d'une coque. Une bonne partie de ce travail a été intégrée à un projet majeur de la Direction de recherche et de développement pour la défense du Canada, intitulé «Gestion améliorée de la maintenance de la structure des navires» (GAMSN). Un des éléments de ce travail est l'évaluation du comportement des fissures de fatigue sur les structures des navires. Il existe plusieurs modèles de propagation des fissures de fatigue (PFF), chacun ayant une méthode différente pour la modélisation des charges de fatigue et des propagations connexes. Le choix du modèle le plus pertinent pour l'évaluation de PFF du navire est toujours difficile et peut être fort complexe, en partie parce que les charges exercées par les vagues sont semi-aléatoires. Comme la plupart de ces modèles se fondent sur des charges à amplitude constante, ils ne réussissent pas souvent à prédire la PFF dans de telles applications et sont donc jugés inadéquats. L'université Dalhousie a procédé sous contrat à une étude approfondie des modèles existants de PFF et des méthodes d'essai de fatigue; elle a également examiné en détail dix-neuf modèles de PFF. Le travail comprenait aussi un programme expérimental d'essais de propagation des fissures de fatigue en soumettant des éprouvettes d'acier 350 WT (utilisé sur les frégates de la classe Halifax) fissuré au centre à des charges à amplitude constante et à des charges semi-aléatoires. Elle comprenait aussi la mesure du facteur d'intensité du seuil de contrainte K_{th} car certains modèles PFF sont sensibles à ce paramètre. Enfin, on a procédé à une étude non linéaire par éléments finis pour examiner l'etat des contrainte (p ex. la zone de déformation plastique) et les contraintes résiduelles connexes, complétant ainsi les résultats expérimentaux.

Principaux résultats : le programme expérimental a fourni des données précieuses sur la propagation des fissures dans l'acier 350WT, sur les effets des sous-charges de compression, des surcharges de traction, une sous-charge de compression étant suivie par une surcharge de traction, ainsi que sur les effets des rapports de contraintes variables, avec des rapports de surcharge variés. On a mis au point un modèle de Wheeler modifié qui peut prédire de façon satisfaisante la propagation des fissures observées dans les séquences expérimentales de contraintes à amplitude variable étudiées.

Importance des résultats : Ces travaux ont abouti à l'identification et au développement de modèles convenables et de paramètres de modélisation pour la propagation des fissures de fatigue sur l'acier 350WT soumis à des charges à amplitude variable. Ces résultats devraient contribuer à fournir de meilleurs outils de prédiction de la propagation des fissures de fatigue dans le logiciel de GAMSN

Projets futurs : La recherche a identifié plusieurs domaines pour des travaux futurs. La plupart des modèles de propagation des fissures de fatigue contiennent un certain nombre de paramètres empiriques qu'il faut établir pour des matériaux particuliers, grâce à des essais coûteux et longs. Un modèle proposé par Zheng et Hirt est séduisant car il fait appelà des paramètres physiques importants comme le seuil de contrainte et le module de Young. Ce modèle sera examiné de façon plus poussée et permettra d'améliorer les mesures du seuil des contraintes Des essais supplémentaires sont nécessaires pour vérifier les modifications proposées au modèle de retardement de Wheeler, avec à la fois les séquences de surcharge/sous-charge et les sous-charges seulement. On envisagera également d'autres séquences de charges aléatoires plus réalistes.

TABLE OF CONTENTS

Page

Abstract........ ii
Sommaire........ iii
Executive Summary........ v
Resume........ vi
Table of Contents........ vii
List of Figures........ xii
List of Tables........ xxii
List of Abbreviations and Symbols........ xxiii
Acknowledgements........ xxvii

Chapter 1:

Introduction........ 1
1.1 Historical Perspective........ 1
1.2 Methods of Analysis and Design........ 3
Chapter 2: Fracture Mechanics........ 5
2.1 Introduction........ 5
2.2 Linear Elastic Fracture Mechanics (LEFM)........ 6
  2.2.1 The Stress Intensity Factor (K)........ 7
    2.2.1.1 Stress Intensity Factors for Mixed-Mode Loading........ 10
    2.2.1.2 Material Fracture Toughness (K_C)........ 13
  2.2.2 The Strain Energy Release Rate (G)........ 16
  2.2.3 Crack Tip Plastic Zones........ 21
  2.2.4 Extension of LEFM Validity: Plastic Zone Adjustment........ 25
2.3 Elastic Plastic Fracture Mechanics (EPFM)........ 26
  2.3.1 The J Contour Integral........ 27
  2.3.2 Crack Tip Opening Displacement (CTOD)........ 33
2.4 LEFM Versus EPFM........ 34
Chapter 3: Fatigue........ 36
3.1 Introduction........ 36

3.2 Categories of Fatigue Loading 37
3.2.1 Constant Amplitude Loading (CAL) 37
3.2.2 Variable Amplitude Loading (VAL) 38
3.3 Fatigue Testing 40
3.3.1 Testing Equipment 40
3.3.2 Specimens Used in Fatigue Testing 42
3.3.3 Standards for Fatigue Testing 44
3.4 Micromechanics of Fatigue Damage 46
3.5 Stress-Life Curves 51
Chapter 4: Fatigue Crack Propagation and Life Assessment Methods 62
4.1 Introduction 62
4.2 Fatigue Crack Growth Data Representation 63
4.3 Fatigue Crack Growth Modeling 70
4.3.1 Fatigue Crack Growth Models for Constant Amplitude Loading 71
4.3.1.1 The Paris Model for Constant Amplitude Loading 71
4.3.1.2 The Walker Model for Constant Amplitude Loading 72
4.3.1.3 The Forman Model for Constant Amplitude Loading 74
4.3.1.4 Modified Forman Models for Constant Amplitude Loading 75
4.3.1.5 The Pook and Frost Model for Constant Amplitude Loading 76
4.3.1.6 The Zheng and Hirt Model for Constant Amplitude Loading 77
4.3.1.7 The Wang and Hsu Model for Constant Amplitude Loading 80
4.3.1.8 The Dowling and Begley Model for Constant Amplitude Loading 81
4.3.2 Fatigue Crack Growth Models for Variable Amplitude Loading 81
4.3.2.1 Load Interaction (Sequence) Effects 82
4.3.2.2 The Use of Constant Amplitude Loading Models in Fatigue Crack Growth Prediction for Variable Amplitude Loading 85
4.3.2.3 The Barsom Root-Mean-Square (rms) Model for Variable Amplitude Loading 86
4.3.2.4 The Hudson Root-Mean-Square (rms) Model for Variable Amplitude Loading 89
4.3.2.5 The Elber Model for Variable Amplitude Loading 90

4.3.2.6 The Wheeler Model for Variable Amplitude Loading 93
4.3.2.7 The Willenborg Model for Variable Amplitude Loading 96
4.3.2.8 The Johnson Model for Variable Amplitude Loading 98
4.3.3 Calibration of Fatigue Crack Growth Models 99
4.3.3.1 Calibration of Paris' Law for Fatigue Crack Growth 100
4.3.3.2 Calibration of the Walker Model for Fatigue Crack Growth 102
4.3.3.3 Calibration of the Forman Model for Fatigue Crack Growth 103
4.3.3.4 Calibration of the Zheng and Hirt Model for Fatigue Crack Growth 104
4.3.3.5 Calibration of the Dowling and Begley Model for Fatigue Crack Growth 105
4.3.3.6 Calibration of Barsom's Root-Mean-Square Model for Fatigue Crack Growth 105
4.3.3.7 Calibration of Hudson's Root-Mean-Square Model for Fatigue Crack Growth 106
4.3.3.8 Calibration of Wheeler's Model for Fatigue Crack Growth Retardation 106
4.3.4 Guidelines for Selection of a Fatigue Crack Growth Model 108
4.4 Life Assessment Techniques for Fatigue Crack Growth 109
4.4.1 Life Assessment for Constant Amplitude Loading 109
4.4.2 Life Assessment for Variable Amplitude Loading 112
4.4.3 Cumulative Damage Theories 116
4.5 Crack Growth in Corrosive Environments 119
4.5.1 Stress Corrosion Cracking 120
4.5.2 Corrosion Fatigue Crack Growth 123
Chapter 5: Fracture Control 126
5.1 Introduction 126
5.2 Fundamental Fracture Control Methodologies 126
5.3 Secondary Fracture Control Methodologies 129
5.3.1 Periodic Inspection 129
5.3.2 Durable Design Approach 132
5.3.3 Proof Testing 133

    5.3.4 Surface Layer Machining (Stripping) 134
    5.3.5 Multiple Load Paths (Structural Redundancy) 135
    5.3.6 Crack Arrestors 136
  5.4 Crack Repair Techniques 141
Chapter 6: Experimental Method 147
  6.1 Introduction 147
  6.2 Test Material 147
  6.3 Test Specimen Configuration 149
  6.4 Specimen Preparation 150
  6.5 Test Apparatus 150
  6.6 Test Procedure 154
    6.6.1 Fatigue Crack Growth Threshold Testing 154
    6.6.2 Semi-Random Fatigue Crack Growth Testing 156
Chapter 7: Experimental Results and Data Analysis 161
  7.1 Introduction 161
  7.2 Data Reduction Techniques 161
  7.3 Results of Fatigue Crack Growth Threshold Testing 163
  7.4 Results of Semi-Random Fatigue Crack Growth Testing 166
  7.5 Data Analysis 184
    7.5.1 Constant Amplitude Predictions Using the Zheng and Hirt Model 185
    7.5.2 Variable Amplitude Predictions Using the Wheeler Model 188
    7.5.3 VAL Predictions Based on a Modified Wheeler Model 195
    7.5.4 Compressive Loading and Crack Growth Acceleration Revisited 200
    7.5.5 Finite Element Investigation Into Crack Tip Plasticity Under Compressive Loading 202
    7.5.6 A Revised Form of Trask's Exponential Delay Model 216
Chapter 8: Conclusions and Recommendations 226
  8.1 Conclusions 226
  8.2 Recommendations for Future Investigations 230

References 235

Appendix A: Fatigue Crack Growth Data for Threshold Testing........................ 238
Appendix B: Fatigue Crack Growth Data for Semi-Random Loading Tests............. 244
Appendix C: Fatigue Life Predictions Using the Wheeler Model........................ 263
Appendix D: Fatigue Life Predictions Using the Modified Wheeler Model... 272

List of Figures

Figure	Title	Page
Figure 1.1	Fracture of the USS Schenectady while docked in San Diego	2
Figure 2.1	Three modes of loading	5
Figure 2.2	Conditions for which LEFM is (a) valid, and (b,c, and d) invalid	6
Figure 2.3	Center-cracked plate of infinite width, subjected to mode I loading	8
Figure 2.4	Superposition of stress intensity factors (Example 1)	9
Figure 2.5	Superposition of stress intensity factors (Example 2)	9
Figure 2.6	Superposition of stress intensity factors (Example 3)	10
Figure 2.7	Plate containing a crack oriented at angle β	11
Figure 2.8	Representation of (a) a kinked and (b) a forked fatigue crack	12
Figure 2.9	Local stress intensity factors (k_1 and k_2) as a function of (a) kink angle α, and (b) fork angle 2α	13
Figure 2.10	Effect of thickness on fracture toughness	14
Figure 2.11	Effect of yield strength on fracture toughness	15
Figure 2.12	Effect of temperature on fracture toughness	15
Figure 2.13	Effect of loading rate on fracture toughness	16
Figure 2.14	Crack extension at constant displacement	18
Figure 2.15	Crack extension at constant load	18
Figure 2.16	Area within which strain energy is affected by a central crack	20
Figure 2.17	Irwin's approximation of plane stress plastic zone size	22
Figure 2.18	Dugdale's approximation of plane stress plastic zone size	23
Figure 2.19	Through-thickness plastic zone variation	24

Figure 2.20	Cyclic plastic zone	24
Figure 2.21	Stress-strain relationship for a nonlinear elastic material	28
Figure 2.22	Contour integrals. (a) Elastic body, (b) Cracked body, (c) Path independent contour	31
Figure 2.23	Contour integral based on a simple circular path	32
Figure 2.24	Definitions of crack tip opening displacement (CTOD)	34
Figure 2.25	LEFM versus EPFM	35
Figure 3.1	Various forms of constant amplitude fatigue loading: (a) Completely Reversed, (b) Non-zero mean stress, and (c) Zero-to-tension	37
Figure 3.2	Variable amplitude fatigue loading: (a) Repeated, (b) Semi-random, and (c) Completely random loading	39
Figure 3.3	The R.R. Moore rotating beam fatigue testing machine	41
Figure 3.4	A reciprocating bending machine (cantilever bending)	41
Figure 3.5	A closed-loop servo-hydraulic testing machine	42
Figure 3.6	Various fatigue testing specimens	43
Figure 3.7	Fatigue crack propagation testing specimens: (a) Center-cracked tension, (b) Compact tension, and (c) Three-point bending specimen	44
Figure 3.8	Slip band formation and progressive damage intensification	47
Figure 3.9	Fracture surfaces showing beach marks	48
Figure 3.10	Fatigue striation pattern formed by a typical repeated variable amplitude load sequence	49
Figure 3.11	Mechanisms of fatigue striation formation and crack advance: (a) Crack opening and blunting due to slip on alternate slip planes during increasing tensile stress, and (b) Crack closure and crack tip resharpening by partial slip reversal on alternate slip planes during decreasing tensile stress	50
Figure 3.12	Fatigue crack growth transition from tensile mode to shear mode, along with corresponding shear lip formation	51

Figure 3.13 Stress-life (S-N) curve 52

Figure 3.14 Comparison of typical S-N curves for steel and nonferrous materials 54

Figure 3.15 Effect of an aggressive chemical environment on the S-N curve 55

Figure 3.16 Effects of stress raisers on the S-N curve 56

Figure 3.17 Effect of mean stress on the S-N curve 57

Figure 3.18 Effect of stress ratio on the S-N curve based on (a) Stress amplitude, and (b) Maximum stress 57

Figure 3.19 Effects of shot peening and presetting on fatigue strength 58

Figure 3.20 A family of stress-life-probability of failure curves 59

Figure 3.21 Typical constant life diagram 60

Figure 4.1 Effect of initial crack length on resulting a-versus-N curve 64

Figure 4.2 Effect of cyclic stress range on resulting a-versus-N curve 64

Figure 4.3 Typical da/dN-versus-ΔK curve (fatigue rate curve) 65

Figure 4.4 Schematic illustration of various mechanisms of crack-closure 67

Figure 4.5 Effect of mean stress (stress ratio, R) on fatigue crack growth rate 69

Figure 4.6 Fatigue data representation based on the Walker model 73

Figure 4.7 Effect of Forman's model on consolidation of fatigue rate data 75

Figure 4.8 Concept of Lal and Weiss model, basis for Zheng and Hirt model 77

Figure 4.9 Crack growth retardation via residual stress field near the crack tip 83

Figure 4.10 Retardation with (a) Multiple overloads, and (b) Single overloads 84

Figure 4.11 Relative sequence effects under (a) Tension overload, (b) Compression-tension overload, (c) Tension-compression overload, and (d) Compression underload 85

Figure 4.12 Schematic representation of loading profiles for Barsom's model 88

Figure 4.13 Use of Barsom's model in describing irregular load spectra 88

Figure 4.14	Evaluation of K_{open} for Elber model	91
Figure 4.15	Illustration of terms defining Wheeler's retardation parameter	94
Figure 4.16	Schematic representation of load interaction zones	95
Figure 4.17	Selection of Wheeler shaping exponent	107
Figure 4.18	Life estimation using numerical integration techniques	111
Figure 4.19	Schematic representation of N_D following a tensile overload	114
Figure 4.20	Life estimates using the Palmgren-Miner rule	117
Figure 4.21	Nonlinear accumulation of fatigue damage	117
Figure 4.22	Effect of environmental conditions on fatigue behavior	119
Figure 4.23	Cantilever beam test fixture to measure crack growth in a corrosive environment	120
Figure 4.24	Evaluation of stress corrosion cracking threshold (K_{ISCC})	121
Figure 4.25	Typical a-versus-t curve used to determine K_{ISCC}	122
Figure 4.26	Typical da/dt-versus-K curve used to determine K_{ISCC}	122
Figure 4.27	Typical results from fatigue testing in a corrosive environment	124
Figure 5.1	Fracture control through reduction in design stress level	127
Figure 5.2	Fracture control through reduction in initial flaw size	127
Figure 5.3	Fracture control through improved fracture toughness	128
Figure 5.4	Time interval available for crack detection and repair	129
Figure 5.5	Opportunities for crack detection based on I = H/2	131
Figure 5.6	Proof testing	133
Figure 5.7	Fracture control by surface layer machining (stripping)	135
Figure 5.8	Influence of typical crack arrestor on residual strength	137
Figure 5.9	Effect of arrestor tensile strength on overall residual strength diagram	139

Figure 5.10 Crack development at fastener location 140

Figure 5.11 Principles of various types of crack arrestors: (a) High toughness strake, (b) Stringer or doubler, and (c) Hybrid arrestor 140

Figure 5.12 Crack repair using welded cover plates 142

Figure 5.13 Crack repair using adhesively bonded composite patches 143

Figure 5.14 Crack repair using crack arrest holes (stop holes) 144

Figure 5.15 Simple devices used for stop hole expansion when (a) Stop hole accessible from both sides, and (b) Stop hole accessible from one side only 145

Figure 5.16 Comparison of crack retardation (repair) methods used on specimens subjected to (a) Constant amplitude loading, and (b) Variable amplitude loading 146

Figure 6.1 Test specimen layout and dimensions 149

Figure 6.2 Instron 8501 universal testing machine, control panel, and load cell 151

Figure 6.3 Top and bottom fixtures, along with specimen and specimen grips 151

Figure 6.4 Specimen grips 152

Figure 6.5 Attachment of specimen grips to top and bottom test fixtures 153

Figure 6.6 Travelling microscope and support structure 153

Figure 6.7 Completely assembled test setup 154

Figure 6.8 Fatigue crack growth (a) Emanating from an initial EDM starter notch, and (b) Subsequent crack growth away from EDM notch 157

Figure 6.9 Formation of crack tip plastic zone (OLR = 1.67) 158

Figure 6.10 Schematic representation of aforementioned overload and underload terms 160

Figure 7.1 Use of both the secant and seven-point incremental polynomial method 163

Figure 7.2 Fatigue rate curves used in crack growth threshold testing: 165
(a) 'Normal' axes orientation, and (b) 'Inverted' axes orientation

Figure 7.3 Effect of stress ratio (R) on the (a) a-versus-N, and (b) da/dN-versus-ΔK curves 170

Figure 7.4 Effects of OLR on the (a) a-versus-N, and (b) da/dN-versus-ΔK curves at R = 0.1 172

Figure 7.5 Effects of OLR on the (a) a-versus-N, and (b) da/dN-versus-ΔK curves at R = 0.3 173

Figure 7.6 Effect of varying the OL/UL ratio on the a-versus-N curve 175

Figure 7.7 Effect of varying the OL/UL ratio on the fatigue rate curve 175

Figure 7.8 Effect of varying the OLR and OL/UL on fatigue life (R = 0.1) 180

Figure 7.9 Effect of varying OLR on fatigue life (R = 0.3 and OL/UL = 1.0) 180

Figure 7.10 Variation in fatigue rate curves for OLR = 1.20 (R = 0.1) 181

Figure 7.11 Variation in a-versus-N curves for OLR = 1.20 (R = 0.1) 181

Figure 7.12 Effect of OLR & OL/UL on (normalized) minimum crack growth rate 183

Figure 7.13 da/dN-versus-ΔK curve predictions using Zheng & Hirt model in conjunction with the two-curve Paris model 186

Figure 7.14 Comparison of a-versus-N predictions: Zheng versus two-curve Paris 187

Figure 7.15 Typical a-versus-N prediction obtained using the Wheeler model 190

Figure 7.16 Wheeler shaping exponent (m) expressed as a function of OLR 193

Figure 7.17 Comparison of Wheeler 'm'-versus-OLR relationship for R=0.10 & R=0.30 194

Figure 7.18 Description of the modified Wheeler model 196

Figure 7.19 'm'-versus-OLR for R=0.10 & R=0.30: modified Wheeler model 199

Figure 7.20 Schematic representation of potential crack tip prying under compressive overloads due to mis-matched crack faces 201

Figure 7.21 Application of boundary conditions to the FE model 203

Figure 7.22 Original crack tip mesh discretization: 449 elements (total) 205

Figure 7.23 Orthogonal and radial refinements of FE model crack tip mesh 207

Figure 7.24 Y-Displacement contours of loadstep 40 209

Figure 7.25 – Axial (Syy) stresses during loadstep 40 ($p_{max} \approx 240$ psi, $P_{max} \approx 120$ kN) 210

Figure 7.26 Axial (Syy) stress distribution for loadstep 80: compressive residual stresses upon return to zero load form P_{max} 211

Figure 7.27 Axial (Syy) stress distribution for loadstep 120: compressive plastic zone at minimum compressive load 212

Figure 7.28 Axial (Syy) stress distribution for loadstep 160: tensile residual stresses upon return to zero load from P_{min} 213

Figure 7.29 Axial (Syy) stress distribution for loadstep 120: crack face separation reduced by 10X 214

Figure 7.30 Axial (Syy) stress distribution for loadstep 160: crack face separation reduced by 10X 215

Figure 7.31 Preliminary evaluation of revised delay model 218

Figure 7.32 Incorporation of stress ratio into revised delay model 219

Figure 7.33 Relationship between intercept (β) and OL/UL ratio 222

Figure 7.34 Graphical comparison of delay model predictions and experimental data 224

Figure 7.35 Delay model predictions illustrating influence of R and OL/UL ratio on N_D 224

Figure 8.1 Overlapping plastic zones 232

Figure A.1 Sample data sheet for threshold testing 239

Figure A.2 'a-versus-N' data and fatigue rate data for specimen K_{th}#1 240

Figure A.3 'a-versus-N' data and fatigue rate data for specimen K_{th}#2 241

Figure A.4 'a-versus-N' data and fatigue rate data for specimen K_{th}#3 242

Figure A.5 'a-versus-N' data and fatigue rate data for specimen K_{th}#4 243

Figure B.1 Sample data sheet for semi-random testing 245

Figure B.2 'a-versus-N' data and fatigue rate data for specimen VAL VIIIa 246

Figure B.3 'a-versus-N' data and fatigue rate data for specimen VAL Ia 247

Figure B.4 'a-versus-N' data and fatigue rate data for specimen VAL VIIa 248

Figure B.5 'a-versus-N' data and fatigue rate data for specimen VAL IIa 249

Figure B.6 'a-versus-N' data and fatigue rate data for specimen VAL VIa 250

Figure B.7 'a-versus-N' data and fatigue rate data for specimen VAL IIIa 251

Figure B.8 Sample data sheet for Paris fatigue life prediction 252

Figure B.9 'a-versus-N' data and fatigue rate data for specimen VAL IIIa-2 253

Figure B.10 'a-versus-N' data and fatigue rate data for specimen VAL Va 254

Figure B.11 'a-versus-N' data and fatigue rate data for specimen VAL IVa 255

Figure B.12 'a-versus-N' data and fatigue rate data for specimen VAL Ib 256

Figure B.13 'a-versus-N' data and fatigue rate data for specimen VAL Ib-2 257

Figure B.14 'a-versus-N' data and fatigue rate data for specimen VAL IIb 258

Figure B.15 'a-versus-N' data and fatigue rate data for specimen VAL IIb-2 259

Figure B.16 'a-versus-N' data and fatigue rate data for specimen VAL IIIb 260

Figure B.17 'a-versus-N' data and fatigue rate data for specimen VAL IIIb-2 261

Figure B.18 'a-versus-N' data and fatigue rate data for specimen VAL IIIb-3 262

Figure C.1 Wheeler prediction for specimen VAL VIIIa 264

Figure C.2 Wheeler prediction for specimen VAL Ia 264

Figure C.3 Wheeler prediction for specimen VAL VIIa 265

Figure C.4 – Wheeler prediction for specimen VAL IIa 265

Figure C.5 Wheeler prediction for specimen VAL VIa 266

Figure C.6 Wheeler prediction for specimen VAL IIIa 266

Figure C.7	Wheeler prediction for specimen VAL IIIa-2	267
Figure C.8	Wheeler prediction for specimen VAL Va	267
Figure C.9	Wheeler prediction for specimen VAL IVa	268
Figure C.10	Wheeler prediction for specimen VAL Ib	268
Figure C.11	Wheeler prediction for specimen VAL Ib-2	269
Figure C.12	Wheeler prediction for specimen VAL IIb	269
Figure C.13	Wheeler prediction for specimen VAL II-2b	270
Figure C.14	Wheeler prediction for specimen VAL IIIb	270
Figure C.15	Wheeler prediction for specimen VAL IIIb-2	271
Figure C.16	Wheeler prediction for specimen VAL IIIb-2	271
Figure D.1	Modified Wheeler prediction for specimen VIIIa	273
Figure D.2	Modified Wheeler prediction for specimen Ia	273
Figure D.3	Modified Wheeler prediction for specimen VIIa	274
Figure D.4	Modified Wheeler prediction for specimen IIa	274
Figure D.5	Modified Wheeler prediction for specimen VIa	275
Figure D.6	Modified Wheeler prediction for specimen IIIa	275
Figure D.7	Modified Wheeler prediction for specimen IIIa-2	276
Figure D.8	Modified Wheeler prediction for specimen Va	276
Figure D.9	Modified Wheeler prediction for specimen IVa	277
Figure D.10	Modified Wheeler prediction for specimen 1b	277
Figure D.11	Modified Wheeler prediction for specimen 1b-2	278
Figure D.12	Modified Wheeler prediction for specimen IIb	278
Figure D.13	Modified Wheeler prediction for specimen IIb-2	279

Figure D.14 Modified Wheeler prediction for specimen IIIb 279

Figure D.15 Modified Wheeler prediction for specimen IIIb-2 280

Figure D.16 Modified Wheeler prediction for specimen IIIb-5 280

List of Tables

Table	Title	Page
Table 5.1	Summary of inspection techniques	130
Table 6.1	Chemical composition of 350WT steel	148
Table 6.2	Material Properties of 350WT steel	148
Table 7.1	Results of fatigue crack growth threshold testing	164
Table 7.2	Summary of specimen dimensions	167
Table 7.3	Summary of specimen loading spectra	168
Table 7.4	Summary of semi-random loading tests	169
Table 7.5	Paris parameters for 'two-curve' model proposed by Trask (1998)	174
Table 7.6	Conversion of OLR into equivalent OLR_{EQ} used by Trask (1998)	178
Table 7.7	Summary of Wheeler model fatigue life predictions	191
Table 7.8	Summary of fatigue life predictions based on modified Wheeler model	198
Table 7.9	Summary of FE model convergence study	208
Table 7.10	Summary of delay data for each specimen	218
Table 7.11	Fatigue life predictions based on delay model of Equation 7.29	223

List of Abbreviations and Symbols

a	Crack length (half-crack length for center-cracked specimens)
a_i	Initial crack length
a_{yld}	Crack length at yielding
a_f	Final crack length
ASTM	American Society for Testing and Materials
α	Parameter used to determine plastic zone size based on plane stress or plane strain conditions
β	Parameter used with the revised delay model, a function of OL/UL
CAL	Constant Amplitude Loading
C_P, m_P	Curve fitting parameters for Paris model
C_W, m_W, n_W	Curve fitting parameters for Walker model
C_F, m_F	Curve fitting parameters for Forman model
CTOD, δ_t	Crack Tip Opening Displacement
D	Damage fraction used with most cumulative damage theories
da/dN	Fatigue crack growth rate
da/dt	Crack velocity for stress corrosion cracking
δ	Crack face separation
E	Modulus of elasticity (i.e., Young's modulus)
EDM	Electron Discharge Machining
EPFM	Elastic Plastic Fracture Mechanics
ε_f	Material fracture ductility
F	Work done by the applied loads

FEM	Finite Element Method
F_{tu}	Ultimate strength of a crack arrestor
G	Griffith's strain energy release rate
I	Inspection interval
J	Rice's J-integral, a fracture parameter for EPFM (equivalent to K for LEFM)
J_c, J_{Ic}	EPFM fracture toughness
K	Stress intensity factor, fracture parameter for LEFM
ΔK	Stress intensity factor range
K_{1c}, K_{Ic}	LEFM fracture toughness for plane stress and plane strain conditions under mode I loading
K_{2c}, K_{IIc}	LEFM fracture toughness for plane stress and plane strain conditions under mode II loading
K_{SCC}, K_{ISCC}	Threshold stress intensity factor for stress corrosion cracking under plane stress and plane strain conditions, respectively
K_{max}, K_{min}	Maximum and minimum stress intensity factors for a given fatigue cycle
K_{open}	Stress intensity factor at which a fatigue crack is considered fully open
K_{th}	Fatigue crack growth threshold stress intensity factor
L	Specimen length; stress concentration factor for a crack arrestor
LEFM	Linear Elastic Fracture Mechanics
m	Shaping exponent used in conjunction with the Wheeler model
N	Number of elapsed fatigue cycles
N_D	Number of delay cycles caused by a given tensile overload
N_{yld}	Number of elapsed fatigue cycles from crack length a_i to a_{yld}
N_{if}	Number of elapsed fatigue cycles from crack length a_i to a_f

NISA	Numerically Integrated System Analysis (commercially available finite element package)
ν	Poisson's ratio
OL, UL	Magnitude of a tensile overload and compressive underload, respectively
OLR	Overload ratio
$P_{max,CAL}$, $P_{min,CAL}$	Maximum and minimum load applied during a given fatigue cycle under constant amplitude loading (CAL)
$P_{max\,OL}$, $P_{min,UL}$	Maximum and minimum load applied during a tensile overload and compressive underload, respectively
ϕ_R	Crack growth retardation parameter for Wheeler model
ϕ_R^{T-C}	Crack growth retardation parameter for the proposed modified Wheeler model
ϕ_R^C	Modified Wheeler acceleration parameter
R	Stress ratio
R^2	Coefficient of determination for regression analyses
RA	Percent reduction in area at fracture, obtained from a simple tension test
r_p	Crack tip plastic zone diameter for tensile loading
r_{cp}	Compressive plastic zone diameter
rms	Root-mean-square value
σ_{max}, σ_{min}	Maximum and minimum far-field stresses applied to a component during a given fatigue cycle
$\Delta\sigma$	Applied stress range during a given fatigue cycle
σ_a	Stress amplitude of a given fatigue cycle
σ_{ar}	Equivalent completely reversed stress

σ_{yld}	Material yield stress
σ_{ult}	Ultimate material stress
t	Specimen thickness
U	Internal work (strain energy); Elber's effective stress intensity ratio
U_o	Strain energy density
UTM	Universal Testing Machine
VAL	Variable Amplitude Loading
W	Specimen width; work required to fracture a given material over an incremental length 'da'
Y	Geometric correction factor for a given mode of loading, section geometry and crack configuration

Acknowledgements

I wish to express my sincerest thanks and appreciation to my supervisor, Dr. Farid Taheri, for all the encouragement, guidance and support he has given to me over the past two years during the course of this investigation. I would also like to thank Dr. David Stredulinsky for all his help and advice, and for making available the steel plating required to perform the experimental investigation. Further appreciation is extended to the Defense Research Establishment Atlantic (DREA) and also the National Science and Engineering Research Council of Canada (NSERC) for their financial support during the course of this investigation.

To Mr. John Porter of the Halifax Dockyard, special thanks are extended for arranging to have the required electron discharge machining performed on each of the test specimens, and to Dr. Graeme Lee, for the use of his travelling microscope. I would also like to thank the Civil Engineering department for the use of their laboratory facilities.

Appreciation is extended to Mr. David Trask for all the help and advice he has given me, and also to the Civil Engineering department's technicians, Mr. Mark MacDonald and Mr. Blair Nickerson, for their assistance in the preparation of test specimens and the maintenance of test fixtures and laboratory equipment.

To Mom, Dad, and the rest of my family, I would like thank you all for your love and support and for always encouraging me to strive to do my very best and make the most of the opportunities presented to me.

Finally, to Gail, your love, understanding, encouragement, and undying patience over the past seven years have meant more to me than you may ever know…Thank you.

Chapter 1
Introduction

1.1 Historical Perspective

It is most certainly a tribute to early architects and engineers that many of the structures commissioned by the Pharaohs of ancient Egypt and the Caesars of Rome remain standing today. Prior to the 1800's, the primary construction materials were brick, mortar, and wood; with the former two materials being used more commonly for large structures due to the unavailability of trees large enough to be used as support beams. However, the brittle nature of brick and mortar made them unsuitable for carrying tensile loads. As a result, "...pre-Industrial Revolution structures were usually designed to be loaded in compression..." [Anderson, 1995], and the arch shape was commonly selected for its ability to transfer applied loads into compressive stresses throughout the structure, not to mention its aesthetic appeal.

With the arrival of the Industrial Revolution, mass production of iron and steel became common. The increased ductility of these materials allowed new structures to be built that could carry tensile loads, which had previously been restricted. The use of these new materials in design was not without difficulty, however. It was noticed that steel structures would occasionally fail suddenly and unexpectedly, and at stresses well below their expected tensile strength. One of the earliest and most famous of these failures occurred in January of 1919. A molasses tank in Boston ruptured, spilling over 2.3 million gallons of molasses. The rupture killed 12, injured 40 others, and drowned several horses, not to mention the extensive property damage [Anderson, 1995].

In 1920, a man by the name of A.A. Griffith published a report that finally made a qualitative connection between flaw size and fracture stress. Griffith based his fracture theory on a simple energy balance, reasoning that fracture would occur "...when the strain energy change that results from an increment of crack growth is sufficient to overcome the surface energy of the material..." [Anderson, 1995]. Unfortunately, his approach was applicable only to brittle solids, and a modification to Griffith's model (made by Dr. G.R. Irwin), which would make it more applicable to ductile metals, was not presented until 1948.

The progression of fracture mechanics from a simple scientific wonder to an engineering field is due mainly to the failure of many Liberty ships during World War II. During World War II, the United States supplied many cargo ships to Great Britain for carrying supplies. However, with the existing ship building methods, the ships could not be replaced nearly as fast as the German Navy could sink them. As a result, the construction of new vessels was proposed, with "…an all-welded hull, as opposed to the riveted construction of traditional ship designs…" [Anderson, 1995]. These new ships, which could be built much faster than their riveted counterparts, later became known as the Liberty ships. Approximately 2700 Liberty ships were built during World War II, of which about 400 incurred fractures. Of these 400 fractured ships, 90 were considered serious, and about 10 fractured completely [Anderson, 1995 and Barsom et al, 1987]. Numerous investigations revealed that the Liberty ship failures were caused by a combination of factors, including poor welding practices, the use of square hatch corners (which would cause extremely high local stresses), and the use of low-toughness steel. Figure 1.1 illustrates one of the most spectacular Liberty ship failures.

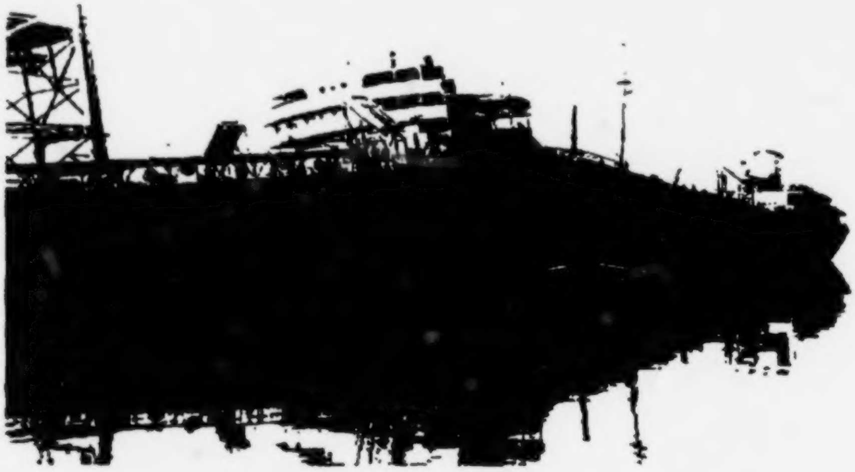

Figure 1.1 – Fracture of the USS Schenectady while docked in San Diego [Lampman, 1996]

For as long as man-made structures have existed, so too has the problem of fracture. However, the consequences of fracture are possibly worse today than ever before. With our advancing technology, today's structures are typically much larger, and our vessels and aircraft can now carry more cargo and move faster than ever before. Furthermore, today's larger population means that more people are at risk of injury in case of a failure. Fortunately, considerable progress has been made in the field of fracture mechanics, and our understanding of material failure and knowledge of failure prevention have increased dramatically since World War II. Today, components are designed such that the possibility of brittle fracture is minimal during their service lives. This design philosophy, combined with strict quality control measures and regularly scheduled inspection programs, has allowed engineers to control but still not eliminate the problem.

1.2 Methods of Analysis and Design

The effective engineering design of any component involves the selection of suitable materials and dimensioning of the selected geometry and cross section such that the component can perform its intended function in a safe, economic, and reliable fashion. Conventional design methods entail proportioning the cross section of a component such that the factored applied loads do not exceed the factored material resistance.

Unfortunately, due to a number of factors, not the least of which include inherent material defects, flaws and stresses induced during the manufacturing process, or simply the wear and tear of everyday use, it is virtually inevitable that a given component will develop a crack during its design life. The growth or presence of a crack can reduce a component's strength to the point where it may fail by brittle fracture ("...a type of catastrophic failure in structural materials that usually occurs without prior plastic deformation and at extremely high speeds..." [Barsom et al, 1987]) at a stress level well below the material's yield strength. In addition, other crack-like flaws or discontinuities such as voids in welds, foreign inclusions, deep surface gouges, and delaminations may easily develop into cracks, and should therefore be treated as if they were so.

The total prevention of brittle fracture would require the elimination of any structural details that could act as fracture-initiation sites or stress raisers. Unfortunately, the impracticality of this design approach usually renders it futile. The design approach should instead focus on minimizing the number of such discontinuities, and insure that they do not propagate to a critical size during the service life for which the component was designed.

The type of loading to which a component is subjected greatly influences the onset of brittle failure. The failure of a given component due to a monotonically increasing load and a cyclic load are referred to as fracture and fatigue failure, respectively. As components of most machines, vehicles, and structures are subjected to fatigue loading, it will be the focus of much of the remainder of this report.

There are currently three main approaches used to analyze and design against fatigue failures. The traditional approach, known as the stress-based approach, considers an analysis based on the average stresses in the area of the component being analyzed. In other words, "…the nominal stress that can be resisted under cyclic loading is determined by considering mean stresses and by making adjustments for the effects of stress raisers, such as grooves, holes, fillets, and keyways…" [Dowling, 1993]. Due to its relative simplicity, this approach is still used frequently today for quick, preliminary approximations. The strain-based approach, on the other hand, requires a more detailed analysis of any "…localized yielding that may occur at stress raisers during cyclic loading…" [Dowling, 1993]. Finally, there is the fracture mechanics approach, which has become the preferred approach among most engineers. This approach considers the effects of a growing crack on the strength of a component. The theory of fracture mechanics will be the focus of Chapter 2.

Chapter 2
Fracture Mechanics

2.1 Introduction

Various theories of fracture mechanics have been developed over the years as a means of analyzing and predicting the failure of cracked components. Early developments in fracture mechanics date back to the early 1900's; however, fracture mechanics has been greatly refined since the days of Griffith and Irwin. Present-day fracture mechanics is comprised of two major methodologies, namely Linear Elastic Fracture Mechanics (LEFM) and Elastic Plastic Fracture Mechanics (EPFM) (also known as Nonlinear Elastic Fracture Mechanics). These methodologies have incorporated several fracture parameters, which are used to describe the stress field that exists around a crack tip, and also serve as a basis for failure prediction. These parameters are generally accompanied by the subscripts I, II, or III, depending on the mode of loading to which a particular component is subjected. The three modes of loading are illustrated in Figure 2.1. Mode I, known as the opening mode, applies to a load acting perpendicular to the crack plane and causing the crack faces to move apart. Mode II is referred to as the sliding mode and applies to in-plane shear loading, which causes the crack surfaces to slide over each other in the same plane. Lastly, mode III loading, the tearing mode, occurs when out-of-plane shear loading causes the crack surfaces to slide in the plane of the crack and parallel to the leading edge of the crack.

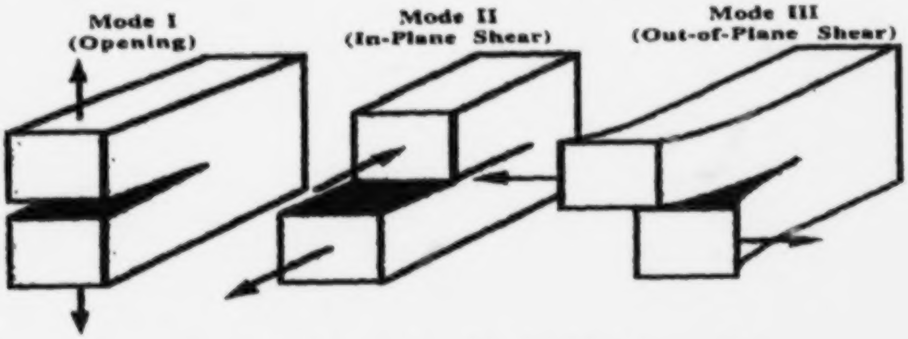

Figure 2.1 – Three modes of loading [Anderson, 1995]

Any one mode or combination thereof can be used to fully describe a given component subjected to any type of arbitrary loading. In practice, however, the majority of crack problems are caused by mode I loading. In fact, modes II and III seldom occur individually, but may occur in combination with mode I loading.

It should not be forgotten that, in addition to fracture, a cracked component may fail due to yielding of the remaining cross section, depending on which of these two competing criteria is satisfied first. Therefore, predicting the failure of a cracked component based solely on a fracture mechanics analysis could prove disastrous, and the conditions governing yielding of the component must be considered as well.

Several important aspects of fracture mechanics will be discussed in the next few sections.

2.2 Linear Elastic Fracture Mechanics (LEFM)

As the name suggests, Linear Elastic Fracture Mechanics (LEFM) was developed for use with materials that obey Hooke's Law. It is also necessary that these materials exhibit little or no plastic deformation ahead of the crack tip. General conditions governing the applicability of LEFM are given by Equation 2.1 and illustrated in Figure 2.2.

$$a,(b-a),h \geq \frac{4}{\pi}\left(\frac{K}{\sigma_y}\right)^2 \quad \text{(LEFM Applicable)} \qquad (2.1)$$

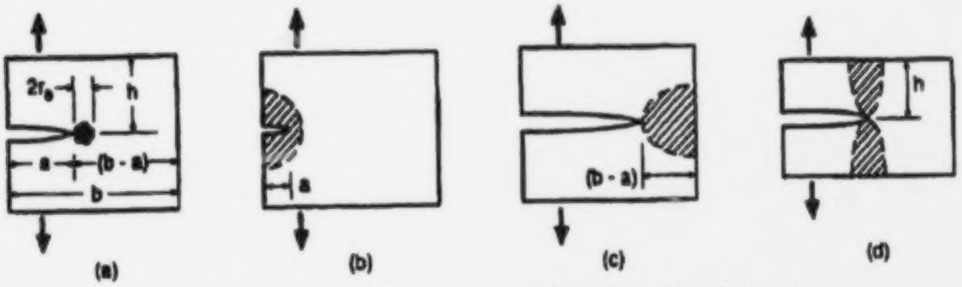

Figure 2.2 – Conditions for which LEFM is (a) valid, and (b,c,and d) invalid [Dowling, 1993]

The term "K" in Equation 2.1 is known as the stress intensity factor, and will be discussed in the next section. For applied stresses slightly higher than permitted by Equation 2.1, a plastic zone adjustment may be made to extend the validity of the LEFM approach. This technique will be covered in section 2.2.4 of this report.

2.2.1 The Stress Intensity Factor (K)

One of the most commonly used fracture parameters for LEFM is the stress intensity factor (K). In any stressed material, a crack acts as a stress raiser, typically producing high stress gradients near the crack tip. Figure 2.3 shows an infinitely wide plate containing a sharp crack (of arbitrary width) and subjected to mode I loading. For such a plate, it has been shown that the stresses at any point with coordinates (r,θ) are given by Equation 2.2. The term "K_I" in the elastic stress field equations (Equation 2.2) denotes the stress intensity factor for mode I loading. The stress intensity factor essentially describes the severity of the crack as a function of the applied (far-field) stress, crack size, and specimen geometry. The stress intensity factor should not be confused with the stress concentration factor, which is usually denoted by the symbol "k_t". Equation 2.3a represents the general equation for the stress intensity factor; however, Equation 2.3b is the more commonly used expression. In equation 2.3b, σ represents the gross far-field stress applied to the section, a is the half crack length, and Y is a correction factor for a given mode of loading, section geometry and crack configuration. Expressions for this factor have been determined experimentally for many common crack configurations and are available in various handbooks and textbooks.

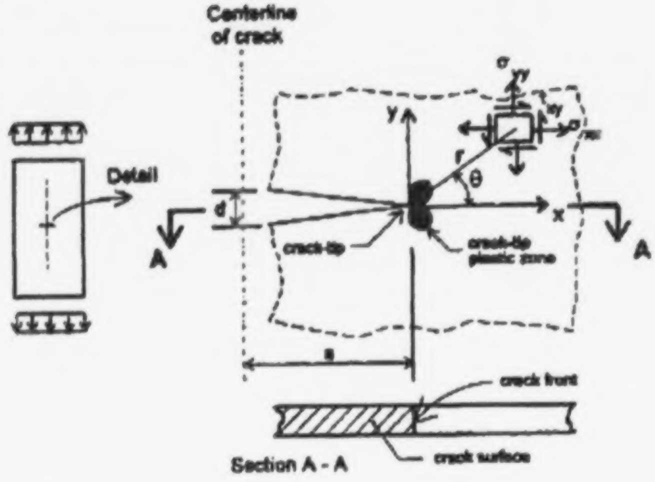
Centerline of crack
Detail
d
A
A
y
x
r
θ
σ_{yy}
τ_{xy}
σ_{xx}
crack-tip
crack-tip plastic zone
a
crack front
Section A - A
crack surface

Figure 2.3 – Center-cracked plate of infinite width, subjected to mode I loading [Trask, 1998]

$$\sigma_x = \frac{K_I}{\sqrt{2\pi r}} \cos\frac{\theta}{2}\left[1 - \sin\frac{\theta}{2}\sin\frac{3\theta}{2}\right] + \ldots \qquad (2.2a)$$

$$\sigma_y = \frac{K_I}{\sqrt{2\pi r}} \cos\frac{\theta}{2}\left[1 + \sin\frac{\theta}{2}\sin\frac{3\theta}{2}\right] + \ldots \qquad (2.2b)$$

$$\tau_{xy} = \frac{K_I}{\sqrt{2\pi r}} \cos\frac{\theta}{2}\sin\frac{\theta}{2}\cos\frac{3\theta}{2} + \ldots \qquad (2.2c)$$

$$\sigma_z = 0 \quad \text{(planestress)} \qquad (2.2d)$$

$$\sigma_z = \nu(\sigma_x + \sigma_y) \quad \text{(planestrain)} \qquad (2.2e)$$

$$\tau_{yz} = \tau_{xz} = 0 \qquad (2.2f)$$

$$K_I = \lim_{r,\theta \to 0} (\sigma_y \sqrt{2\pi r}) \qquad (2.3a)$$

$$K_I = Y\sigma\sqrt{\pi a} \qquad (2.3b)$$

By replacing K_I with K_{II} and K_{III} (respectively), and then substituting the proper shear stress (τ_{xz} or τ_{yz}) for the applied stress σ, the stress intensity factors for mode II and III loading can be determined using Equation 2.3b. It should be pointed out, however, that the evaluation of the stress intensity factors for mode II and mode III is generally more difficult.

For cases involving more complex loading and crack configurations, the principle of superposition can be used to determine the overall stress intensity factor, as illustrated by Figure 2.4, Figure 2.5 and Figure 2.6. From Figure 2.6, one can see that $K_{Ia} = K_{Ic}$ and further deduce that $K_{Ia} = 0.5(K_{Ib} + K_{Id})$.

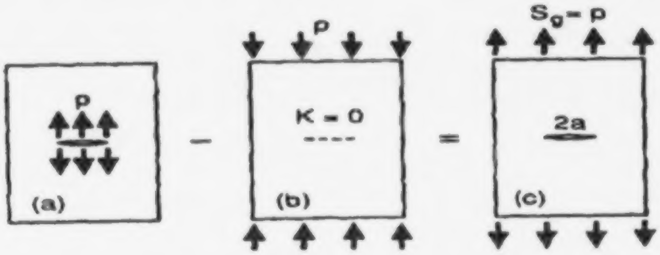

Figure 2.4 – Superposition of stress intensity factors (Example 1) [Dowling, 1993]

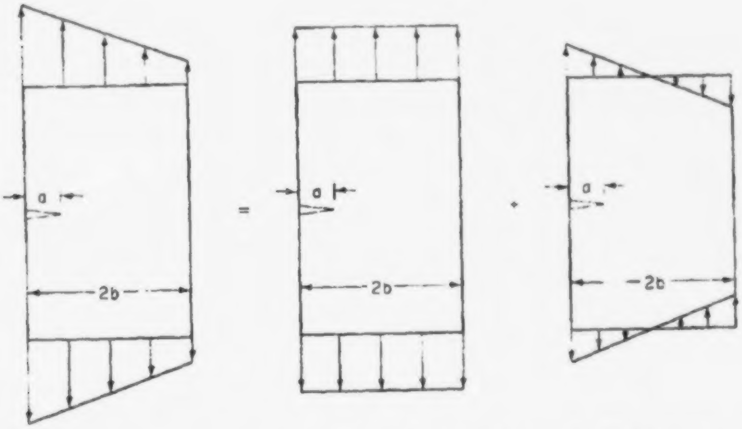

Figure 2.5 – Superposition of stress intensity factors (Example 2) [Barsom et al., 1987]

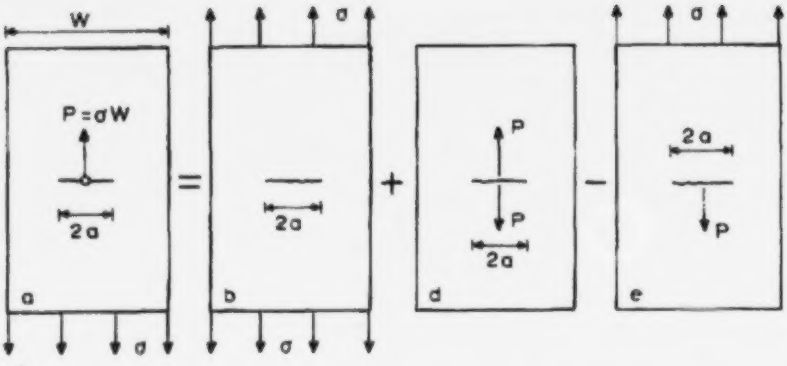

Figure 2.6 – Superposition of stress intensity factors (Example 3) [Broek, 1982]

2.2.1.1 Stress Intensity Factors for Mixed-Mode Loading

Although the occurrence of mixed-mode loading is not as predominant as pure mode I loading, a discussion of the stress intensity factor would not be complete without a brief mention of mixed-mode loading.

Even when a cracked component is subjected to purely mode I tensile loading, "…mixed-mode conditions may prevail ahead of the crack tip if it is inclined at some arbitrary angle to the tensile axis, or microstructural and environmental factors promote nonplanar fatigue crack growth…" [Suresh, 1998]. For example, a fatigue crack located at the lamina interface of two different materials within a composite is typically subjected to localized mixed-mode loading, even though the applied loading may be entirely mode I. Mixed-mode loading can greatly affect the size of the plastic zone ahead of the crack tip, the crack propagation rate, even the extent of crack closure and fatigue damage. Consider the case of a plate containing a crack oriented at an angle of 90°-β with the applied stress, as shown in Figure 2.7. In this case, the crack is subjected to combined mode I and mode II loading. If the coordinate axis is oriented such that it coincides with the crack, the applied stress can be resolved into its normal and shear components. The resolved components can then be substituted into Equation 2.3b to calculate the stress intensity factors K_I and K_{II} given in Equation 2.4.

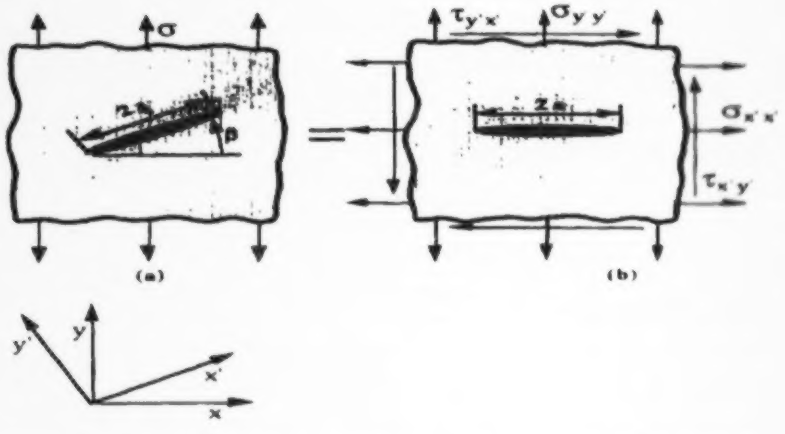

Figure 2.7 – Plate containing a crack oriented at angle β [Anderson, 1995]

$$K_I = Y\sigma\cos^2\beta\sqrt{\pi a} \tag{2.4a}$$

$$K_{II} = Y\sigma\sin\beta\cos\beta\sqrt{\pi a} \tag{2.4b}$$

In addition, the deflection of a mode I fatigue crack can induce mixed-mode conditions at the crack tip. Figure 2.8a represents a fatigue crack of length a, with a deflected portion (or kink) of length b inclined at an angle α with the plane of the main crack. Figure 2.8b shows a symmetrically forked crack (one containing two kinks) with an included angle of 2α. The local mode I and mode II stress intensity factors (k_1 and k_2) are given by Equation 2.5, in which K_I and K_{II} represent the mode I and mode II stress intensity factors for the main crack (in the absence of a kink or fork).

$$k_1 = a_{11}(\alpha)K_I + a_{12}(\alpha)K_{II} \tag{2.5a}$$

$$k_2 = a_{21}(\alpha)K_I + a_{22}(\alpha)K_{II} \tag{2.5b}$$

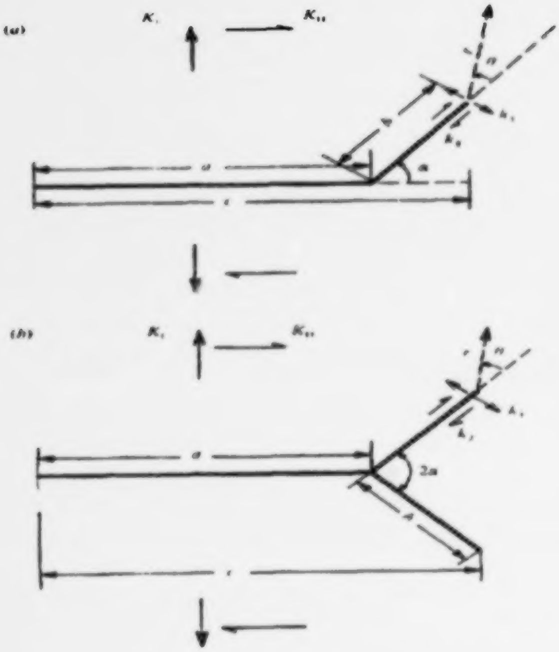

Figure 2.8 – Representation of (a) a kinked and (b) a forked fatigue crack [Suresh, 1998]

First order approximations of the dimensionless factors $a_{ij}(\alpha)$ are given by Equation 2.6

$$\begin{aligned} a_{11}(\alpha) &= \frac{1}{4}\left(3\cos\frac{\alpha}{2} + \cos\frac{3\alpha}{2}\right) \\ a_{12}(\alpha) &= -\frac{3}{4}\left(\sin\frac{\alpha}{2} + \sin\frac{3\alpha}{2}\right) \\ a_{21}(\alpha) &= \frac{1}{4}\left(\sin\frac{\alpha}{2} + \sin\frac{3\alpha}{2}\right) \\ a_{22}(\alpha) &= \frac{1}{4}\left(\cos\frac{\alpha}{2} + 3\cos\frac{3\alpha}{2}\right) \end{aligned} \tag{2.6}$$

Figures 2.9a and 2.9b can also be used to determine the local stress intensity factors (k_1 and k_2).

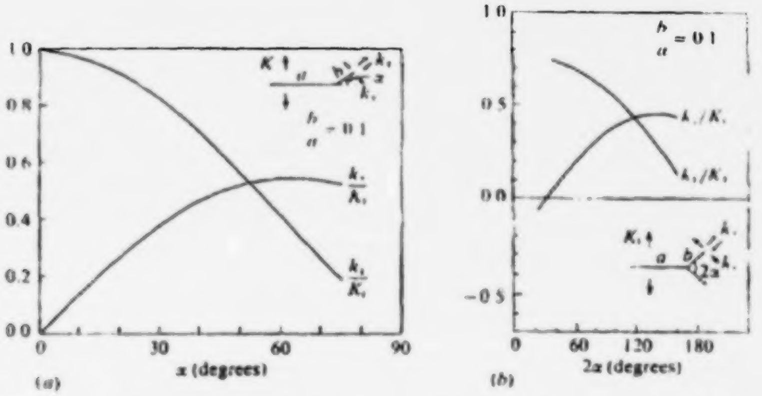

Figure 2.9 – Local stress intensity factors (k_1 and k_2) as a function of (a) kink angle α, and (b) fork angle 2α [Suresh, 1998]

In an effort to provide somewhat of a fracture criteria for components subjected to mixed-mode loading, Dowling (1993) suggests the use of Equation 2.7, which represents an elliptical failure envelope.

$$\left(\frac{K_I}{K_{Ic}}\right)^2 + \left(\frac{K_{II}}{K_{IIc}}\right)^2 \leq 1 \tag{2.7}$$

The terms K_{Ic} and K_{IIc} in Equation 2.7 denote the mode I and mode II fracture toughness, respectively. A similar equation could be used as a fracture criteria for components subjected to combined mode I and mode III loading. The concept of material fracture toughness will be the focus of section 2.2.1.2 of this report.

2.2.1.2 Material Fracture Toughness (K_c)

Every material has an ultimate strength that will induce fracture. Similarly, there exists a stress intensity factor above which fracture will occur. This value, referred to as fracture toughness, is a material property governed by ASTM Standard No. E399, entitled "*Standard Test Method for Plane Strain Fracture Toughness of Metallic Materials*", and is usually denoted by the symbol K_c. Fracture toughness carries units of MPa$\sqrt{m}$, and varies greatly depending on the material in question. For example, steel typically has a fracture toughness in the range of 50 MPa$\sqrt{\text{m}}$ to 200 MPa$\sqrt{\text{m}}$, while the fracture toughness of aluminum alloys usually falls in the range of 30 MPa$\sqrt{\text{m}}$ to 40 MPa$\sqrt{\text{m}}$. On the other hand, most ceramics and polymers have a much lower fracture toughness, generally lying between 1 MPa$\sqrt{\text{m}}$ and 5 MPa$\sqrt{\text{m}}$.

A discussion of the stress intensity factor would not be complete without a brief mention of the various factors affecting fracture toughness. A material's fracture toughness is affected by a number of variables, including thickness, yield strength, temperature, and loading rate.

The effect of thickness on fracture toughness is illustrated in Figure 2.10, in which both the plane strain and plane stress fracture toughness are collectively denoted by K_Q (due to the transition from plane stress to plane strain with increasing thickness). For most metals, fracture toughness tends to decrease with increasing specimen thickness. As the specimen thickness increases, a transition from plane stress to plane strain takes place and the characteristics of the plastic zone ahead of the crack tip also change. Provided the specimen thickness exceeds the requirement of Equation 2.8 below, the fracture toughness is considered constant. This constant value represents a lower bound, or worst case fracture toughness, and is called the plane strain fracture toughness.

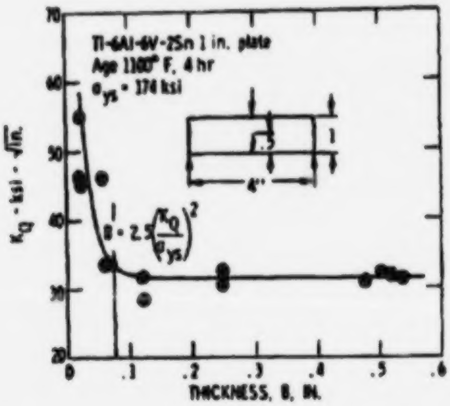

Figure 2.10 – Effect of thickness on fracture toughness [Dowling, 1993]

$$t \geq 2.5\left(\frac{K_c}{\sigma_{yld}}\right)^2 \tag{2.8}$$

It has been observed that fracture toughness tends to decrease with increasing yield strength, as illustrated in Figure 2.11. On the other hand, it has a tendency to increase with temperature, as shown in Figure 2.12.

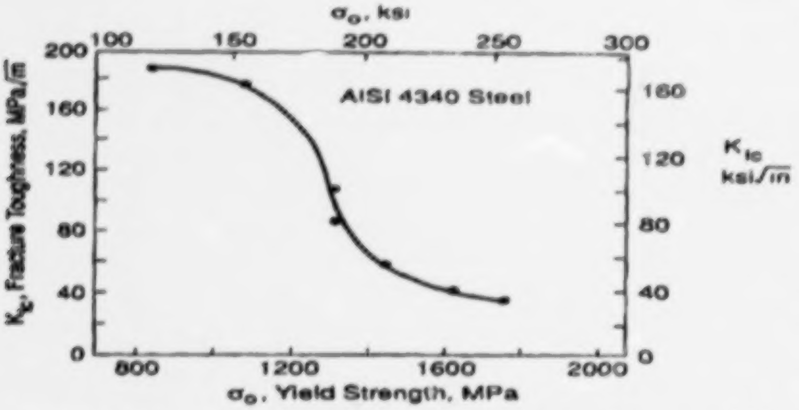

Figure 2.11 – Effect of yield strength on fracture toughness [Dowling, 1993]

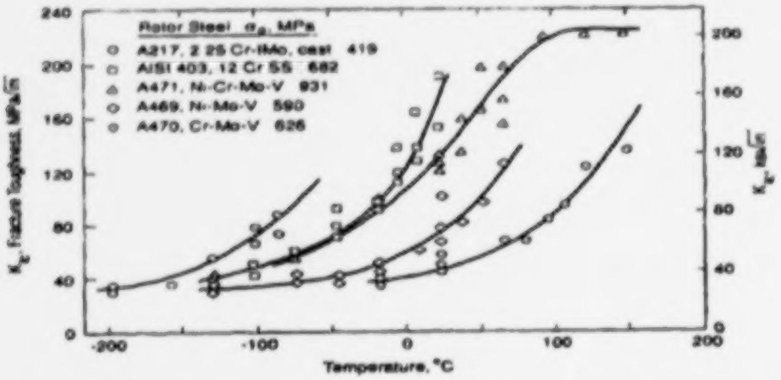

Figure 2.12 – Effect of temperature on fracture toughness [Dowling, 1993]

As illustrated in Figure 2.12, there is a noticeable transition from a lower-level fracture toughness to an upper-level fracture toughness. This phenomenon can be explained in terms of both an increase in ductility (caused by an increase in temperature) and an apparent shift in the physical mechanism of fracture from one of cleavage (little plastic deformation) to one of ductile tearing (large amount of plastic deformation).

A material's sensitivity to loading rate also plays a very important role in defining its fracture toughness. A higher rate of loading generally reduces a material's fracture toughness, an effect similar to decreasing the temperature. Figure 2.13 shows that at a given temperature, an increase in loading rate can cause a dramatic reduction in fracture toughness. For specimens tested at slower loading rates, the aforementioned transition from brittle to ductile behavior begins at a lower temperature than for similar specimens tested at relatively high loading rates.

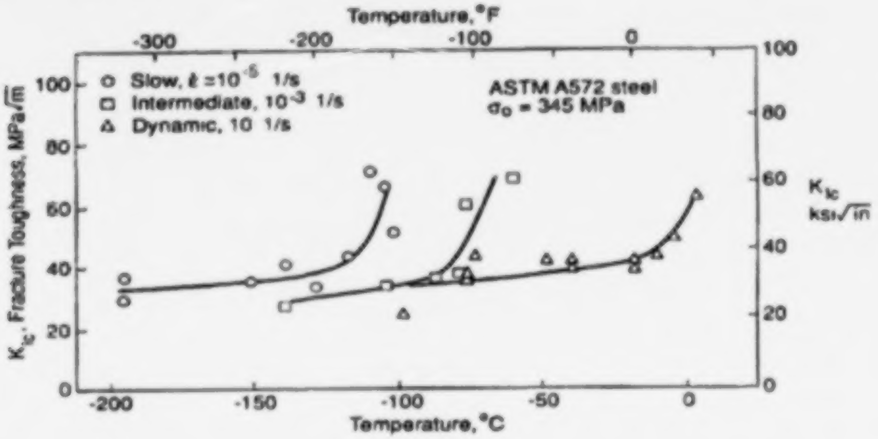

Figure 2.13 – Effect of loading rate on fracture toughness [Dowling, 1993]

2.2.2 The Strain Energy Release Rate (G)

The concept of the strain energy release rate is based on the fact that when a body undergoes elastic deformation, elastic strain energy is stored within the body. As a crack grows through the body, the stored energy is released and is essentially consumed during the production of new crack surfaces.

In deriving an expression for the strain energy release rate, one must first consider a plate with a crack extending through its thickness. Recall that Griffith theorized "…for a unit crack extension to occur under the influence of the applied stress, the decrease in potential energy of the system, by virtue of the displacement of the outer boundaries and the change in the stored elastic energy, must equal the increase in surface energy due to crack extension…" [Suresh, 1998]. The total potential energy (π) for the system is given by Equation 2.9, in which U represents the work done internally (strain energy), F denotes the work done by the applied loads, and W is the work required to fracture the material over an incremental length of da.

$$\pi = U - F + W \tag{2.9}$$

Differentiating Equation 2.9 with respect to crack length a and setting the derivative equal to zero (minimum potential energy theory), one obtains an expression that represents the conservation of energy principle per unit thickness.

$$\frac{d\pi}{da} = 0 = \frac{dU}{da} - \frac{dF}{da} + \frac{dW}{da} \tag{2.10a}$$

$$\frac{d}{da}(F - U) = \frac{dW}{da} \tag{2.10b}$$

Consider first a typical load versus displacement record corresponding to an incremental increase in crack length (da) at constant displacement (as illustrated in Figure 2.14). As the crack is extended by an amount da, the stiffness of the specimen is reduced and consequently, a smaller applied load is required to maintain the constant displacement. Furthermore, since a constant displacement is maintained, the applied load does no work and thus the dF term in Equation 2.10b reduces to zero. Referring to Figure 2.14, area OAB ($^1/_2\,P_1\delta_1$ minus $^1/_2\,P_2\delta_1$) represents the decrease in internal energy (strain energy) as the crack is extended. According to Equation 2.10b, this amount must be equal to the work required to fracture the material and lengthen the crack by an incremental amount da (i.e., dW/da).

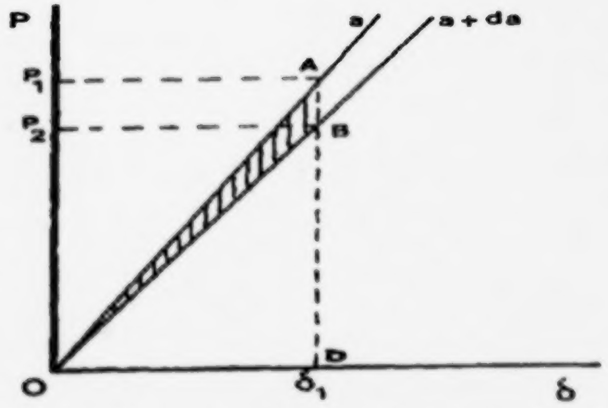

Figure 2.14 – Crack extension at constant displacement [Broek, 1989]

Next, consider the case in which the load remains constant as the plate fractures over da (as illustrated in Figure 2.15 below). Although the load remains constant here, it does work in the amount of $P_1(\delta_2\text{-}\delta_1)$. There is also a change in strain energy, namely an increase from $^1/_2\ P_1\delta_1$ to $^1/_2\ P_1\delta_2$ (i.e., $^1/_2\ P_1(\delta_2\text{-}\delta_1)$). Substituting these values into Equation 2.10b, one can see that the available energy for fracture is $^1/_2\ P_1(\delta_2\text{-}\delta_1)$, which is exactly equal to the change in strain energy during crack extension (i.e., dU/da).

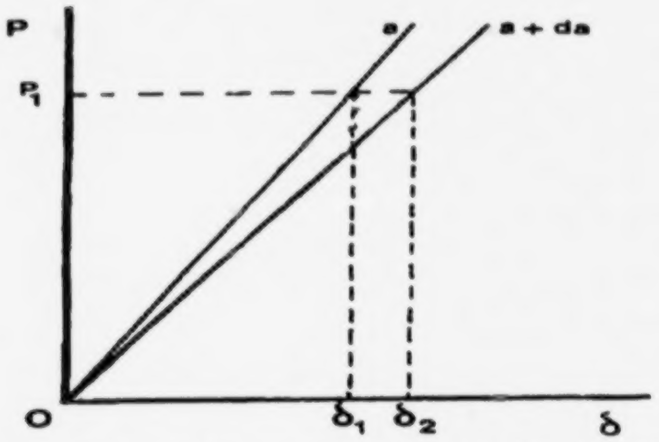

Figure 2.15 – Crack extension at constant load [Broek, 1989]

It seems that the energy available for fracture, regardless of whether it occurs under constant load or constant displacement, is always the same (i.e., dU/da). One could consider Equation 2.10b as somewhat of a fracture criterion. It essentially states that if there is a large enough energy surplus (in the form of d(F-U)/da) to satisfy the fracture energy required (dW/da), then fracture will occur. If one denotes the strain energy release rate (G) by dW/da, then Equation 2.10b yields the following expressions:

$$G = \frac{dW}{da} = -\frac{dU}{da} \qquad \text{(per unit thickness)} \qquad (2.11a)$$

$$G = -\frac{1}{t}\frac{dU}{da} \qquad \text{(thickness "t")} \qquad (2.11b)$$

The strain energy release rate (G) essentially represents the change in energy (dU) required per increment of crack area (t x da) to lengthen the crack by an amount da The negative sign simply means that this energy must be released from the system during fracture.

The dU/da term in Equation 2.11b depends on the specimen geometry and loading condition. As an example, dU/da will be evaluated for a center-cracked plate subjected to mode I tensile loading. Because the plate's strain energy is affected by the presence of a crack, one must combine the strain energy due to the crack and the strain energy of the uncracked plate to yield the total strain energy of the plate. In the case of an uncracked plate, the axial strain energy density (U_o) at any point is given by the area under the stress strain curve up to that point. However, since we are dealing with a linear elastic material, the integration is greatly simplified.

$$U_{o,Axial} = \int \sigma d\varepsilon = \frac{1}{2}\frac{\sigma^2}{E} \qquad \text{(linear elastic material)} \quad (2.12)$$

The strain energy density must be further integrated over the entire volume to obtain the total strain energy for the uncracked plate. The integration here is simplified because the plate is subjected to an axial load only, and thus σ is not a function of x, y, or z coordinates.

$$U_{\text{Uncracked}} = \iiint \frac{\sigma^2}{2E} \, dxdydz = \frac{\sigma^2}{2E} LWt \tag{2.13}$$

As for the cracked plate, the strain energy due to a crack of length 2a is equal to the plate's axial strain energy density (Equation 2.12) multiplied by the volume of material affected by the crack. The volume of affected material can be approximated by projecting the area of an ellipse (as illustrated in Figure 2.16) through the plate's thickness.

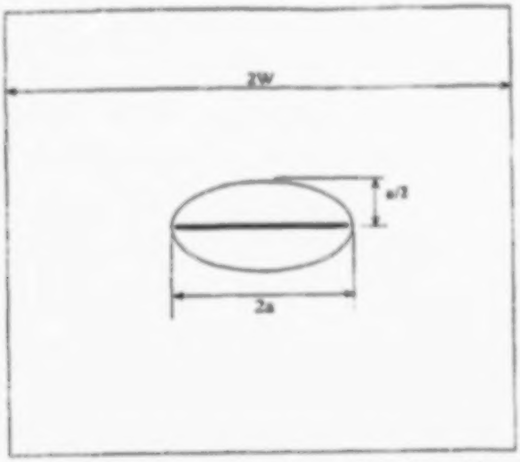

Figure 2.16 – Area within which strain energy is affected by a central crack

Equation 2.14 represents the strain energy due to the crack.

$$U_{\text{Crack}} = [\pi(2a)(a)t](\frac{\sigma^2}{2E}) = 2\pi a^2 t(\frac{\sigma^2}{2E}) = \frac{\pi\sigma^2 a^2 t}{E} \tag{2.14}$$

Combining Equation 2.13 and Equation 2.14, and differentiating with respect to crack length a, we have the following expressions for the strain energy and strain energy release rate for a cracked plate:

$$U_{Total} = U_{Uncracked} + U_{Crack} = \frac{\sigma^2}{2E}LWt + \frac{\pi\sigma^2 a^2 t}{E} \qquad (2.15)$$

$$\frac{dU_{Total}}{da} = \frac{2\pi\sigma^2 at}{E} \qquad (2.16)$$

However, this applies to a central crack of thickness 't'. By dividing Equation 2.16 by 2t, we have an expression for the strain energy release rate per crack tip and per unit thickness (note the negative sign has been omitted):

$$(2.17) \quad G = \frac{dU_{Total}}{da} = \frac{\pi\sigma^2 a}{E}$$

A critical strain energy release rate (G_c) can be determined experimentally, analogous to the critical stress intensity factor (K_c) mentioned earlier. It can be shown that G and K are directly related by the following:

$$G = \frac{K^2}{E} \qquad \text{(plane stress)} \qquad (2.18a)$$

$$G = \frac{(1-\nu)K^2}{E} \qquad \text{(plane strain)} \qquad (2.18b)$$

Both fracture parameters (G and K) can be used when the plastic zone ahead of the crack tip is expected to be small. However, the stress intensity factor (K) has become the preferred LEFM fracture parameter.

2.2.3 Crack Tip Plastic Zones

The elastic stress field equations (Equation 2.2) predict infinite stresses at the tip of a sharp crack, where both r and θ are zero. Obviously, infinite stresses cannot be supported by real materials. Instead, the crack tip becomes blunted upon loading and a region of yielding and intense deformation is formed, known as the plastic zone.

Under plane stress conditions, the elastic stress field equations (Equation 2.2) predict the following stresses in the plane of the crack (where θ is equal to zero):

$$\sigma_x = \sigma_y = \frac{K_I}{\sqrt{2\pi r}} \tag{2.19a}$$

$$\sigma_z = \tau_{xy} = \tau_{yz} = \tau_{xz} = 0 \tag{2.19b}$$

Substitution of these stresses into either the von Mises or the maximum shear stress yield criteria predict yielding at $\sigma_x = \sigma_y = \sigma_{yld}$. Further substitution into Equation 2.19a yields an expression known as Irwin's first estimate of plastic zone size:

$$r_{o\sigma} = \frac{1}{2\pi}\left(\frac{K}{\sigma_{yld}}\right)^2 \tag{2.20}$$

This is simply the distance ahead of the crack tip where the theoretical elastic stress is equal to the stress predicted by the aforementioned yield criteria. However, yielding within the plastic zone results in stresses lower than those predicted by Equation 2.2. Therefore, within this initial plastic zone, material resistance is less than expected, thus causing the plastic zone to be extended further than estimated by Equation 2.20 (as illustrated in Figure 2.17).

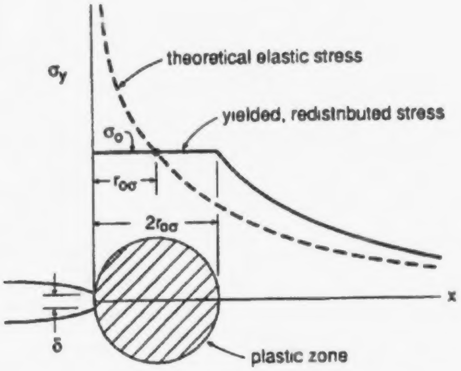

Figure 2.17 – Irwin's approximation of plane stress plastic zone size [Dowling, 1993]

It has been generally accepted that yielding extends to a distance $2r_{o\sigma}$ beyond the crack tip. Therefore, a more refined estimate of Irwin's plastic zone size is given by Equation 2.21.

$$r_p = 2r_{o\sigma} = \frac{1}{\pi}\left(\frac{K}{\sigma_{yld}}\right)^2 \tag{2.21}$$

A similar prediction of plane stress plastic zone size, known as the Dugdale approximation, is given by Equation 2.22. In the Dugdale model, however, the plastic zone is approximated as a narrow strip of yielded material ahead of the crack tip.

$$r_p = \frac{\pi}{8}\left(\frac{K}{\sigma_{yld}}\right)^2 \tag{2.22}$$

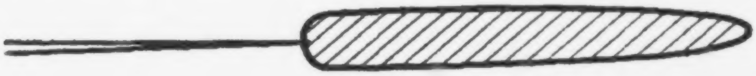

Figure 2.18 – Dugdale's approximation of plane stress plastic zone size [Lui, 1998]

Under plane strain conditions, σ_z is nonzero, which elevates the value of σ_x and σ_y (which are equal) required to cause yielding. The commonly used Irwin approximation of plane strain plastic zone size (Equation 2.23) estimates a plastic zone three times smaller than that given by Equation 2.21 for plane stress.

$$2r_{o\varepsilon} = \frac{1}{3\pi}\left(\frac{K}{\sigma_{yld}}\right)^2 \tag{2.23}$$

The crack tip of any specimen may, in fact, simultaneously experience plane stress and plane strain conditions. For example, consider the crack tip in a plate of thickness 't' subjected to mode I loading. Further consider two elements along the crack front: one near mid-thickness and one near the edge. The element near mid-thickness is restricted from moving in the z-direction, while the element near the edge is free to move in the z-direction. Therefore, as illustrated in Figure 2.19, there is a transformation from a condition of plane strain (near the center of the crack front) to that of plane stress (near the edges of the crack front).

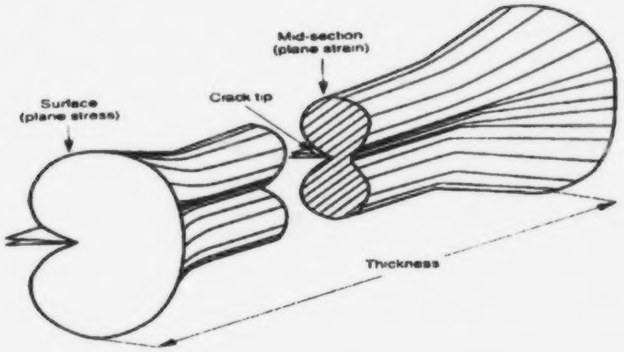
Mid-section
(plane strain)
Surface
(plane stress)
Crack tip
Thickness

Figure 2.19 – Through-thickness plastic zone variation [Lui, 1998]

Thus far, the discussion of crack tip plastic zone size has focused mainly on loading that is monotonic in nature. Therefore, a brief mention of the effects of cyclic loading on plastic zone size is in order. Consider a cracked plate of an elastic material subjected to a remote tensile load P. A monotonic plastic zone of size r_p (as given by Equations 2.21 and 2.22) is created as a result of material yielding at the crack tip. If the load is then reduced to a tensile load of P-ΔP, reversed plastic flow is initiated. As illustrated in Figure 2.20, a zone of reversed plastic flow is created within the already existing plastic zone.

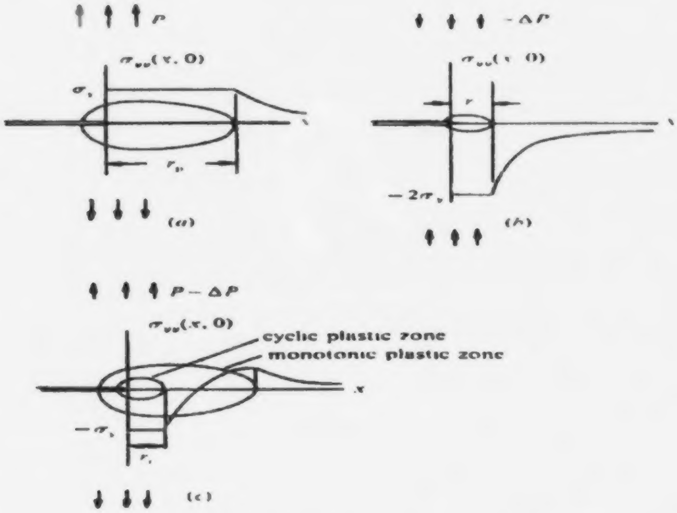
P
$\sigma_{yy}(x, 0)$
σ_y
r_p
(a)
$-\Delta P$
$\sigma_{yy}(x, 0)$
$-2\sigma_y$
(b)
$P-\Delta P$
$\sigma_{yy}(x, 0)$
cyclic plastic zone
monotonic plastic zone
x
$-\sigma_y$
r_c
(c)

Figure 2.20 – Cyclic plastic zone [Suresh, 1998]

Therefore, in the case of a crack which is "...only partially unloaded from a far-field tensile load, there exists within the monotonic plastic zone a region of reversed flow (termed the cyclic plastic zone) of size r_c, in which residual compressive stresses are induced..." [Suresh, 1998]. Slightly modifying Irwin's plane stress estimate to account for reversed plastic flow, we have an expression for the size of the cyclic plastic zone:

$$r_c = \frac{1}{\pi}\left(\frac{\Delta K}{2\sigma_{yld}}\right)^2 \tag{2.24}$$

Similarly, if the remote load were compressive, a zone of residual tensile stress would result. Even after the remote load has been fully removed, this zone of residual stress remains, and can have a significant effect on variable amplitude fatigue crack growth.

2.2.4 Extension of LEFM Validity: Plastic Zone Adjustment

Recalling Equation 2.1 and Figure 2.2, the validity of LEFM requires that the plastic zone ahead of the crack tip be relatively small. If it is small enough, there will be an area surrounding it for which the elastic stress field equations (Equation 2.2) still apply. In cases where the limits of Equation 2.1 are tested, the value of K can be slightly increased via a plastic zone adjustment. This procedure extends the applicability of LEFM to stress levels beyond the limits of Equation 2.1.

As one can see from Figure 2.17, the redistributed stresses outside the plastic zone are analogous to those predicted by the elastic stress field equations (Equation 2.2). The only difference appears to be a horizontal shift (of the crack tip) through a distance $r_{o\sigma}$. Therefore, consider a hypothetical crack of the following length:

$$a_{eff} = a + r_{o\sigma} = a + \frac{1}{2\pi}\left(\frac{K}{\sigma_{yld}}\right)^2 \tag{2.25}$$

Substituting Equation 2.25 into Equation 2.3b yields the following expression for an effective stress intensity factor (accounting for excessive plastic zone yielding):

$$K_{eff} = Y\sigma\sqrt{\pi\left[a + \frac{1}{2\pi}\left(\frac{K_{eff}}{\sigma_{yld}}\right)^2\right]}$$

$$K_{eff}^2\left[\left(\frac{1}{Y\sigma}\right)^2 - \frac{1}{2}\left(\frac{1}{\sigma_{yld}}\right)^2\right] = \pi a$$

$$K_{eff}^2 (Y\sigma)^2\left[\left(\frac{1}{Y\sigma}\right)^2 - \frac{1}{2}\left(\frac{1}{\sigma_{yld}}\right)^2\right] = \pi a (Y\sigma)^2$$

$$K_{eff}^2\left[1 - \frac{1}{2}\left(\frac{Y\sigma}{\sigma_{yld}}\right)^2\right] = \pi a (Y\sigma)^2$$

$$K_{eff} = Y\sigma\sqrt{\frac{\pi a}{1 - \frac{1}{2}\left(\frac{Y\sigma}{\sigma_{yld}}\right)^2}} \qquad \text{(plane stress)} \quad (2.26)$$

In a similar fashion, K_{eff} corresponding to plane strain conditions is calculated as follows:

$$K_{eff} = Y\sigma\sqrt{\frac{\pi a}{1 - \frac{1}{6}\left(\frac{Y\sigma}{\sigma_{yld}}\right)^2}} \qquad \text{(plane strain)} \quad (2.27)$$

With the development of nonlinear elastic fracture mechanics, this method currently receives only moderate usage. Furthermore, if the applied loads were to cause stresses that could yield the entire cross section, then the use of an effective crack length becomes disputable. Therefore, it is generally recommended that this approach, if chosen over those of EPFM, be limited to loads and moments below 80% of their fully plastic values.

2.3 Elastic Plastic Fracture Mechanics (EPFM)

In many instances, considerable plastic deformation occurs at the crack tip, and the limits of LEFM (Equation 2.1) are exceeded. Unfortunately, when used beyond the limits of its applicability, LEFM can yield unconservative estimates of strength and useful service life, etcetera. In such cases, an alternative concept, known as Elastic Plastic Fracture Mechanics (EPFM), must be employed, which can deal with the presence of large plastic zones ahead of the crack tip.

There are two fracture parameters commonly used with EPFM, namely the J contour integral and the crack tip opening displacement (CTOD). The development of these two fracture parameters will be the focus of the next few sections of this report. Although the J integral and CTOD are extremely useful in cases where extensive plastic deformation has occurred, they are not valid for cases in which the remaining uncracked section of the component has yielded. This situation obviously corresponds to the plastic collapse of the member and not to its fracture.

2.3.1 The J Contour Integral

The J integral, aside from having the ability to handle materials that exhibit large plastic zones and nonlinear stress-strain relationships, is based on essentially the same principle as the LEFM strain energy release rate parameter, G. The J integral can be thought of as a generalization of the strain energy release rate to cases in which the limits of LEFM (and therefore, the validity of G) have been exceeded. As with the LEFM parameters K and G, the J integral has a critical value for mode I loading, J_{Ic}, above which fracture will theoretically occur. ASTM Standard No. 813, entitled "*Standard Test Method for J_{Ic}, A Measure of Fracture Toughness*" governs the evaluation of material fracture toughness in terms of the J integral.

To illustrate the generalization of the strain energy release rate to the aforementioned cases, the value of J will be evaluated for a center-cracked plate. Suppose the plate is comprised of a material that exhibits a nonlinear stress-strain curve similar to the one shown in Figure 2.21.

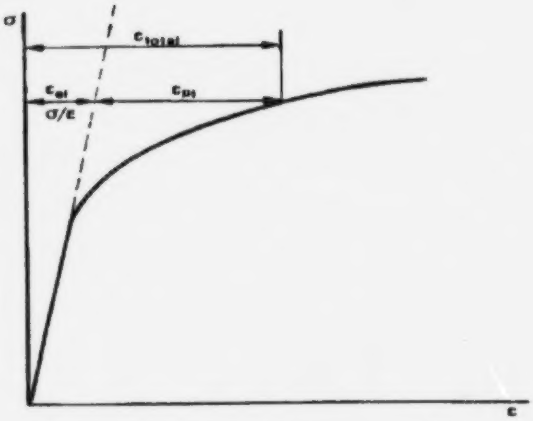

Figure 2.21 – Stress-strain relationship for a nonlinear elastic material [Broek, 1989]

Any empirical curve-fitting equation can be used to describe the stress-strain relationship, as long as it is sufficiently accurate. The most common and most convenient curve fit for such a relationship is a power function. The resulting stress-strain equation (Equation 2.28) is known as the Ramberg-Osgood equation.

$$\varepsilon_{\text{total}} = \varepsilon_{\text{elastic}} + \varepsilon_{\text{plastic}} = \frac{\sigma}{E} + \frac{\sigma^n}{F} \qquad (2.28)$$

In Equation 2.28, n is a strain-hardening exponent and F is a proportionality constant, often called the plastic modulus. The first term in Equation 2.28 represents the elastic portion of the stress-strain curve, while the last term corresponds to the plastic part. The expressions given in Equation 2.11 for the strain energy release rate are still valid, however, in this case, the dU/da term must be modified to include the nonlinear segment of the stress-strain curve of Figure 2.21. The dU/da expression for the linear portion of the curve (Equation 2.17) was previously shown to be equal to $\pi\sigma^2 a/E$ (per crack tip and per unit thickness). Similar to Equations 2.13 and 2.14, the expression for dU/da for the nonlinear portion of the curve is obtained by combining the strain energies of the uncracked plate and the cracked plate. It can be shown that the total strain energy of the nonlinear segment is obtained as follows:

$$U_{\text{Total,Plastic}} = U_{\text{Uncracked,Plastic}} + U_{\text{Cracked,Plastic}}$$

$$U_{\text{Total,Plastic}} = \frac{\sigma^{n+1}LWt}{2F} + H\frac{\sigma^{n+1}a^2t}{F} \tag{2.29}$$

In the above expression, H is a dimensionless plasticity factor, which has been previously evaluated for a number of different specimen configurations. Differentiating Equation 2.29 with respect to crack length a, and dividing by 2t, we have the following expression for dU/da of the plastic portion of the curve (in terms of per crack tip and per unit thickness):

$$\left(\frac{dU}{da}\right)_{\text{Plastic}} = H\frac{\sigma^{n+1}a}{F} \tag{2.30}$$

Combining the dU/da terms for both the elastic and plastic segments of the stress-strain curve (Equations 2.17 and 2.30), and denoting J by dW/da, we have a general expression for the strain energy release rate as it applies to nonlinear elastic materials:

$$J = \frac{dW}{da} = \left(\frac{dU}{da}\right)_{\text{Elastic}} + \left(\frac{dU}{da}\right)_{\text{Plastic}} = \frac{\pi\sigma^2 a}{E} + H\frac{\sigma^{n+1}a}{F} \tag{2.31}$$

In the event that the stress-strain curve is entirely nonlinear, the first term of Equation 2.31 completely vanishes. On the other hand, if the strain hardening exponent is equal to one (an elastic-perfectly plastic material), the Ramberg-Osgood power function reduces to Equation 2.17, thus proving the J integral to be simply a generalization of the strain energy release rate to materials exhibiting nonlinear elastic behavior.

Along with the modulus of elasticity, E, both n and F can be determined from a basic tensile test. At any point on the stress-strain curve, the plastic strain can be calculated using the following relationship:

$$\varepsilon_{\text{Plastic}} = \varepsilon_{\text{Total}} - \varepsilon_{\text{Elastic}} = \varepsilon_{\text{Total}} - \frac{\sigma}{E} = \frac{\sigma^n}{F} \tag{2.32}$$

Taking the logarithms of Equation 2.32, we have the following:

$$\log \varepsilon_{Plastic} = \log \sigma^{n} - \log F = n \log \sigma - \log F \qquad (2.33)$$

If, on a plot of $\log\sigma$ versus $\log(\varepsilon_{Plastic})$, the data falls on a straight line, then the Ramberg-Osgood equation is valid. Furthermore, the slope of this line will be equal to n and the intercept will be equal to –logF. It should be noted the stress-strain relationship for some materials cannot be fully described by the Ramberg-Osgood power function. In order to apply EPFM, however, the power function must be fitted to some portion of the stress-strain curve (for example, high strain or low strain regions). Unfortunately, the decision as to which portion cannot be categorized, but must instead be made on an individual material basis.

The original development of the J integral dates back to the mid-1960's and a professor by the name of J. Rice, who presented a path independent line integral for the analysis of cracks. A commonly used expression for Rice's J integral along any contour encircling the crack tip is given by Equation 2.34.

$$J = \oint (U_o dy - T \frac{du}{dx} ds) \qquad (2.34)$$

In the above expression, U_o represents the strain energy per unit volume (i.e., the strain energy density) and y is measured perpendicular to the crack plane. As illustrated by Figure 2.22a, T is the tension (or traction) acting perpendicular to the closed contour S (followed counter-clockwise), u is the displacement and ds is an increment of arc length along the contour S. The first term of Equation 2.34 represents the strain energy (U), while the second term represents the work done by the force T over a distance described by (du/dx)ds.

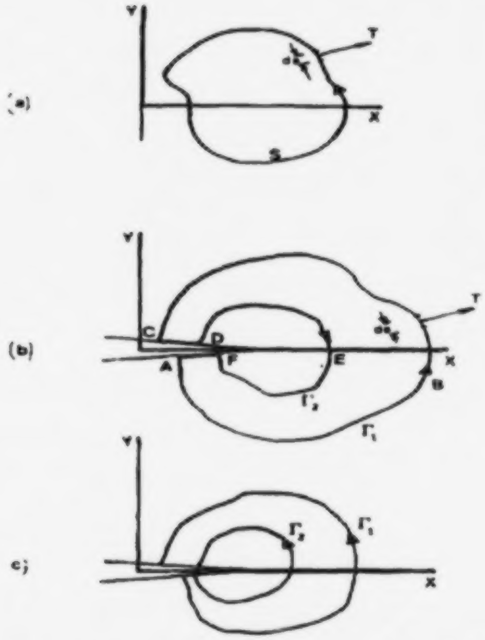

Figure 2.22 – Contour integrals. (a) Elastic body, (b) Cracked body, (c) Path independent contour [Broek, 1989]

Using Equation 2.34 to construct a closed contour around a crack tip, as illustrated by the contour ABCDEF in Figure 2.22b, we have:

$$\int_{\Gamma_1} + \int_{CD} + \int_{\Gamma_2} + \int_{FA} = 0 \qquad (2.35)$$

Assuming the traction forces (T) and dy are negligible along crack faces AF and CD, Equation 2.35 reduces to:

$$\int_{\Gamma_1} + \int_{\Gamma_2} = 0 \text{ or } \int_{\Gamma_1} = -\int_{\Gamma_2} \qquad (2.36)$$

Note that if the integrals along the arbitrary contours Γ_1 and Γ_2 were taken in the same direction, as shown in Figure 2.22c, they would have the same value. The evaluation of this integral will be discussed next.

Consider a simple circular contour of radius r, as illustrated in Figure 2.23, with its center at the crack tip. In this case we have, $y=r\sin\theta$, so that $dy=r\cos\theta\, d\theta$, and $ds=rd\theta$.

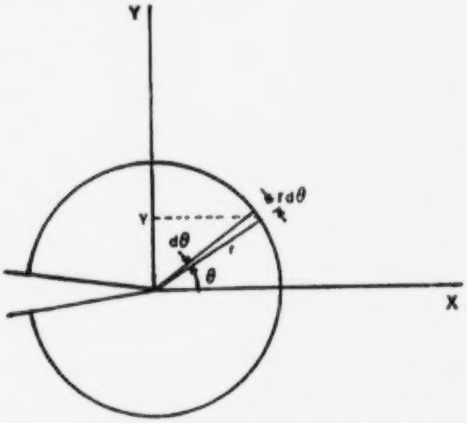

Figure 2.23 – Contour integral based on a simple circular path [Broek, 1989]

After making these substitutions in Equation2.34, and knowing that $U=\int\sigma\, d\varepsilon$, the following expression for the J integral is obtained:

$$J=\int_{-\pi}^{\pi}\left[\left(\int_{0}^{\varepsilon}\sigma d\varepsilon\right)\cos\theta-T\frac{\partial y}{\partial x}\right]rd\theta \tag{2.37}$$

Knowing that regardless of the stress-strain relationship, the general integral $\int\sigma\, d\varepsilon$ can always be described by $\alpha(\theta)\sigma\,\varepsilon$ (where α is a dimensionless factor that depends on θ), Equation 2.37 can be reduced further to yield the following:

$$J=\int_{-\pi}^{\pi}\left[\sigma\varepsilon\alpha_1(\theta)\cos\theta-\sigma\varepsilon\alpha_2(\theta)\right]rd\theta \tag{2.38a}$$

$$J=\sigma\varepsilon r\int_{-\pi}^{\pi}f(\theta)d\theta=\sigma\varepsilon rF(\theta)\Big|_{-\pi}^{\pi}=\sigma\varepsilon rQ \tag{2.38b}$$

The variable Q is simply a dimensionless number resulting from the integration of $f(\theta)$

between $-\pi$ and $+\pi$. Incorporating the Ramberg-Osgood relationship into Equation 2.38b, we have:

$$J = \frac{\sigma^{n+1} r Q}{F} \tag{2.39}$$

In this case, the radius r is equal to the half crack length a. One can see that if $n=1$, $Q=\pi$ and $F=E$, then Equation 2.39 is, in fact, equal to the expression for the strain energy release rate given by Equation 2.17, namely:

$$J = \frac{\pi\sigma^2 a}{E} \tag{2.40}$$

By substituting the calculated value for J into Equation 2.18 (in place of G), an equivalent stress intensity factor (K_{EQ}) can be obtained which accounts for the nonlinearity of the stress-strain curve.

$$K_{EQ} = \sqrt{EJ} \tag{2.41}$$

2.3.2 Crack Tip Opening Displacement (CTOD)

The origin of the CTOD elastic plastic fracture parameter can be traced to a man by the name of Wells. There are two methods commonly used to describe the CTOD, namely the displacement at the original crack tip and at the 90° intercept, as illustrated in Figure 2.24. It has been established that the CTOD fracture parameter is directly related to the fracture parameters K, G and J. Equation 2.42 expresses CTOD in terms of K, G, J, E and σ_{yld}.

$$\mathrm{CTOD} = \delta_t \approx \frac{G}{\sigma_{yld}} = \frac{K^2}{E\sigma_{yld}} \quad \text{(LEFM)} \tag{2.42a}$$

$$\mathrm{CTOD} = \delta_t \approx \frac{J}{\sigma_{yld}} \quad \text{(EPFM)} \tag{2.42b}$$

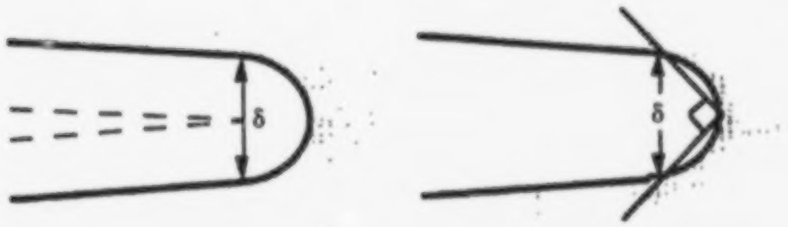

(a) Displacement at the original crack tip. **(b) Displacement at the intersection of a 90° vertex with the crack flanks.**

Figure 2.24 – Definitions of crack tip opening displacement (CTOD) [Anderson, 1995]

Similar to the other fracture parameters discussed thus far, CTOD has a critical value ($CTOD_c$) above which fracture will occur. This critical value of CTOD can be determined using Equation 2.42 in conjunction with K_c, G_c or J_c. The evaluation of CTOD is governed by ASTM Standard No. E1290, entitled "*Standard Test Method for Crack Tip Opening Displacement Fracture Toughness Measurement*".

Due to load fluctuations, the magnitude of CTOD varies continuously during cyclic loading. The effective range of CTOD during a fatigue cycle depends on several factors, namely the extent of reversed plastic flow ahead of the crack tip, the degree of residual stresses present, the roughness of the crack surfaces, and the presence of any corrosion pits or films. It has been proven that the cyclic crack tip opening displacement can be expressed as follows:

$$\Delta\delta_t = \frac{\Delta K^2}{2\sigma_{yld} E} \qquad \text{(Cyclic CTOD)} \qquad (2.43)$$

2.4 LEFM Versus EPFM

The flowchart of Figure 2.25 compares the applicability of the various fracture analysis techniques. If the initial conditions are met, then a condition of plane strain exists and the theories of LEFM are applicable. In this case, as previously mentioned, the fracture toughness obtained is the material's minimum toughness. If, on the other hand, the initial conditions are not met, then plane stress behavior predominates, and a less stringent criterion is evaluated to determine the validity of LEFM. If LEFM is deemed valid, the fracture toughness obtained can be much higher than that obtained for plane strain conditions. Therefore, in light of the added safety produced, the more conservative plane strain estimate of fracture toughness is often used. Finally, if this second, less stringent condition is still not met, then there is no other option than to use either the plastic zone adjustment method discussed in section 2.2.4 or the more applicable EPFM fracture parameters such as the J integral or the crack tip opening displacement (CTOD) discussed in section 2.3.

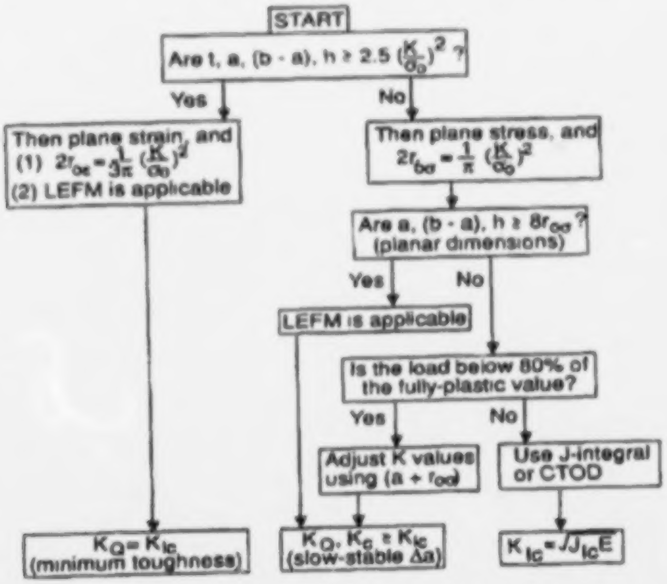
START
Are t, a, (b - a), h ≥ 2.5 $(\frac{K}{\sigma_o})^2$?
Yes
No
Then plane strain, and
(1) $2r_{o\varepsilon} = \frac{1}{3\pi}(\frac{K}{\sigma_o})^2$
(2) LEFM is applicable
Then plane stress, and
$2r_{o\sigma} = \frac{1}{\pi}(\frac{K}{\sigma_o})^2$
Are a, (b - a), h ≥ $8r_{o\sigma}$?
(planar dimensions)
Yes
No
LEFM is applicable
Is the load below 80% of the fully-plastic value?
Yes
No
Adjust K values using $(a + r_{o\sigma})$
Use J-integral or CTOD
$K_Q = K_{Ic}$
(minimum toughness)
$K_Q, K_c \geq K_{Ic}$
(slow-stable Δa)
$K_{Ic} = \sqrt{J_{Ic}E}$

Figure 2.25 – LEFM versus EPFM [Dowling, 1993]

Again, it should be noted that fracture and collapse (yielding) are competing conditions, and the one satisfied first will prevail. Therefore, consideration of the conditions governing cross-sectional yielding is a necessary part of a fracture analysis.

Chapter 3
Fatigue

For the most part, the previous chapter concentrated on fracture and failure criteria for components subjected to monotonically increasing loads. In practice, however, many structural components of aircraft, automobiles, bridges, cranes, ships and the like are subjected to cyclic loading. Depending on the magnitude of this loading, considerable physical damage may occur at the microscopic level due to high localized stresses. As the cyclic loading continues, this damage can progress and small cracks may develop and propagate within the material, ultimately leading to the failure of the component. Furthermore, this can all take place at a stress level well below the ultimate strength of a given material. This progressive accumulation of damage, leading to failure due to cyclic loading, is known as fatigue. Fatigue, and how it pertains to fracture mechanics, will be the topic of much of the remainder of this report.

3.1 Introduction

Fatigue failures have been a topic of interest since the early 1800's. As early as 1828, a man by the name of W. A. Albert performed crude fatigue tests on mine hoist chains. Motivated by numerous railway axle and bridge girder failures, a German engineer by the name of August Wohler began investigating fatigue failures in the 1850's. He recognized the need for the development of design practices aimed at avoiding fatigue failure. Wohler also established that fatigue was not only affected by cyclic stresses, but also by the corresponding average stresses.

There are currently three main approaches to fatigue failure analysis and design. The simplest approach is the stress-based approach, which calculates components' fatigue resistance by considering the average stresses to which they are subjected. If necessary, the resulting stresses are then modified in order to account for the effects of stress raisers such as holes, grooves, and fillets, etcetera. On the other hand, the more complicated strain-based approach to fatigue requires a relatively detailed analysis of any localized yielding that may occur around any of the aforementioned stress raisers. Finally, the fracture mechanics approach to fatigue uses the methods of fracture mechanics to handle propagating cracks.

3.2 Categories of Fatigue Loading

Prior to any crack growth analysis, an accurate assessment must be made of the loading scenario to which a component is likely to be subjected. However, the loading scenario used is typically a simplified version of the in-service load history experienced by a given component. Structural components may be subjected to either constant amplitude loading or variable amplitude (random) loading. Some of the general concepts and terminology used in these two loading categories will be discussed in the following sections.

3.2.1 Constant Amplitude Loading (CAL)

The simplest type of fatigue loading, which involves cycling between some constant maximum and minimum stress levels, is known as constant amplitude loading. There are several forms of constant amplitude loading (as illustrated in Figure 3.1), all of which use similar nomenclature to describe their characteristics.

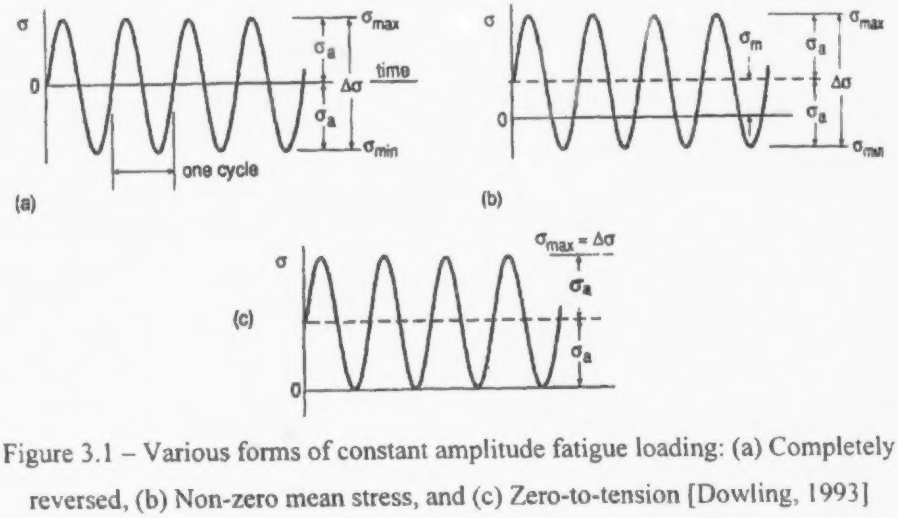

Figure 3.1 – Various forms of constant amplitude fatigue loading: (a) Completely reversed, (b) Non-zero mean stress, and (c) Zero-to-tension [Dowling, 1993]

Some of the terms commonly used to define constant amplitude loading include:

σ_{max} = the maximum stress experienced during a given cycle

σ_{min} = the maximum stress experienced during a given cycle

$$R = \text{the stress ratio experienced during a given cycle} = \frac{\sigma_{min}}{\sigma_{max}} \tag{3.1}$$

$$\sigma_{avg} = \text{the average stress during a given cycle} = \frac{\sigma_{max} + \sigma_{min}}{2} = \frac{\sigma_{max}}{2}(1+R) \tag{3.2}$$

$$\sigma_{a} = \text{the stress amplitude of a given cycle} = \frac{\sigma_{max} - \sigma_{min}}{2} = \frac{\sigma_{max}}{2}(1-R) \tag{3.3}$$

$$\Delta\sigma = \text{the stress range during a given cycle} = \sigma_{max} - \sigma_{min} = 2\sigma_{a} = \sigma_{max}(1-R) \tag{3.4}$$

Referring to Figure 3.1, some common constant amplitude load histories are completely reversed stressing (in which case R = -1), non-zero mean stressing (where $-1 < R < 1$), and zero-to-tension stressing (with R = 0).

Unfortunately, despite the inherent simplicity in describing constant amplitude loading, its occurrence is rather limited. Components of rotating machinery (helicopter blades, propellers, turbomachinery, etcetera) and piping components of nuclear power facilities are among the few areas in which constant amplitude loading prevails.

3.2.2 Variable Amplitude Loading (VAL)

The predominant type of fatigue loading for the majority of practical applications is that of variable amplitude. As illustrated in Figure 3.2, variable amplitude loading may take the form of repeated (block) loading, semi-random loading, or completely random loading.

The least complicated type of variable amplitude loading is repeated (block) loading, which involves describing one segment or block of simple load data. This data is then continuously repeated during the life of the component. On the other hand, completely random loading is the most complex type of variable amplitude loading. Fortunately, for many structures, such as automobiles, airplanes, ships, and offshore structures, the loading sequence to which they are subjected is not completely random in nature, but rather semi-random. For example, the load history for an automobile component depends on factors such as vehicle speed and road conditions, which vary from location to location. In this case, the semi-random nature arises from the fact that the milder loads are generally grouped together during highway driving, whereas the higher loads correspond to driving on rougher roads.

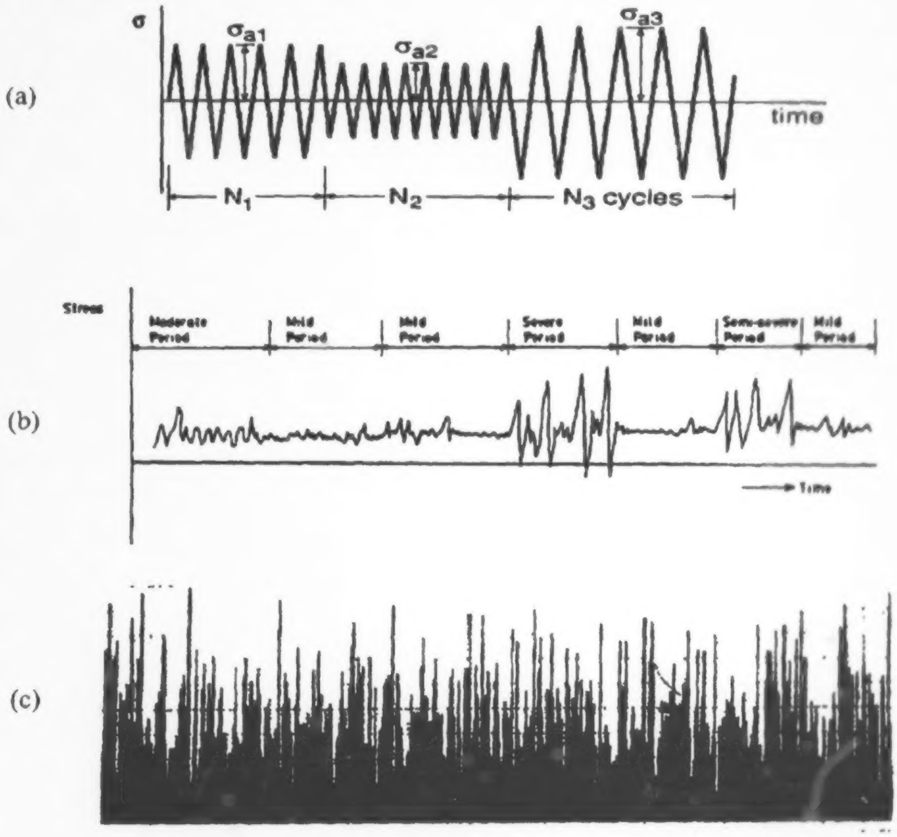

Figure 3.2 – Variable amplitude fatigue loading: (a) Repeated [Dowling, 1993], (b) Semi-random [Trask, 1998], and (c) Completely random loading [Lampman, 1996]

One of the most difficult tasks associated with variable amplitude loading remains the notion of how to accurately define a cycle of load sequence data. Several cycle counting techniques have been proposed, including level-crossing counting, peak counting, mean-crossing peak counting, range-pair counting, and rainflow counting. The consensus regarding the best cycle counting method appears to point toward the rainflow counting method, which was developed in 1968 by a Japanese professor by the name of T. Endo. A description of each of the previously mentioned counting methods is presented in ASTM Standard No. E1049, entitled "*Standard Practices for Cycle Counting in Fatigue Analysis*".

3.3 Fatigue Testing

The purpose of any fatigue test is to obtain data that will give information on the fatigue performance of a given material or component. Ideally, the conditions under which the testing is performed should closely approximate actual service conditions.

3.3.1 Testing Equipment

Depending on the type of fatigue test to be performed, there are several testing machines available. As previously mentioned, a German engineer by the name of August Wohler was a pioneer in the design of fatigue testing machines. In the 1850's, he designed a crude rotating bending machine to investigate the fatigue performance of railway car axles. Similar rotating bending machines are still in use today, one of the most common being a variation of Wohler's crude design, developed by R.R. Moore, which incorporates four-point bending into the fatigue test (as illustrated in Figure 3.3). This results in a constant bending moment and zero shear over the entire length of the specimen. During a rotating beam test, due to the fact that every point on the sample is subjected to completely reversed loading as it rotates from the compression (top) side to the tension (bottom) side during each cycle, the average applied stress is zero.

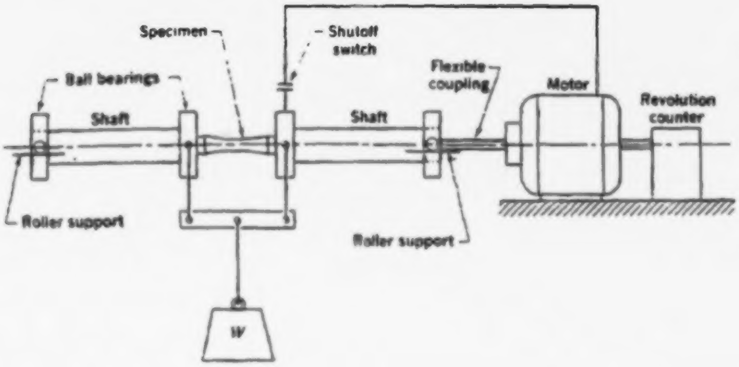
Specimen
Shutoff switch
Ball bearings
Flexible coupling
Motor
Revolution counter
Shaft
Shaft
Roller support
Roller support
W

Figure 3.3 – The R.R. Moore rotating beam fatigue testing machine [Dowling. 1993]

A deflection-controlled reciprocating bending machine like the one shown in Figure 3.4 can be used to induce any desired nonzero mean stress simply by adjusting the length of the connecting rod.

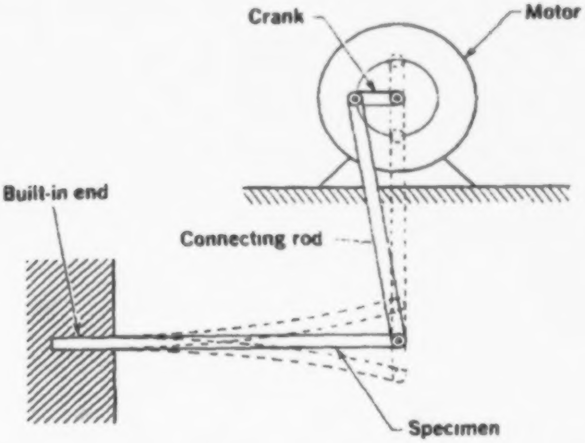
Crank
Motor
Built-in end
Connecting rod
Specimen

Figure 3.4 – A reciprocating bending machine (cantilever bending) [Dowling, 1993]

The potential of fatigue testing machines has increased drastically since the mid-1960's and the introduction of closed-loop servo-hydraulic testing machines. Figure 3.5 illustrates a modern closed-loop servo-hydraulic testing system, along with a brief schematic description of how the system works. Despite being extremely complex and outrageously expensive, these machines have very distinct advantages, including the luxuries of computer-controlled input, automated data collection and the ability to generate both constant and variable amplitude load sequences through controlled deflections, loads or strains.

One major limitation of fatigue testing is time. For most of the equipment discussed above, the use of cyclic waveforms with frequencies greater than approximately 100 Hertz is generally limited by either the speed of the motor or the operating nature of the servo-valves. From a practical perspective, this essentially restricts the range of fatigue lives that can be tested. For example, at a frequency of 100 Hertz, a test to five million cycles would take 14 hours, while one to 50 million cycles would require 6 days!

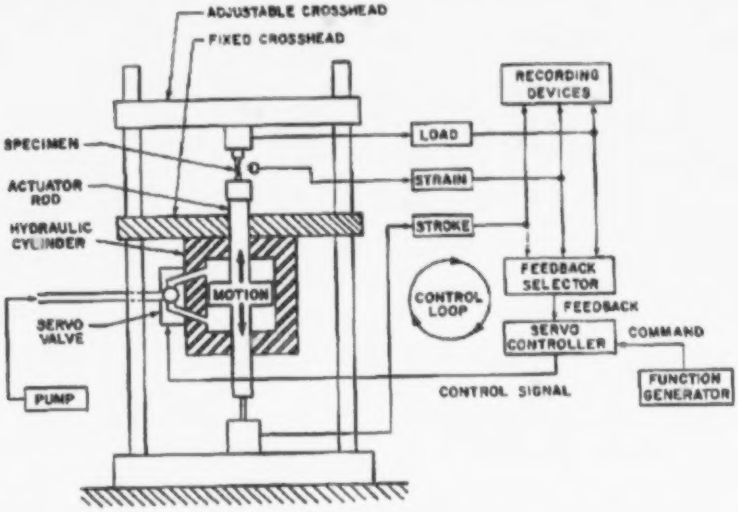
ADJUSTABLE CROSSHEAD
FIXED CROSSHEAD
RECORDING DEVICES
SPECIMEN
LOAD
STRAIN
ACTUATOR ROD
STROKE
HYDRAULIC CYLINDER
FEEDBACK SELECTOR
MOTION
CONTROL LOOP
FEEDBACK
SERVO VALVE
SERVO CONTROLLER
COMMAND
FUNCTION GENERATOR
PUMP
CONTROL SIGNAL

Figure 3.5 – A closed-loop servo-hydraulic testing machine [Dowling, 1993]

3.3.2 Specimens Used in Fatigue Testing

There is a variety of specimen types available for fatigue testing, each one designed to fit a particular test fixture. Due to the complex equipment required and the expense involved, fatigue testing on full-scale structures like automobiles and aircraft wings is very rarely done. Furthermore, data obtained from full-scale testing such as this may only be applied to that particular structure, and only under the exact conditions for which it was tested. On the other hand, much smaller specimens are used to gather fatigue performance data that is valid for samples made of the same material. Before using any of this data in practice, one should always be aware of, and very familiar with, the effects of the differences between the fatigue testing conditions and those of the actual application. Figure 3.6 illustrates some of the notched and unnotched specimens commonly used in fatigue testing. On the other hand, to obtain fatigue crack propagation data, the most commonly used test specimens are the center-cracked tension, compact tension, and three-point bending specimens, as illustrated in Figure 3.7.

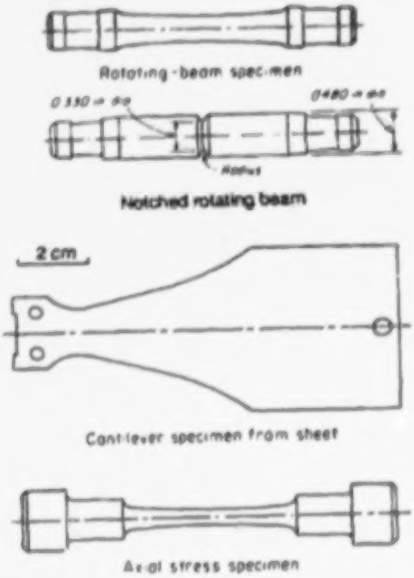
Rotating-beam specimen
0.330 in dia
0.480 in dia
Radius
Notched rotating beam
2 cm
Cantilever specimen from sheet
Axial stress specimen

Figure 3.6 – Various fatigue testing specimens [Dowling, 1993]

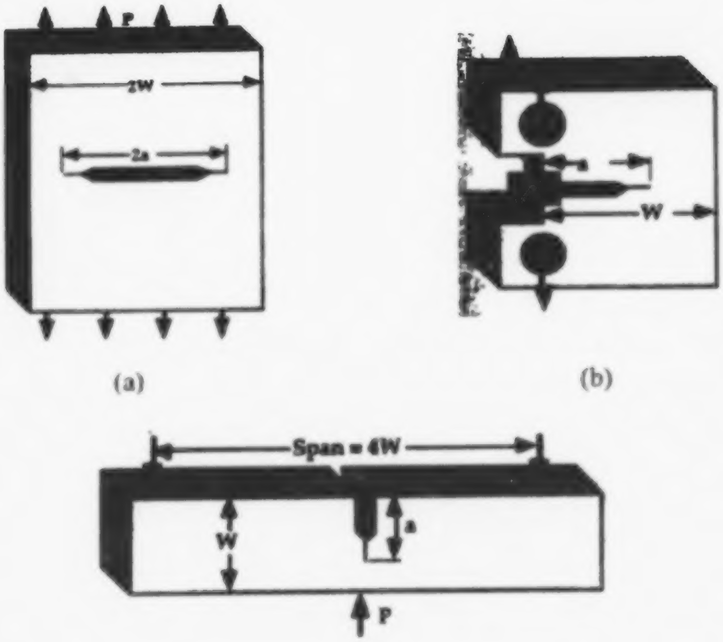

(a) (b) (c)

Figure 3.7 – Fatigue crack propagation testing specimens: (a) Center-cracked tension, (b) Compact tension, and (c) Three-point bending specimen [Anderson, 1995]

3.3.3 Standards for Fatigue Testing

Fatigue testing of metals (both notched and unnotched specimens) is governed by ASTM Standard No. E466, entitled "*Standard Practice for Conducting Constant Amplitude Axial Fatigue Tests of Metallic Materials*". The applicability of this Standard is limited to axial fatigue testing of notched and unnotched specimens subjected to constant amplitude loading in air at room temperature. The test is used to evaluate the effects of variation in material, geometry, and applied stresses, etcetera, on the fatigue performance of a given material. The most common graphical representation of data from fatigue tests such as this is the stress life (S-N) or fatigue life curve, which will be the topic of section 3.5 of this report. It should be noted that results obtained from ASTM E466 are applicable to design only when the expected service conditions are identical to those under which the corresponding specimen was tested.

ASTM Standard No. D671, entitled "*Standard Test Method for Flexural Fatigue of Plastics by Constant Amplitude of Force*", measures the ability of rigid plastic materials to resist deterioration caused by cyclic stresses. This test method employs a type of fixed-cantilever testing machine (similar to the one illustrated in Figure 3.4), which is designed to subject plastic specimens to cycles of constant force amplitude. Similar to ASTM E466, this test is useful in determining the effects of variables such as material type, geometry and applied stress on the fatigue performance of plastics. Test results provide information on the number of cycles required to cause specimen failure by fracture, softening, or stiffness reduction (due to internal friction). Again, it should be noted that results from this test method can be applied directly to design only when the probable service conditions are identical to the testing conditions. It is interesting to note that when plastic materials (which readily creep and undergo stress relaxation) are subjected to a non-zero mean stress, there is a tendency to stress relax such that the mean stress is effectively forced to zero.

Fatigue crack propagation testing should be done in accordance with ASTM Standard No. E647, entitled "*Standard Test Method for Measurement of Fatigue Crack Growth Rates*". A starter notch is generally machined into crack propagation specimens. In order to provide a sharpened fatigue crack of adequate length and straightness, fatigue crack propagation specimens are precracked prior to performing the actual test. Precracking requires cycling the specimen until a small fatigue crack begins to protrude from the edges of the machined starter notch. Using some visual technique or another equivalent method, crack propagation (da) can be monitored and recorded as a function of elapsed cycles (dN). The most common graphical representation of fatigue crack propagation data is the fatigue rate curve, wherein crack growth rates (da/dN) can then be expressed as a function of the stress intensity factor range (ΔK). This yields results that are independent of planar geometry, thus allowing the comparison and exchange of data obtained from a wealth of different loading conditions and specimen configurations. Furthermore, da/dN versus ΔK data can be used in the analysis and design of engineering structures to estimate fatigue lives, critical crack lengths, inspection intervals, etcetera. The fatigue rate curve will be discussed further in Chapter 4 of this report.

3.4 Micromechanics of Fatigue Damage

All materials can be considered both anisotropic and non-homogeneous when observed at a sufficiently small scale. Most engineering metals consist of small crystal grains bounded by crystal planes. Due to the variability in the orientation of these crystal planes, the behavior within each grain is anisotropic. Inhomogeneities exist not only due to the anisotropic grain structure, but also due to the presence of tiny voids or inclusions in the material. As a result of this irregular microstructure, stresses are distributed non-uniformly at the microscopic level. Fatigue damage typically initiates in areas where these stresses are most severe, such as voids, inclusions, notches and other features that cause localized stress concentration.

This microstructural behavior varies greatly for different materials. In ductile engineering metals, slip bands develop on the boundaries of grains that are oriented unfavorably with respect to the applied stress. Slip bands are regions of intense deformation resulting from shear motion (slip) between the crystal planes of adjacent grains. As cyclic loading continues, more and more slip bands are formed until a given region has become saturated and the rate of slip band formation slows. When the number of slip bands has reached this saturation level, small microcracks may develop. Figure 3.8 illustrates the progressive development of slip bands as they approach a saturation level. These microcracks, which tend to propagate along planes of maximum shear, are termed stage I fatigue cracks. Stage I fatigue cracks are typically associated with high-cycle fatigue, where the deformation (away from the crack tip) is primarily elastic. Further microcrack propagation is accompanied by a rotation from the plane of maximum shear to that of maximum tensile stress. This marks the transition from a stage I fatigue microcrack to a stage II fatigue macrocrack.

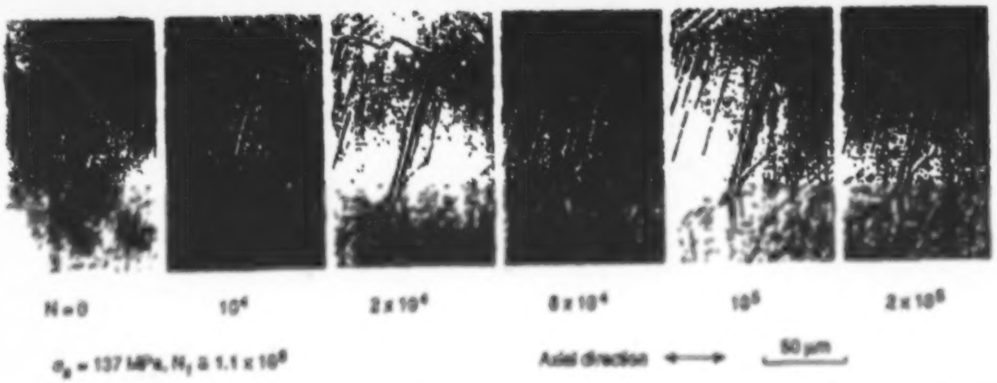

Figure 3.8 – Slip band formation and progressive damage intensification [Dowling, 1993]

In more brittle, high-strength metals, progressive damage intensification is less extensive, tending to concentrate at voids, inclusions, or other such defects in the material. Any cracks that may develop due to this damage concentration typically propagate in a direction normal to the applied stress, joining with other cracks in the process, until failure results. In contrast to the progressive damage intensification that occurs in ductile materials, fatigue damage in brittle materials is characterized by the propagation of only a few defects In fiber-reinforced composite materials, the appearance of numerous fiber breaks and widespread delamination are typical features of fatigue damage.

Careful observation of a fatigue fracture surface can reveal a considerable amount of important information concerning the load history to which a given component has been subjected. Fatigue fracture surfaces generally become rougher where the component has been subjected to higher crack growth rates. The various stages of crack growth are often indicated by a change in the texture of the fracture surface and curved lines known as beach marks, which are concentric about the crack origin. For example, changes in stress range, crack growth rates, temperature and chemical environment are typically accompanied by the appearance of beach marks. Figure 3.9 illustrates the appearance of beach marks on the fracture surfaces of three specimens, each having been subjected to a different load history.

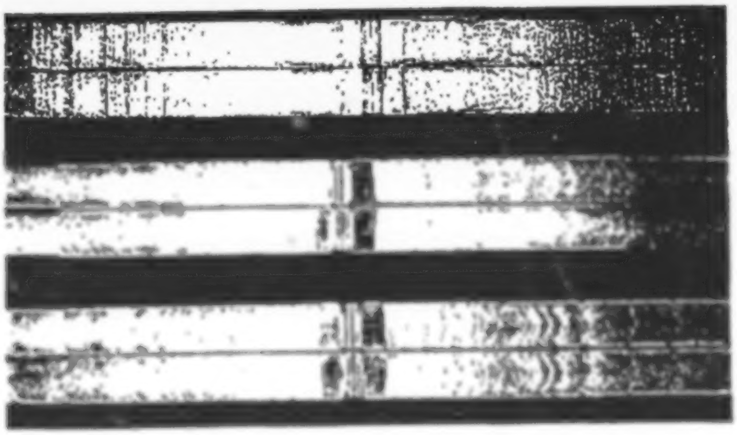

Figure 3.9 – Fracture surfaces showing beach marks [Lampman, 1996]

In the case of ductile material fracture under high-cycle fatigue, microscopic examination of the fracture surface often reveals the presence of tiny lines running essentially perpendicular to the direction of crack propagation. These lines are known as fatigue striations, and they effectively mark the progress of the fatigue crack. According to Lampman (1996), striation spacing is approximately equal to the fatigue crack growth rate for growth rates above one micrometer per cycle, whereas for lower growth rates, many cycles may be required to produce one striation. Figure 3.10 illustrates a typical fracture surface containing fatigue striations and the corresponding load sequence that produced them. It should be noted that not all materials exhibit fatigue striations. Furthermore, the visibility of fatigue striations is greatly affected by the severity of the load sequence.

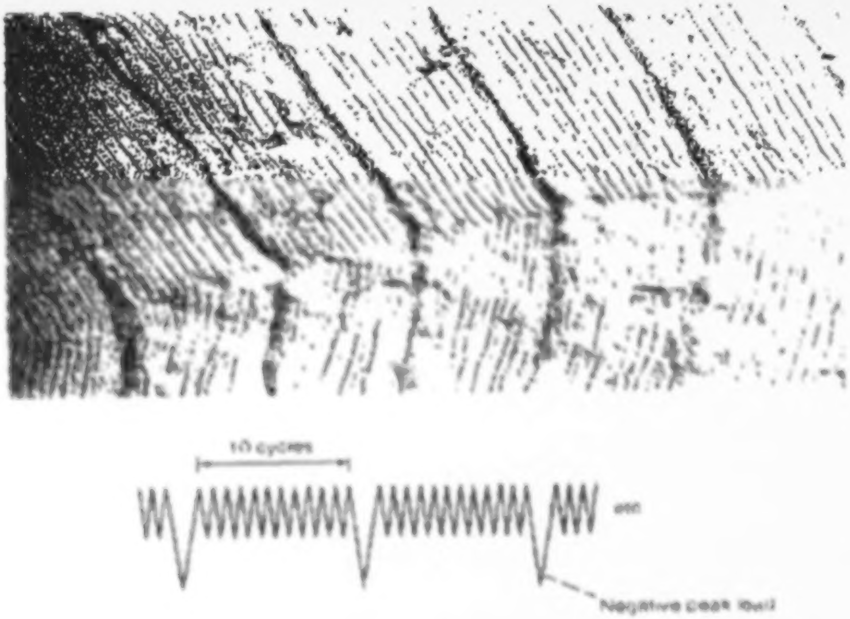

Figure 3.10 – Fatigue striation pattern formed by a typical repeated variable amplitude load sequence [Lampman, 1996]

The process by which fatigue striations are formed essentially involves two steps. The crack opens during the rising tension portion of the load cycle due to slip on alternating slip planes, and as this alternating slip continues, the crack tip becomes blunted. As the crack closes during the declining tension portion of the load cycle, partial slip reversal on alternating slip planes tends to resharpen the crack tip. The residual tensile stresses induced at the crack tip during the loading portion of the cycle tend to relax upon unloading, resulting in compressive stresses at the crack tip. Figure 3.11 illustrates the process of fatigue striation formation and crack growth.

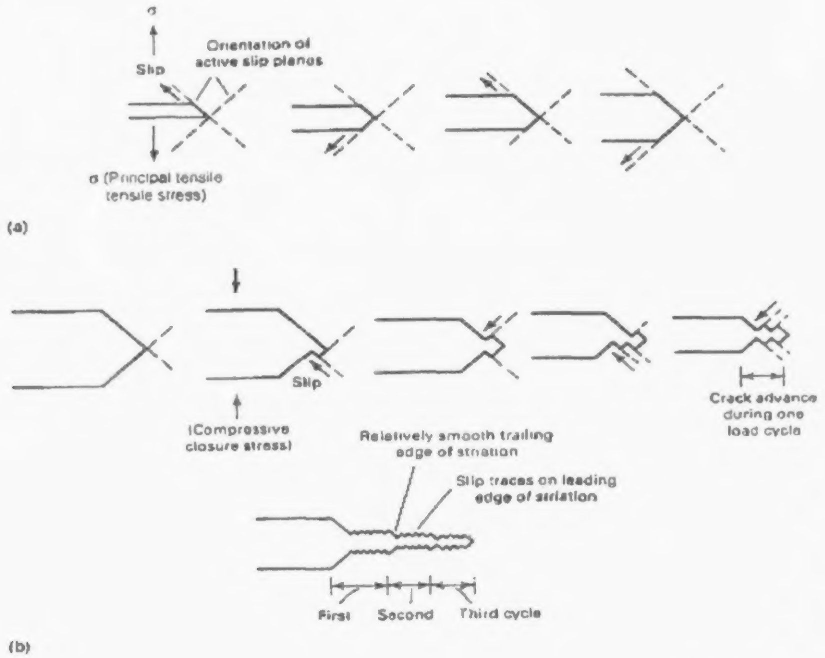
σ
Slip
Orientation of active slip planes
σ (Principal tensile tensile stress)
(a)
Slip
(Compressive closure stress)
Relatively smooth trailing edge of striation
Slip traces on leading edge of striation
Crack advance during one load cycle
First
Second
Third cycle
(b)

Figure 3.11 – Mechanisms of fatigue striation formation and crack advance: (a) Crack opening and blunting due to slip on alternate slip planes during increasing tensile stress, and (b) Crack closure and crack tip resharpening by partial slip reversal on alternate slip planes during decreasing tensile stress [Lampman, 1996]

Ultimate fracture involves one final transition from a stage II fatigue crack to a stage III fatigue crack, for which the growth rate is much larger. For ductile materials, fatigue crack growth changes from a tensile mode to a shear mode, accompanied by the formation of shear lips, inclined at approximately 45° to the applied stress. This final transition, along with the corresponding shear lip formation, is illustrated in Figure 3.12.

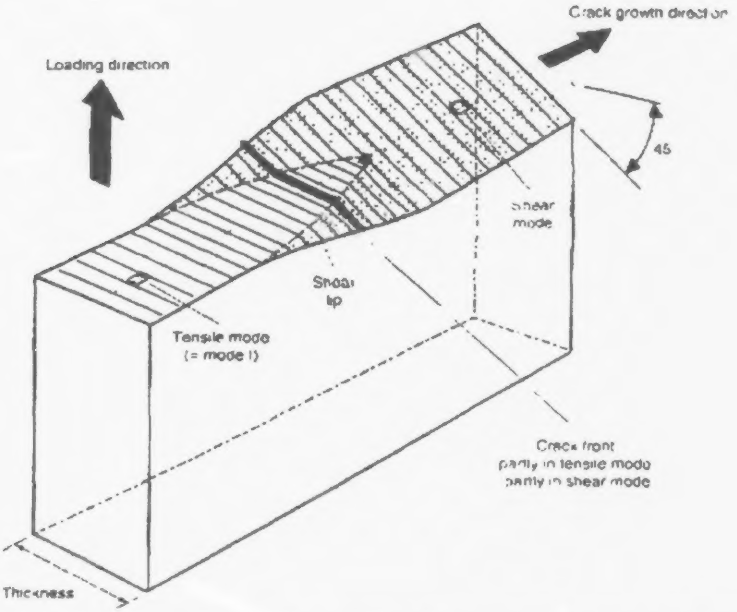
Crack growth direction
Loading direction
45
Shear mode
Shear lip
Tensile mode
(= mode I)
Crack front
partly in tensile mode
partly in shear mode
Thickness

Figure 3.12 – Fatigue crack growth transition from tensile mode to shear mode, along with corresponding shear lip formation [Lui, 1998]

3.5 Stress-Life Curves

If an engineering component is subjected to sufficiently large cyclic stresses, a fatigue crack will develop. Subsequent propagation of this crack may lead to the overall failure of the component. At a given stress amplitude (or maximum stress), the number of cycles required to initiate a fatigue crack is referred to as the fatigue crack initiation life (N_i), whereas the number of cycles required to propagate the crack to a critical size is known as the fatigue crack propagation life (N_f). The total fatigue life of a given component (N_T) is given by Equation 3.5.

$$N_T = N_i + N_f \tag{3.5}$$

When subjected to lower stress amplitudes, the number of cycles required to fail the component will be increased. This fatigue behavior is graphically illustrated using stress-life (S-N) curves (also referred to as fatigue life curves) such as the one shown in Figure

3.13. For all intensive purposes, fatigue crack initiation can be thought of as the development of a crack that is only a few millimeters long. Crack growth beyond the initiation stage can be described by one of the many crack propagation models used today.

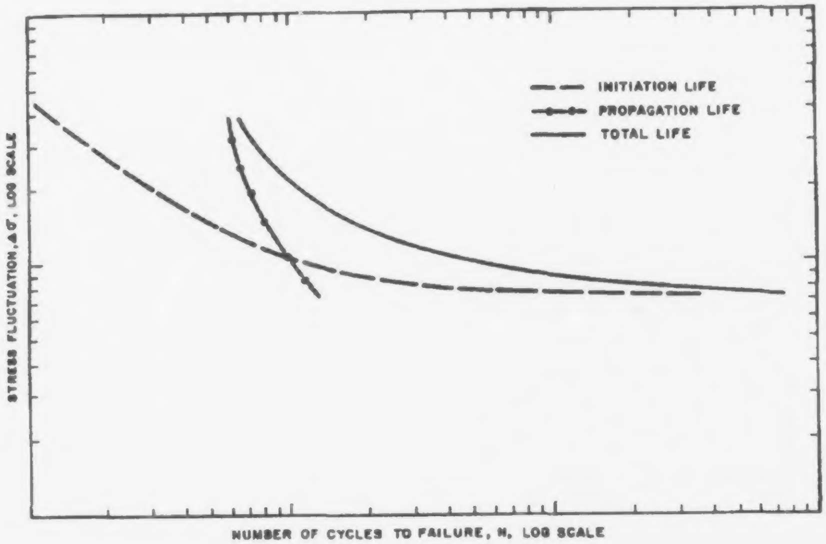

Figure 3.13 – Stress-life (S-N) curve [Barsom et al, 1987]

In the case of a component containing a pre-existing flaw, whether it was caused by the steel manufacturing process or by the welding process, the initiation life is rather small. Therefore, the majority of the total fatigue life can be represented by the fatigue propagation component. On the other hand, for a component with no initial flaws or imperfections of any kind, the majority of its fatigue life is typically consumed during the crack initiation phase. Unfortunately, the elimination of all flaws is neither a practical option, nor an economical one. For this reason, a damage tolerant design approach is usually adopted, in which case pre-existing flaws are assumed to be present in a given component prior to service. Hence, a more conservative and less time-consuming estimate of total fatigue life is obtained using only the crack propagation life.

Using the rotating bending test apparatus, stress-life curves are derived by subjecting a number of specimens (either notched or unnotched) to constant amplitude load scenarios, each at a different magnitude of stress amplitude. The resulting S-N curves are typically plotted showing only the total fatigue life. As the stress amplitude decreases, the number of cycles to failure (N_f) increases very quickly, and is therefore usually plotted on a logarithmic scale. If the S-N data from a given fatigue test appears to exhibit a linear relationship on a log-linear plot, then the S-N curve can be represented by Equation 3.6.

$$\sigma_a = b + m\log(N_f) \tag{3.6}$$

On the other hand, for data displaying a linear relationship on a log-log plot, the curve can be represented by Equation 3.7.

$$\sigma_a = A(N_f)^X \tag{3.7}$$

In Equations 3.6 and 3.7, the variables A, b, m, and X are simply curve fitting parameters and have been tabulated for a number of engineering metals.

The stress-life curves for steel typically exhibit a stress amplitude (or maximum stress) below which fatigue failure does not normally occur. This stress level is known as the fatigue limit or endurance limit (S_e) of a given material, and is indicated by the asymptotic nature of the S-N curve. For ductile steel specimens, the endurance limit is generally about one half of the ultimate tensile strength. Conversely, for higher-strength steels, which are typically more brittle, this ratio is usually less than one half, thus indicating the importance of ductility in providing fatigue resistance. Most other nonferrous materials do not appear to exhibit a distinct endurance limit, but rather display a continuously decreasing stress-life response. In cases such as these, an arbitrary endurance limit is typically defined as the fatigue strength corresponding to a fatigue life of 2 million to 100 million cycles. The S-N curves shown in Figure 3.14 illustrate the distinct endurance limit for steels and the continuously decreasing nature of the S-N curve for most nonferrous materials.

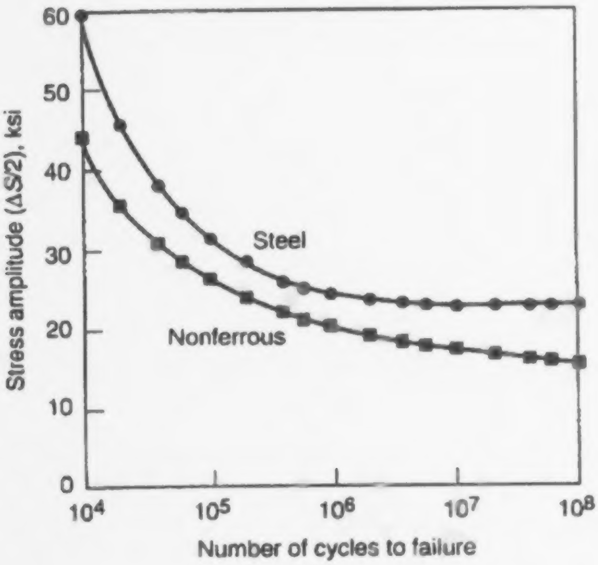

Figure 3.14 – Comparison of typical S-N curves for steel and nonferrous materials [Lampman, 1996]

Any process that causes a change in a material's mechanical properties or microstructure is likely to affect its S-N curve. Variables such as chemical environment, temperature, cyclic frequency, geometry, mean stress, and residual stresses also affect a material's stress-life curve.

The fatigue resistance of metals is generally improved by reducing the size of microstructural grains, inclusions, and voids. However, some of the processes that are used to accomplish these reductions may sacrifice ductility, which, as previously mentioned, is very important in providing increased resistance to fatigue. In addition, the fabrication process itself typically yields microstructures that vary with direction. For example, fatigue resistance is typically somewhat higher in the case of an applied stress parallel to the rolling direction. These effects are much more apparent in fiber reinforced composites, where both microstructure and mechanical properties are highly dependent on direction. As one could intuitively expect, the fatigue resistance of fibrous composites is much higher in the longitudinal (fiber) direction.

Aggressive chemical environments can accelerate both the initiation and propagation of fatigue cracks. In uncracked components, chemical oxidation may eventually result in corrosion pits, which then act as stress raisers. Chemical reactions may also take place that cause accelerated crack growth via dissolution of material at the tip of an existing crack. For example, fatigue testing in salt water tends to lower the S-N curve for a given material, as illustrated in Figure 3.15. The effects are more pronounced for testing done at lower frequencies, in which case the crack is more directly exposed to chemical attack for longer periods.

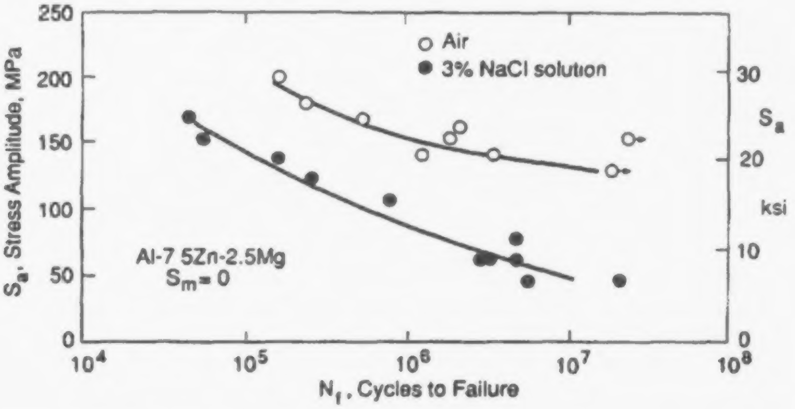

Figure 3.15 – Effect of an aggressive chemical environment on the S-N curve [Dowling, 1993]

At higher temperatures, the moisture and gases in the atmosphere can induce a hostile environment. Creep is also more likely to occur at higher temperatures, and may combine with cyclic stresses to lower the S-N curve for a given material. Considerable heat may also be generated within a specimen during fatigue testing. Many polymeric composites do not dissipate this heat efficiently. Therefore, their S-N curves are not only affected by cyclic frequency, but also by specimen thickness, as thinner specimens tend to dissipate heat more efficiently.

The presence of stress raisers such as grooves, holes, and other changes in geometry can affect stress-life curves. Notched members tend to have shorter fatigue lives, which corresponds to a lower S-N curve compared to an identical unnotched member. The amount of lowering is proportional to the stress concentration factor (k_t) that applies to the particular stress raiser present, as illustrated in Figure 3.16. In addition, higher strength, less ductile materials tend to be more severely affected by stress raisers.

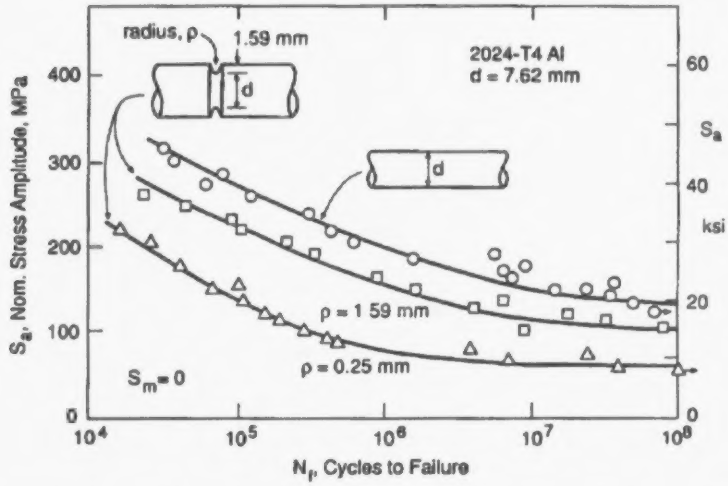

Figure 3.16 – Effects of stress raisers on the S-N curve [Dowling, 1993]

The value of mean stress can also affect the stress-life curve to a large extent. As illustrated in Figure 3.17, for a given stress amplitude, tensile mean stresses yield shorter fatigue lives than does a mean stress of zero, while compressive mean stresses result in longer fatigue lives. The end result is a relative lowering or raising of the S-N curve.

Stress ratio (R) has an effect very similar to that of mean stress. Higher stress ratios correspond to more tensile mean stresses, and therefore, for a given stress amplitude, an increased stress ratio corresponds to a lowered S-N curve. This trend is illustrated in Figure 3.18a. If, on the other hand, the data is plotted in terms of maximum stress, as illustrated in Figure 3.18b, an increase in stress ratio raises the corresponding S-N curve. This appears to contradict the data of Figure 3.18a, but in fact, the data are identical. This apparent contradiction can be explained by rearranging Equation 3.3 to yield Equation 3.8.

$$\sigma_a = \frac{(\sigma_{max} - \sigma_{min})}{2} = \left(\frac{\sigma_{max}}{2}\right)(1 - R) \tag{3.3}$$

$$\sigma_{max} = \frac{2\sigma_a}{(1 - R)} \tag{3.8}$$

One can see that for the same stress ratio, the stress amplitudes illustrated in Figure 3.18a are equal to the corresponding maximum stresses illustrated in Figure 3.18b.

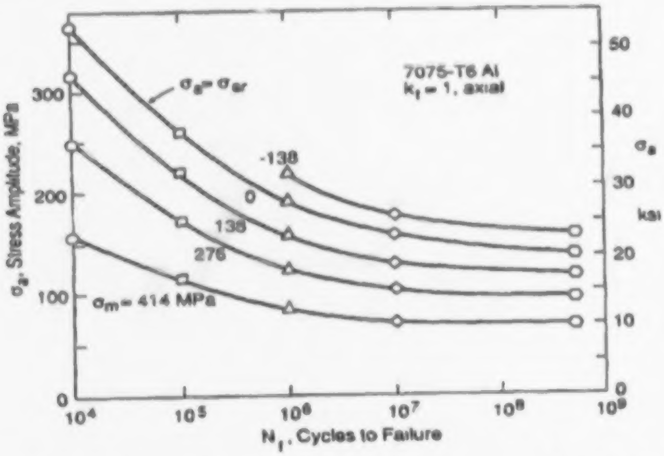

Figure 3.17 – Effect of mean stress on the S-N curve [Dowling, 1993]

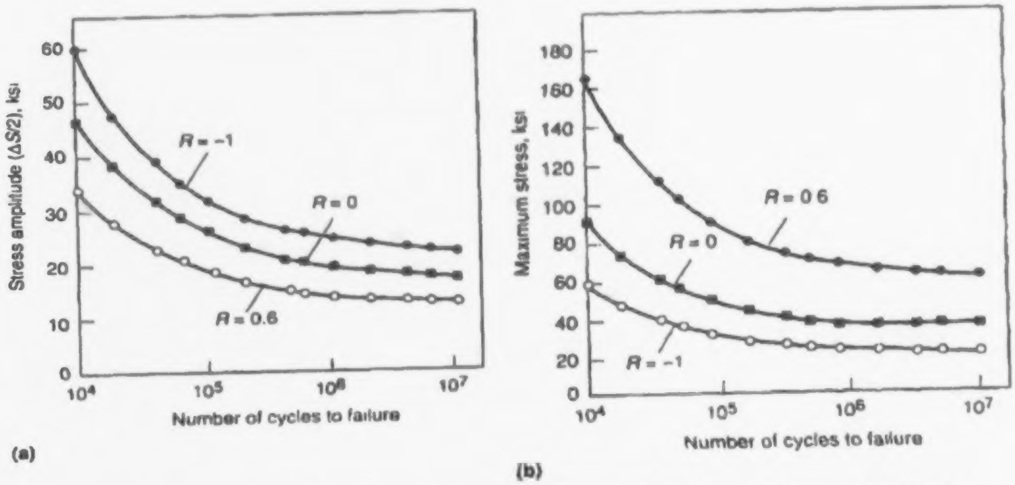

Figure 3.18 - Effect of stress ratio on the S-N curve based on (a) Stress amplitude, and (b) Maximum stress [Lampman, 1996]

Residual stresses also affect the S-N curve in a manner similar to mean stress. That is, tensile residual stresses are detrimental, while compressive stresses are beneficial. Compressive residual stresses can be introduced by essentially forcing a thin surface layer to yield in tension. Upon removal of this pseudo load, the underlying material will attempt to rebound to its original shape, effectively forcing the surface layer into compression. This can be accomplished through a variety of processes, including shot peening and presetting.

In the shot peening process, the surface is essentially sandblasted with small glass or steel ball bearings. The magnitude and sense (tension or compression) of any additionally applied strain during shot peening is very important. As illustrated in Figure 3.19, additional tensile strains applied during shot peening significantly increases the fatigue strength.

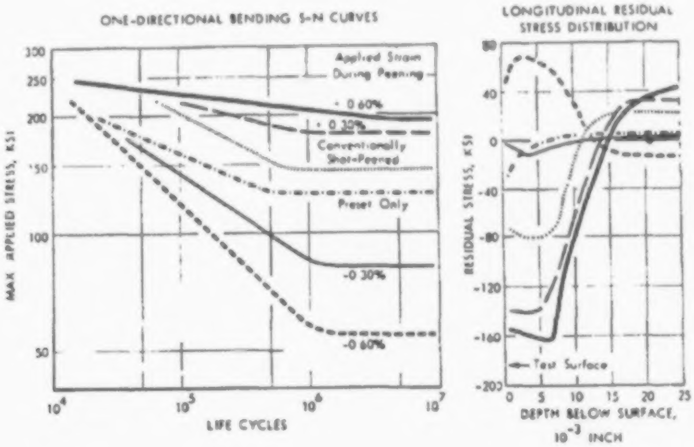

Figure 3.19 – Effects of shot peening and presetting on fatigue strength [Dowling, 1993]

The process of presetting employs bending to yield a thin surface layer in tension. However, due to the nature of this process, it is useful only where bending is predominantly in one direction. The rear leaf springs on pick-up trucks are a prime example of presetting. As illustrated in Figure 3.19, presetting typically yields lower fatigue strength than does shot peening, except where the applied strain (if any) during shot peening is compressive. The welding process often results in residual stresses due to uneven cooling between the fused weld metal and the base metal. Therefore, welded members and connections generally have lower fatigue strengths and should be given special attention during their design against fatigue failure.

When several fatigue tests are conducted at the same stress level, a considerable amount of scatter in the fatigue life data can be expected. For this reason, families of stress-life-probability of failure (S-N-P) curves are often published to give more information on the variability and scatter in fatigue life. A typical S-N-P curve is illustrated in Figure 3.20.

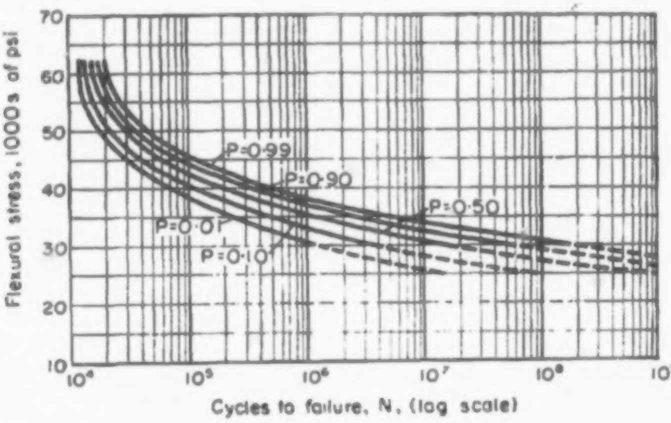

Figure 3.20 – A family of stress-life-probability of failure curves [Dowling, 1993]

The concept of an equivalent completely reversed stress amplitude (σ_{ar}) may prove useful for those cases in which the applied mean stresses do not correspond to an available S-N curve. Equation 3.9 can be used to calculate σ_{ar} for a given mean stress and stress amplitude.

$$(3.9) \quad \sigma_{ar} = \frac{\sigma_a}{1 - \frac{\sigma_m}{\sigma_{ult}}}$$

The significance of this equivalent completely reversed stress is that, "any combination of mean stress σ_m and amplitude σ_a is thus expected to produce the same life as the stress amplitude σ_{ar} applied at zero mean stress" [Dowling, 1993]. Once σ_{ar} is calculated using

Equation 3.9, it can be used to determine the expected fatigue life by entering the proper S-N curve corresponding to zero mean stress.

Constant life diagrams are often used as an alternative means of presenting the data found on typical stress-life curves. Constant life diagrams are generated by plotting combinations of mean stress and stress amplitude that cause failure at a specific value of fatigue life. The process is repeated several times, producing a series of curves, each one representing a specific value of fatigue life. For each combination of stress amplitude and mean stress, there exists a combination of maximum and minimum stress, and correspondingly, a specific value of stress ratio. By using two sets of coordinate axes separated by 45°, all this information can be presented on a single diagram; thus allowing the data to be interpreted several ways. A typical constant life diagram is illustrated below in Figure 3.21.

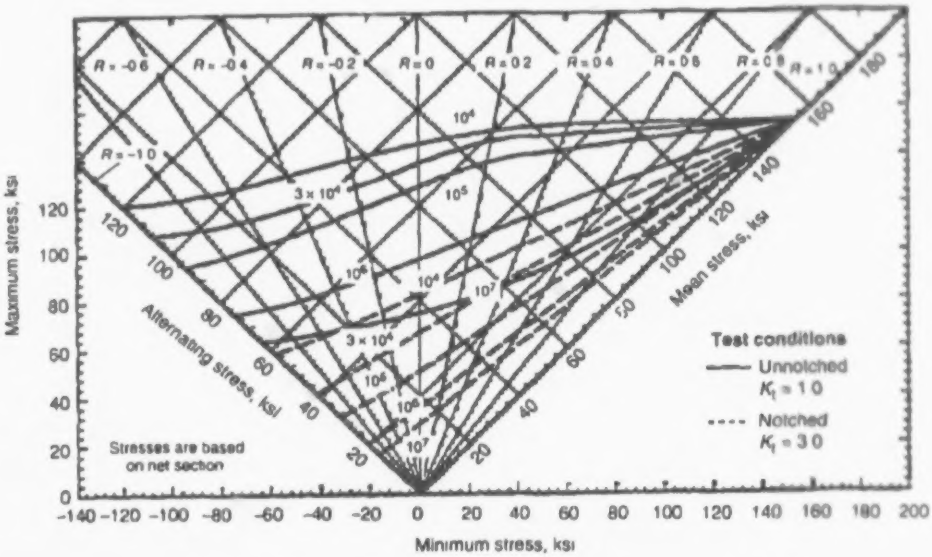

Figure 3.21 – Typical constant life diagram [Lampman, 1996]

As an example of how to use a constant life diagram such as the one illustrated in Figure 3.21, suppose a component is subjected to a minimum stress of 40 ksi and a maximum stress of 80 ksi. Intersecting these values and dropping two perpendiculars to the mean stress and stress amplitude axes, one can see that the corresponding mean stress and stress amplitude are 60 ksi and 20 ksi, respectively. As expected, the radial line for stress ratio falls halfway between those for R = 0.4 and R = 0.6. In the case of an unnotched specimen subjected to the aforementioned stresses, the number of cycles to failure (N_f) appears to be greater than 10 million. On the other hand, for a similar notched specimen, failure can be expected at approximately 80 thousand cycles. Where necessary, one can simply interpolate between the curves to determine fatigue lives for various applied stresses.

Chapter 4

Fatigue Crack Propagation and Life Assessment Methods

4.1 Introduction

Although the presence of a crack can significantly reduce the strength of an engineering component, it is quite rare for a crack of critical size to exist prior to any service loading. A more common situation is the initial presence of small flaws that develop into larger cracks, which eventually propagate to fatigue cracks of critical size. Careful inspection often reveals the presence of fatigue cracks in structural components of aircraft, bridges, cranes, pressure vessels, ship structures, turbine rotors, and etcetera. It is this inevitable presence of flaws and their subsequent growth into macrocracks that dictates the need for some type of crack growth analysis to evaluate the structural integrity and safety of a given component on an ongoing basis. As opposed to the previously mentioned stress life approach, a damage tolerant design approach can be taken to ensure that structural components be capable of surviving even in the presence of growing cracks. The most effective approach to crack growth analysis and life assessment is based on the concepts of fracture mechanics.

A crack growth analysis is extremely important not only to determine the useful life of a given structural component, but also to establish suitable inspection intervals. These inspection intervals are chosen such that an inspector will have several opportunities to detect a growing fatigue crack prior to it reaching a critical size (a_{crit}) and recommend either the repair or replacement of the affected component. Commonly used inspection techniques include electric current application, x-ray photography, ultrasonic wave reflection, and visual examination. Any given inspection technique has associated with it a minimum detectable crack length ($a_{d,min}$), below which crack detection is not possible. This minimum detectable crack length ($a_{d,min}$) is often used as a conservative estimate of the initial crack length (a_i) in fatigue crack growth analyses. In any crack growth analysis, cost, in addition to safety, is a major consideration in the selection of both inspection technique and inspection interval.

The following sections will discuss the methods of crack growth data representation, modeling of crack propagation under both constant amplitude and variable amplitude loading, and various methods of fatigue life assessment. A brief mention will also be made of fatigue crack propagation in corrosive environments.

4.2 Fatigue Crack Growth Data Representation

Proper evaluation and representation of pertinent crack growth data forms the basis of any fatigue crack growth analysis. As previously mentioned in section 3.3.3, fatigue crack propagation testing for compact tension and center-cracked tension specimens is done in accordance with ASTM Standard No. E647, entitled "*Standard Test Method for Measurement of Fatigue Crack Growth Rates*". Test specimens are subjected to constant amplitude cyclic loading while incremental changes in crack length (a) are measured and recorded as a function of the corresponding elapsed cycles (N). The data are then presented on a plot of crack length versus number of cycles, referred to as an 'a-versus-N' curve. For a given geometry and stress ratio, Figure 4.1 and Figure 4.2 illustrate how a-versus-N curves differ with initial crack length and cyclic stress range. As one could expect, for the same geometry and stress ratio (R), fatigue life tends to decrease with increasing initial crack length (a_i) and cyclic stress range ($\Delta\sigma$). One can also see that by the time the fatigue crack has grown to only a fraction of its critical size, much of the fatigue life has been expended.

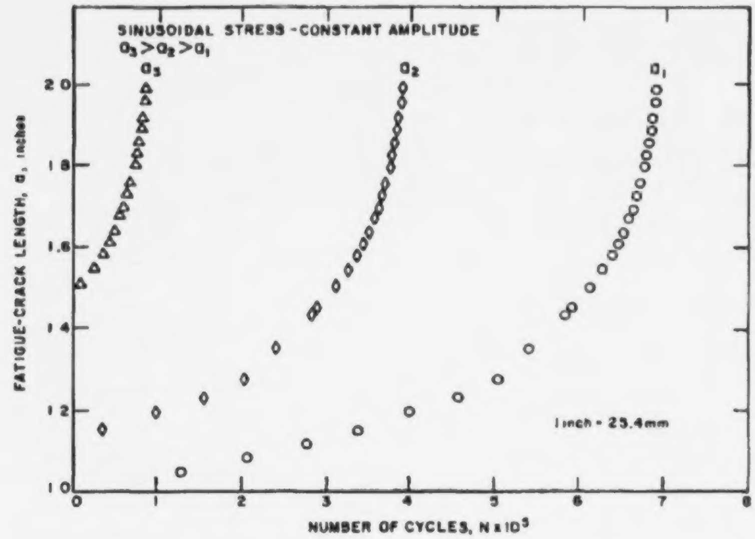

Figure 4.1 – Effect of initial crack length on resulting a-versus-N curve [Barsom et al, 1987]

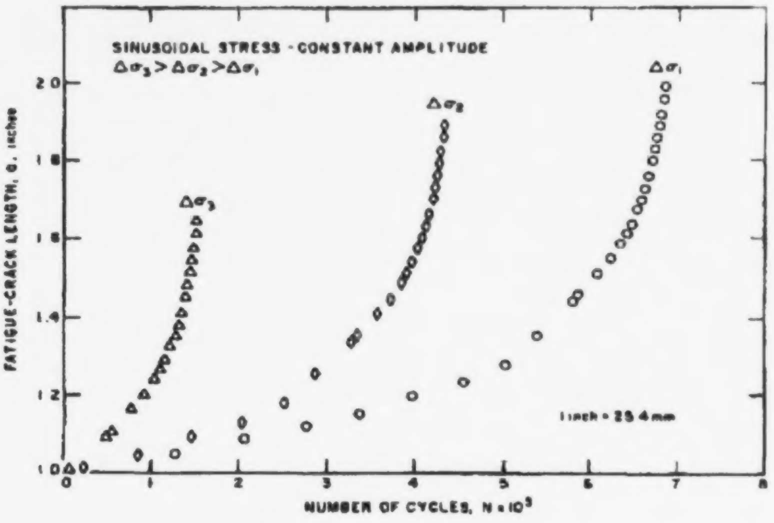

Figure 4 .2 – Effect of cyclic stress range on resulting a-versus-N curve [Barsom et al, 1987]

Unfortunately, a-versus-N curves greatly depend on factors such as specimen geometry, initial crack length, and cyclic stress range. Therefore, they must be processed further to obtain results that are independent of these factors. This is best accomplished via the use of the stress intensity factor range (ΔK). Recalling Equation 2.3b, one can see how the use of ΔK incorporates the effect of changing geometry, initial crack length, and cyclic stress range. Fatigue crack growth rates (da/dN) are typically calculated as the slope of the a-versus-N curve between successive data points. These da/dN values are then plotted as a function of the corresponding stress intensity factor range (ΔK), usually on a log-log scale. Expressing da/dN as a function of ΔK yields results that are independent of planar geometry, crack length, and stress range, thus allowing the comparison of data obtained from a number of different specimen configurations and loading scenarios. The result is a sigmoidal-shaped curve, as illustrated in Figure 4.3, referred to as either a da/dN-versus-ΔK curve or a fatigue rate curve. The fatigue rate curve exhibits three distinct regions (region I, region II, and region III) in which both crack growth behavior and the factors by which it is influenced vary greatly.

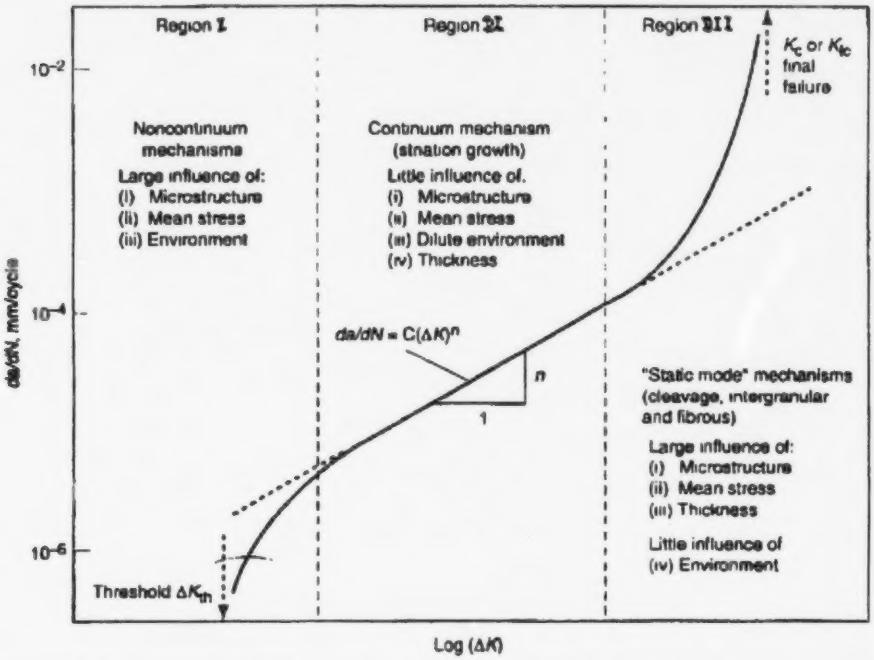

Figure 4.3 – Typical da/dN-versus-ΔK curve (fatigue rate curve) [Lampman, 1996]

Region I of the fatigue rate curve represents the early growth and development of a fatigue crack. Fatigue crack growth rates in region I are typically 10^{-9} m/cycle or less and are mainly influenced by the material's microstructural characteristics (grain size, etcetera), the applied mean stress, and the surrounding environment.

As Figure 4.3 illustrates, the most significant feature of region I is the apparent existence of a stress intensity factor range below which the fatigue crack growth rate is essentially zero. This stress intensity factor range, referred to as the fatigue crack growth threshold and denoted by the symbol ΔK_{th}, can be determined experimentally via the decreasing-K test of ASTM Standard No. E647, entitled "*Standard Test Method for Measurement of Fatigue Crack Growth Rates*". In this decreasing-K test method, which is suggested to obtain data for fatigue crack growth rates less than 10^{-8} m/cycle, the specimens are first precracked by a small amount in order to remove the effects of any machined starter notch. Thereafter, loads are shed (decreased) in a controlled manner and data are recorded until the lowest ΔK or crack growth rate of interest is obtained. Loads are typically shed such that the load reduction in adjacent steps does not exceed 10% of the previous maximum load. A minimum fatigue crack extension of 0.50 mm is suggested between load shedding steps. The fatigue crack growth rate threshold (ΔK_{th}) is operationally defined as the stress intensity factor range corresponding to a growth rate of 10^{-10} m/cycle, which is determined by means of the best-fit line from a linear regression of log da/dN-versus-log ΔK between growth rates of approximately 10^{-9} m/cycle and 10^{-10} m/cycle.

Crack closure is another factor that is thought to influence near-threshold crack growth behavior. Crack closure simply refers to the contacting of top and bottom crack surfaces prior to the minimum load in a given loading cycle being reached. Lampman (1996) defines the crack opening load as "that load level during the loading portion of a cycle at which the crack surfaces become fully separated". The crack closure load and crack opening load are essentially the same, in that the load at which the crack surfaces become fully separated during the loading portion of the cycle is approximately equal to the load at which crack closure commences during the unloading portion of a cycle. The significance of crack closure is that it is thought that only the portion of the loading cycle above the crack opening load contributes to fatigue crack growth. Therefore, any mechanism causing premature crack closure can quite conceivably affect ΔK_{th}. W. Elber first put forth the concept of crack closure in the late 1960's when he noticed that fatigue crack surfaces might actually interfere with each other by means of some type of closure mechanism. Elber noted that when ΔK is large, "plastic stretching of the material at the crack tip imposes a compressive stress on the reverse loading, causing the crack to close prior to the tensile stress becoming zero" [Lampman, 1996]. He defined an effective stress intensity range as the difference between the applied K_{max} and that required to fully open the fatigue crack, given by Equation 4.1.

$$\Delta K_{eff} = K_{max} - K_{open} \tag{4.1}$$

Plasticity-induced closure results from residual plastic deformation left in the wake of a growing fatigue crack. Due to the fact that near the fatigue crack growth threshold, the maximum stress intensity (and therefore the extent of residual plastic deformation) is still relatively small, plasticity-induced crack closure is not thought to be an important factor affecting ΔK_{th}. However, as illustrated in Figure 4.4, there are other sources of crack closure, including roughness-induced closure, shear-induced closure, and environmentally induced closure.

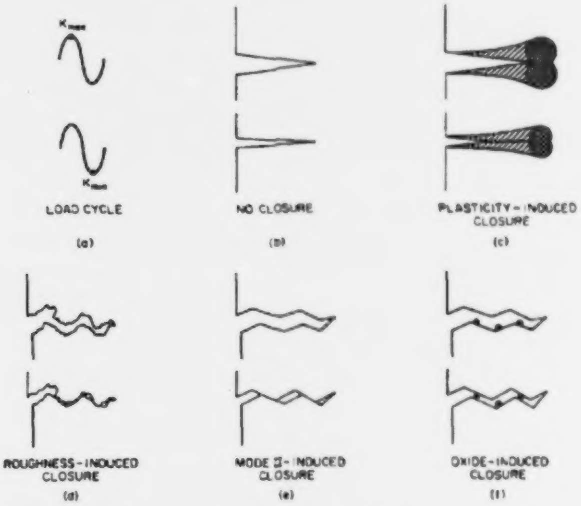

Figure 4.4 – Schematic illustration of various mechanisms of crack-closure [Barsom et al, 1987]

Roughness-induced crack closure is the result of deviations in the crack trajectory, which are associated with microstructural characteristics of the material. This type of crack closure is thought to be the most important type of closure near the threshold region. Shear-induced (or mode II-induced) crack closure results if the fatigue crack propagates in a mixed shear-tensile mode. This essentially prevents the top and bottom fatigue crack surfaces from matching up perfectly when the load is removed. Therefore, the surfaces in the wake of the crack tip tend to contact prior to the minimum load or zero load being reached. Lastly, environmentally induced closure or oxide-bridging results when corrosion products wedge themselves between the crack surfaces, thus preventing full closure of the fatigue crack upon removal of the load.

In summary, considering all the aforementioned factors that can affect the fatigue crack growth threshold, it appears that the stress ratio (R) is the most important. Barsom et al (1987) suggest that for $R \geq 0.1$, conservative estimates of ΔK_{th} can be predicted using Equation 4.2.

$$\Delta K_{th} = 6.4(1\text{-}0.85R) \quad \text{ksi}\sqrt{\text{in}} \tag{4.2a}$$

$$\Delta K_{th} = 7.0(1\text{-}0.85R) \quad \text{MPa}\sqrt{\text{m}} \tag{4.2b}$$

On the other hand, for $R < 0.1$, the fatigue crack growth threshold appears to be constant at 5.5 $\text{ksi}\sqrt{\text{in}}$ (6.0 $\text{MPa}\sqrt{\text{m}}$). Barsom et al (1987) also suggest that the fatigue crack growth threshold for various materials can be inferred by using the parameter $\Delta K_{th}/E$. Wasen et al (1998) suggest the use of Equation 4.3 to calculate ΔK_{th}.

$$\Delta K_{th} = 2.72\text{x}10^{-5}E \quad (\text{MPa}\sqrt{\text{m}};\ E \text{ in MPa}) \tag{4.3}$$

In light of the aforementioned crack closure concept, Wasen et al (1998) have also shown that the effective threshold stress intensity factor range, $\Delta K_{th,eff}$, is directly proportional to the modulus of elasticity, E. They suggest the use of Equation 4.4 for a variety of metallic materials.

$$\Delta K_{th,eff} = 1.64 \times 10^{-5} E \quad (\text{MPa}\sqrt{\text{m}};\ E \text{ in MPa}) \qquad (4.4)$$

Region II of the fatigue rate curve encompasses intermediate crack growth rates, which typically range from 10^{-9} m/cycle to 10^{-6} m/cycle. Region II corresponds to stable crack growth and the log da/dN-versus-log ΔK data follows a linear relationship. In region II, the "length of the plastic zone ahead of the crack tip is long compared with the mean grain size, but much smaller than the crack length" [Trask, 1998], and therefore, the principles of LEFM are entirely acceptable. Many of the fatigue crack propagation models that will be discussed in section 4.3 were developed mainly to model crack growth in region II. The influence of such factors as environment, mean stress, microstructural features, and specimen thickness appears to be relatively insignificant for crack growth rates in region II. As illustrated in Figure 4.5, the effect of the applied mean stress (an indication of the stress ratio (R)) appears to be the most significant factor controlling crack growth in region II. The extent to which this factor affects crack growth varies depending on the material in question, but for most low-strength, highly ductile structural metals, the effect is relatively small.

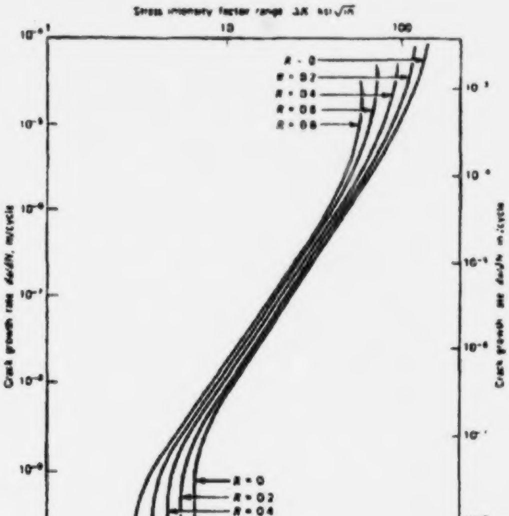

Figure 4.5 – Effect of mean stress (stress ratio, R) on fatigue crack growth rate [Trask, 1997]

Conversely to region I of the fatigue rate curve, region III corresponds to rapid, unstable fatigue crack growth just prior to failure. Crack growth rates are typically of the order 10^{-6} m/cycle or greater as the curve asymptotically approaches the fracture toughness (K_c) of the material. The mean stress, material microstructure, and thickness have a large influence in region III, while environmental effects are insignificant. Due to the high stresses typically associated with crack growth in region III, the resulting crack tip plastic zones are relatively large compared with the specimen geometry and crack length. As such, the nonlinear material properties generally have a larger influence on crack growth and EPFM principles should therefore be applied. Although the analysis for region III crack growth is relatively complex, it is often ignored in most practical applications. This is due to the fact that by the time a fatigue crack has reached the high growth rates of region III, so little of the component's total fatigue life remains that any activity in region III can be neglected.

4.3 Fatigue Crack Growth Modeling

The most commonly used approach to fatigue crack growth analysis involves the use of a differential equation to describe or model the fatigue rate data. Using region II of the fatigue rate curve as a basis for model development, it was previously mentioned that the major factors affecting crack growth rates in region II are the stress ratio (R) and, of course, the stress intensity factor range (ΔK). Most crack growth models are therefore expressed as some variation of Equation 4.5, usually in the form of a power law.

$$\frac{da}{dN} = f(\Delta K, R) \tag{4.5}$$

The main drawback to most crack growth models is associated with the curve fitting parameters that are used to describe f (ΔK,R). These parameters typically have no physical significance, but are instead representative of the particular curve fitting technique employed to fit the model to experimental fatigue rate data. Due to the activities of a large number of researchers in this field, most of whom have developed their own models, it is virtually impossible to discuss each and every crack growth model. Therefore, only those that are more commonly used will be discussed further in section 4.3.1 and section 4.3.2 of this report. For more information on fatigue crack growth models not discussed in this report, the reader is referred to an excellent review of such models by Trask (1997).

4.3.1 Fatigue Crack Growth Models for Constant Amplitude Loading

Fatigue crack growth analysis of a component subjected to constant amplitude loading is the least difficult to perform due to the fact that in the case of constant amplitude loading, fatigue damage and crack growth are independent of any prior load history (i.e., sequence or load interaction effects). Many commonly used models are capable of describing fatigue rate data resulting from constant amplitude loading, the only major differences among the models to be discussed in this section are the factors that they consider and the number of curve fitting parameters they require.

4.3.1.1 The Paris Model for Constant Amplitude Loading

This model, also referred to as Paris' law, is a power law developed by P.C. Paris in the early 1960's. Paris was the first to apply the principles of fracture mechanics to the area of fatigue, and his power law, given by Equation 4.6, is typically used to describe crack growth behavior in region II of the fatigue rate curve.

$$\frac{da}{dN} = C_P(\Delta K)^{m_P} \tag{4.6}$$

In the above relation, m_P represents the slope of the linear portion (region II) of the fatigue rate curve, while C_P is simply a constant equivalent to the projected y-intercept of the curve. An example outlining the calculation of Paris' curve fitting parameters can be found in chapter five of the textbook by Dowling (1993).

Paris' law is extremely simple to use and has the advantage of requiring only two easily obtainable curve fitting parameters. However, Paris' law is neither capable of modeling the near-threshold fatigue crack growth of region I, nor the accelerated unstable fatigue crack growth of region III. Furthermore, Paris' law does not consider the effect of stress ratio (R), whose influence, as previously mentioned, depends greatly on material type. As illustrated in Figure 4.5, a family of parallel lines typically results from testing at various stress ratios. One can therefore deduce that the value of m_P is essentially the same for all stress ratios, whereas the value of C_P varies with stress ratio. For this reason, one must be careful that the particular Paris law equation being used corresponds to the stress ratio for which it applies.

4.3.1.2 The Walker Model for Constant Amplitude Loading

In 1970, E.K. Walker proposed a model that could deal with the limitations of the Paris model by incorporating the effect of the stress ratio (R). Walker suggested the use of a new parameter, $\overline{\Delta K}$, representing an equivalent zero-to-tension (R = 0) stress intensity factor range that causes the same crack growth rate as the actual combination of K_{max} and R. Equation 4.7, in which γ_W represents a curve fitting parameter, can be used to calculate this equivalent stress intensity factor range.

$$\overline{\Delta K} = K_{max}(1-R)^{\gamma_W} \tag{4.7}$$

Using Equation 2.3b and Equation 3.4, it can also be shown that the following relationship is true.

$$K_{max} = \frac{\Delta K}{(1-R)} \tag{4.8}$$

Substitution of Equation 4.8 into Equation 4.7 yields the following relationship:

$$\overline{\Delta K} = \frac{\Delta K}{(1-R)^{1-\gamma_W}} \tag{4.9}$$

Finally, substitution of $\overline{\Delta K}$ from Equation 4.9 into Equation 4.6, we have the following:

$$\frac{da}{dN} = C_w(\overline{\Delta K})^{m_w} = C_w\left[\frac{\Delta K}{(1-R)^{1-\gamma_w}}\right]^{m_w} \tag{4.10}$$

Note that for the case of $R = 0$, Equation 4.10 reduces to the Paris' law relation in Equation 4.6, as expected. The importance of Equation 4.10 lies in the fact that $\overline{\Delta K}$, when plotted versus da/dN should result in a single straight line, regardless of the stress ratio. However, this added capability comes at the expense of a third curve fitting parameter, γ_w, which is determined by trial and error as the value that best concentrates the data onto a straight line on a log-log plot of da/dN-versus-$\overline{\Delta K}$. It is conceivable that "no value of γ_w can be found which consolidates the data onto a straight line, and in this situation, Walker's model cannot be used" [Trask, 1998].

Figure 4.6 illustrates the representation of fatigue rate data based on the Walker model.

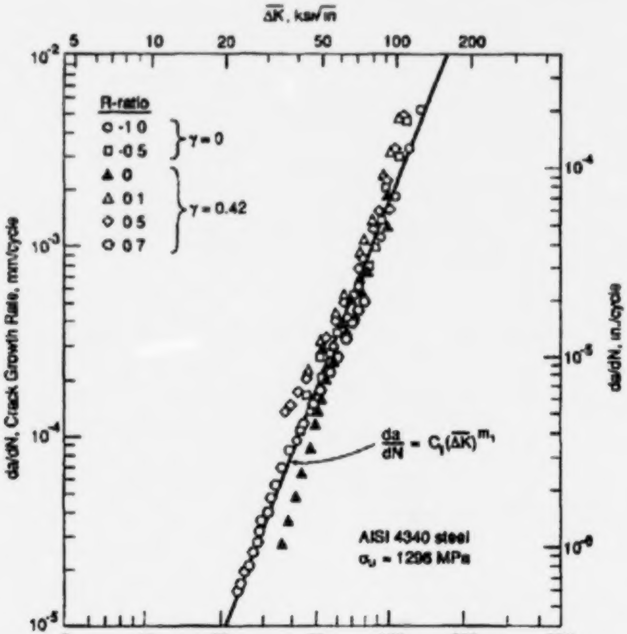

Figure 4.6 – Fatigue data representation based on the Walker model [Dowling, 1993]

Despite the added capability of the Walker model to handle the effect of varying stress ratio, the large dependence of da/dN on R at both low and high growth rates limits its application to only region II of the fatigue rate curve.

4.3.1.3 The Forman Model for Constant Amplitude Loading

Just as Walker refined Paris' model to include the effects of stress ratio, Forman proposed a refinement to Walker's model to allow for fatigue crack growth analysis in region III of the fatigue rate curve. Forman's law, which incorporates the material fracture toughness (K_c), is given by Equation 4.11.

$$\frac{da}{dN} = \frac{C_F(\Delta K)^{m_F}}{(1-R)K_C - \Delta K} = \frac{C_F(\Delta K)^{m_F}}{(1-R)(K_C - K_{max})} \tag{4.11}$$

As one can see from Equation 4.11, as K_{max} approaches the material's fracture toughness (K_c), the crack growth rate approaches infinity. Forman's curve fitting parameters can be determined by first calculating the quantity, Q, of Equation 4.12.

$$Q = \frac{da}{dN}\left[(1-R)K_C - \Delta K\right] \tag{4.12}$$

The applicability of the Forman model can then be evaluated by the noting how well the fatigue rate data for various ΔK and R can be consolidated onto a single straight line on a plot of log Q versus log ΔK. Provided the log Q-versus-log ΔK consolidates well onto a single straight line, as illustrated in Figure 4.7, then Forman's model is applicable, and the corresponding parameters, m_F and C_F, can be determined in a similar fashion as those for Paris' law. That is, m_F and C_F represent the slope and y-intercept, respectively of the log Q-versus-log ΔK plot.

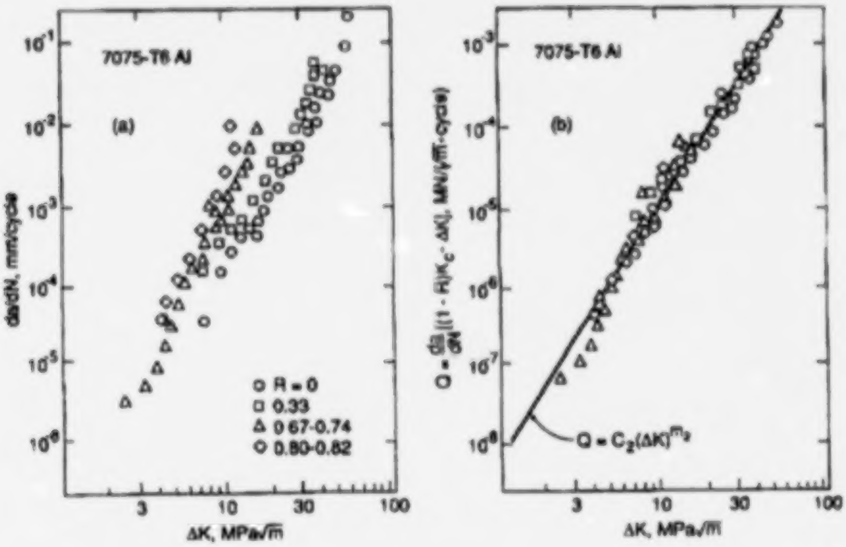

Figure 4.7 – Effect of Forman's model on consolidation of fatigue rate data [Dowling, 1993]

4.3.1.4 Modified Forman Models for Constant Amplitude Loading

Many researchers have made further modifications to Forman's model, attempting to extend its applicability to region I of the fatigue rate curve through incorporation of the fatigue crack growth threshold (ΔK_{th}). Trask (1998) alludes to a modification to Forman's model proposed by A. Hartman and J. Schijve in the late 1960's, given by Equation 4.13.

$$\frac{da}{dN} = \frac{C_{HS}(\Delta K - \Delta K_{th})^{m_{HS}}}{(1-R)K_C - \Delta K} \tag{4.13}$$

Trask (1998) also recommends a proposed modification to Foreman's model given by Equation 4.14.

$$\frac{da}{dN} = \frac{C_{MOD}(\Delta K)^{m_{MOD}}(\Delta K - \Delta K_{th})^{1/2}}{(1-R)K_C - \Delta K} \tag{4.14}$$

Lui (1998) suggests one final modification to Forman's model, given by Equation 4.15, in which the exponent on the (ΔK - ΔK_{th}) term is dropped.

$$\frac{da}{dN} = \frac{C_{MOD}(\Delta K)^{m_{MOD}}(\Delta K - \Delta K_{th})}{(1-R)K_C - \Delta K} \tag{4.15}$$

Although all of these modifications produce the typical sigmoidal shaped fatigue rate curve, their differences lie in the method used to fine-tune the shape of their respective curve. The main disadvantage to extending Forman's model into region I of the fatigue rate curve is that ΔK_{th} is quite sensitive to R, and as such, the specific value of ΔK_{th} must be known for any given stress ratio.

4.3.1.5 The Pook and Frost Model for Constant Amplitude Loading

L.P. Pook and N.E. Frost noticed that the majority of previously developed crack growth laws were simply empirical relations and, therefore, attempted to develop a model with some physical significance. They believed that cyclic crack growth was not a result of any progressive damage accumulation, but simply because the unloading portion of each cycle resharpened the crack tip. They could therefore relate the incremental crack growth per cycle to the repeated blunting and resharpening of the crack tip as the crack would open and close, respectively. Their model, which considers both plane stress and plane strain, is given by the relationships of Equation 4.16.

$$\frac{da}{dN} = \frac{9}{\pi}\left(\frac{\Delta K}{E}\right)^2 \quad \text{(plane stress)} \tag{4.16a}$$

$$\frac{da}{dN} = \frac{7}{\pi}\left(\frac{\Delta K}{E}\right)^2 \quad \text{(plane strain)} \tag{4.16b}$$

They found that when compared to experimental data plotted in terms of ΔK/E, the plane stress predictions were in good agreement for crack growth rates near 3 x 10^{-8} m/cycle.

Unfortunately, this model underestimates the relatively high growth rates near region III of the fatigue rate curve, and overestimates the relatively low fatigue crack growth rates in the vicinity of region I.

4.3.1.6 The Zheng and Hirt Model for Constant Amplitude Loading

As noted by Trask (1998), Zheng and Hirt's crack growth law is another model that was developed with the objective of improving upon an already existing one, namely the one proposed by Lal and Weiss in 1978. The concept of Lal and Weiss' proposed static fracture model is illustrated in Figure 4.8, where the incremental increase in crack length per cycle is equated to that distance over which the maximum normal stress exceeds the critical fracture stress (σ_{ff}) of the material. Although their model experienced moderate success in crack growth prediction, it too used material constants that were of no physical importance.

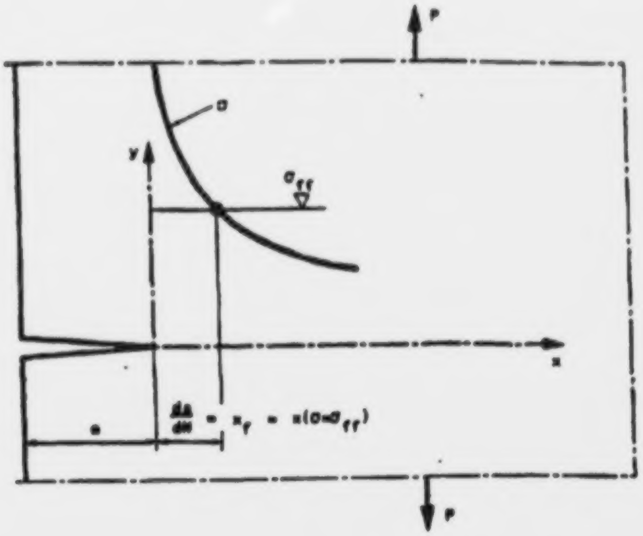

Figure 4.8 – Concept of Lal and Weiss model, basis for Zheng and Hirt model [Trask, 1998]

In 1983, Zheng and Hirt refined the Lal and Weiss model such that the new material constants could be defined by material tensile properties. They found that upon loading, blunting of the crack tip took place at the stress intensity threshold (K_{th}), below which no crack growth occurred. For this reason, as opposed to employing the conventional definition of ΔK (i.e., $K_{max} - K_{min}$), Zheng and Hirt decided to incorporate the use of an effective stress intensity factor range, ΔK_{eff} (i.e., $K_{max} - K_{th}$). Incorporating this ΔK_{eff}, along with the assumption made in Figure 4.8, Zheng and Hirt's model was developed as follows:

$$\frac{da}{dN} = x_f = x(\sigma = \sigma_{ff}) \tag{4.17}$$

Recalling Equation 2.2b, the stress in the y-direction at any distance 'x' ahead of the crack tip is given by the following relation

$$\sigma_{yy} = \frac{K_I}{\sqrt{2\pi x}} \tag{4.18}$$

Equation 4.18 can be rearranged as follows to determine the location 'x_f' in Figure 4.8

$$x_f = \frac{K_I^2}{2\pi\sigma_{ff}^2} \tag{4.19}$$

Combining Equation 4.19 and Equation 4.17, and incorporating the parameter ΔK_{eff},

$$\frac{da}{dN} = \frac{K_{eff}^2}{2\pi\sigma_{ff}^2} = \frac{(K_{max} - K_{th})^2}{2\pi\sigma_{ff}^2} \tag{4.20}$$

The theoretical strength of metallic materials, σ_{ff}, is equal to $\sqrt{E\sigma_f\varepsilon_f}$, where σ_f and ε_f represent the material's true fracture strength and fracture ductility, respectively. Therefore, Equation 4.20 can be further reduced to yield the following relation

$$\frac{da}{dN} = \frac{(K_{max} - K_{th})^2}{2\pi E \sigma_f \varepsilon_f} \tag{4.21}$$

The aforementioned material fracture strength (σ_f) and fracture ductility (ε_f) can be determined using Equation 4.22 and Equation 4.23, respectively.

$$\sigma_f = \sigma_{ult}(1 + RA) \tag{4.22}$$

$$\varepsilon_f = -\ln(1 - RA) \tag{4.23}$$

In these equations, the variables σ_{ult} and RA represent the specimen's ultimate strength and reduction in area at fracture, respectively. Both can be readily obtained from a simple tension test.

In the case of zero-to-tension loading ($R = 0$), $\Delta K = K_{max}$ and $\Delta K_{th} = K_{th}$. Making these substitutions into Equation 4.21 yields the following relation

$$\frac{da}{dN} = \frac{(\Delta K - \Delta K_{th})^2}{2\pi E \sigma_{ult}(1 + RA)(-\ln(1 - RA))} \tag{4.24}$$

As previously mentioned, the value of ΔK_{th} is relatively sensitive to stress ratio R, and therefore, in cases for which $R \neq 0$, Zheng and Hirt suggest the use of Equation 4.25 to calculate a suitable crack growth threshold, where $\Delta K_{th,0}$ represents the fatigue crack growth threshold for $R = 0$, and the parameter γ is a shaping exponent that varies between zero and one.

$$\Delta K_{th(R \neq 0)} = \Delta K_{th,0}(1 - R)^{\gamma} \tag{4.25}$$

Although the Zheng and Hirt model is not capable of representing fatigue rate data from region III, the parameters involved do appear to have some physical significance. Furthermore, crack growth data from region III is of minimal importance in the overall analysis, as so little fatigue life remains at that point.

4.3.1.7 The Wang and Hsu Model for Constant Amplitude Loading

Wang and Hsu (1994) proposed a formula to evaluate fatigue crack growth in regions II and III of the fatigue rate curve by means of a "damage accumulation theory which considers the plastic component of the J integral as a damage factor" [Trask, 1997]. Wang and Hsu's theory makes two important assumptions regarding absorption of strain energy density. Firstly, it is assumed that any elastic strain energy density absorbed by a material during loading is subsequently released upon unloading, and as such, causes no fatigue damage. Lastly, prior to a material reaching its ultimate strength, the total plastic strain energy density that can be absorbed is assumed to be a constant, and is the driving force behind any fatigue damage accumulation in a given material. Wang found that the fatigue crack growth rate, da/dN, was not only a function of ΔK, but was also dependent on such factors as fracture toughness, local yield strength, and the applied effective stress intensity factor. Wang and Hsu's model for constant amplitude fatigue crack growth is given by Equation 4.26.

$$\frac{da}{dN} = \alpha \frac{K_{max}^{4}}{\bar{\sigma}_{yld}^{2}} \left[\frac{1}{1-\xi^{2}} - \frac{1}{1-(R\xi)^{2}} \right] \left[\frac{1}{\sqrt{1-\xi^{2}}} - \frac{1}{\sqrt{1-(R\xi)^{2}}} \right] \qquad (4.26)$$

Where $\xi^{2} = \frac{1}{2} \left(\frac{K_{max}}{\sigma_{yld} \sqrt{\pi a}} \right)^{2}$

α = a constant related to material type and loading condition

σ_{yld} = local yield strength

$\bar{\sigma}_{yld}$ = average local yield strength

Although the Wang and Hsu model may appear complicated, it must be noted that all but one of its parameters (α) have some physical significance.

4.3.1.8 The Dowling and Begley Model for Constant Amplitude Loading

Thus far, all of the fatigue crack growth models discussed have assumed small-scale yielding at the crack tip, therefore validating the use of LEFM concepts. However, it is quite conceivable that in some instances, the limits for which LEFM applies, as given by Equation 2.1, may be surpassed - even if the plastic zone adjustment of section 2.2.4 is considered. Under such conditions, use of the stress intensity factor range, ΔK, is no longer acceptable. Therefore, Dowling and Begley have suggested the use of a similar EPFM parameter, ΔJ, to model fatigue crack growth under large-scale yielding. Similar to Paris' law, the Dowling and Begley model is capable of describing fatigue rate data in region II, but does not account for stress ratio effects. The Dowling and Begley model is given by Equation 4.27.

$$\frac{da}{dN} = C_{DB}(\Delta J)^{m_{DB}} \qquad (4.27)$$

4.3.2 Fatigue Crack Growth Models for Variable Amplitude Loading

While some engineering components do experience constant amplitude loading, in practice, the majority are subjected to variable amplitude loading. Whether the form of variable amplitude loading is repeated, semi-random, or completely random, it is well known that load interaction (sequence) effects may occur during variable amplitude loading, and these interaction effects can significantly affect crack growth behavior during the life of the component. The next few sections of this report will review the nature of these sequence effects, along with a discussion of several of the more commonly used variable amplitude loading fatigue crack growth models.

4.3.2.1 Load Interaction (Sequence) Effects

The influence of any given load cycle on crack growth behavior depends upon the prior load history, thus the term 'load interaction' is used to describe these effects. With this in mind, one can appreciate why fatigue crack growth analysis for a component subjected to variable amplitude loading can be much more complex than for one subjected to constant amplitude loading. There are essentially three load sequences that affect crack growth rate: a tensile overload, a compressive underload, and a tensile overload followed by a compressive underload. The effects of these three sequences are commonly referred to as crack retardation, crack acceleration, and reduction in crack retardation, respectively. There is also a fourth sequence effect, where a compressive underload is followed by a tensile overload; however, for conservative reasons, it is seldom used. Despite the importance of an accurate prediction of the loading sequence, the very nature of random loading renders this practically impossible.

When a tensile overload, or 'spike', is applied within an otherwise constant amplitude load history, the crack growth rate immediately following the overload is significantly less. However, after a number of cycles of retarded growth, the original growth rate is resumed. This phenomenon is referred to as crack growth retardation. Consider a fatigue crack in a plate subjected to constant amplitude loading with a stress ratio of zero (R=0), as illustrated in Figure 4.9. The first load cycle follows path A-B-C. The dashed circle at the crack tip in Figure 4.9a denotes the material to undergo plastic deformation upon loading to B. When the plate is loaded to B, plastic deformation at the crack tip produces the plastic zone shown in Figure 4.9b. Suppose that the material within this new plastic zone were then removed from the plate. Upon unloading to C, the hole at the crack tip in Figure 4.9d relaxes to the same size as the dashed circle of Figure 4.9a. The plastic zone, which was previously removed, has now become permanently deformed, and will no longer fit into the hole of Figure 4.9d. Broek (1989) notes that, "in order to squeeze the permanently deformed material back to its original size, reverse yielding is necessary", thus creating a zone of compressive residual stress in the vicinity of the crack tip.

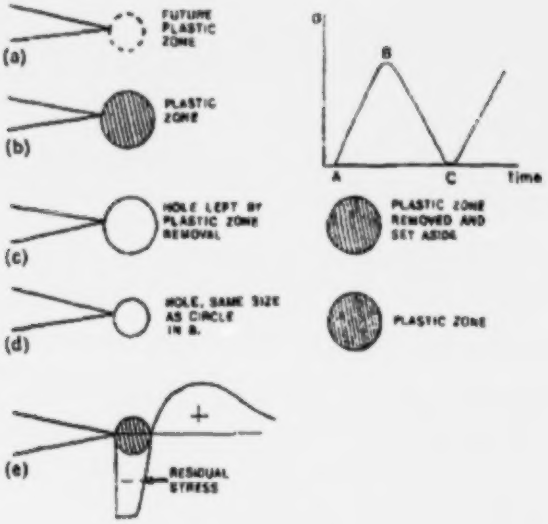
FUTURE PLASTIC ZONE
(a)
PLASTIC ZONE
(b)
HOLE LEFT BY PLASTIC ZONE REMOVAL
(c)
HOLE, SAME SIZE AS CIRCLE IN B.
(d)
σ
B
A
C
time
PLASTIC ZONE REMOVED AND SET ASIDE
PLASTIC ZONE
+
–
(e)
RESIDUAL STRESS

Figure 4.9 – Crack growth retardation via residual stress field near the crack tip [Broek, 1989]

In the event of a tensile overload, a much larger plastic zone is produced, which in turn, creates a much more extensive residual stress distribution. Accordingly, the larger compressive residual stresses in the vicinity of the crack tip tend to retard any subsequent crack growth until the crack has grown through the overload residual stress field and the original stress field is restored.

As illustrated in Figure 4.10, the application of multiple overloads tends to have a more pronounced effect on crack growth retardation. The degree of retardation is characterized by a quantity referred to as the overload ratio (OLR), which is commonly defined as the ratio of the peak overload stress to the peak stress under 'normal' conditions. Crack growth retardation increases exponentially with increasing overload ratio. In fact, as OLR approaches values of two or three, full crack arrest may occur. Crack growth behavior due to successive overloads "depends on their relative proximity, the difference between their respective overload ratios, and the baseline stress range applied between them" [Hammouda et al, 1998]. Hammouda et al (1998) also found that the retardation effect can be 'optimized' by controlling the ratio of successive overloads and the crack growth increment between which they are applied. Conversely, application of tensile overloads with OLR's less than about 1.2 have little effect on crack growth behavior.

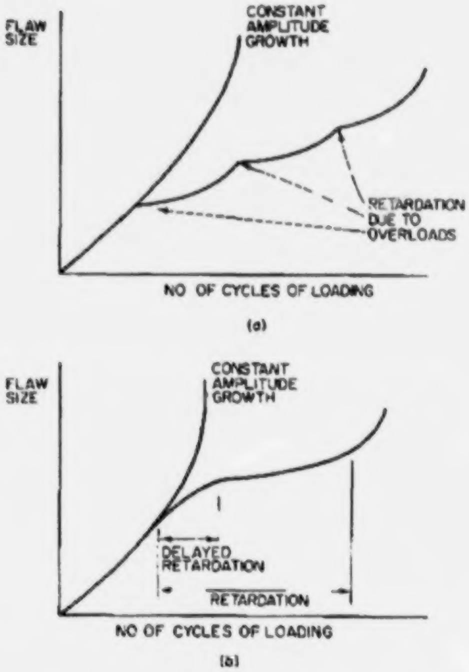

Figure 4.10 – Retardation with (a) Multiple overloads, and (b) Single overloads [Barsom, 1987]

If, on the other hand, a compressive underload is applied within an otherwise constant amplitude load history, the crack growth rate immediately following the underload is accelerated. However, as illustrated by curve (d) in Figure 4.11, the degree of crack growth acceleration following a compressive underload is typically smaller than the retardation resulting from an equivalent tensile overload. Some researchers explain this phenomenon by considering a compressive underload that is greater than that required to fully close the fatigue crack. The remaining 'unused' portion of the underload is often assumed to be ineffective in accelerating the crack and therefore, the degree of acceleration is less than the corresponding degree of retardation following an equivalent tensile overload. In fact, because the retardation caused by tensile overloads typically dominates crack growth behavior, compressive underloads are often neglected in fatigue crack growth analyses.

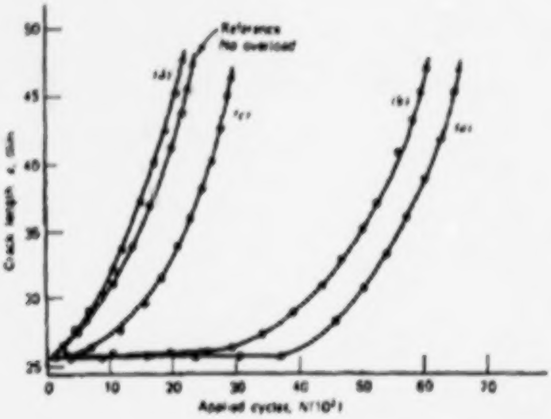

Figure 4.11 – Relative sequence effects under (a) Tension overload, (b) Compression-tension overload, (c) Tension-compression overload, and (d) Compression underload [Trask, 1998]

If one further considers a tensile overload immediately followed by a compressive underload, as illustrated by curve (c) in Figure 4.11, the degree of retardation is reduced significantly, but not eliminated. Conversely, if a compressive underload is applied prior to a tensile overload, as illustrated by curve (b) in Figure 4.11, the extent of reduction in crack growth retardation appears rather insignificant.

When overloads occur predominantly in one direction, their effects are much more pronounced than if the load sequence is highly random, with both tensile and compressive overloads occurring frequently. Moreover, the effect of mild overloads on acceleration and retardation is very minimal.

4.3.2.2 The Use of Constant Amplitude Loading Models in Fatigue Crack Growth Prediction for Variable Amplitude Loading

Any of the previously mentioned fatigue crack growth models for constant amplitude loading can also be used to characterize crack growth behavior under variable amplitude loading. However, this procedure dictates that all sequence effects be neglected and requires a cycle-by-cycle analysis of fatigue crack growth using one of several constant amplitude crack growth laws. On the other hand, neglecting sequence effects typically yields conservative life estimates that are usually more than adequate for most preliminary analyses. In cases where load sequence effects are relatively unpredictable or tend to nullify each other, the added expense and computational effort required by a more detailed analysis may not be justified by the increased accuracy provided.

The main area of uncertainty with this approach is the notion of an instantaneously adjusted fatigue crack growth rate, which most constant amplitude models assume. In the case of variable amplitude loading, the ever-changing stress range ($\Delta\sigma$) may cause significant fluctuations in the stress intensity factor range (ΔK), and therefore, in the fatigue crack growth rate (da/dN). In reality, when the mean stress (or stress ratio) changes from cycle to cycle (or block to block) within a variable amplitude load history, the corresponding growth rate is not realized immediately. However, this is often ignored, because the load sequence effects would likely offset any resulting errors.

4.3.2.3 The Barsom Root-Mean-Square (rms) Model for Variable Amplitude Loading

Depending on the application, load spectrum, and even the material, fatigue crack growth under variable amplitude loading does not always exhibit sequence effects. If it has been shown that fatigue crack behavior is not greatly affected by sequence effects, then crack growth under variable amplitude loading can be estimated from baseline (constant amplitude) da/dN-versus-ΔK data. The use of a more complicated cycle-by-cycle analysis accounting for load interaction would therefore be unnecessary.

In the early 1970's, Barsom endeavored to calculate "the magnitude of constant amplitude cyclic load fluctuation that results in the same a-versus-N curve obtained under variable amplitude cyclic load fluctuation" [Barsom et al, 1987], under the condition that both load histories are applied to identical specimens. However, to correlate fatigue rate data for variable amplitude loading with that for constant amplitude loading, the various stress intensity factor ranges during the loading spectrum must be normalized in some fashion. Barsom proposed the use of a root-mean-square (rms) value of the stress intensity factor range, denoted by ΔK_{rms}. As given by Equation 4.28, ΔK_{rms} represents the square root of the mean of the sum of the squares of each individual stress intensity factor range in a load spectrum.

$$\Delta K_{rms} = \sqrt{\frac{\sum_{i=1}^{N} (\Delta K_i)^2}{N}} \qquad (4.28)$$

Using this ΔK_{rms} parameter, Barsom proposed the use of a model similar to Paris' law, given by Equation 4.29.

$$\frac{da}{dN} = C_B (\Delta K_{rms})^{m_B} \qquad (4.29)$$

Although Barsom's model does not deal specifically with load interaction effects, it does provide excellent results when used to model crack growth under highly irregular load spectra such as those illustrated in Figure 4.12. In load spectra such as these, where sequence effects are more likely to balance each other, Equation 4.29 represents an average fatigue crack growth rate. Figure 4.13 illustrates the effectiveness of Barsom's model in consolidating the load spectra of Figure 4.12.

On the other hand, when used to model load histories with few overloads applied, Barsom's model does not accurately predict fatigue crack growth behavior, and therefore, a model that specifically accounts for sequence effects should be used instead.

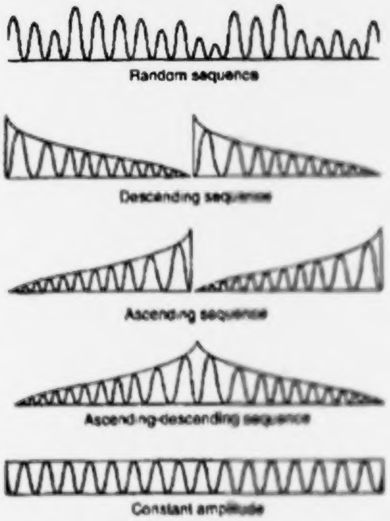
Random sequence
Descending sequence
Ascending sequence
Ascending-descending sequence
Constant amplitude

Figure 4.12 – Schematic representation of loading profiles for Barsom's model [Lui, 1998]

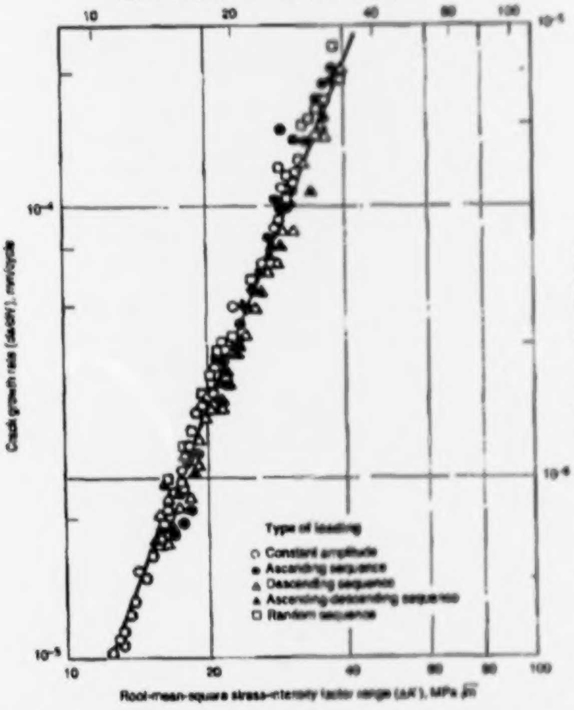

Figure 4.13 – Use of Barsom's model in describing irregular load spectra [Lui, 1998]

4.3.2.4 The Hudson Root-Mean-Square (rms) Model for Variable Amplitude Loading

C.M. Hudson (1981) also proposed a root-mean-square model to predict fatigue crack growth under random spectrum loading. Hudson's model is similar to that proposed by Barsom, but instead of using Paris' law to calculate crack growth rates, the model proposed by Hudson incorporates Forman's model for constant amplitude loading. Hudson's model also neglects load interaction effects, and therefore provides more accurate results when used to describe crack growth under highly irregular load sequences. Instead of determining ΔK_{rms}, Equation 4.30 and Equation 4.31 are used to calculate the root-mean-square maximum and minimum stresses for the entire load spectrum.

$$S_{max,rms} = \sqrt{\frac{\sum_{i=1}^{N} (S_{i,max})^2}{N}} \tag{4.30}$$

$$S_{min,rms} = \sqrt{\frac{\sum_{i=1}^{N} (S_{i,min})^2}{N}} \tag{4.31}$$

In the above relations, $S_{i,max}$ and $S_{i,min}$ are the maximum and minimum stresses, respectively, for each cycle 'i', and N denotes the total number of $S_{i,max}$ and $S_{i,min}$ values. Using Equation 4.30 and Equation 4.31, a root-mean-square stress ratio, R_{rms}, can be calculated as follows.

$$R_{rms} = \frac{S_{min,rms}}{S_{max,rms}} \tag{4.32}$$

Furthermore, the root-mean-square stress intensity factor range can be determined using Equation 4.30 and Equation 4.31, in conjunction with the proper geometric correction factor Y.

$$\Delta K_{rms} = (S_{max,rms} - S_{min,rms})Y\sqrt{\pi a} \tag{4.33}$$

For example, in the case of a center-cracked specimen of width W containing a fatigue crack of half-length a, Equation 4.33 becomes

$$\Delta K_{rms} = (S_{max,rms} - S_{min,rms})\sqrt{\pi a \sec\left(\frac{\pi a}{W}\right)} \tag{4.34}$$

The aforementioned root-mean-square parameters, used in conjunction with Forman's model for constant amplitude loading, yields the following relation

$$\frac{da}{dN} = \frac{C_F \Delta K_{rms}^{m_F}}{(1 - R_{rms})K_C - \Delta K_{rms}} \tag{4.35}$$

4.3.2.5 The Elber Model for Variable Amplitude Loading

W. Elber based his model on the concept of crack closure, which he first introduced in the late 1960's. Elber noticed that during the unloading portion of a load cycle, fatigue cracks often begin to close prior to the removal of the entire tensile load. Elber theorized that this seemingly 'premature' crack closure under tensile load was due to plasticity-induced closure, a result of residual compressive stresses left in the wake of the crack. Similarly, Elber observed that the crack surfaces did not open immediately during the subsequent loading portion of a load cycle. These observations have led to the assumption that the net effect of crack closure is to reduce the applied ΔK to some effective level ΔK_{eff}, as given earlier by Equation 4.1.

$$\Delta K_{eff} = K_{max} - K_{open} \tag{4.1}$$

In the above relation, K_{open} represents "the minimum stress intensity level of that cycle required to reopen the crack, and its magnitude is usually higher than the applied K_{min}" [Lui, 1998]. This approach assumes that fatigue crack propagation can only occur during the portion of each loading cycle for which the fatigue crack is fully open. The parameter K_{open} is highly dependent on factors such as loading type, material type, material thickness, crack length, environment, maximum stress intensity level, and stress ratio. Elber determined the value of K_{open} using a stress-displacement curve similar to the one illustrated in Figure 4.14. The initial linear slope AB corresponds to the uncracked specimen (i.e., a closed crack), while the linear portion CD applies to the cracked specimen. The nonlinear segment BC corresponds to the transition from a fully closed crack to a fully open crack. The value of K_{open} can be determined using the value of 'S_{op}' given in Figure 4.14.

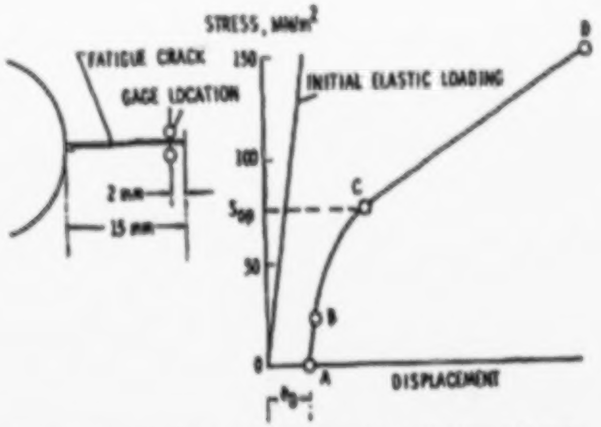

(a) CRACK CONFIGURATION AND GAGE LOCATION (b) APPLIED STRESS - DISPLACEMENT RELATION

Figure 4.14 – Evaluation of K_{open} for Elber model [Trask, 1998]

Elber then introduced the concept of an effective stress intensity ratio, U, defined as

$$U = \frac{\Delta K_{eff}}{\Delta K} = \frac{K_{max} - K_{open}}{K_{max} - K_{min}} \tag{4.36}$$

For a given stress ratio, this effective stress intensity ratio should lie between zero and one, where U = 0 corresponds to a fully closed crack (i.e., $K_{open} = K_{max}$) and U = 1 corresponds to a fully open crack (i.e., $K_{open} = K_{min}$). For cases where $K_{open} \geq K_{min}$, one could further define an effective stress ratio, R_{eff}, as

$$R_{eff} = \frac{K_{open}}{K_{max}} \tag{4.37}$$

Therefore, since $R = K_{min}/K_{max}$ and $K_{open} \geq K_{min}$, R_{eff} is always greater than R. As long as $K_{open} \geq K_{min}$, both K_{open} and R_{eff} can be negative and should therefore not be set to zero for those load cycles involving compression.

Dividing both the numerator and denominator of Equation 4.36 by K_{max}, one obtains a unique relationship between U and R_{eff}, given by

$$U = \frac{\left(\dfrac{K_{max} - K_{open}}{K_{max}}\right)}{\left(\dfrac{K_{max} - K_{min}}{K_{max}}\right)} = \frac{(1 - R_{eff})}{(1 - R)} \tag{4.38}$$

Simply by replacing ΔK with UΔK, any existing crack growth model can be used, but for the sake of simplicity, Elber proposed a modified Paris law, given by Equation 4.39.

$$\frac{da}{dN} = C_E (\Delta K_{eff})^{m_E} = C_E (U\Delta K_{eff})^{m_E} \tag{4.39}$$

Many variable amplitude models theorize that crack growth retardation is a consequence of the residual compressive stresses ahead of the crack tip. Elber's crack closure model instead considers the retardation following an overload as a result of the residual deformation left in the wake of a propagating crack. Furthermore, through the use of the stress intensity ratio U, Elber's model is capable of explaining environmental effects on ΔK_{th} and the influence of nonzero mean stress on growth rates.

One of the main difficulties with Elber's approach lies in how to properly evaluate K_{open}, which is required for the calculation of U. Furthermore, the value of K_{open} may change from cycle to cycle, resulting in a relatively time consuming analysis. To overcome this pitfall, Elber and Schijve suggested the use of Equation 4.40 and Equation 4.41, respectively, based on constant amplitude tests for aluminum. Similar relationships for various other materials have been reported in the literature.

$$U = 0.5 + 0.4R \qquad (-0.1 \leq R \leq 0.7) \tag{4.40}$$

$$U = 0.55 + 0.33R + 0.12R^2 \tag{4.41}$$

Moreover, values for K_{open} are often based on test data from constant amplitude loading, under the assumption that crack opening behavior is similar for random load spectra. As described by Kim et al (1994), this is the subject of much controversy among researchers in the field of crack closure. Another drawback to this model is the cycle-by-cycle counting method required to repredict the crack growth curve. Despite these limitations, Elber's crack closure model appears to provide crack growth predictions with adequate accuracy.

4.3.2.6 The Wheeler Model for Variable Amplitude Loading

The Wheeler model is quite possibly one of the least difficult models for fatigue crack growth under variable amplitude loading. Proposed by O.E. Wheeler in 1972, it accounts for crack growth retardation following a tensile overload by introducing a retardation parameter, ϕ_R. Wheeler's retardation parameter can be applied to any fatigue crack growth law of the form da/dN = f (ΔK, R). Using Paris' law as an example, application of Wheeler's retardation parameter yields a fatigue crack growth rate described by Equation 4.42.

$$\left(\frac{da}{dN}\right)_{\text{retarded}} = \phi_R\left[C_P(\Delta K)^{m_P}\right] \tag{4.42}$$

Sheu et al (1995) defined the Wheeler retardation parameter as "a power function of the ratio of the present plastic zone size to the distance from the crack tip to the border of the plastic zone caused by the overload", with a magnitude given by Equation 4.43.

$$\phi_R = \begin{cases} \left[\dfrac{r_{pi}}{(a_{OL} + r_{p,OL} - a_i)}\right]^m & , a_i + r_{pi} \le a_{OL} + r_{p,OL} \\ 1 & , a_i + r_{pi} \ge a_{OL} + r_{p,OL} \end{cases} \tag{4.43}$$

Where a_i = the current crack length corresponding to the ith cycle

r_{pi} = the current plastic zone size corresponding to the i^{th} cycle

a_{OL} = the crack length at which the overload was applied

$r_{p,OL}$ = the plastic zone created by the overload

m = an empirically adjustable parameter referred to as the shaping exponent

The above terms defining Wheeler's model are illustrated in Figure 4.15 below.

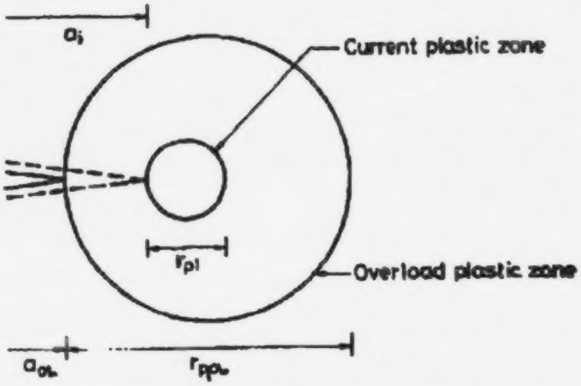

Figure 4.15 – Illustration of terms defining Wheeler's retardation parameter [Sheu et al, 1995]

According to Wheeler's approach, there will be no crack growth retardation (i.e., $\phi_R=1$) if the elastic-plastic boundary for the current plastic zone lies outside the largest elastic-plastic interface corresponding to a preceding plastic zone. In other words, load interaction effects will occur so long as the "plastic zone for the current stress cycle is inside the elastic-plastic boundary remaining from any of the preceding stress cycles" [Lui, 1998]. Although any suitable equation may be used to calculate the plastic zone sizes, Irwin's plane stress and plane strain estimates are often used, given by Equation 2.21 and Equation 2.23, respectively.

To further illustrate the concept behind the Wheeler retardation model, consider the load spectrum and plastic zone boundaries of Figure 4.16.

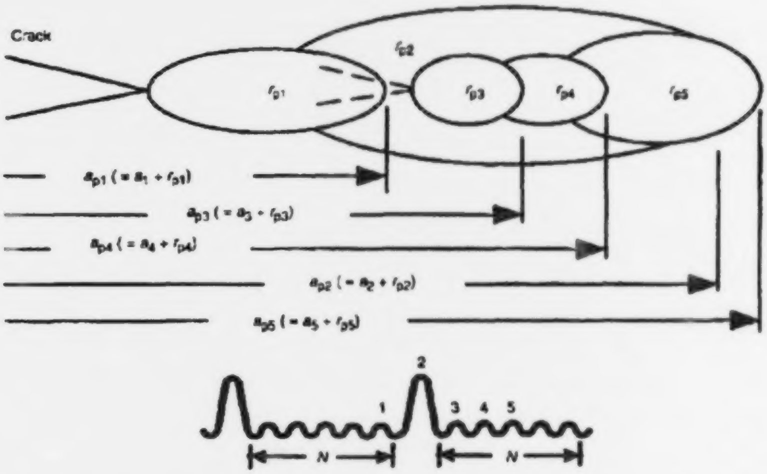
Crack
r_{p2}
r_{p1}
r_{p3}
r_{p4}
r_{p5}
a_{p1} (= a_1 + r_{p1})
a_{p3} (= a_3 + r_{p3})
a_{p4} (= a_4 + r_{p4})
a_{p2} (= a_2 + r_{p2})
a_{p5} (= a_5 + r_{p5})
2
1
3
4
5
N
N

Figure 4.16 – Schematic representation of load interaction zones [Liu, 1998]

Consider stress level σ_1 applied at a crack length a_1, resulting in a plastic zone of size r_{p1}. The elastic-plastic boundary for this stage of crack growth lies at $a_{p1} = a_1 + r_{p1}$. After the crack has grown to length a_2, σ_2 is applied, resulting in a plastic zone of size r_{p2}. The elastic-plastic boundary is extended to $a_{p2} = a_2 + r_{p2}$. Since $a_{p2} > a_{p1}$, no retardation will occur during crack growth from a_2 to a_3. However, subsequent application of σ_3 and σ_4 results in crack growth retardation, as the corresponding elastic-plastic boundaries both lie within a_{p2}. Finally, application of σ_5 results in a plastic zone boundary which lies outside a_{p2}, and therefore crack growth from a_5 to a_6 will not be affected by the residual stress field created by σ_2.

Evaluation of the Wheeler shaping exponent involves empirically fitting Wheeler's model to the variable amplitude test data. However, since the shaping exponent varies with material and loading spectrum, it should only be used to predict crack growth for materials and load spectra similar to those for which it was evaluated. Typical values for Wheeler's shaping exponent range from 1 to 3.

4.3.2.7 The Willenborg Model for Variable Amplitude Loading

The Willenborg model considers the amount of crack growth retardation as a function of the stress intensity factor required to negate the effects of the plastic zone created by any previously applied overload. Fatigue crack growth behavior within interacting plastic zones can be described as a function of the prevailing effective stresses. Unlike the Wheeler model, Willenborg's model does not rely on any empirically derived parameters. However, the model does not account for crack growth acceleration due to compressive underloads. For a description of the basic derivation of the Willenborg model, the reader is referred to the report written by Willenborg et al (1971).

Several researchers have generalized the original Willenborg model to include such factors as varying crack growth threshold and crack arrest. To account for crack growth retardation, the Willenborg model incorporates a residual stress intensity factor (K_{res}), given in Equation 4.44.

$$K_{res} = K_{max,OL}\sqrt{\left(1-\frac{\Delta a_{OL}}{Z_{OL}}\right)} - K_{max,i} \tag{4.44}$$

Where $K_{max,OL}$ = the maximum stress intensity factor during the overload cycle

$K_{max,i}$ = the maximum stress intensity factor during the current cycle

Δa_{OL} = the amount of crack growth since the overload cycle

Z_{OL} = the size of the plastic zone created by the overload cycle, considered by some researchers to be the full plastic zone diameter, and by others, the plastic zone radius

This residual stress intensity factor "physically represents the difference between the stress intensity required to produce a current plastic zone equal to 'Z_{OL} - Δa_{OL}' and the current applied maximum stress intensity" [Johnson, 1981].

Willenborg's model can be used in conjunction with any of the previously discussed crack growth laws for constant amplitude loading simply by replacing ΔK and R with their corresponding effective values, given by Equation 4.45 and Equation 4.46.

$$\Delta K_{eff} = (K_{max})_{eff} - (K_{min})_{eff} \tag{4.45}$$

$$R_{eff} = \frac{(K_{min})_{eff}}{(K_{max})_{eff}} \tag{4.46}$$

The Willenborg model does not consider crack growth acceleration due to compressive underloads, and therefore it is recommended that neither $K_{min\,eff}$ nor R_{eff} be less than zero. The effective stress intensity factors $(K_{min})_{eff}$ and $(K_{max})_{eff}$, as given in Rudd and Engle (1981), are described by

$$(K_{max})_{eff} = K_{max,i} - \Phi\left[K_{max,OL}\sqrt{1-\frac{\Delta a_{OL}}{Z_{OL}}} - K_{max,i}\right] = K_{max,i} - \Phi K_{res} \tag{4.47}$$

and

$$(K_{min})_{eff} = K_{min,i} - \Phi\left[K_{max,OL}\sqrt{1-\frac{\Delta a_{OL}}{Z_{OL}}} - K_{max,i}\right] = K_{min,i} - \Phi K_{res} \tag{4.48}$$

in which

$$\Phi = \frac{1-\dfrac{K_{th,0}}{K_{max,i}}}{OLR_{ARR} - 1} \tag{4.49}$$

Where OLR_{ARR} = the overload ratio corresponding to full crack arrest (typical values range from 2 to 3)

As an example of how the Willenborg model is implemented, when used in conjunction with the Walker model, as done by Rudd and Engle (1981), Equation 4.50 results.

$$\frac{da}{dN} = C_W \left[\frac{\Delta K_{eff}}{(1 - R_{eff})^{1-\gamma_w}} \right]^{m_w} \tag{4.50}$$

4.3.2.8 The Johnson Model for Variable Amplitude Loading

W.S. Johnson (1981) proposed a load interaction model known as the Multi-Parameter Yield Zone (MPYZ) load interaction model. Johnson's model is capable of predicting crack growth behavior under both tensile overloads and compressive underloads. For his MPYZ load interaction model, Johnson used a slightly modified Forman model, given by Equation 4.51.

$$\frac{da}{dN} = \frac{C_F \Delta K^{m_J}}{(1 - R_{eff})^{n_J} K_C - \Delta K} \tag{4.51}$$

Where $n_J = 1$ for $R_{eff} \geq 0$, and

$n_J = 2$ for $R_{eff} < 0$

In using Equation 4.51 to calculate crack growth increments, Johnson considers two situations. If the stress intensity factor is below threshold for a given R_{eff}, then no crack growth results. On the other hand, if ΔK is above threshold, load interaction effects are accounted for via proper adjustment of the effective stress ratio, R_{eff}. Equation 4.52, which is very similar to Equation 4.25, may be used to determine the threshold stress intensity factor corresponding to a given effective stress ratio, where $\Delta K_{th,0}$ again corresponds to the threshold stress intensity factor for $R = 0$.

$$\Delta K_{th} = (1 - R_{eff})\Delta K_{th,0} \tag{4.52}$$

Johnson's load interaction model also implements the residual stress intensity factor (K_{res}) previously described in the Willenborg model. Once the effective stress intensity factor range and effective stress ratio are calculated using Equation 4.45 and Equation 4.46, respectively, crack growth retardation and acceleration are accounted for by simply decreasing or increasing, respectively, the effective stress ratio (R_{eff}) as necessary during each cycle. Johnson (1981) suggests a maximum limit for R_{eff}, given by Equation 4.53, which ranges from 0.6 for plane strain conditions to 0.8 for those of plane stress.

$$R_{eff}^{max} = \frac{0.2\,Z_i}{t} + 0.6 \tag{4.53}$$

Where Z_i = plastic zone diameter for current load cycle (in millimeters or inches), based on Irwin's estimate

t = the material thickness (in millimeters or inches)

Although the concept of Johnson's MPYZ model is rather simple, the equations and parameters involved appear to be relatively complex and tedious to evaluate. Nevertheless, the model does have the attractive option of accounting for both crack growth retardation due to tensile overloads and crack growth acceleration due to compressive underloads. Interested readers are referred to the article by Johnson (1981), which provides a thorough explanation of all parameters used in the model.

4.3.3 Calibration of Fatigue Crack Growth Models

The successful calibration of a fatigue crack growth model involves determining the value of any empirical curve fitting parameters (if applicable) such that the resulting model produces the 'best fit' to the crack growth test data. The best fit to the da/dN-versus-ΔK data is usually accomplished by mathematical technique such as a least-squares regression analysis. However, oftentimes more accurate results are obtained using a hand-drawn best-fit line. This is partially due to the fact that in a least-squares linear regression, each data point considered to be of equal weight or equal importance. However, as previously mentioned, much of a component's total life is consumed during the initial stages of crack growth, while only a small portion of the total life remains by the time crack growth rates approach region III of the fatigue rate curve. Therefore, data points corresponding to the lower crack growth rates near region I should carry more weight in the overall analysis.

The ultimate test of the 'best-fit line' is in the re-prediction of the original a-versus-N test data. Often empirical parameters that correctly model fatigue rate data do not accurately model the original a-versus-N data. In this case minor adjustments must be made to one or more of the curve fitting parameters. It should be noted that if unit conversion is required, it is much easier to convert the original a-versus-N data or the da/dN-versus-ΔK data initially. Conversion of units for a crack growth model that has already been calibrated is an extremely complicated process, and the possibility of incurring errors is much greater.

The next few sections of this report will review the techniques employed to evaluate the empirical parameters of the more commonly used fatigue crack growth models.

4.3.3.1 Calibration of Paris' Law for Fatigue Crack Growth

As mentioned earlier, if the fatigue rate data (log da/dN-versus-log ΔK) follows a linear relationship, the Paris' law may be used. Taking the logarithm of both sides of Equation 4.6 yields

$$\log \frac{da}{dN} = \log\left[C_P(\Delta K)^{m_P}\right] = m_P \log(\Delta K) + \log C_P \qquad (4.54)$$

This relation follows the general equation for a straight line, $y = mx + b$, therefore one can further deduce that $x = \log(\Delta K)$ and $y = \log(da/dN)$, while $m = m_P$ represents the slope of the line and $b = \log C_P$ represents the y-intercept.

Consider two points on the best-fit line of the fatigue rate data with coordinates (x_1, y_1) and (x_2, y_2). Substitution of these coordinates into Equation 4.6 yields

$$y_1 = C_P x_1^{m_P} \tag{4.55a}$$

$$y_2 = C_P x_2^{m_P} \tag{4.55b}$$

Dividing Equation 4.55b by Equation 4.55a, eliminating C_P, and taking the logarithm of both sides

$$\log\left(\frac{y_2}{y_1}\right) = \log\left(\frac{x_2}{x_1}\right)^{m_P} = m_P \log\left(\frac{x_2}{x_1}\right)$$

and therefore,

$$m_P = \frac{\log\left(\frac{y_2}{y_1}\right)}{\log\left(\frac{x_2}{x_1}\right)} \tag{4.56}$$

The value of C_P can then be determined by simply substituting the value of m_P back into Equation 4.55.

Once C_P and m_P have been determined, the newly calibrated law is put to the ultimate test: re-prediction of the original a-versus-N data. Oftentimes, the calibrated parameters predict an a-versus-N curve with the appropriate curvature (m_P), but result in a slightly overpredicted or underpredicted fatigue life. Broek (1989) suggests that by 'fine-tuning' the calculated value of C_P, a more accurate prediction can be obtained. For example, if the predicted life (N_{Pred}) is greater than that obtained experimentally (N_{Expt}), then simply multiplying the value of C_P by the ratio N_{Pred}/N_{Expt} can usually solve the problem. If, on the other hand, the curvature of the re-predicted a-versus-N curve is incorrect, the value of m_P must be adjusted by trial and error. It may then be necessary to make a final readjustment to the value of C_P, as described above.

If it so happens that the original a-versus-N data are unavailable, then there is no other alternative than to provide the best fit for the da/dN-versus-ΔK data and to note that the values may not be exact.

The final values of m_P and C_P may be used in future fatigue crack growth analyses for the same material, provided the expected service conditions are similar to those under which testing was performed.

4.3.3.2 Calibration of the Walker Model for Fatigue Crack Growth

In the event that fatigue rate data is available for a number of different stress ratios and follows a linear relationship for all stress ratios, the Walker equation may be used. As noted earlier, crack growth testing at different stress ratios typically results in a family of parallel lines, each with a different y-intercept. This means that their m_P values are all the same (thus, $m_W = m_P$), but their C_P values differ. Calibration of the Walker equation requires that the Paris parameters m_P and C_P be known for each stress ratio of interest. Comparing Equation 4.6 and Equation 4.10, it follows that

$$C_P = \frac{C_W}{(1-R)^{m_W(1-\gamma_W)}} \tag{4.57}$$

If there are only two stress ratios of interest, the Walker parameters C_W and γ_W (recall that $m_W = m_P$) may be determined using the Paris parameters from the fatigue rate data corresponding to each stress ratio. For example, suppose that for some material and loading history, the Paris parameters for say $R = 0.1$ and $R = 0.5$ are known. Substitution of the known values into Equation 4.57 yields

$$C_{01} = \frac{C_W}{(0.9)^{m_{01}(1-\gamma_W)}} \tag{4.58a}$$

and

$$C_{05} = \frac{C_W}{(0.5)^{m_{05}(1-\gamma_W)}} \tag{4.58b}$$

Since $C_{0\,1}$, $C_{0\,5}$, and m are known, there are two equations with two unknowns, which can be solved by means of elimination or substitution.

In the event that a single equation is desired to describe the crack growth rate for several stress ratios, the calibration process is slightly more involved. Taking the logarithm of both sides of Equation 4.57 yields

$$\log C_P = \log\left[\frac{C_W}{(1-R)^{m_w(1-\gamma_w)}}\right] = \log C_W - \log[(1-R)^{m_w(1-\gamma_w)}] \qquad (4.59a)$$

or

$$\log C_P = \log C_W - [m_W(1-\gamma_W)]\log(1-R) \qquad (4.59b)$$

If $\log C_P$ were then plotted against $\log(1\text{-}R)$, and the best-fit straight line drawn through the data points, Equation 4.59b would represent this best-fit straight line, with a slope of $[m_W(1-\gamma_W)]$ and an intercept of $\log C_W$. As previously described for the Paris law, coordinates of two data points can then be substituted into Equation 4.59b, creating two equations from which the values of C_W and γ_W can be determined (the value of m_P should be approximately equal for all stress ratios). However, if the $\log C_P$-versus-$\log(1\text{-}R)$ data do not indicate a linear relationship, the Walker model cannot be applied.

As suggested for the Paris law, the accuracy of the calibrated Walker parameters should be verified through re-prediction of the original fatigue crack growth (a-versus-N) data.

4.3.3.3 Calibration of the Forman Model for Fatigue Crack Growth

Calibration of the Forman model is a relatively simple process, similar to the Paris model technique described earlier. Recalling the quantity Q from Equation 4.12, it follows that

$$\frac{da}{dN}\left[(1-R)K_C - \Delta K\right] = C_F(\Delta K)^{m_F} \qquad (4\ 60)$$

If on a log-log plot of $\frac{da}{dN}\left[(1-R)K_C - \Delta K\right]$-versus-$\Delta K$ (i.e., logQ-versus-logΔK), the data exhibit a linear relationship, then the Forman model may be applied. The curve fitting parameters m_F and C_F correspond to the slope and intercept, respectively, of the best-fit line through the Q-versus-ΔK data. They can be found in a manner identical to that used in evaluating the coefficients for Paris' law.

The modified Forman models previously discussed are calibrated in a similar fashion. For example, the modified Forman model proposed by Hartman and Schijve and given by Equation 4.13, can be calibrated by plotting log $\frac{da}{dN}\left[(1-R)K_C - \Delta K\right]$ against log(ΔK-ΔK_{th}). It should not be forgotten that ΔK_{th} varies with stress ratio, as indicated by several previous equations. If the data follow a linear relationship, the model may be applicable. Again, the parameters m_{HS} and C_{HS} represent the slope and intercept, respectively, of the best-fit straight line drawn through the log $\frac{da}{dN}\left[(1-R)K_C - \Delta K\right]$-versus-log($\Delta K$-$\Delta K_{th}$) data.

4.3.3.4 Calibration of the Zheng and Hirt Model for Fatigue Crack Growth

The fatigue crack growth model proposed by Zheng and Hirt (Equation 4.24) offers an attractive alternative to those models requiring calibration of several empirical parameters, as it is based instead on parameters which are easily determined and physically significant. The Zheng parameters require knowledge of only the material's tensile properties and the threshold stress intensity factor.

Although Zheng's model does not employ any empirical parameters, a curve fit should nevertheless be performed simply to confirm the accuracy of the model parameters. Taking the logarithm of both sides of Equation 4.21 results in the following relation

$$\log\frac{da}{dN} = \log\left[\frac{(K_{max}-K_{th})^2}{2\pi E\sigma_f\varepsilon_f}\right] = 2\log(K_{max}-K_{th}) - \log(2\pi E\sigma_f\varepsilon_f) \qquad (4.61)$$

Equation 4.61 represents a straight line with a slope of 2 and an intercept of $-\log(2\pi E\sigma_f\varepsilon_f)$ when log da/dN is plotted against $\log(K_{max}-K_{th})$. Provided that the best-fit line through the data points of such a plot exhibits a slope of 2 ± 0.004, it can be used to verify the assumed parameters (K_{th}, E,σ_f and ε_f). Conversely, if a plot of log da/dN versus $\log(K_{max}-K_{th})$ does not exhibit a slope of approximately 2, the *Zheng model* should not be used.

4.3.3.5 Calibration of the Dowling and Begley Model for Fatigue Crack Growth

The Dowling and Begley model of Equation 4.27 is calibrated in exactly the same manner as the Paris model. That is, if the fatigue rate data follow a linear relationship when log da/dN is plotted versus $\log\Delta J$, then the Dowling and Begley EPFM model may be applied. The curve-fitting parameters m_{DB} and C_{DB} are then determined as the slope and intercept, respectively, of the best-fit line passing through the log da/dN-versus-$\log\Delta J$ data. Substituting the coordinates ($\log\Delta J_i$, log da/dN_i) of two points on the best-fit line into Equation 4.27 results in two equations and two unknowns (m_{DB} and C_{DB}), which can then be solved using simple elimination and back substitution.

4.3.3.6 Calibration of Barsom's Root Mean Square Model for Fatigue Crack Growth

The Barsom root mean square model, given by Equation 4.29, is yet another model that can be calibrated in the same manner as the Paris model. In this case, log da/dN is plotted against $\log\Delta K_{rms}$. Provided the fatigue crack growth data from the variable amplitude loading spectrum can be reasonably consolidated onto a straight line, Barsom's curve fitting parameters m_B and C_B represent the slope and intercept of the straight-line regression equation that best fits the data. If the data cannot be consolidated such that it exhibits a linear relationship, then Barsom's model is not a wise choice and a variable amplitude model that specifically accounts for load interaction effects, such as the Elber model, the Wheeler model, or the Willenborg model should be used. Once again, it is a good idea to verify the accuracy of the curve fitting parameters by attempting to re-predict the original a-versus-N data.

4.3.3.7 Calibration of Hudson's Root Mean Square Model for Fatigue Crack Growth

Similar to Barsom's root mean square model, the Hudson model for variable amplitude loading employs root mean square values of maximum and minimum stress, stress ratio, and stress intensity factor range. However, Hudson's root mean square model incorporates the use of Forman's model, and thus has the added convenience of accounting for variations in stress ratio. Therefore, in the event that Barsom's model adequately consolidates the fatigue rate data, but the stress ratios for the anticipated loading spectrum vary widely, Hudson's root mean square model may prove to be a more attractive alternative. The curve fitting parameters for Hudson's model are evaluated using the same techniques previously discussed for Forman's model. Again, if this root mean square model does not adequately consolidate the fatigue rate data into a reasonably linear relationship on a plot of logQ versus $\log\Delta K_{rms}$, the use of Hudson's model should be rejected in favor of one of the load-interaction models.

4.3.3.8 Calibration of Wheeler's Model for Fatigue Crack Growth Retardation

Variable amplitude loading models that specifically account for load interaction effects are typically more complex and time consuming to calibrate than both the previously mentioned root mean square models and those used for constant amplitude loading. The empirical parameters for most load interaction models are highly load-spectrum specific, depending not only on the range of loads involved, but also on the relative mixture of high and low loads in the spectrum. Since retardation also depends on yield strength, empirical retardation parameters are also material specific. Therefore, each retardation model "should be calibrated for the particular spectrum (and material) relevant to the application" [Broek, 1989].

Calibration of a load interaction model such as Wheeler's retardation model typically cannot be accomplished (at least not entirely accomplished) by means of any of the simple curve fitting techniques previously discussed. Instead, calibration of such a model usually requires that tests be conducted under both constant amplitude loading and variable amplitude loading.

The Paris coefficients used in the Wheeler model can be determined from the constant amplitude tests by means of the technique previously discussed for the Paris model. Several attempts are then made to re-predict the variable amplitude test results by applying the Wheeler retardation parameter (ϕ_R) to the constant amplitude fatigue rate data, each attempt using a different value of the empirically adjustable Wheeler shaping exponent (m). The value that provides the best approximation of the actual variable amplitude test data is the one chosen for the analysis, as illustrated by Figure 4.17 (note that Broek (1989) has chosen to use 'γ' to represent the Wheeler shaping exponent).

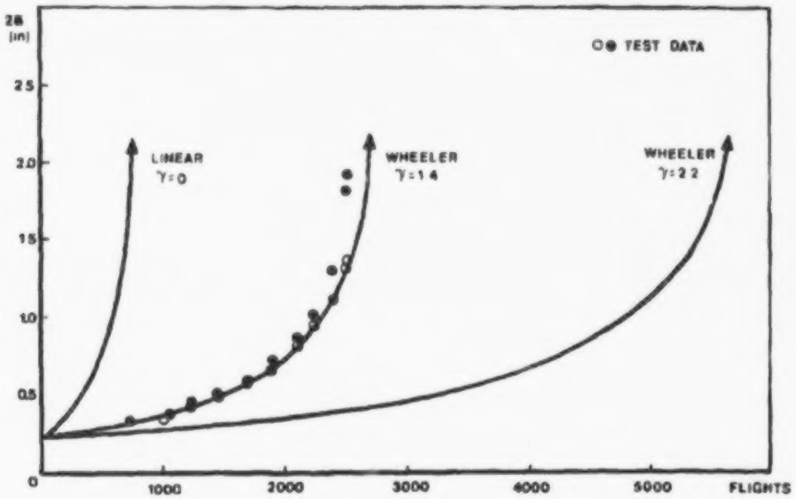

Figure 4.17 – Selection of Wheeler shaping exponent [Broek, 1989]

4.3.4 Guidelines for Selection of a Fatigue Crack Growth Model

As mentioned previously, there are numerous fatigue crack growth models available in the literature. No one equation can accurately model all fatigue rate data, and therefore, instead of relying on a single crack growth law, one needs to be aware of both the benefits and drawbacks of as many of the available models as possible. A general rule of thumb is to select a model that while satisfying the objectives of a given analysis, also provides the best possible fit to the actual fatigue rate data for a given application.

It is imperative that a model employing the proper fracture parameter be used. The majority of fatigue crack growth models incorporate the stress intensity factor, K. However, several models have been proposed which use the crack tip opening displacement (CTOD), the J integral, and even the strain energy release rate (G). If it is known that small scale yielding (LEFM) will dominate the crack growth behavior, then a model employing an EPFM fracture parameter should not be used.

One should try to select a model that can account for the type of load interaction effects, if any, that the structural component can be expected to experience. Obviously, a model used solely for predicting crack growth under constant amplitude cannot be expected to provide the same degree of accuracy when used to predict crack growth under variable amplitude loading spectra characterized by intermittent overloads. Conversely, time should not be wasted calibrating a model that has the capacity to provide more information than required by a given analysis. For example, if fatigue crack growth retardation were expected to be the dominant interaction effect, use of a model requiring calibration for the effects of crack growth acceleration would be a waste of both time and resources.

One should usually consider a trade off between factors such as calibration difficulty, computational cost, and predictive accuracy when selecting a crack growth model. For example, a preliminary life estimate would not justify the time and resources, both computational and financial, required for the use of an elaborate model requiring extensive parametric calibration.

Finally, much consideration should be given to the effects of environmental conditions on fatigue crack growth behavior. For instance, fatigue crack growth predictions for components used in marine applications should not be made using a model developed for use in non-saline environments. The results of such predictions should be 'taken with a grain of salt', so to speak.

As noted by Trask (1998), the ideal crack growth model should be both easy to use and easy to understand, require few empirical parameters, and provide reasonably accurate predictions in the least amount of time.

4.4 Life Assessment Techniques for Fatigue Crack Growth

As mentioned earlier, once a fatigue crack growth model has been calibrated, it is used to re-predict the original a-versus-N data. Furthermore, if the model accurately predicts the original crack growth data, then the fatigue rate equation can be integrated to determine the number of cycles required to propagate a fatigue crack from an initial length (a_i) to a final length (a_f). The initial length, a_i, is often taken as the minimum detectable crack length, which is a function of the inspection technique used. The final length, a_f, corresponds to some critical crack length based on either material fracture or material yielding. Closed form solutions have been evaluated for a few models, however, most require either numerical integration or the use of some cycle-by-cycle counting technique. Cumulative damage theories are also commonly used to provide life estimates for a number of different loading scenarios. The next few sections will discuss the various methods of life estimation used with constant amplitude loading and variable amplitude loading.

4.4.1 Life Assessment for Constant Amplitude Loading

Life estimates for constant amplitude loading are by far the easiest to assess. Consider the general equation for the fatigue crack growth rate given by Equation 4.5. Writing Equation 4.5 in terms of dN and integrating both sides, it follows that

$$\int_{N_i}^{N_f} dN = N_{if} = \int_{a_i}^{a_f} \frac{da}{f(\Delta K, R)} \tag{4.62}$$

Where N_{if} = the number of elapsed cycles as the crack grows from an initial size (a_i) to a final size (a_f)

Now the appropriate expression for f (ΔK, R) can be substituted into Equation 4.62 and the necessary integration performed using either a closed form solution or one of several numerical integration techniques.

The Paris equation is likely the simplest model for which a closed form solution can be derived. Combining Equation 2.3b and Equation 4.6, the Paris expression for f (ΔK, R) can be substituted into Equation 4.62 to give

$$N_{if} = \int_{a_i}^{a_f} \frac{da}{C_P(\Delta K)^{m_P}} = \int_{a_i}^{a_f} \frac{da}{C_P(\Delta\sigma Y\sqrt{\pi a})^{m_P}} = \int_{a_i}^{a_f} \frac{1}{C_P(\Delta\sigma Y\sqrt{\pi})^{m_P}} \frac{da}{a^{m_P/2}} \tag{4.63}$$

Notice that the variables C_P, $\Delta\sigma$, and m_P are constants during the integration and as such, can be brought outside the integral. However, the geometric correction factor, Y, is a function of the crack length 'a' and is often expressed using a lengthy polynomial. For some situations, Y may be assumed constant without incurring any appreciable error. If Y is assumed constant, a closed form solution of Equation 4.63 can be obtained as follows

$$N_{if} = \frac{1}{C_P(\Delta\sigma Y\sqrt{\pi})^{m_P}} \int_{a_i}^{a_f} \frac{da}{a^{m_P/2}} = \frac{1}{C_P(\Delta\sigma Y\sqrt{\pi})^{m_P}} \left(\frac{a^{(1-mP/2)}}{(1-m_P/2)} \right) \Bigg|_{a_i}^{a_f} \tag{4.64a}$$

which becomes

$$N_{if} = \frac{a_f^{(1-m_P/2)} - a_i^{(1-m_P/2)}}{C_P(\Delta\sigma Y\sqrt{\pi})^{m_P}(1-m_P/2)} \tag{4.64b}$$

Note that the use of this closed form solution of Paris' law precludes the use of $m_P = 2$.

In the event that a more complicated expression is used to describe $f(\Delta K, R)$, or if the geometric correction factor (Y) cannot be assumed constant for the integral of crack growth considered, evaluation of a closed form can be extremely difficult. However, a finite element analysis can be performed employing special crack tip elements (such as NISA's 'ENDURE' module, or a fracture analysis program such as *FAST*) to accurately express the stress intensity factor K, thus providing a more accurate estimate of Y.

In some instances, the complexity of the expression for f $(\Delta K, R)$ is such that derivation of a closed form solution is impossible, and therefore numerical integration must be used instead. It follows from Equation 4.62 that

$$\int_{N_i}^{N_f} dN = N_{if} = \int_{a_i}^{a_f} \frac{da}{(da/dN)} = \int_{a_i}^{a_f}\left(\frac{dN}{da}\right)da \qquad (4.65)$$

Where dN/da, the inverse of the fatigue crack growth rate, essentially represents the number of elapsed cycles per unit increase in fatigue crack length. Recall that $\int_{x_1}^{x_2} f(x)\,dx$ represents the area under the curve of f(x)-versus-x between the limits of x_1 and x_2; therefore, as illustrated by Figure 4.18, Equation 4.65 represents the area under the curve of dN/da-versus-a between the limits of a_i and a_f.

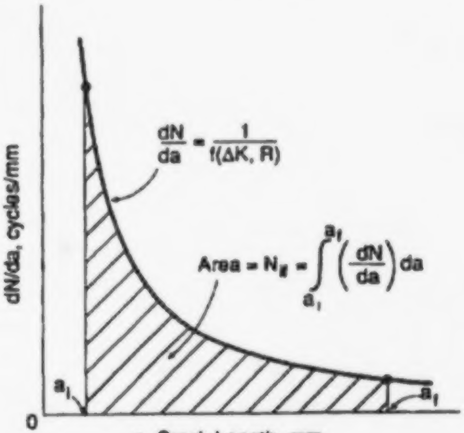

Figure 4.18 – Life estimation using numerical integration techniques [Dowling, 1993]

As previously mentioned, much of a component's total life is consumed in the early stages of crack growth. This is substantiated by the fact that most of the area under the curve in Figure 4.18 corresponds to crack growth increments near a_i. Further simplification of Equation 4.65 yields

$$N_{if} = \sum_{i=1}^{n} \left(\frac{dN}{da} \right)_i (\Delta a)_i \qquad (4.66)$$

Therefore, the number of cycles required to propagate the fatigue crack through a given interval is obtained through multiplying the average dN/da for the interval by the interval width Δa. A cumulative cycle count is kept as the process is repeated until the final crack length is reached. As with any numerical integration technique, the smaller the (crack growth) interval (Δa), the more accurate the approximation. Due to the fact that much of the total life is associated with early crack growth, it is especially important that at small crack lengths, this interval be relatively small. Customarily, Δa is increased by a fixed percentage, say two or three percent, for each successive interval. This allows larger intervals to be used at larger crack lengths, where the dN/da-versus-a curve levels out somewhat.

Several numerical integration techniques are available, including the Midpoint rule, the Trapezoidal rule, and Simpson's rule. A FORTRAN program or simple spreadsheet program can be written to simplify the numerical integration process.

4.4.2 Life Assessment for Variable Amplitude Loading

Life estimates for components subjected to variable amplitude loading are typically much more difficult and time-consuming to predict, mainly due to the inherent variability among the loading spectra, which may necessitate the use of a cycle counting method or consideration of load interaction effects. The two most commonly used methods for estimating fatigue life under variable amplitude loading include calculating incremental crack growth on a cycle-by-cycle basis, and the use of statistical loading definitions.

Crack growth analyses that employ a cycle-by-cycle approach involve a linear piecewise integration and usually consider load interaction effects. Crack growth increments for each cycle (Δa_i) can be estimated from the crack growth rate (da/dN) equation for a given model. A life estimate is obtained by maintaining a running total of these crack growth increments per cycle and simply noting the number of cycles required to reach a final crack length (a_f). To further illustrate this method, suppose that the current crack length is denoted by a_i and the growth increment for the next cycle is Δa_i. Then the crack length at the end of the next cycle is given by the following

$$a_{i+1} = a_i + \Delta a_i = a_i + \left(\frac{da}{dN}\right)_i = a_i + \left(\frac{\Delta a}{\Delta N}\right)_{i(\Delta N=1)} \qquad (4.67)$$

Since ΔN_i is always one for a cycle-by-cycle approach, the crack growth increment for a given cycle is numerically equal to the crack growth rate (da/dN) for that cycle. Following the above procedure, the crack length after N cycles is given by Equation 4.68.

$$a_N = a_i + \sum_{i=1}^{N}\left(\frac{da}{dN}\right)_i \qquad (4.68)$$

The cycle-by-cycle approach often incorporates various cycle counting methods, which aid in essentially 'prioritizing' the individual cycles in a loading sequence based on their expected contributions to the overall crack growth behavior. These methods are used to summarize irregular and oftentimes lengthy loading spectra by simply counting the occurrences of cycles with various stress ranges. The definition of a cycle varies depending on the counting method used. Some of the cycle counting techniques that have been proposed include peak counting, mean-crossing peak counting, and rainflow counting, with the latter being the most commonly used technique. A full description of these cycle counting methods is given in ASTM Standard No. E1049, entitled "*Standard Practices for Cycle Counting in Fatigue Analysis*".

The use of statistical loading definitions is based on the premise that for any highly irregular load spectra, there exists an equivalent constant amplitude load history that produces the same average crack growth rate. This notion has led to the development and use of root mean square parameters, such as those implemented in the fatigue crack growth models proposed by Barsom and Hudson. As previously mentioned, this statistical approach is more effective for highly irregular load spectra, where load interaction effects tend to balance each other. Upon evaluation of the root mean square values, the corresponding crack growth rate equations can be integrated, either numerically or in closed form, as previously discussed for constant amplitude loading.

Life prediction is much easier for cases in which the variable amplitude load spectra are less irregular in nature, such as those comprised of tensile overloads interspersed within otherwise constant amplitude loading spectra. For such cases, the total life prediction consists of two separate components: a component that accounts for the constant amplitude portion of a given spectrum, and a component that accounts for the fatigue crack growth retardation caused by any tensile overloads. Life predictions for the constant amplitude portion of a given loading spectrum can be made using any of the methods previously discussed in section 4.4.1 of this report. In lieu of using either the Wheeler or Willenborg model, the degree of fatigue crack growth retardation caused by a given tensile overload can be quantified by expressing the number of delay cycles (N_D) as a function of the corresponding overload ratio (OLR). The number of delay cycles resulting from a given OLR is illustrated schematically in Figure 4.19.

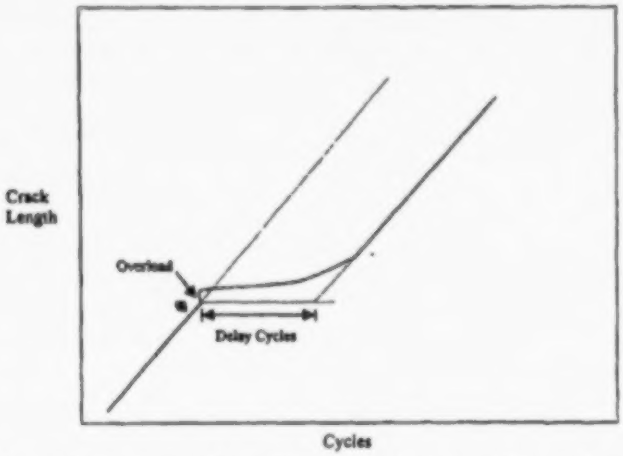

Figure 4.19 - Schematic representation of N_D following a tensile overload [Trask, 1998]

Rosenberg (1999) suggests the use of Equation 4.69 to determine the number of delay cycles for a given tensile overload.

$$N_D = \frac{8.5 \times 10^7 (OLR)^{7.4}}{\sigma_{yld}^2} \qquad (4.69)$$

Trask (1998) recommends the use of Equation 4.70 to evaluate N_D for a given tensile overload.

$$\log_{10}(N_D) = 1.8115(OLR) + 1.6497 \qquad (4.70a)$$

$$N_D = 10^{1.8115(OLR)+1.6497} \qquad (4.70b)$$

Kumar et al (1996) further proposed the use of Equation 4.71 to determine N_D for a given tensile overload.

$$N_D = 2149.34(OLR)^{6.86} \qquad (4.71)$$

As an example of how to predict the total fatigue life, consider a given component subjected to any number of tensile overloads (N_{OL}) of varying overload ratio. The total life is obtained simply via the superposition of one of the above equations for N_D and an equation such as Equation 4.64 (representing the closed form integration of Paris' model). Equation 4.72 represents the corresponding total fatigue life prediction.

$$N_{tf} = \frac{a_f^{(1-m_p/2)} - a_i^{(1-m_p/2)}}{C_p(\Delta\sigma Y\sqrt{\pi})^{m_p}(1-m_p/2)} + \sum_{i=1}^{N_{OL}}(N_D)_i \qquad (4.72)$$

4.4.3 Cumulative Damage Theories

Cumulative damage theories are based on the concept that during each load cycle in a given load spectrum, a component typically incurs a small amount of fatigue damage. As loading continues, these 'damage fractions' are accumulated until their total exceeds one. The number of cycles required to accumulate a total damage fraction of one corresponds to the estimated fatigue life of the component. Individual damage fractions are calculated using the stress-life (S-N)

curves previously discussed in Chapter 3. Therefore, the degree of precision provided by each damage theory depends greatly on the establishment of accurate S-N curves. Damage fractions can be accumulated using either linear or non-linear damage theories.

Several cumulative damage theories exist, including those proposed by Henry, Gatts, Markov and Starkey, and Palmgren and Miner. The interested reader is referred to the text by Collins (1993) for a more thorough explanation of these damage theories. To further illustrate the use of linear and non-linear damage theories, the Palmgren-Miner theory and the Markov-Starkey theory will be described further.

The Palmgren-Miner rule for linear damage accumulation, the first of its kind, was originally proposed by A. Palmgren in Germany in 1924 and later developed by M.A. Miner in 1945. Due to its simplicity and inherent conservatism, it is the most commonly used damage theory. The Palmgren-Miner rule assumes that the total damage that can be absorbed by a given component is constant, regardless of stress level or loading sequence. Palmgren and Miner theorized that the damage fraction associated with any stress amplitude, σ_{ai}, is linearly proportional to the ratio n_i/N_{fi}, where n_i represents the number of cycles for which a given component is subjected to σ_{ai}, and N_{fi} represents the corresponding number of cycles that would cause fatigue failure at a stress amplitude of σ_{ai}. Therefore, the Palmgren-Miner damage theory predicts failure when

$$\frac{n_1}{N_{f1}} + \frac{n_2}{N_{f2}} + \frac{n_3}{N_{f3}} + \ldots + \frac{n_i}{N_{fi}} \geq 1 \tag{4.73}$$

Figure 4.20 below further illustrates the use of the Palmgren-Miner rule.

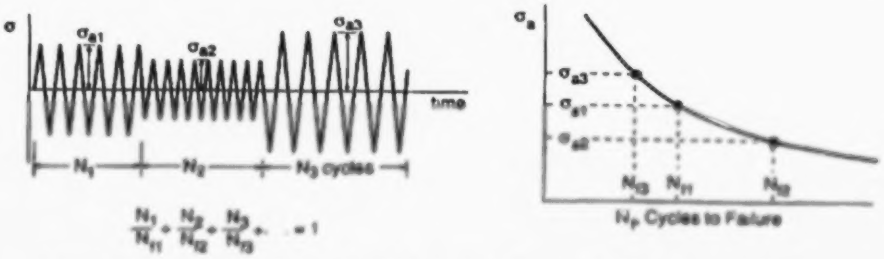

Figure 4.20 – Life estimates using the Palmgren-Miner rule [Dowling, 1993]

One of the disadvantages of the a cumulative damage theory such as the one developed by Palmgren and Miner lies in the fact that it does not in any way distinguish between the fatigue crack initiation and propagation stages. In addition, there is no way to account for load interaction effects with this method. Therefore, use of the Palmgren-Miner rule is most appealing when the load history is quasi-random in nature.

Although the Palmgren-Miner theory was based on the concept of linear damage accumulation, experimental evidence indicates that damage accumulation curves may also follow a nonlinear relationship, as illustrated by Figure 4.21. The Markov-Starkey theory was the first cumulative damage theory to account for this potential nonlinear relationship.

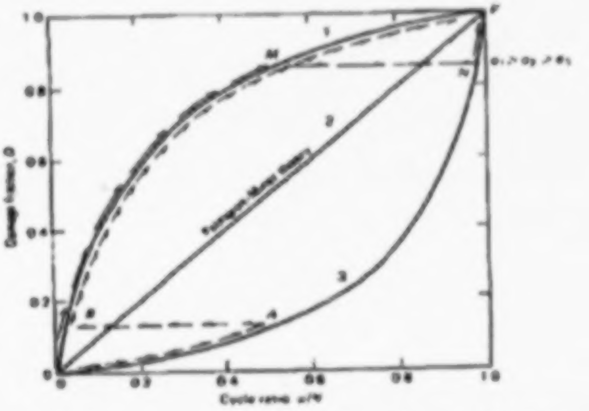

Figure 4.21 – Nonlinear accumulation of fatigue damage [Collins, 1993]

In Figure 4.21, curves 1, 2, and 3 correspond to three stress levels of successively lower amplitude. Each of the curves were defined for a different stress amplitude under completely reversed loading. The difference between the three curves can be accentuated by comparing their relative damage fractions at a given cycle ratio. For example, at a cycle ratio of 0.6, the damage fractions for curves 1, 2, and 3 are approximately 0.89, 0.58, and 0.16, respectively. The damage fraction corresponding to each cycle ratio is given by

$$D_i = \left(\frac{n_i}{N_{fi}}\right)^{m_i} \tag{4.74}$$

where D_i is the damage fraction incurred at a particular stress amplitude, and m_i is a function of the stress amplitude. As with the Palmgren-Miner rule, the Markov-Starkey damage accumulation theory predicts fatigue failure when the sum of all the individual damage fractions exceed one. To construct the curves of Figure 4.21, one must first plot the damage fraction (D_i) versus cycle ratio (n_i/N_{fi}) as a function of the stress amplitude causing failure. The curvature of each individual curve is adjusted by varying the exponent m_i in Equation 4.74. Once the damage curves have been defined for the stresses in a given load spectrum, life estimates can be obtained by proceeding, in order, along the proper curves until the total cumulative damage fraction exceeds one.

As an example of how to use the Markov-Starkey fatigue damage curves, consider a component subjected to a block loading spectrum consisting of three successively decreasing stress amplitudes, σ_{a1}, σ_{a2}, and σ_{a3}, applied in that order. For the sake of simplicity, it can be assumed that the three corresponding damage curves are given by those of Figure 4.21 and that their respective S-N curves are known with a reasonable degree of accuracy.

Suppose it has been determined that the component has been subjected to σ_{a1} for a cycle ratio of 0.2. Using curve 1 in Figure 4.21, one can see that a damage fraction of 0.58 has been 'absorbed' by the component.

Suppose now that stress amplitude σ_{a2} is applied for a cycle ratio of 0.3. Proceeding along a horizontal line of constant damage from curve 1 to curve 2, and following curve 2 down to a cycle ratio of 0.3, a corresponding damage fraction of 0.30 is determined. Thus, prior to application of σ_{a3}, a total damage fraction of 0.88 has already been absorbed by the component, leaving an available damage fraction of 0.12 before the onset of fatigue failure. The number of cycles required to induce fatigue failure can be evaluated as follows. Proceeding along a horizontal line of constant damage from curve 2 to curve 3, and then dropping to a damage fraction of 0.12, one can see that a cycle ratio of approximately 0.46 would cause fatigue failure.

Finally, using a cycle ratio of 0.46, the appropriate S-N curve should be referenced to determine the actual number of cycles for which the component may be subjected to σ_{a3} prior to the onset of fatigue failure.

4.5 Crack Growth in Corrosive Environments

As mentioned briefly in section 4.2, crack growth rate may be strongly affected by the chemical environment to which a component is subjected. The presence of an aggressive chemical environment results in higher crack growth rates than those corresponding to an environment of purely air. The more aggressive the chemical environment, the more pronounced effect on crack growth rate and fatigue life, as illustrated by Figure 4.22. Figure 4.22 also illustrates that the reduction in fatigue strength of a given component is most apparent when the component is continually subjected to cyclic loading in an aggressive environment. Furthermore, under such conditions, an endurance limit or fatigue limit no longer exists.

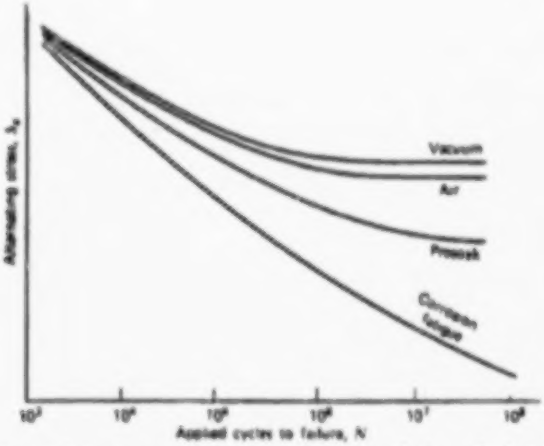

Figure 4.22 – Effect of environmental conditions on fatigue behavior [Trask, 1997]

The presence of a saline environment is the most important corrosive environment that must be considered for most practical engineering applications. Therefore, structural components of such things as automobiles, bridges and buildings located on or near the ocean, ships (including any cargo that they carry), and offshore structures must be designed to handle the detrimental effects of a saline environment.

4.5.1 Stress Corrosion Cracking

Stress corrosion cracking refers to crack growth that occurs under the combined effects of a sustained applied load and a corrosive environment. Figure 4.23 illustrates one of the cantilever beam test fixtures commonly used to experimentally measure crack growth in a specimen subjected to an aggressive environment.

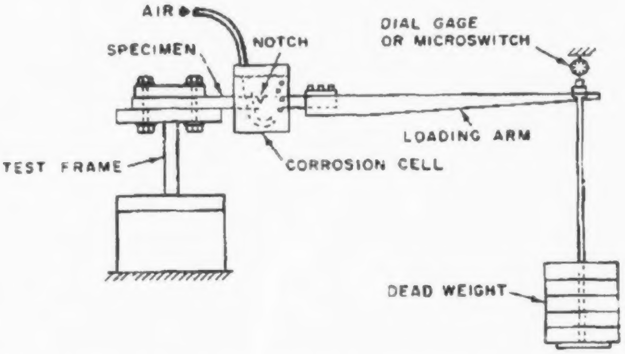

Figure 4.23 – Cantilever beam test fixture to measure crack growth in a corrosive environment [Barsom et al, 1987]

The test consists of submerging a precracked specimen into a corrosive environment and subjecting it to a sustained load for a prolonged period of time. At some point, provided the sustained load is large enough, the crack will start to grow. Crack growth will continue until the combination of crack length and sustained load are such that the resulting stress intensity factor exceeds the fracture toughness for the material used. Several precracked specimens of the same material are often used, each one subjected to a different sustained load (i.e., initial stress intensity factor, K_I). The initial stress intensity factor for each specimen is typically plotted versus the corresponding time to failure, resulting in a curve such as the one illustrated in Figure 4.24. The horizontal asymptote of Figure 4.24 corresponds to the stress corrosion cracking threshold (K_{SCC} or K_{ISCC}, corresponding to plane stress or plane strain, respectively) for the material tested, which represents the initial stress intensity factor below which no crack growth will occur under static loading in such an environment. The evaluation of K_{ISCC} is governed by ASTM Standard No. E1681, entitled "*Standard Test Method for Determining a Threshold Stress Intensity Factor for Environment-Assisted Cracking of Metallic Materials Under Constant Load*". The value of K_{ISCC} in a given environment is, in fact, a material property, and is independent of factors such as specimen geometry, etcetera. Trask (1997) noted that for some types of steel subjected to saline environments, the value of K_{ISCC} decreases drastically with increasing yield strength (above 1000 MPa). Therefore, the benefits of using high strength steel in some marine applications may be overshadowed by their increased susceptibility to stress corrosion cracking.

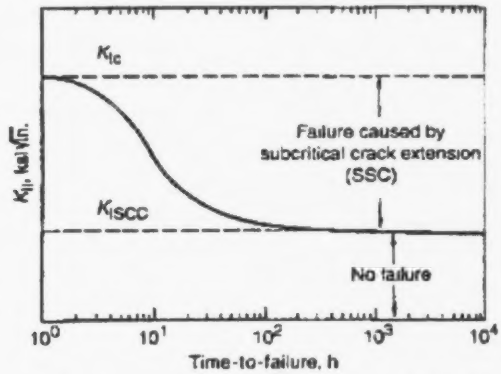

Figure 4.24 – Evaluation of stress corrosion cracking threshold (K_{ISCC}) [Lui, 1998]

Another method of presenting stress corrosion cracking test data involves recording crack growth increments as a function of time, as illustrated in Figure 4.25 The rate of crack growth (i.e., the crack velocity), da/dt, is simply equal to the tangent of the a-versus-t curve at any point. Furthermore, a da/dt-versus-K curve similar to that of Figure 4.26 can be plotted in the same manner as was done for the da/dN-versus-ΔK curves previously discussed.

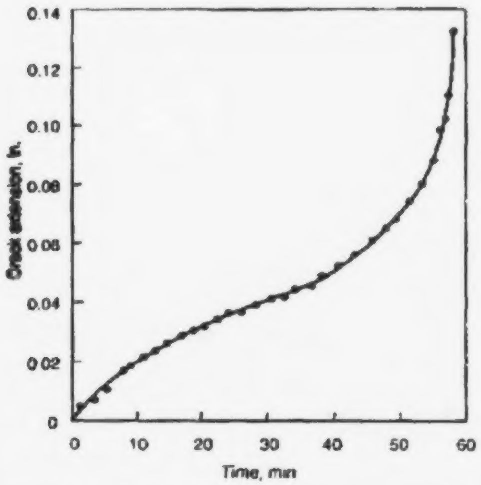

Figure 4.25 – Typical a-versus-t curve used to determine K_{ISCC} [Lui, 1998]

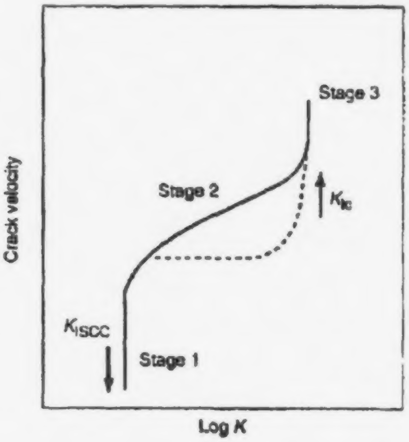

Figure 4.26 – Typical da/dt-versus-K curve used to determine K_{ISCC} [Lui, 1998]

In the event that the stage 2 crack growth data exhibit a linear relationship on a log-log plot of da/dt-versus-K, the growth in region II can be expressed in a form similar to Paris' law. That is

$$\frac{da}{dt} = CK^{m} \tag{4.75}$$

Life estimates can be further obtained using either numerical integration or a closed form solution similar to that given by Equation 4.64b. Lui (1998) suggests that for many alloy/environment systems, stage 2 crack growth rates appear to be approximately constant regardless of stress intensity factor (as indicated by the dashed line in Figure 4.26). In this case, it is assumed that da/dt = 0 for stress intensity factors below K_{ISCC}, and that a constant crack growth rate, $(da/dt)_{const}$, occurs over the region $K_{ISCC} < K < K_{IC}$. A much easier life estimate can be obtained in this case, as given by Equation 4.76.

$$t_{if} = \frac{(a_f - a_i)}{(da/dt)_{const}} \tag{4.76}$$

A good design will prevent stress corrosion cracking by stipulating the use of a material with a high value of K_{ISCC}, such that the value of K throughout the service life of a given component will always be less than K_{ISCC}.

4.5.2 Corrosion Fatigue Crack Growth

The combination of cyclic loading and a corrosive environment has a much more detrimental effect than either acting alone. Although the exact mechanisms affecting corrosion fatigue are not fully understood, it is thought to be caused by the combined interaction of electrochemical, mechanical, and metallurgical processes acting within a given system. The effects of a corrosive environment vary with material, and it is possible that some material/environment combinations would not have a pronounced effect on fatigue behavior. Corrosion fatigue behavior is typically studied by comparing the behavior in a corrosive environment to that in a benign environment. Typical test results are illustrated in Figure 4.27 below.

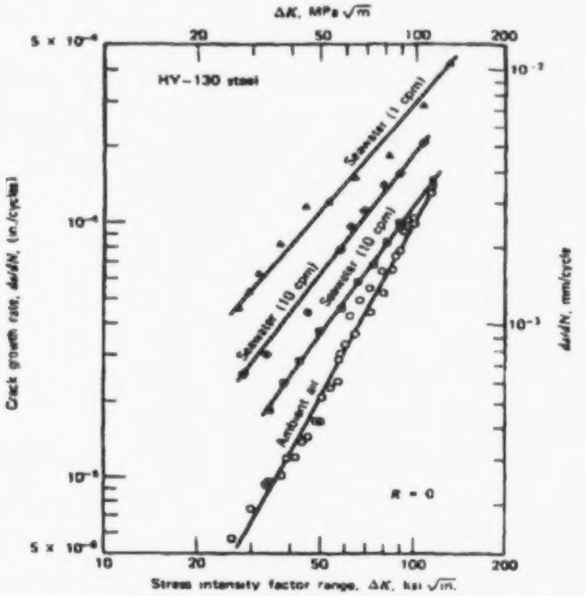

Figure 4.27 – Typical results from fatigue testing in a corrosive environment [Trask, 1997]

Corrosion fatigue testing is extremely time consuming, and therefore fairly expensive. For example, a fatigue test in a typical air environment is usually conducted at a frequency of 5 Hz to 25 Hz. However, to obtain fatigue rate data more representative of actual service conditions, frequencies as low as 0.02 Hz are required. At these frequencies, it could take years to conduct a single test.

Lui (1998) suggests the use of the Wei-Landes model for conducting corrosion fatigue crack growth analyses. The model is based on the assumption that linear superposition of the da/dN-versus-ΔK and da/dt-versus-K curves is valid. That is, the crack growth rate in a corrosive environment is "considered to be equal to the algebraic sum of the crack growth rate in an inert reference environment and that of an environmental component, computed from sustained-load crack growth data obtained in an identical aggressive environment and the load profile represented by K(t)" [Lui, 1998].

$$\left(\frac{da}{dN}\right)_{\text{corrosive}} = \left(\frac{da}{dN}\right)_{\text{inert}} + \int \frac{da}{dt} \cdot K(t) \cdot dt \qquad (4.77)$$

Under constant amplitude loading, the load profile K(t), which accounts for the effects of frequency, mean load, and cyclic load range, is given by Equation 4.78.

$$K(t) = \frac{K_{max}}{2}\left[(1+R)+(1-R)\cdot\cos(\omega t)\right] \tag{4.78}$$

From Equation 4.77, one can determine the crack growth increment per cycle in a corrosive environment ($\Delta a_{corrosive}$) as the sum of the crack growth increment per cycle corresponding to crack growth in an inert environment (Δa_{inert}) and that corresponding to crack growth under sustained load in a corrosive environment ($\Delta a_{sustained}$). That is,

$$\Delta a_{corrosive} = \Delta a_{inert} + \Delta a_{sustained} \tag{4.79}$$

Although this model offers a reasonable approximation for medium to high crack growth rates, the load profile representation, K(t), is not always as simple as that given by Equation 4.78, and therefore, the model should be used only as an approximation.

Since an aggressive environment has no effect on crack growth rates corresponding to stress intensity factors below K_{ISCC}, application of the Wei-Landes model will provide conservative estimates of crack growth rates for $K < K_{ISCC}$.

Several methods exist to protect materials from the deleterious effects of corrosion fatigue, including surface treatments such as shot peening, cold working, and nitriding. All of these protection methods induce compressive residual stresses, which, as previously discussed, are typically very beneficial. Alternatively, stainless or galvanized steels may be used to provide protection from a particular environment. Traditional surface coatings such as paints and oils may also be used.

Unfortunately, due to the large number of test variables, there is really no easy solution to predict fatigue crack growth behavior in aggressive environments. In each situation, the application of good engineering judgement is perhaps the best solution.

Chapter 5
Fracture Control

5.1 Introduction

The objective in the design of structures such as aircraft, bridges, ships and pressure vessels, etcetera, is to optimize the desired performance, safety requirements, and overall cost, thereby producing a structure "that will perform the operating function efficiently, safely, and economically" [Barsom et al, 1987]. Engineers typically consider three structural failure modes: yielding, buckling, and subcritical crack growth. However, engineers often under-emphasize the potential for failure by subcritical crack growth and assume that it can be avoided through proper selection of materials and design stress levels. Unfortunately, failure to properly consider this potential failure mode has led to several catastrophic structural failures.

To help minimize the potential of structural failure by subcritical crack growth, a number of fracture control methods have been developed over the years. These include proper inspection techniques, the use of crack arrestors, minimization of stress concentrations, quality control during fabrication, strict adherence to proper welding techniques, the use of structural materials with good fracture toughness, etcetera. In essence, any technique that is capable of either extending the crack-initiation life or retarding the subsequent crack growth in a given component will provide an effective means of fracture control. "Using fracture mechanics terminology, fracture control is simply making sure that $K_{applied} < K_C$ at all times" [Barsom et al, 1987].

5.2 Fundamental Fracture Control Methodologies

The three basic factors that dictate a given structure's susceptibility to brittle fracture are the design stress level, the initial crack (or discontinuity) size, and the material fracture toughness. Hence, the most fundamental methods of reducing the potential for brittle fracture include decreasing the design stress range, minimizing the size of any initial flaws, and using materials with improved fracture toughness.

Figure 5.1 illustrates that for a material with a given fracture toughness, decreasing the design stress (or stress range) greatly increases the corresponding critical crack size. Note the resulting increase in the overall safety factor against brittle fracture.

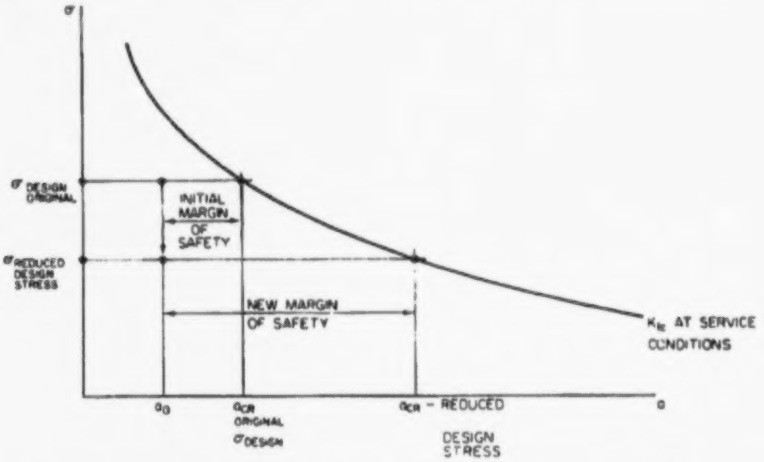
σ
σ DESIGN ORIGINAL
σ REDUCED DESIGN STRESS
INITIAL MARGIN OF SAFETY
NEW MARGIN OF SAFETY
K_Ic AT SERVICE CONDITIONS
a_0
a_CR ORIGINAL σ_DESIGN
a_CR - REDUCED DESIGN STRESS
a

Figure 5.1 – Fracture control through reduction in design stress level [Barsom et al, 1987]

Figure 5.2 illustrates the effect of reducing the size of any initial flaws. Such results can usually be obtained by means of improved quality control during the fabrication process and the use of superior inspection techniques. Since most of a component's total fatigue life is consumed during the initial stages of crack growth, a reduction in initial flaw size can have a profound effect on the corresponding margin of safety.

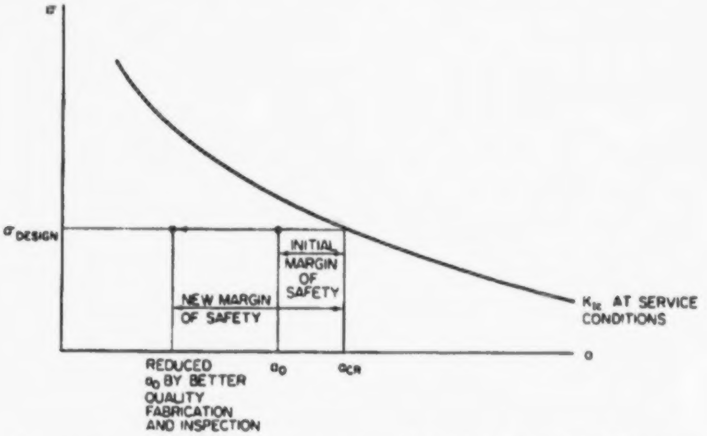
σ
σ DESIGN
INITIAL MARGIN OF SAFETY
NEW MARGIN OF SAFETY
K_Ic AT SERVICE CONDITIONS
REDUCED a_0 BY BETTER QUALITY FABRICATION AND INSPECTION
a_0
a_CR
a

Figure 5.2 – Fracture control through reduction in initial flaw size [Barsom et al, 1987]

Figure 5.3 illustrates how the use of a material with improved fracture toughness can increase the factor of safety against brittle fracture. For a given design stress level, an improved fracture toughness permits a significantly greater amount of crack growth prior to fracture.

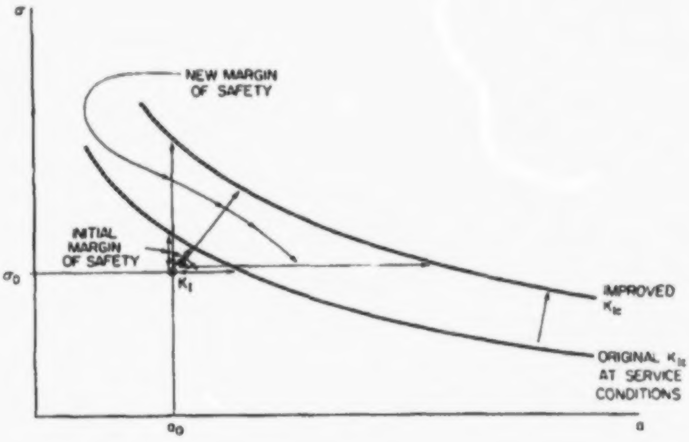

Figure 5.3 - Fracture control through improved fracture toughness [Barsom et al, 1987]

The decision as to which fracture control approach should be followed depends on both the type of structure and the corresponding service conditions. For example, in cases where the structural loads can be accurately determined, modest reductions in design stress levels may provide some degree of fracture control. Furthermore, since fatigue crack growth rates are typically proportional to the stress range raised to some power, a small reduction in design stress range may result in a significant reduction in fatigue crack growth. On the other hand, in cases for which the structural loads are not determined as accurately, or the quality of fabrication and inspection techniques are not well defined, the use of materials with improved fracture toughness may be a more effective means of fracture control. Higher levels of quality control during fabrication often yields structural components containing smaller initial flaws. Similarly, superior inspection techniques may facilitate the detection of smaller flaws than normally possible, leading to significant increases in the useful design life of a given structural component.

5.3 Secondary Fracture Control Methodologies

In addition to the three aforementioned 'primary' fracture control techniques, several secondary methods may also prove to be very effective. Some of these secondary fracture control methodologies include conducting periodic inspections, providing multiple load paths, adopting a 'durable design' approach, performing proof tests, surface layer machining (stripping), and providing crack arrestors. The following sections will provide a review of these fracture control techniques.

5.3.1 Periodic Inspection

Periodic inspection and repair (if necessary) is likely the most universal method of fracture control. Periodic inspections permit the detection and repair of propagating fatigue cracks prior to their reaching a maximum allowable length (a_p), which is typically a percentage of the critical crack length (a_c). Although several inspection techniques are available, regardless of the inspection technique chosen, there is a specific crack length (a_0) below which a cost-effective detection is highly unlikely. This dictates that crack detection and any necessary repairs must be completed during the time interval H required for the crack to propagate between lengths of a_0 and a_p, as illustrated by Figure 5.4 below.

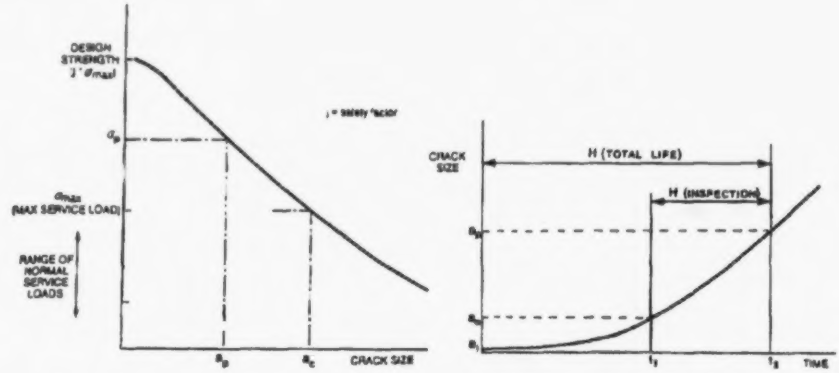
DESIGN STRENGTH $j \cdot \sigma_{max}$
j = safety factor
σ_p
σ_{max} (MAX SERVICE LOAD)
RANGE OF NORMAL SERVICE LOADS
a_p
a_c
CRACK SIZE
CRACK SIZE
H (TOTAL LIFE)
H (INSPECTION)
a_p
a_0
a_i
t_1
t_2
TIME

Figure 5.4 – Time interval available for crack detection and repair [Broek, 1989]

Some of the more commonly used inspection techniques are summarized in Table 5.1.

Table 5.1 – Summary of inspection techniques

Inspection Technique	Underlying Principle	Comments
Visual Inspection	Performed with the naked eye; assisted by magnifying glass, lamps, and mirrors	Possible only at locations containing visible cracks which are easily accessible
Colored Penetrant	Colored liquid is applied to surface, penetrates crack and is washed off; quick-drying suspension of chalk is applied; penetrant in crack is drawn out by the chalk suspension, leaving a colored line representing the crack	Possible only at locations which are easily accessible
Magnetic Particles	Component is placed in a liquid containing iron powder and subjected to a magnetic field; when observed under ultraviolet light, the magnetic field lines indicate the location of cracks	Suitable only for ferrous materials; components must be disassembled and inspected in a special cabin
X-ray	X-rays are passed through components and caught on film; location of cracks are represented by black lines on the film	Versatile and sensitive inspection technique; detection of small surface flaws is somewhat difficult
Ultrasonic Waves	High frequency waves transmitted into component and reflected back by the crack; time between wave transmission and reflection indicates relative location of cracks	Universal inspection technique; variety of transmitters (probes) and input pulses available
Eddy Current	A coil induces an eddy current in the metal component; this, in turn, induces a current in the coil; changes in current indicate the presence of a crack	Cheap and relatively sensitive technique, easy to perform; coils can be made small enough to fit into holes
Acoustic Emission	Measurement of the intensity of waves emitted in the component due to plastic deformation at the crack tip	Inspection can be performed while component is under service loading; continuous surveillance possible; interpretation of results is difficult

Table 5.1 – Summary of inspection techniques

Inspection Technique	Underlying Principle	Comments
Visual Inspection	Performed with the naked eye; assisted by magnifying glass, lamps, and mirrors	Possible only at locations containing visible cracks which are easily accessible
Colored Penetrant	Colored liquid is applied to surface, penetrates crack and is washed off; quick-drying suspension of chalk is applied; penetrant in crack is drawn out by the chalk suspension, leaving a colored line representing the crack	Possible only at locations which are easily accessible
Magnetic Particles	Component is placed in a liquid containing iron powder and subjected to a magnetic field; when observed under ultraviolet light, the magnetic field lines indicate the location of cracks	Suitable only for ferrous materials; components must be disassembled and inspected in a special cabin
X-ray	X-rays are passed through components and caught on film; location of cracks are represented by black lines on the film	Versatile and sensitive inspection technique; detection of small surface flaws is somewhat difficult
Ultrasonic Waves	High frequency waves transmitted into component and reflected back by the crack; time between wave transmission and reflection indicates relative location of cracks	Universal inspection technique; variety of transmitters (probes) and input pulses available
Eddy Current	A coil induces an eddy current in the metal component; this, in turn, induces a current in the coil; changes in current indicate the presence of a crack	Cheap and relatively sensitive technique, easy to perform; coils can be made small enough to fit into holes
Acoustic Emission	Measurement of the intensity of waves emitted in the component due to plastic deformation at the crack tip	Inspection can be performed while component is under service loading; continuous surveillance possible; interpretation of results is difficult

Considering Figure 5.4, in the event that an inspection were performed at some time $t < t_1$, the crack would be missed. Suppose that a second inspection were later performed at $t > t_2$. In this case, the crack would already have grown beyond a_p. Therefore, the required inspection interval (I) must obviously be less than the aforementioned time interval H, during which the crack grows from. a_o to a_p.

An inspection interval (I) is typically chosen as H/2 or H/3. Provided that inspections are scheduled as such, starting from time zero, there will always be at least two or three opportunities, respectively, for crack detection, regardless of when crack initiation takes place (as illustrated in Figure 5.5).

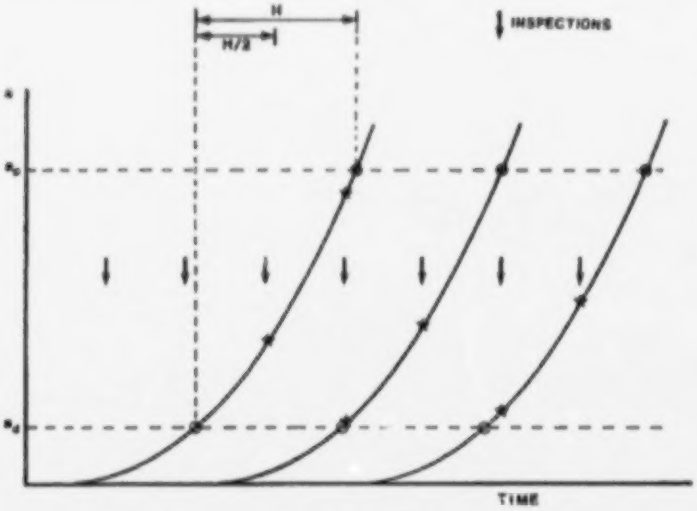

Figure 5.5 – Opportunities for crack detection based on I = H/2 [Broek, 1989]

If so desired, one could schedule fewer inspections or longer inspection intervals by opting to use a more refined inspection method, capable of detecting smaller cracks (i.e., smaller a_o). Although fewer inspections would be required, the use of more elaborate inspection techniques could possibly increase the cost of each individual inspection, thereby offsetting any savings afforded by scheduling fewer inspections.

Alternatively, inspection intervals may be selected based on maintaining a specific cumulative probability of crack detection (typically 95% to 98%), regardless of the inspection method used or level of component accessibility, etcetera. Interested readers are referred to the text by Broek (1989) for a thorough explanation of this approach to selecting an appropriate inspection interval.

It should be noted that because a_p is a 'permissible' crack length rather than a 'critical' one, coupled with the fact that a given crack is generally detected prior to reaching a_p, immediate crack repair may not be necessary. Furthermore, immediate repair may not always be convenient. In fact, "large savings may be realized if remedial action can be scheduled for the next major overhaul or shut down, or when at least operations can continue until a new part or component has been manufactured and received" [Broek, 1989]. However, postponing any repairs more than necessary essentially defeats the purpose of any crack growth analyses and inspection efforts.

5.3.2 Durable Design Approach

In the event that no inspections are performed early on in the life of a given component, a small initial crack (a_i) must be assumed to exist. The available safe life is then the time (H) required for the initial crack to grow to the maximum permissible length (a_p). In the absence of periodic inspections, the durability approach to fracture control requires that a given component be either retired or replaced after a certain percentage of its safe life (e.g. H/2 or 2H/3). Obviously this is not the most efficient or cost-effective means of fracture control. The available safe life, H, must be quite long in order to yield a practical value of H/2 or 2H/3, etcetera. This may require a much heavier and more expensive component design.

On the other hand, if periodic inspections are performed throughout the life of a given component, and any cracks are repaired immediately upon detection, the durability approach can be used to maintain the safe operation of a given component - essentially forever.

The main drawback associated with the durability approach concerns the assumption of initial crack size (a_i). At best, this initial flaw may be small enough to barely escape detection during initial quality control.

5.3.3 Proof Testing

In some instances, a material's fracture toughness may be so low that the maximum permissible crack size (a_p) may be smaller than the minimum detectable crack length (a_d). In other cases (e.g. a pipeline several hundred feet in length), it would simply not be practical to inspect the entire structure for cracks. In such instances, a procedure known as proof testing may be the most effective means of fracture control.

Suppose that a given component is subjected to a certain proof stress (σ_{proof}). As illustrated in Figure 5.6, fracture would occur if a corresponding crack of length a_{proof} were 'detected'. Provided that no fracture occurs upon application of σ_{proof}, the maximum possible crack length is a_{proof}. On the other hand, should a failure occur upon application of σ_{proof}, the component (or some portion thereof) must be repaired or replaced to eliminate any cracks larger than a_{proof}. Regardless, a safe operating period H remains, during which a crack may grow from a_{proof} to the maximum permissible crack length a_p. Similar to the durability approach, the life of a given component can be extended essentially forever, provided that proof tests are performed at every interval H and repairs (or replacements) are made as necessary.

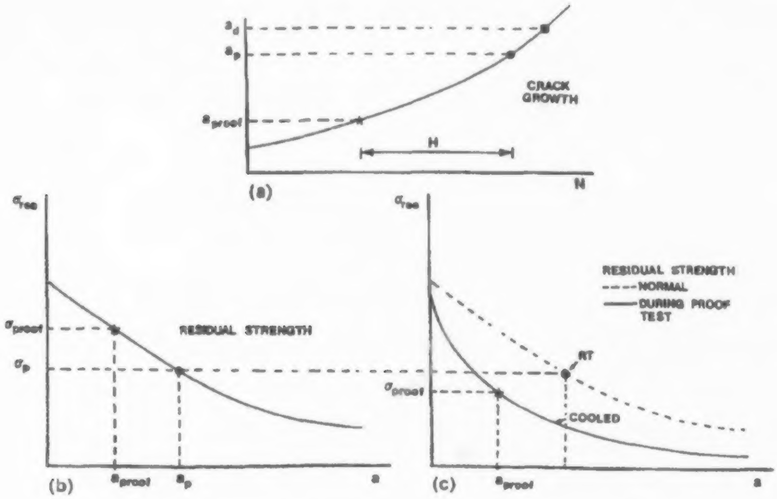

Figure 5.6 – Proof testing [Broek, 1989]

Proof testing is best suited to structures such as pipelines or pressure vessels, which are often filled with gas or other potentially dangerous chemicals. By filling the line or vessel with water prior to conducting proof tests, any failures during these 'hydro-tests' would result in a water leak only. As illustrated in Figure 5.6, by cooling a component, one can lower its fracture toughness, thereby allowing the use of lower proof stresses to 'detect' the same flaw size 'a_{proof}'. Although best suited to pipelines and pressure vessels, proof testing may be a viable fracture control option for any component that can be easily removed and loaded.

5.3.4 Surface Layer Machining (Stripping)

Surface layer machining, or 'stripping', is another effective means of fracture control in cases where the permissible crack length (a_p) is less than that which can be detected (a_o). Consider a crack that has already reached its maximum permissible length (a_p). By 'shaving' off a very small surface layer (δ) around the crack location, the effective crack length would be reduced to $a_{stripped} = a_p - \delta$, as illustrated in Figure 5.7. Suppose that H represents the time required for the crack to grow from $a_{stripped}$ to a_p. This dictates that the stripping process would have to be repeated in intervals of approximately H hours.

Through experience, one can learn to anticipate the probable location of these undetectable cracks, such as in a fillet radius or a fastener hole. Because the surface layer δ is so small, the stripping process can typically be repeated several times without affecting the stress level within the component.

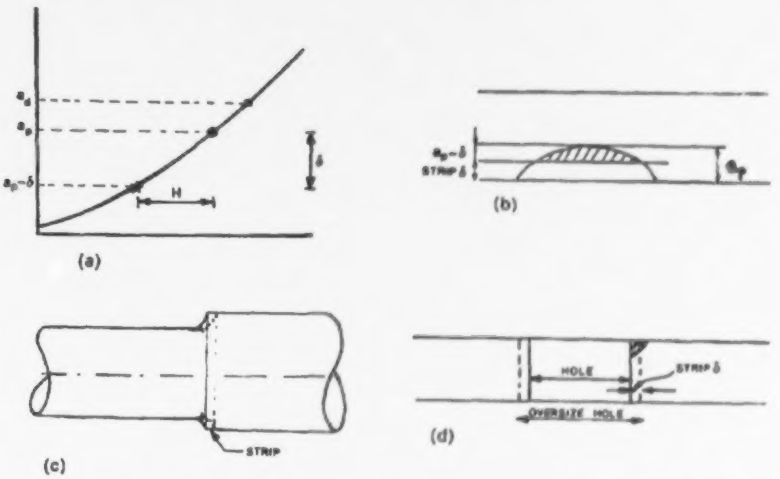

Figure 5.7 – Fracture control by surface layer machining (stripping) [Broek, 1989]

5.3.5 Multiple Load Paths (Structural Redundancy)

Structures containing multiple (redundant) load paths are generally more resistant to fracture than those containing only single load paths. The underlying principle governing the use of multiple load paths is that the fracture of a single structural member must not lead to the total collapse of the entire structure. The structure must be designed such that in the event of a fracture in a primary structural member, the loads carried by the fractured member can be transferred to (and successfully carried by) other members in the structure. The presence of multiple load paths within a given structure may significantly reduce the required factor of safety for fracture toughness and applied stress.

A good example of a multiple load path structure is the Kings Bridge in Australia, which failed in 1970. It was found that the failed bridge span contained three fractured girders. It was determined that the first girder had cracked prior to construction, while the second one failed during the first winter of operation. Failure of the third girder, which led to the overall structural failure, did not occur until a year later. Engineers concluded that total collapse was prevented by the bridge's concrete sidewalls (an architectural addition), which added to the multiple load paths for the entire structure.

Barsom et al (1987) pointed out that "fatigue crack propagation in multiple load path structures may occur essentially under constant deflection…rather than under constant load". Crack growth under constant deflection corresponds to a continuously decreasing stress intensity factor range (ΔK), and therefore may eventually lead to crack arrest. Hence, although individual components may require repair or replacement, the likelihood of total structural failure is greatly reduced by the incorporation of multiple load paths in a given structure.

5.3.6 Crack Arrestors

Crack arrestors are often incorporated into various components within a given structure for the purpose of either completely arresting or at least retarding the growth of any crack so that the component can still function properly until such time as the crack is detected and remedial action can be taken. This 'fail-safe' design approach has been employed for years in the aircraft and shipbuilding industries. Several types of crack arrestors are available, including stringers, strakes, and hybrid arrestors.

In the event that a primary structural element develops a crack, arrestors act as 'secondary elements' to which loads can be transferred. Providing another load path allows part of the load to bypass the crack through the arrestor, resulting in a decrease in the crack tip stress intensity factor (K). The addition of crack arrestors also reduces the effective plate width, thereby reducing the geometric correction factor (Y). These reductions can have such a profound effect on crack growth and the residual strength of a given component that crack arrest may become a possibility.

Unfortunately, the benefits resulting from lower stress intensity factors do come at a price. As the crack elongates, arrestors are subjected to higher and higher stress concentration factors (L). However, as long as the nominal stress in the arrestor remains below its ultimate strength (F_{tu}), the arrestor will be effective in retarding crack growth. Figure 5.8 illustrates the influence of crack arrestors on the residual strength of a wide plate.

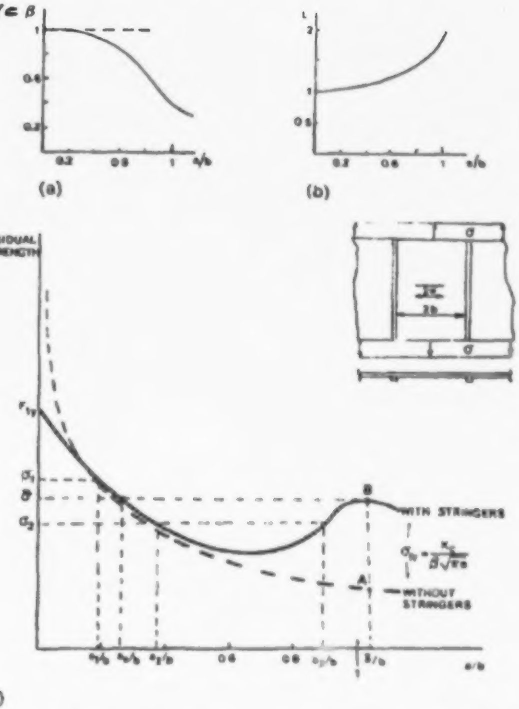

Figure 5.8 – Influence of typical crack arrestor on residual strength [Broek, 1989]

Using Equation 2.3b, the fracture stress for an unstiffened plate (i.e., one containing no crack arrestors) can be calculated for a number of crack lengths and plotted as the dashed line in Figure 5.8c. For small cracks, the ratio a/b is much less than one and the geometric correction factor (denoted as β in Figure 5.8) is therefore very close to unity. Thus, in the case of small cracks, the residual strength curve for the stiffened plate very closely resembles the one corresponding to the unstiffened plate. However, as the ratio a/b approaches one, the effective plate width is greatly reduced. Consequently, the geometric correction factor Y for the stiffened plate drops significantly and the required fracture stress (i.e., residual strength) rises. The degree of reduction in Y depends on both the stiffness and spacing of the arrestors. Crack arrestors that are stiff and spaced close together are more effective in reducing the geometric correction factor Y.

To further explain the information presented in Figure 5.8, consider a stiffened plate containing a fatigue crack of length a_1. In the event that a sufficiently large stress σ_1 is applied (equal to the residual strength corresponding to a_1), complete fracture would occur. On the other hand, suppose the fatigue crack grows to a length of a_2, at which time the application of a stress σ_2 would again result in fracture. However, the fracture would only run to a crack length of a_3, at which time it would be arrested because the residual strength of the stiffened plate at a crack length of a_3 is greater than the corresponding applied stress σ_2. If the applied stress is then increased to $\bar{\sigma}$, fracture will continue from a_3 to $\bar{a}$, followed by rapid and unstable crack growth to failure.

As the crack approaches an arrestor, there is a notable increase in the stresses within the arrestor. Furthermore, load transfer to an arrestor must be accommodated by some type of fastener (rivets, bolts, welds, etcetera), usually resulting in very high shear stresses within the fasteners. In the event that a crack arrestor is initially uncracked, the required fracture stress (σ_{fs}) is given by Equation 5.1.

$$\sigma_{fs} = \frac{F_{tu}}{L} \tag{5.1}$$

Using the stress concentration (L) curve of Figure 5.8b, Equation 5.1 can be used to plot the 'stringer' (i.e., arrestor) fracture line illustrated in Figure 5.9a. Suppose that a remote stress $\bar{\sigma}$ were applied at a crack length of a_s in Figure 5.9a. The result is a fracture running to $\bar{a}$, at which point the stringer will fracture, thus prohibiting any further load transfer from the plate. This undesirable situation can be remedied by selecting a stringer material with a higher ultimate tensile strength, which shifts the stringer fracture line upward as illustrated in Figure 5.9b.

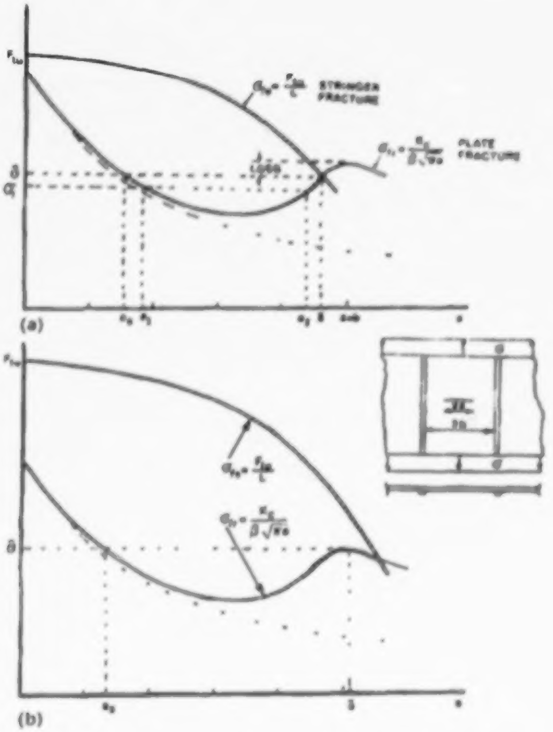

Figure 5.9 – Effect of arrestor tensile strength on overall residual strength diagram [Broek, 1989]

In the event of an initially cracked arrestor, overall strength would be governed by the fracture toughness of the arrestor, and failure would occur at a lower stress level.

In order to understand the fundamental principles associated with crack arrestors, the previous discussions have all considered crack development between crack arrestors. However, in reality, cracks will instead develop at a fastener location on an arrestor, as illustrated in Figure 5.10. Consequently, the corresponding arrestor (now cracked) will be highly stressed and will likely fracture entirely before long. If the arrestor does in fact fracture, the load must be redistributed to the adjacent uncracked arrestors. Now the problem becomes familiar, and by simply redefining the arrestor spacing as 'b' (instead of '2b', as before), all of the principles previously discussed still apply. It is common practice in the aircraft industry to ensure that a structure is capable of sustaining a 'two-bay crack', where the central arrestor has been completely fractured.

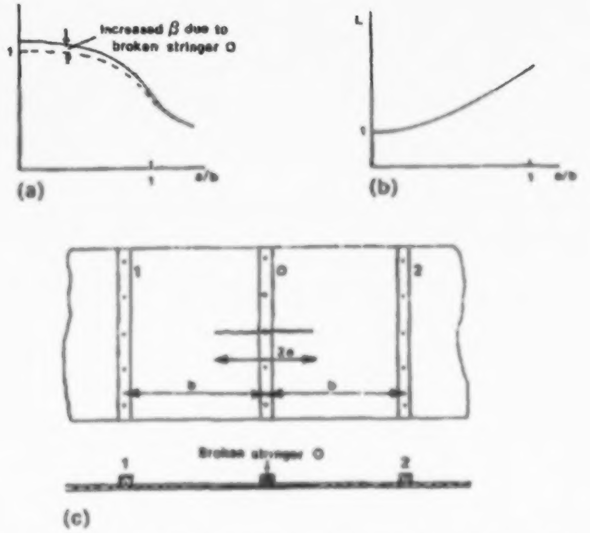

Figure 5.10 – Crack development at fastener location [Broek, 1989]

As previously mentioned, some of the more commonly used crack arrestors include stringers, strakes, and hybrid arrestors. Figure 5.11 illustrates the fundamental principle corresponding to each type of arrestor.

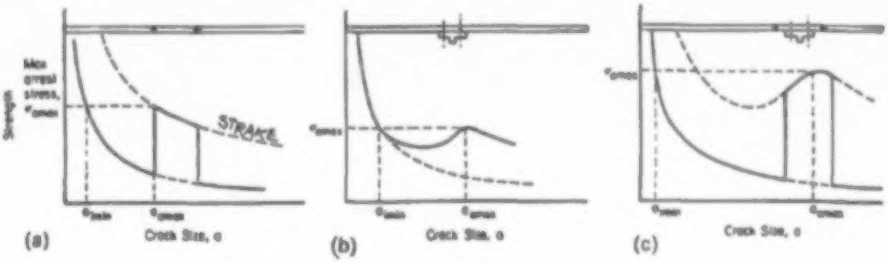

Figure 5.11 – Principles of various types of crack arrestors (a) High toughness strake, (b) Stringer or doubler, and (c) Hybrid arrestor [Broek, 1989]

Stringers afford the transfer of load from a cracked plate, thereby reducing the crack tip stress intensity factor K and retarding subsequent crack growth. A 'strake', on the other hand, is essentially a welded-in strip of material that has a higher fracture toughness (K_c) than the adjacent material. Thus, when a crack propagates into a strake, the increased fracture toughness may result in crack arrest. A hybrid crack arrestor is simply a combination of a stringer and a high toughness strake. This type of arrestor incorporates the best of both worlds, and is often a more effective (and more expensive) means of fracture control.

One of the major benefits associated with the use of crack arrestors is that conducting inspections that are focused on large cracks and more extensive damage may be sufficient. Furthermore, since such extensive damage can sometimes be sustained for a period of time, any required repairs may often be delayed slightly, if necessary.

A discussion of fracture control would not be complete without mentioning some of the repair techniques available.

5.4 Crack Repair Techniques

The main objective of a damage tolerance analysis is not to evaluate how long fatigue cracks can be sustained once they are detected. It is instead to prevent fractures by establishing fracture control plans to eliminate cracks before they become critical. When cracks are discovered and repair or replacement is deemed necessary, one of several remedial measures must be taken. The system may be unloaded and the cracked component replaced. However, complete replacement may be time consuming and relatively expensive. Alternatively, one may opt to reduce the applied loads and continue crack growth monitoring, but this remedial measure is rather questionable. The only remaining option is to retard, arrest, or otherwise eliminate the crack using some repair technique that is relatively simple and can be done quickly. The repair must be designed such that the loads and stresses in the cracked component can be successfully transferred through the repair. Any given repair is only a temporary solution, and fracture control methods must therefore be reinstated for the repair.

Several commonly used repair techniques include the use of repair welds, cover plates, and crack arrest (stop) holes. In addition, the use of composite patches has become a common practice for crack repair in the aircraft industry. Tensile overloads have also been employed as a means of retarding the growth of a crack.

Repair welding is commonly used when repairs are required in readily weldable metals. The process involves simply removing the material surrounding the crack and replacing it with weld metal. However, application of this technique has experienced only limited success.

A second repair method entails bolting or welding metal cover plates to either side of the cracked component, thus providing an alternative load transfer path. Cover plates are more effective when fastened to both sides of the cracked component, as this maintains a uniform stiffness on either side of the crack and eliminates the tendency for out-of-plane bending. The effectiveness of cover plates also depends on their relative size and shape. Figure 5.12 illustrates the use of welded cover plates.

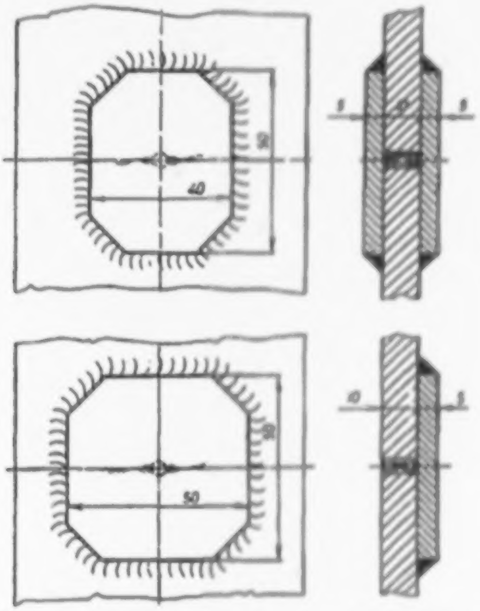

Figure 5.12 – Crack repair using welded cover plates [Domazet, 1996]

The use of composite patches offers several advantages including "the speed of repair, absence of new holes or welds which might act as crack initiators, minimum increase in weight, stiffening and sealing the area around the crack, curved and double curved surface application, etcetera" [Domazet, 1996]. Figure 5.13 illustrates the use of adhesively bonded composite patches. Reducing the length of each successive patch layer helps to reduce stress concentrations and ensure the gradual transfer of load around the crack. For a number of years, composite patches have provided a very successful means of fatigue crack repair in the aircraft industry.

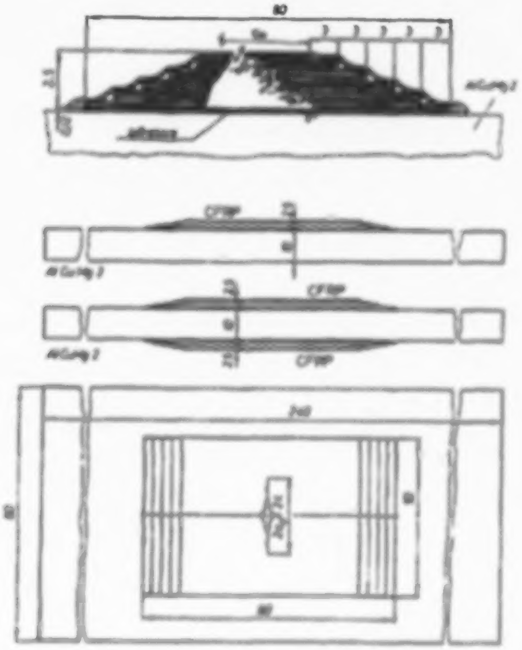

Figure 5.13 – Crack repair using adhesively bonded composite patches [Domazet, 1996]

The use of crack arrest holes (stop holes) is one of the most successful methods of fatigue crack repair. Fatigue crack growth is retarded by simply drilling a hole that intersects the crack tip. Figure 5.14 illustrates this retardation schematically, along with various stop hole configurations. It has been generally accepted that the best stop hole configuration is one that is centered about the crack tip (Figure 5.14d). Such a configuration ensures that the crack tip is intersected, while still requiring considerable time for crack reinitiation.

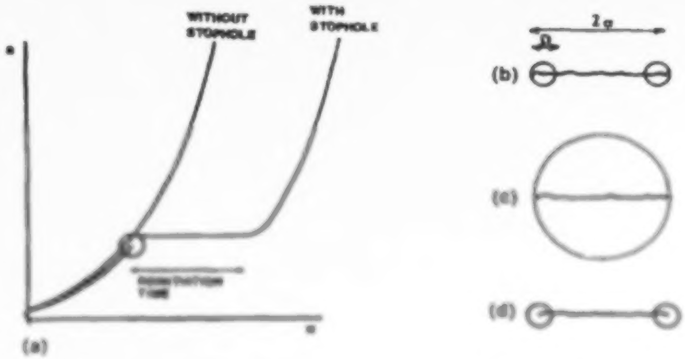

Figure 5.14 – Crack repair using crack arrest holes (stop holes) [Broek, 1989]

One can significantly improve the beneficial effect of a stop hole through cold work. Plastic deformation of the material around the rim of the hole will cause it to stretch permanently. However, in order to 'fit' the surrounding elastic material, it must be compressed to its original size, thereby introducing compressive residual stresses. These residual compressive stresses around the rim of the stop hole essentially delay the reinitiation of the crack, and also reduce the crack growth rates once reinitiation has taken place. The technique most commonly used to introduce these compressive stresses involves expanding the stop hole by pulling a tapered pin through it. To avoid introducing new cracks, the amount of expansion typically does not exceed 3% - 5%. Figure 5.15 illustrates two relatively simple devices used for expanding stop holes. Alternatively, fitting stop holes with pretensioned structural bolts may also introduce compressive residual stresses around the rim of the hole. On the other hand, stop holes may be fitted with oversized steel pins, resulting in localized residual tensile stresses. In this case, subsequent crack growth rates are retarded via a reduction in the effective stress range ($\Delta\sigma$) and the corresponding stress intensity factor range (ΔK).

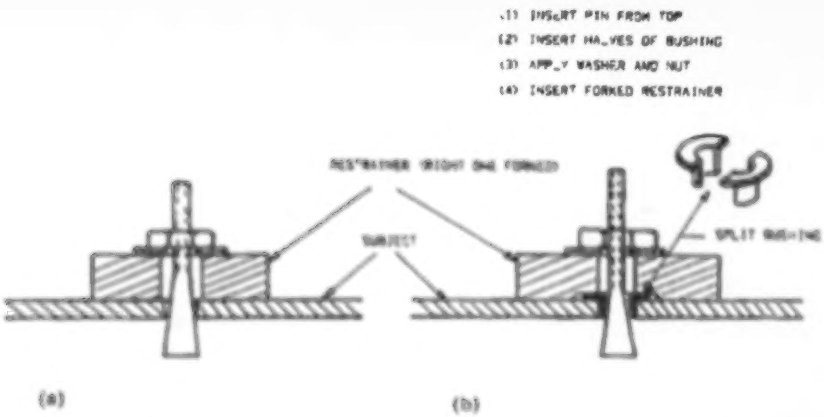
(1) INSERT PIN FROM TOP
(2) INSERT HALVES OF BUSHING
(3) APPLY WASHER AND NUT
(4) INSERT FORKED RESTRAINER
RESTRAINER (RIGHT ONE FORKED)
SUBJECT
SPLIT BUSHING
(a)
(b)

Figure 5.15 – Simple devices used for stop hole expansion when (a) Stop hole accessible from both sides, and (b) Stop hole accessible from one side only [Broek, 1989]

Domazet (1996) investigated several types of crack repair techniques. He ranked the most beneficial techniques by comparing the relative fatigue lives of center-cracked specimens that had first been repaired using one of different methods and then subjected to both constant and variable amplitude loading. The results of his investigation are summarized in Figure 5.16.

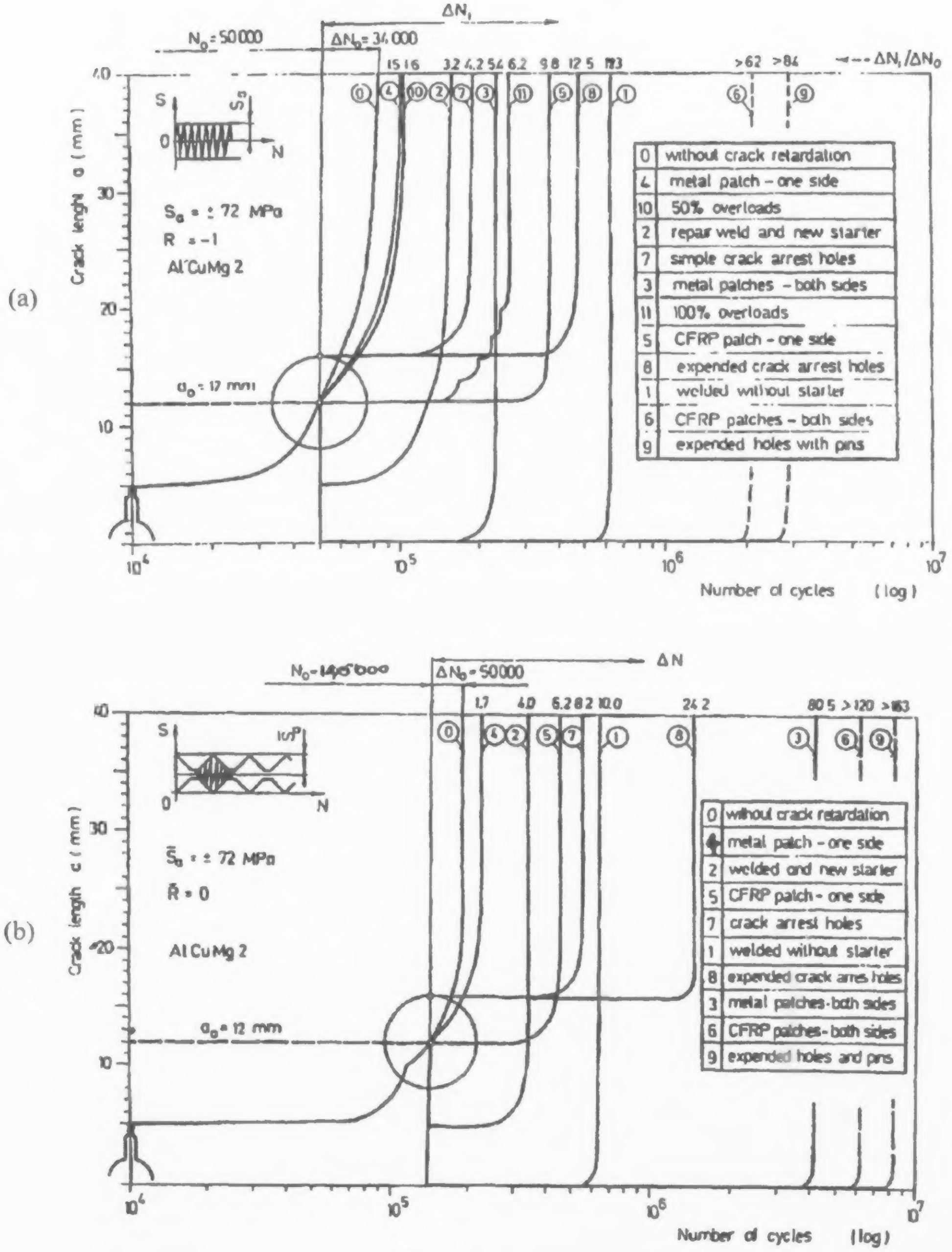

Figure 5.16 – Comparison of crack retardation (repair) methods used on specimens subjected to (a) Constant amplitude loading, and (b) Variable amplitude loading [Domazet, 1996]

Chapter 6

Experimental Method

6.1 Introduction

The experimental fatigue crack propagation testing program consisted of subjecting several center-cracked specimens of 350WT steel to both constant amplitude loading and semi-random loading

The first stage of the experimental program was comprised of fatigue crack growth threshold testing under constant amplitude loading. The evaluation of a threshold stress intensity factor (K_{th}) is required for many of the previously mentioned fatigue crack growth models.

Previous work by Trask (1998) investigated the degree of fatigue crack growth retardation resulting from tensile overloads interspersed within an otherwise constant amplitude loading sequence. Expanding on his work, the second stage of the experimental program investigated the reduction in fatigue crack growth retardation when a compressive underload (UL) immediately followed a tensile overload (OL).

The final stage of the experimental program examined the effects of varying the ratio of the applied tensile overload (OL) to the applied compressive underload (UL).

All fatigue crack growth tests were conducted in accordance with ASTM Standard No. E647, entitled "*Standard Test Method for Measurement of Fatigue Crack Growth Rates*". The use of this standard is valid only under conditions for which the principles of linear elastic fracture mechanics are applicable. The standard includes a discussion of such factors as test apparatus, specimen configuration and preparation, crack measurement techniques, and methods of data analysis.

6.2 Test Material

The material employed in this investigation was 350WT Category 5 steel, similar to that previously used by Trask (1998). One of the principal uses for this material is in the hulls of Halifax class frigates, which typically vary from 5 mm to 12 mm in thickness.

Other common applications for this steel include bridges, offshore structures, and pressure vessels. This type of steel is both tough and readily weldable, with a minimum fracture toughness of 40 Joules at a temperature of –40°C, and a minimum yield strength of 350 MPa. Test specimens were prepared from two 4' x 1' x ¼" sheets of this steel, which were provided by Defense Research Establishment Atlantic, in Dartmouth, Nova Scotia. Results of the chemical analysis of the steel, performed by the Halifax Dockyard Lab, are presented in Table 6.1, while the corresponding material properties for this 350WT Category 5 steel, as determined by Trask (1998), are given in Table 6.2.

Table 6.1 – Chemical composition of 350WT steel [Trask, 1998]

Specimen %	Chemical	350WT
0.075	Carbon	0.220 (Max.)
0.034	Chromium	N/A
0.016	Cobalt	N/A
0.010	Copper	N/A
1.250	Manganese	0.800 – 1.500
0.006	Molybenum	N/A
0.300	Niobium	N/A
0.008	Nickel	N/A
0.009	Phosphorus	0.030 (Max.)
0.230	Silicon	0.150 – 0.400
0.052	Vanadium	N/A
0.004	Sulfur	0.030 (Max.)

Table 6.2 – Material properties of 350WT steel [Trask, 1998]

Material Property	Value
Yield Strength, σ_{yld}	450 MPa
Ultimate Strength, σ_{ult}	524 MPa
Reduction in Area, RA	71%
Modulus of Elasticity, E	205,000 MPa
Poisson's Ration, ν	0.30

Other common applications for this steel include bridges, offshore structures, and pressure vessels. This type of steel is both tough and readily weldable, with a minimum fracture toughness of 40 Joules at a temperature of –40°C, and a minimum yield strength of 350 MPa. Test specimens were prepared from two 4' x 1' x ¼" sheets of this steel, which were provided by Defense Research Establishment Atlantic, in Dartmouth, Nova Scotia. Results of the chemical analysis of the steel, performed by the Halifax Dockyard Lab, are presented in Table 6.1, while the corresponding material properties for this 350WT Category 5 steel, as determined by Trask (1998), are given in Table 6.2.

Table 6.1 – Chemical composition of 350WT steel [Trask, 1998]

Specimen %	Chemical	350WT
0.075	Carbon	0.220 (Max.)
0.034	Chromium	N/A
0.016	Cobalt	N/A
0.010	Copper	N/A
1.250	Manganese	0.800 – 1.500
0.006	Molybenum	N/A
0.300	Niobium	N/A
0.008	Nickel	N/A
0.009	Phosphorus	0.030 (Max.)
0.230	Silicon	0.150 – 0.400
0.052	Vanadium	N/A
0.004	Sulfur	0.030 (Max.)

Table 6.2 – Material properties of 350WT steel [Trask, 1998]

Material Property	Value
Yield Strength, σ_{yld}	450 MPa
Ultimate Strength, σ_{ult}	524 MPa
Reduction in Area, RA	71%
Modulus of Elasticity, E	205,000 MPa
Poisson's Ration, ν	0.30

6.3 Test Specimen Configuration

In accordance with ASTM Standard No. E647, any test specimen configuration may be used for fatigue crack growth testing, provided that acceptable geometric correction factors (Y) are available, and that specimens are large enough to promote predominately elastic conditions during testing. To be consistent with testing previously done by Trask (1998), a center-cracked specimen of similar dimensions was chosen for testing. Furthermore, test apparatus for this type of specimen configuration had previously been manufactured and were readily available. The test specimen layout and dimensions are illustrated in Figure 6.1.

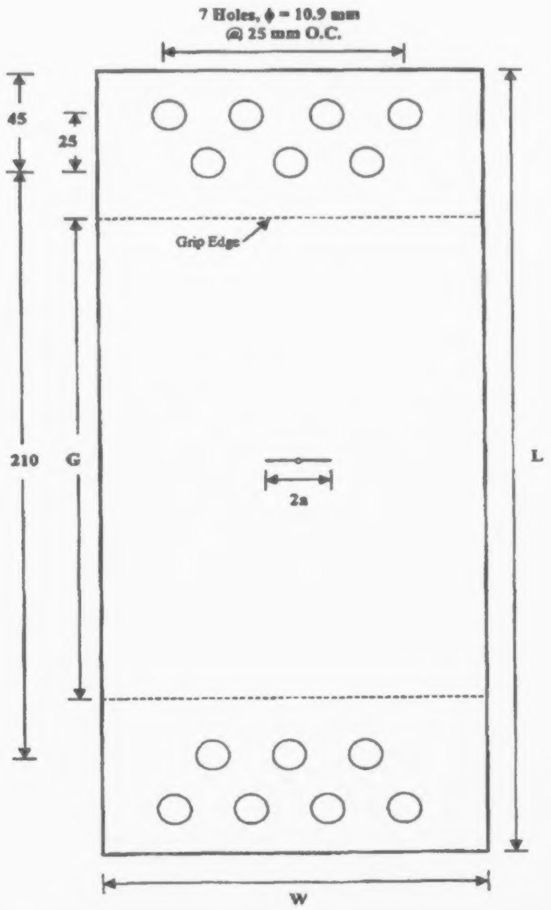

Figure 6.1 – Test specimen layout and dimensions [Trask, 1998]

The overall specimen dimensions were approximately 300 mm x 100 mm x 5 mm, with an EDM starter notch length (2a) of approximately 20 mm.

6.4 Specimen Preparation

The test specimens were cut from the steel sheets such that the starter notch and subsequent crack growth would be perpendicular to the rolling direction. Specimen thickness was then reduced to approximately 5 mm using the surface grinder in the Mechanical Engineering Department. The grip holes (approximately 7/16" diameter) were then laid out and drilled to accommodate the grips of the test fixture. In order to allow the machining of a starter notch, a small hole of 1/8" diameter was drilled at the center of each specimen. The 20 mm long starter notch was then machined at the Halifax Dockyard machine shop using an electron discharge machining (EDM) process. The width of the resulting EDM starter notch was 0.254 mm (1/100").

In order to provide a clear image of the crack tip when viewed through the travelling microscope, the surface of each test specimen was polished to an almost mirror-like shine. This was achieved by tediously sanding the surface with successively finer grades of sandpaper, namely 320 grit, 400 grit, and then 600 grit sandpaper. The ultimate shine was produced using a suspension of 5-micron aluminum oxide (5μ Al_2O_3) applied with a buffering pad attached to an electric drill.

6.5 Test Apparatus

An Instron servo-hydraulic universal testing machine (UTM), model 8501, was used to conduct the fatigue testing. The UTM employed an Instron digital control panel, model 8500^+, with a load cell capacity of ±100 kN under dynamic loading conditions (200 kN capacity under static loading conditions). The Instron UTM, along with its control panel and load cell are illustrated in Figure 6.2.

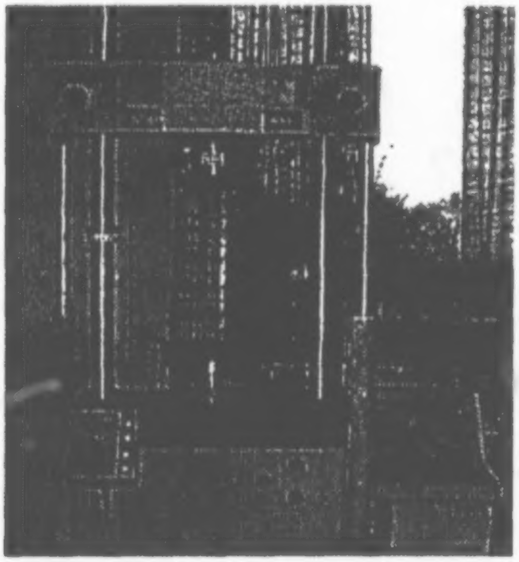

Figure 6.2 – Instron 8501 universal testing machine, control panel, and load cell [Trask, 1998]

The fixtures and grips used to hold the specimen in place are illustrated in Figure 6.3. The top and bottom fixtures are screwed into the load cell and actuator base, respectively.

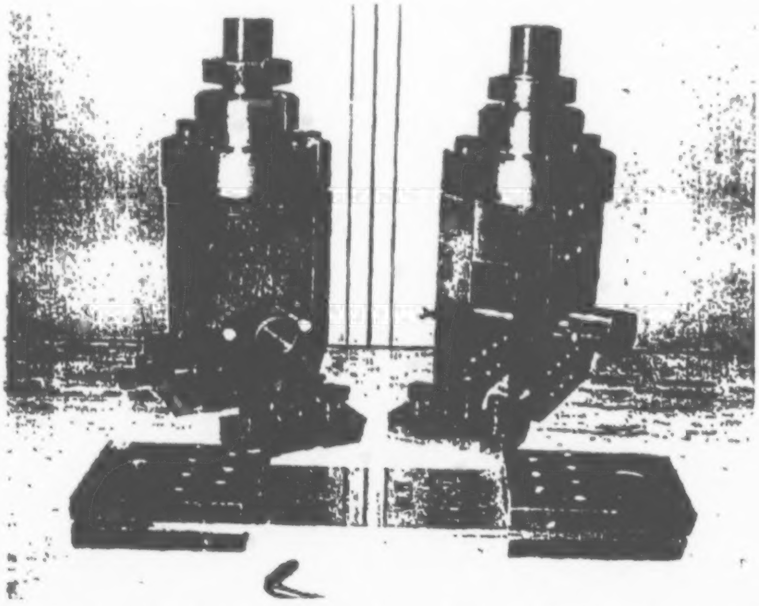

Figure 6.3 – Top and bottom fixtures, along with specimen and specimen grips

The top and bottom specimen grips are comprised of four steel plates (two plates per grip), which are bolted to the specimen using seven 7/16" hex nuts per grip, as illustrated in Figure 6.4.

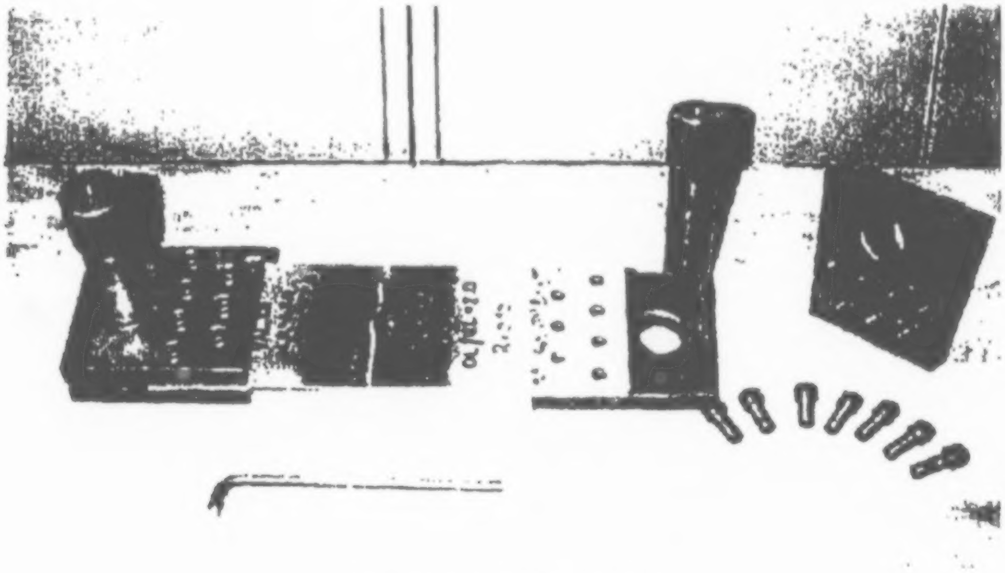

Figure 6.4 - Specimen grips

The specimen grips and the specimen itself are then attached to the top and bottom fixtures by means of two large pins, which are inserted through the fixtures and specimen grips as illustrated in Figure 6.5.

Incremental fatigue crack growth was measured using a Mitutoyo travelling microscope (at 10X magnification) with a micrometer resolution of 0.01 mm All samples tested were sufficiently thin (less than 15% of the specimen width, as required by ASTM E647) that crack measurements were required on one side only. Figure 6.6 illustrates the travelling microscope and its support structure.

Finally, the completely assembled test setup is illustrated in Figure 6.7.

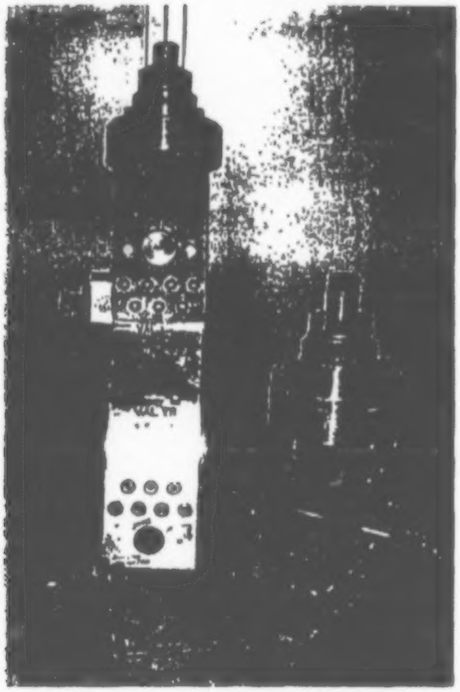

Figure 6.5 – Attachment of specimen grips to top and bottom test fixtures

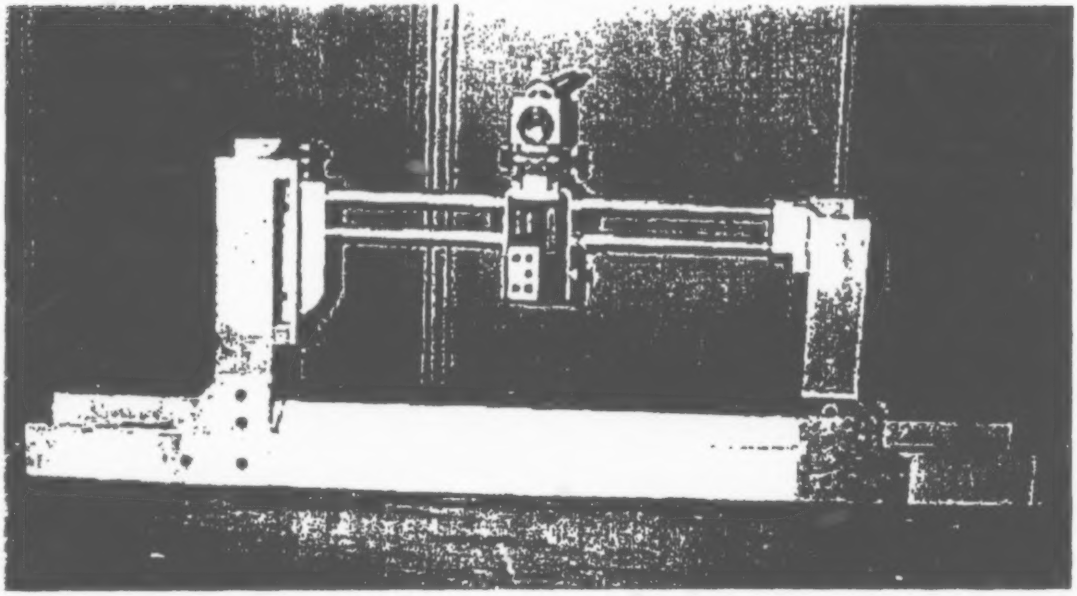

Figure 6.6 – Travelling microscope and support structure

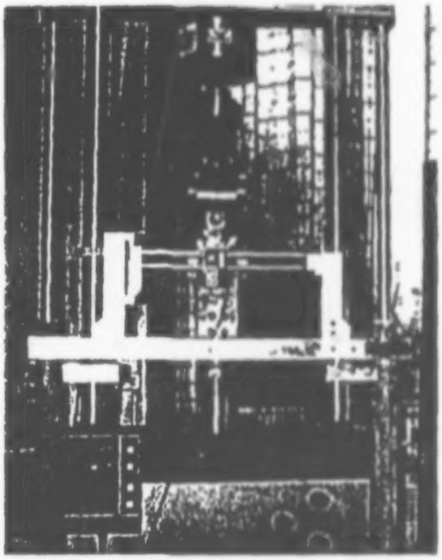

Figure 6.7 – Completely assembled test setup

6.6 Test Procedure

The experimental fatigue crack propagation program was comprised of fatigue crack growth threshold testing under constant amplitude loading, followed by an investigation into the degree of reduction in fatigue crack growth retardation resulting when tensile overloads (OL) are immediately followed by compressive underloads (UL). The final stage of experimental testing included an evaluation of the effects of varying the ratio of the applied tensile overload to the compressive underload (i.e., OL/UL).

6.6.1 Fatigue Crack Growth Threshold Testing

As previously mentioned, the first stage of the experimental program was comprised of fatigue crack growth threshold testing under constant amplitude loading. The evaluation of a threshold stress intensity factor (K_{th}) is required for many of the fatigue crack growth models discussed in Chapter 4.

The fatigue crack growth threshold stress intensity factor range (ΔK_{th}) was measured experimentally via the decreasing-K test of ASTM Standard No. E647. As with all fatigue crack growth rate testing, the specimens were first precracked by a small amount (≥ 1 mm) in order to remove the effects of the EDM starter notch and provide a sharpened fatigue crack of adequate size and straightness. Fatigue precracking in this case was continued until the minimum precrack length of 1 mm was reached, provided that the crack was growing at the same rate from both sides of the initial EDM notch. Using an initial maximum load of 50 kN and maintaining a stress ratio of zero, loads were subsequently shed in a controlled manner, such that the load reduction between adjacent steps was not greater than 10% of the previous maximum load. For example, consider a threshold test for which the initial constant amplitude load sequence varies between a minimum load of zero and a maximum load of 50 kN. During the first load-shedding sequence, the maximum load can be reduced to 45 kN. During the second load-shedding sequence, the maximum load can be reduced to 40.5 kN, and so on. As loads were shed, crack length measurements (a) were recorded as a function of the elapsed cycles (N), and the fatigue rate (da/dN-versus-ΔK) curves were produced concurrently until a sufficiently low stress intensity factor range or crack growth rate was obtained. This load-shedding technique was continued until the crack growth rates became so small that it was no longer practical to continue testing due to the time required to complete each test.

The fatigue crack growth rate threshold stress intensity factor range (ΔK_{th}) was calculated as the stress intensity factor range corresponding to an extrapolated crack growth rate of 10^{-10} m/cycle. Its magnitude was evaluated using simply the best-fit line through the log ΔK-versus-log da/dN data (i.e., the fatigue rate data plotted with the axes interchanged) between growth rates of approximately 10^{-9} m/cycle and 10^{-10} m/cycle. ASTM E647 suggests that because the range of fit for ΔK_{th} is specified in terms of da/dN, ΔK should be used as the dependent (x) variable in determining this best-fit line. This means that in order to plot the best-fit line, the x- and y-axes of the 'normal' fatigue rate curve must be interchanged so that ΔK is plotted on the y-axis and da/dN is plotted on the x-axis.

Finally, for the third threshold specimen, the K-decreasing test was followed by a K-increasing test in order to verify the initial K-decreasing data. Since it was observed that the data were comparable for both tests, the final threshold specimen was not subjected to the K-increasing portion, and it was assumed that data from the two previous tests, which had not included the K-increasing portion, were acceptable.

The results of all fatigue crack growth threshold tests will be presented in Chapter 7.

6.6.2 Semi-Random Fatigue Crack Growth Testing

When tensile overloads are applied within an otherwise constant amplitude loading sequence, crack growth retardation results. However, when a compressive underload is applied immediately following a tensile overload, the amount of fatigue crack growth retardation normally experienced may be significantly reduced. This aspect of fatigue crack growth behavior was the focus of stage two of the experimental testing program.

By varying the ratio of the tensile overload (OL) to the compressive underload (UL) that immediately follows, the amount of reduction in fatigue crack growth retardation can be further quantified. The final stage of the experimental program examined the effects of varying the ratio of the applied overload to the applied underload (i.e., OL/UL).

Fatigue crack growth rates were measured experimentally via the increasing-K test of ASTM Standard No. E647. Again, the specimens were precracked to remove the effects the machined starter notch and provide a sharpened fatigue crack of sufficient length and straightness. The constant amplitude portion of the loading sequence involved cycling at a maximum load of 60 kN. In order to include the effects of varying stress ratio, two stress ratios were used, namely $R = 0.1$ and $R = 0.3$.

The adjusting screws on the small rectangular brackets mounted to either side of the top and bottom fixtures shown in Figure 6.5 allowed the dissipation or cancellation of any possible bending moment induced due to misalignment. This ensured that crack growth rates remained equal on each side of the initial EDM notch. Dial gauges were also attached to the test setup on either side of a given specimen in order to detect the existence of any additional bending moments in the plate.

Photographs of the crack tip were obtained using a digital camera adapted to the Mitutoyo travelling microscope. Figure 6.8a and Figure 6.8b, respectively, illustrate a fatigue crack emanating from the EDM starter notch and subsequent crack growth further from the starter notch.

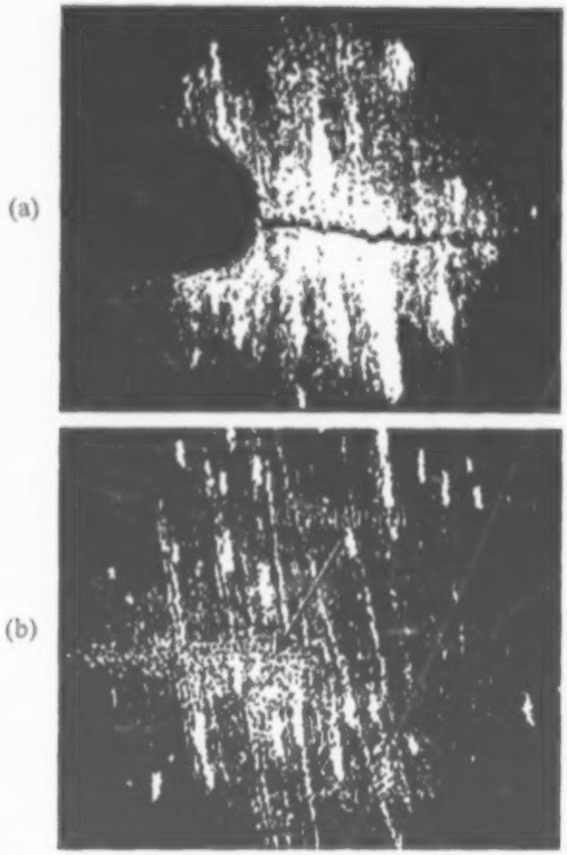

Figure 6.8 – Fatigue crack growth (a) Emanating from an initial EDM starter notch, and (b) Subsequent crack growth away from EDM notch

For each specimen, the tensile overloads and compressive underloads were applied at crack lengths of approximately 15 mm, 20 mm, and 25 mm. Three overload ratios (OLR) were applied at each stress ratio during the testing program, namely 1.20, 1.50, and 1.67 (one test at $R = 0.1$ also employed an OLR of 1.83). Figure 6.9 illustrates the formation of an overload-induced plastic zone surrounding the crack tip. In this case, a tensile overload with OLR=1.67 had just been applied. The two dashed lines are thought to represent the limits of the Irwin plastic zone approximation (recall Figures 2.17 and 2 19) and the commonly observed bean-shaped region of vonMises plastic stresses.

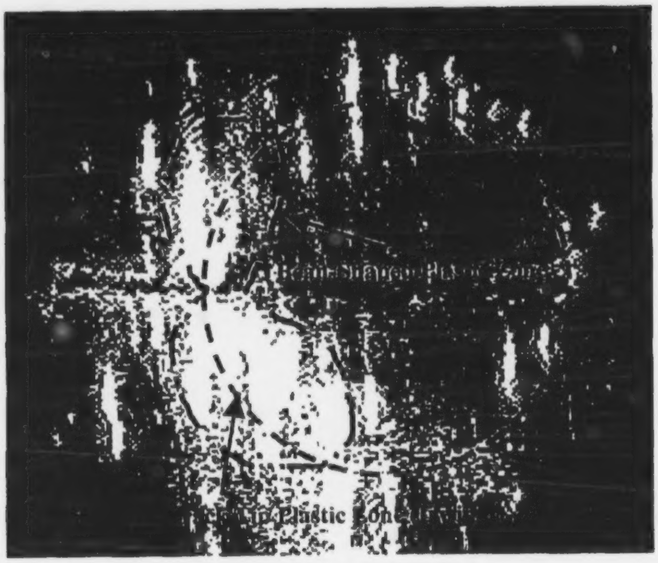

Figure 6.9 – Formation of crack tip plastic zone (OLR = 1.67)

The maximum load during the overload cycle ($P_{max,OL}$) was calculated simply by multiplying the maximum constant amplitude load by the corresponding overload ratio That is

$$P_{max,OL} = (P_{max,CAL})(OLR) \tag{6.1}$$

Since center-cracked specimens were used, all fatigue loading was purely axial, in which case Equation 3.1 yields

$$P_{min,CAL} = (R)(P_{max,CAL}) \tag{6.2}$$

During the second stage of testing, the ratio of the applied overload (OL) to the applied underload (UL), as described by Figure 6.10 below, was always equal to one. Therefore, a third and final stage of fatigue crack growth testing was proposed to investigate the effects of varying this OL/UL ratio. The magnitude of OL is given by Equation 6.3 as

$$\mathrm{OL} = \mathrm{P}_{\mathrm{max,OL}} - \mathrm{P}_{\mathrm{mean,CAL}} = \mathrm{P}_{\mathrm{max,CAL}} \cdot \mathrm{OLR} - \mathrm{P}_{\mathrm{max,CAL}} \cdot \left(\frac{1+\mathrm{R}}{2}\right) = \mathrm{P}_{\mathrm{max,CAL}} \cdot \left(\mathrm{OLR} - \frac{1+\mathrm{R}}{2}\right) \quad (6.3)$$

where

$$\mathrm{P}_{\mathrm{mean,CAL}} = \frac{\mathrm{P}_{\mathrm{max,CAL}} + \mathrm{P}_{\mathrm{min,CAL}}}{2} = \frac{\mathrm{P}_{\mathrm{max,CAL}} + \mathrm{R} \cdot \mathrm{P}_{\mathrm{max,CAL}}}{2} = \mathrm{P}_{\mathrm{max,CAL}} \cdot \left(\frac{1+\mathrm{R}}{2}\right) \quad (6.4)$$

Combining Equations 6.3 and 6.4 above, one obtains the following expressions for the minimum axial load corresponding to the compressive underload, $\mathrm{P}_{\mathrm{min,UL}}$

$$\mathrm{P}_{\mathrm{min,UL}} = \mathrm{P}_{\mathrm{mean,CAL}} - \mathrm{UL} = \mathrm{P}_{\mathrm{mean,CAL}} - \frac{\mathrm{OL}}{(\mathrm{OL}/\mathrm{UL})} \quad (6.5\mathrm{a})$$

$$\mathrm{P}_{\mathrm{min,UL}} = \mathrm{P}_{\mathrm{max,CAL}} \cdot \left[\left(\frac{1+\mathrm{R}}{2}\right) - \frac{1}{\mathrm{OL}/\mathrm{UL}}\left(\mathrm{OLR} - \left(\frac{1+\mathrm{R}}{2}\right)\right)\right] \quad (6.5\mathrm{b})$$

Rearranging Equation 6.5a and substituting Equation 6.5b, one obtains the following expressions for the magnitude of the compressive underload, UL.

$$\mathrm{UL} = \mathrm{P}_{\mathrm{mean,CAL}} - \mathrm{P}_{\mathrm{min,UL}} = \mathrm{P}_{\mathrm{max,CAL}} \cdot \left(\frac{1+\mathrm{R}}{2}\right) - \mathrm{P}_{\mathrm{max,CAL}} \cdot \left[\left(\frac{1+\mathrm{R}}{2}\right) - \frac{1}{\mathrm{OL}/\mathrm{UL}}\left(\mathrm{OLR} - \left(\frac{1+\mathrm{R}}{2}\right)\right)\right] \quad (6.6\mathrm{a})$$

$$\mathrm{UL} = \frac{\mathrm{P}_{\mathrm{max,CAL}}}{\mathrm{OL}/\mathrm{UL}}\left(\mathrm{OLR} - \left(\frac{1+\mathrm{R}}{2}\right)\right) \quad (6.6\mathrm{b})$$

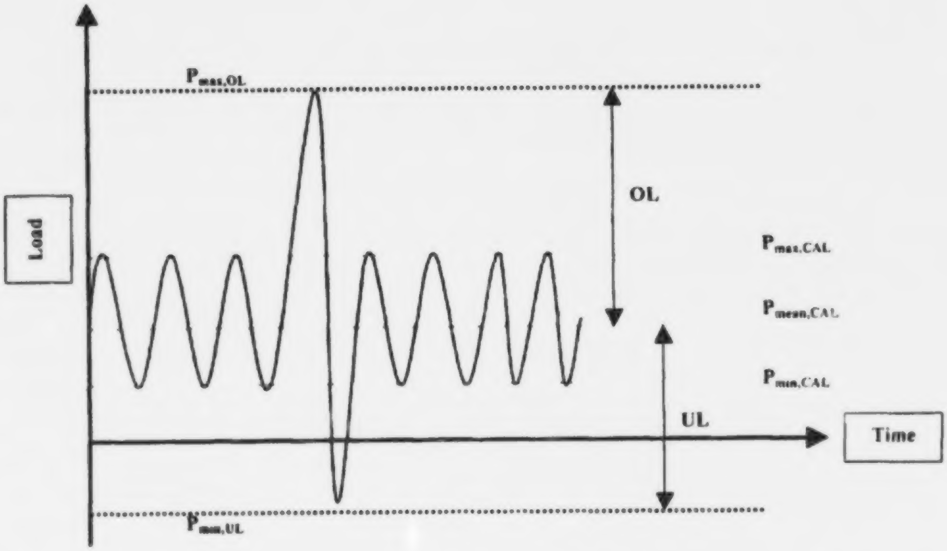
$P_{max,OL}$
OL
Load
$P_{max,CAL}$
$P_{mean,CAL}$
$P_{min,CAL}$
UL
Time
$P_{min,UL}$

Figure 6.10 – Schematic representation of aforementioned overload and underload terms

The *OL/UL* ratios investigated in this study were 0.5, 1.0, and 2.0. For all specimens tested, in both stage two and stage three of the experimental testing program, failure occurred by yielding rather than by fracture.

The results of all semi-random fatigue crack growth tests will be presented and discussed in greater detail in Chapter 7.

Chapter 7
Experimental Results and Data Analysis

7.1 Introduction

This chapter will present the experimental results for both the fatigue crack growth threshold testing under constant amplitude loading and the fatigue crack growth testing under semi-random loading. The experimental results will be analyzed using some of the fatigue crack growth models previously discussed in Chapter 4.

7.2 Data Reduction Techniques

At specific intervals during each fatigue crack growth test, the crack length (a) was measured and recorded as a function of the corresponding number of elapsed cycles (N), thereby facilitating the development of an 'a-versus-N' curve for each test. The crack growth data were then processed to obtain a fatigue rate (da/dN-versus-ΔK) curve for each test. These forms of data representation were each described previously in Chapter 4.

Two data reduction methods were used to process the a-versus-N data from each test into the corresponding da/dN-versus-ΔK curve, namely the secant method and the incremental polynomial method. The secant method is very simple and is best suited to cases where the crack growth (a-versus-N) data exhibits relatively little scatter and the intervals at which crack lengths are measured are relatively short. The secant method calculates the fatigue crack growth rate (da/dN) as the slope of the a-versus-N curve between two adjacent data points. That is,

$$\left(\frac{da}{dN}\right)_j \cong \left(\frac{\Delta a}{\Delta N}\right)_j = \frac{a_j - a_{j-1}}{N_j - N_{j-1}} \qquad (7.1)$$

The corresponding stress intensity factor range (ΔK) is then calculated using the average fatigue crack length during the interval 'a_j - a_{j-1}'.

$$\Delta K_j = \Delta\sigma Y\sqrt{\pi a_{avg}} = \Delta\sigma Y\sqrt{\pi\frac{a_j + a_{j-1}}{2}} \tag{7.2}$$

The incremental polynomial method is a more robust method, which can be used to 'smooth' data with a considerable amount of scatter. This method, fully described in ASTM E647, essentially takes the a-versus-N data and locally 'fits' a parabola to successive sets of 2n + 1 data points. Although typical values of 'n' range from 1 to 4, ASTM E647 suggests the use of n = 3, which represents a seven-point incremental polynomial method. This local fit is described by Equation 7.3.

$$\hat{a}_i = b_o + b_1\left(\frac{N_i - C_1}{C_2}\right) + b_2\left(\frac{N_i - C_1}{C_2}\right)^2 \tag{7.3}$$

Where $-1 \leq \left(\frac{N_i - C_1}{C_2}\right) \leq +1$

$C_1 = ½\,(N_{i+n} + N_{i-n})$

$C_2 = ½\,(N_{i+n} - N_{i-n})$

The parameters C_1 and C_2 are used to properly scale the input data and avoid numerical difficulties when determining the least squares regression parameters b_o, b_1, and b_2. The crack growth rate (da/dN) follows from the derivative of Equation 7.3.

$$\frac{d\hat{a}}{dN} = \frac{d}{dN}\left[b_o + b_1\left(\frac{N_i - C_1}{C_2}\right) + b_2\left(\frac{N_i - C_1}{C_2}\right)^2\right] = \frac{b_1}{C_2} + \frac{2b_2}{C_2^2}(N_i - C_1) \tag{7.4}$$

The corresponding stress intensity factor range (ΔK) is then calculated using the fitted crack length of Equation 7.3.

ASTM E647 includes a Fortran program for data reduction using the seven-point incremental polynomial method. This program was converted into a spreadsheet format for the presentation of data in this report.

Figure 7.1 illustrates a typical fatigue rate curve using both the secant method and the seven- point incremental polynomial method to describe the same fatigue crack growth rate data.

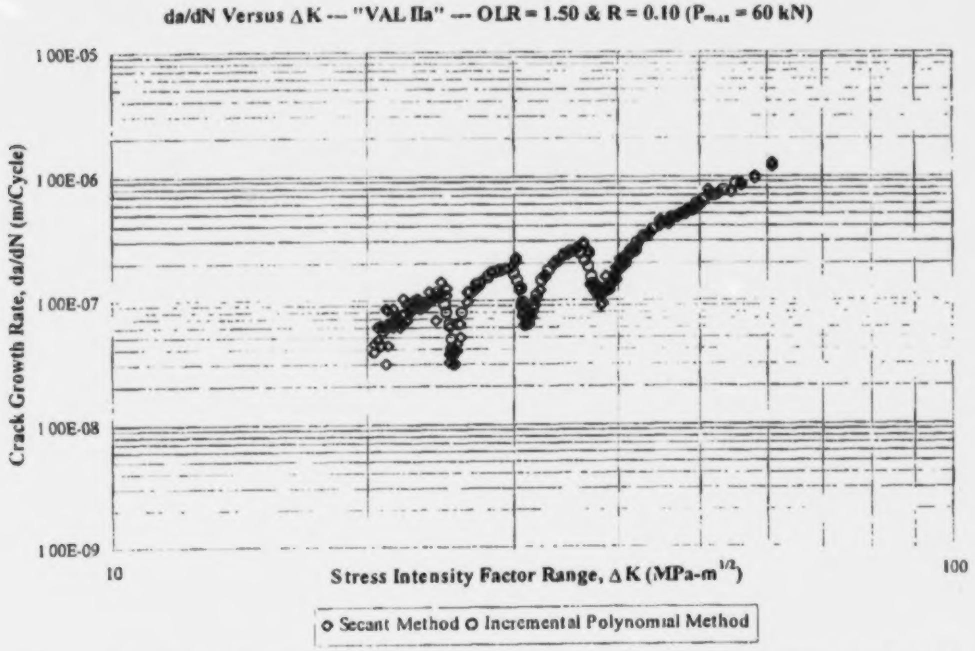

Figure 7.1 – Use of both the secant and seven-point incremental polynomial method

7.3 Results of Fatigue Crack Growth Threshold Testing

Table 7.1 presents a summary of the fatigue crack growth threshold testing results. For all fatigue crack growth threshold tests performed, loads were shed from an initial maximum of 50 kN. Moreover, the stress ratio for each was kept constant at zero. As previously mentioned, the fatigue crack growth rate threshold stress intensity factor range (ΔK_{th}) was evaluated using a 'best-fit line' through the log ΔK-versus-log da/dN data between growth rates of approximately 10^{-9} m/cycle and 10^{-10} m/cycle. Its magnitude was taken as that value of ΔK corresponding to an extrapolated crack growth rate of 10^{-10} m/cycle. The average threshold stress intensity factor so obtained, given in Table 7.1 below, compared relatively well with the limiting value of 6 $\mathrm{MPa}\sqrt{\mathrm{m}}$ (for $R=0$) suggested by Barsom et al (1987), as previously mentioned in section 4.2 of this report.

Table 7.1 – Results of fatigue crack growth threshold testing

Specimen No.	Threshold, K_{th} ($\mathrm{MPa\text{-}m^{1/2}}$)	% Difference
K_{th}-1	5.43	9.50
K_{th}-2	5.30	11.67
K_{th}-3	5.94	1.00
K_{th}-4	5.57	7.17
Average K_{th}	**5.56**	**7.33**

A typical fatigue rate curve (representing both the 'normal' and 'inverted' axes orientation) for the fatigue crack growth threshold testing is illustrated in Figure 7.2. The original fatigue rate (da/dN-versus-ΔK) data for all specimens, along with the corresponding a-versus-N data, are given in Appendix A.

Trask (1998) recommended the evaluation of a suitable K_{th} value for use in Zheng and Hirt's model. In a subsequent section of this report, a fatigue life prediction made using their model (incorporating the average K_{th} value given in Table 7.1) will be compared to the prediction obtained using the 'two-curve' Paris model proposed by Trask (1998).

was taken as that value of ΔK corresponding to an extrapolated crack growth rate of 10^{-10} m/cycle. The average threshold stress intensity factor so obtained, given in Table 7.1 below, compared relatively well with the limiting value of 6 MPa$\sqrt{m}$ (for R=0) suggested by Barsom et al (1987), as previously mentioned in section 4.2 of this report.

Table 7.1 – Results of fatigue crack growth threshold testing

Specimen No.	Threshold, K_{th} (MPa-m$^{1/2}$)	% Difference
K_{th}-1	5.43	9.50
K_{th}-2	5.30	11.67
K_{th}-3	5.94	1.00
K_{th}-4	5.57	7.17
Average K_{th}	**5.56**	**7.33**

A typical fatigue rate curve (representing both the 'normal' and 'inverted' axes orientation) for the fatigue crack growth threshold testing is illustrated in Figure 7.2 The original fatigue rate (da/dN-versus-ΔK) data for all specimens, along with the corresponding a-versus-N data, are given in Appendix A.

Trask (1998) recommended the evaluation of a suitable K_{th} value for use in Zheng and Hirt's model. In a subsequent section of this report, a fatigue life prediction made using their model (incorporating the average K_{th} value given in Table 7.1) will be compared to the prediction obtained using the 'two-curve' Paris model proposed by Trask (1998)

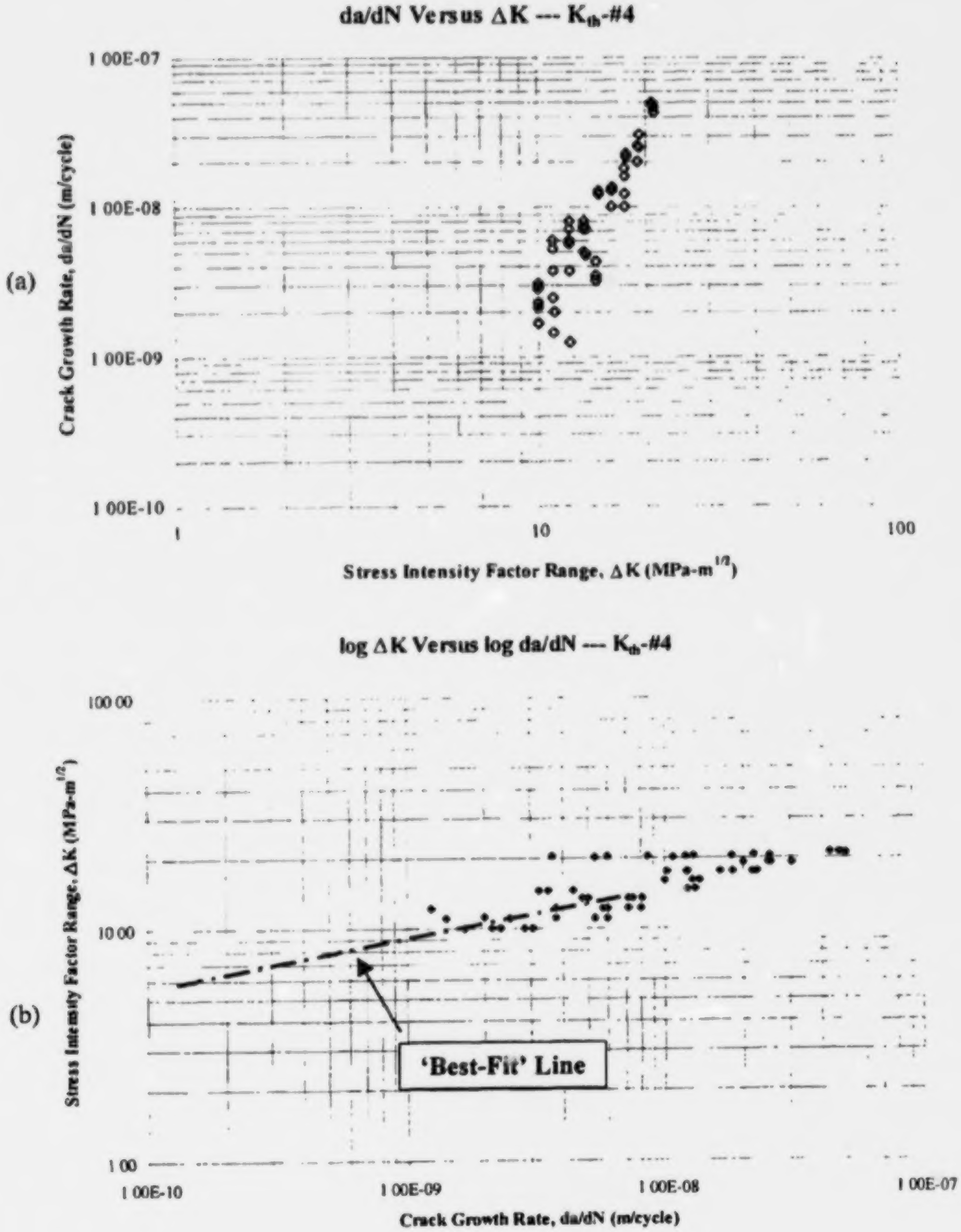

Figure 7.2 – Fatigue rate curves used in crack growth threshold testing: (a) 'Normal' axes orientation, and (b) 'Inverted' axes orientation

7.4 Results of Semi-Random Fatigue Crack Growth Testing

A total of twelve semi-random loading tests were performed to investigate the reduction in fatigue crack growth retardation when a compressive underload occurs immediately following a tensile overload. Using stress ratios of 0.1 (test series 'a') and 0.3 (test series 'b'), tensile overloads (OLR's of 1.20, 1.50, and 1.67) and compressive underloads were applied at crack lengths of approximately 15 mm, 20 mm, and 25 mm. These intervals were chosen such that steady state constant amplitude crack growth rates could be re-established during the interim.

Four additional tests were conducted to examine the effects of varying the ratio of the applied tensile overload (OL) to the applied compressive underload (UL). Using a stress ratio of 0.1 and overload ratios of 1.20 and 1.67, OL/UL ratios of 0.5 and 2.0 were incorporated into the loading scenario. Recall that for the first twelve tests, the OL/UL ratio was held equal to one.

Table 7.2 and Table 7.3, respectively, summarize the specimen dimensions and loading spectra used for the entire testing program. Note that the specimens used for threshold testing were of similar dimensions.

During each test, the fatigue crack length (a) and corresponding number of elapsed cycles (N) were measured and recorded from an initial crack length (a_i) to a final crack length (a_f). When noticeable yield zones began to develop in the uncracked portion beyond each crack tip, one last crack length measurement was taken (a_{yld}), and the microscope was removed from its support. Loading was then continued until specimen failure occurred by yielding. It was observed that the number of cycles that elapsed between the crack length at first yielding (a_{yld}) and that corresponding to complete specimen failure was always relatively small, representing the number of cycles required for the yielded section to 'neck' fully. Table 7.4 summarizes the average crack lengths and corresponding number of cycles to failure for each test.

The original a-versus-N data, along with the resulting fatigue rate (da/dN-versus-ΔK) data for the sixteen semi-random fatigue crack growth tests are given in Appendix B. It was observed that the a-versus-N data for both the left and right crack tip were nearly identical for any N, confirming that crack growth rates from either side of the EDM notch were very similar. The fatigue rate curves for all tests were plotted using both the secant and seven-point incremental polynomial methods. Since crack growth rates from each side of the EDM notch were similar, both of these data reduction methods incorporated an average crack length. It is the author's opinion that while the incremental polynomial method provides excellent results during the constant amplitude portion of a given test, post-overload fatigue crack growth retardation may sometimes be underestimated (Figure 7.1). This can be remedied by taking crack length measurements at shorter intervals following an overload, thereby providing more data points for the periods during which the most rapid fluctuations in crack growth rates occur

Table 7.2 – Summary of specimen dimensions

Specimen ID	Length, L (mm)	Width, W (mm)	Thickness, t (mm)	EDM Notch Width, 2a (mm)
VAL Ia-2	290.50	100.80	5.05	20.08
VAL IIa-2	291.00	100.65	5.00	20.08
VAL IIIa	291.00	100.45	5.06	20.10
VAL IIIa-2	294.00	100.20	5.04	20.14
VAL IVa	291.00	101.30	5.05	20.12
VAL Va	294.00	102.15	5.02	20.08
VAL VIa	296.00	102.00	4.98	20.12
VAL VIIa	290.00	101.00	5.04	20.12
VAL VIIIa	294.00	102.20	5.03	20.10
VAL Ib	295.00	100.50	5.04	20.08
VAL Ib-2	290.00	100.80	4.99	20.10
VAL IIb	290.00	100.90	5.01	20.12
VAL IIb-2	294.00	101.15	5.04	20.04
VAL IIIb	293.50	100.80	4.99	20.14
VAL IIIb-2	295.00	100.85	5.03	20.10
VAL IIIb-3	292.50	101.85	5.00	20.10
Average	**292.35**	**101.10**	**5.02**	**20.10**

were very similar. The fatigue rate curves for all tests were plotted using both the secant and seven-point incremental polynomial methods. Since crack growth rates from each side of the EDM notch were similar, both of these data reduction methods incorporated an average crack length. It is the author's opinion that while the incremental polynomial method provides excellent results during the constant amplitude portion of a given test, post-overload fatigue crack growth retardation may sometimes be underestimated (Figure 7.1). This can be remedied by taking crack length measurements at shorter intervals following an overload, thereby providing more data points for the periods during which the most rapid fluctuations in crack growth rates occur

Table 7.2 – Summary of specimen dimensions

Specimen ID	Length, L (mm)	Width, W (mm)	Thickness, t (mm)	EDM Notch Width, 2a (mm)
VAL Ia	290.50	100.80	5.05	20.08
VAL IIa	291.00	100.65	5.00	20.08
VAL IIIa	291.00	100.45	5.06	20.10
VAL IIIa-2	294.00	100.20	5.04	20.14
VAL IVa	291.00	101.30	5.05	20.12
VAL Va	294.00	102.15	5.02	20.08
VAL VIa	296.00	102.00	4.98	20.12
VAL VIIa	290.00	101.00	5.04	20.12
VAL VIIIa	294.00	102.20	5.03	20.10
VAL Ib	295.00	100.50	5.04	20.08
VAL Ib-2	290.00	100.80	4.99	20.10
VAL IIb	290.00	100.90	5.01	20.12
VAL IIb-2	294.00	101.15	5.04	20.04
VAL IIIb	293.50	100.80	4.99	20.14
VAL IIIb-2	295.00	100.85	5.03	20.10
VAL IIIb-3	292.50	101.85	5.00	20.10
Average:	**292.35**	**101.10**	**5.02**	**20.10**

Table 7.3 – Summary of specimen loading spectra

Specimen ID	R	OLR	OL/UL	$P_{max,CAL}$ (kN)	$P_{min,CAL}$ (kN)	$P_{max,OL}$ (kN)	$P_{min,OL}$ (kN)
VAL Ia	0.10	1.20	1.0	60	6	72	-6.0
VAL IIa	0.10	1.50	1.0	60	6	90	-24.0
VAL IIIa	0.10	1.67	1.0	60	6	100	-34.0
VAL IIIa-2	0.10	1.67	1.0	60	6	100	-34.0
VAL IVa	0.10	1.83	1.0	60	6	110	-44.0
VAL Va	0.10	1.67	2.0	60	6	100	-0.5
VAL VIa	0.10	1.67	0.5	60	6	100	-100.0
VAL VIIa	0.10	1.20	2.0	60	6	72	13.5
VAL VIIIa	0.10	1.20	0.5	60	6	72	-45.0
VAL Ib	0.30	1.20	1.0	60	18	72	6.0
VAL Ib-2	0.30	1.20	1.0	60	18	72	6.0
VAL IIb	0.30	1.50	1.0	60	18	90	-12.0
VAL IIb-2	0.30	1.50	1.0	60	18	90	-12.0
VAL IIIb	0.30	1.67	1.0	60	18	100	-22.0
VAL IIIb-2	0.30	1.67	1.0	60	18	100	-22.0
VAL IIIb-3	0.30	1.67	1.0	60	18	100	-22.0

Table 7.4 – Summary of semi-random loading tests

Specimen ID	R	OLR	OL/UL	a_i (mm)	a_f (mm)	a_{fd} (mm)	No. Cycles a_i to a_f	No. Cycles a_i to a_{fd}	No. Cycles a_i to failure
VAL Ia	0.10	1.20	1.0	11.20	36.68	37.50	140700	142000	143040
VAL IIa	0.10	1.50	1.0	11.16	36.11	37.58	174400	176000	177357
VAL IIIa	0.10	1.67	1.0	11.09	37.05	37.35	224100	224300	225444
VAL IIIa-2	0.10	1.67	1.0	11.10	35.65	37.89	221300	223800	224346
VAL IVa	0.10	1.83	1.0	11.36	36.06	37.81	304700	306400	307803
VAL Va	0.10	1.67	2.0	11.10	36.58	38.04	328200	330100	331850
VAL VIa	0.10	1.67	0.5	11.05	36.89	37.73	198000	199000	200116
VAL VIIa	0.10	1.20	2.0	11.07	36.76	38.42	168200	170500	172092
VAL VIIIa	0.10	1.20	0.5	11.25	37.47	38.50	158000	159500	161523
VAL Ib	0.30	1.20	1.0	11.02	37.47	N/A	268500	270500	272564
VAL Ib-2	0.30	1.20	1.0	11.20	35.89	38.07	262300	266500	269169
VAL IIb	0.30	1.50	1.0	11.19	36.27	37.92	302900	305700	307914
VAL IIb-2	0.30	1.50	1.0	11.17	37.62	38.51	347200	348800	350654
VAL IIIb	0.30	1.67	1.0	11.25	36.60	37.68	370800	372400	374571
VAL IIIb-2	0.30	1.67	1.0	11.12	35.61	37.94	436000	440500	442767
VAL IIIb-3	0.30	1.67	1.0	11.06	36.35	38.05	441000	443800	446928

Figure 7.3a and Figure 7.3b illustrate the effect of stress ratio (R) on a typical a-versus-N curve and the corresponding fatigue rate curve, respectively. As expected, the use of a higher stress ratio, which corresponds to a reduced stress range, yields a lower ΔK (and a much smaller da/dN) at any given crack length. The net result is a leftward shift of the corresponding da/dN-versus-ΔK curve and a much longer fatigue life. Figure 7.3b also confirms that, as expected, components subjected to similar loading scenarios exhibit similar fatigue rate curves.

Figure 7.4 illustrates the effects of overload ratio (OLR) on the a-versus-N curve and resulting fatigue rate curve for R = 0.1. A similar trend was observed for R = 0.3, as illustrated below in Figure 7.5. As expected, the higher the OLR (and OL/UL, as will be shown later), the greater the amount of retardation in fatigue crack growth, which is shown in the figures below via an increased number of delay cycles and a reduced minimum crack growth rate following an overload/underload application.

Table 7.3 – Summary of specimen loading spectra

Specimen ID	R	OLR	OL/UL	$P_{max,CAL}$ (kN)	$P_{min,CAL}$ (kN)	$P_{max,OL}$ (kN)	$P_{min,OL}$ (kN)
VAL Ia	0.10	1.20	1.0	60	6	72	-6.0
VAL IIa	0.10	1.50	1.0	60	6	90	-24.0
VAL IIIa	0.10	1.67	1.0	60	6	100	-34.0
VAL IIIa-2	0.10	1.67	1.0	60	6	100	34.0
VAL IVa	0.10	1.83	1.0	60	6	110	-44.0
VAL Va	0.10	1.67	2.0	60	6	100	-0.5
VAL VIa	0.10	1.67	0.5	60	6	100	100.0
VAL VIIa	0.10	1.20	2.0	60	6	72	13.5
VAL VIIIa	0.10	1.20	0.5	60	6	72	-45.0
VAL Ib	0.30	1.20	1.0	60	18	72	6.0
VAL Ib-2	0.30	1.20	1.0	60	18	72	6.0
VAL IIb	0.30	1.50	1.0	60	18	90	12.0
VAL IIb-2	0.30	1.50	1.0	60	18	90	-12.0
VAL IIIb	0.30	1.67	1.0	60	18	100	-22.0
VAL IIIb-2	0.30	1.67	1.0	60	18	100	-22.0
VAL IIIb-3	0.30	1.67	1.0	60	18	100	-22.0

Table 7.4 – Summary of semi-random loading tests

Specimen ID	R	OLR	OL/UL	a_i (mm)	a_f (mm)	a_{yld} (mm)	No. Cycles a_i to a_f	No. Cycles a_i to a_{yld}	No. Cycles a_i to failure
VAL Ia	0.10	1.20	1.0	11.20	36.68	37.50	140700	142000	143040
VAL IIa	0.10	1.50	1.0	11.16	36.11	37.58	174400	176000	177357
VAL IIIa	0.10	1.67	1.0	11.09	37.05	37.35	224100	224300	225444
VAL IIIa-2	0.10	1.67	1.0	11.10	35.65	37.89	221300	223800	224346
VAL IVa	0.10	1.83	1.0	11.36	36.06	37.81	304700	306400	307803
VAL Va	0.10	1.67	2.0	11.10	36.58	38.04	328200	330100	331850
VAL VIa	0.10	1.67	0.5	11.05	36.89	37.73	198000	199000	200116
VAL VIIa	0.10	1.20	2.0	11.07	36.76	38.42	168200	170500	172092
VAL VIIIa	0.10	1.20	0.5	11.25	37.47	38.50	158000	159500	161523
VAL Ib	0.30	1.20	1.0	11.02	37.47	N/A	268500	270500	272564
VAL Ib-2	0.30	1.20	1.0	11.20	35.89	38.07	262300	266500	269169
VAL IIb	0.30	1.50	1.0	11.19	36.27	37.92	302900	305700	307914
VAL IIb-2	0.30	1.50	1.0	11.17	37.62	38.51	347200	348800	350654
VAL IIIb	0.30	1.67	1.0	11.25	36.60	37.68	370800	372400	374571
VAL IIIb-2	0.30	1.67	1.0	11.12	35.61	37.94	436000	440500	442767
VAL IIIb-3	0.30	1.67	1.0	11.06	36.35	38.05	441000	443800	446928

Figure 7.3a and Figure 7.3b illustrate the effect of stress ratio (R) on a typical a-versus-N curve and the corresponding fatigue rate curve, respectively. As expected, the use of a higher stress ratio, which corresponds to a reduced stress range, yields a lower ΔK (and a much smaller da/dN) at any given crack length. The net result is a leftward shift of the corresponding da/dN-versus-ΔK curve and a much longer fatigue life. Figure 7.3b also confirms that, as expected, components subjected to similar loading scenarios exhibit similar fatigue rate curves.

Figure 7.4 illustrates the effects of overload ratio (OLR) on the a-versus-N curve and resulting fatigue rate curve for R = 0.1. A similar trend was observed for R = 0.3, as illustrated below in Figure 7.5. As expected, the higher the OLR (and OL/UL, as will be shown later), the greater the amount of retardation in fatigue crack growth, which is shown in the figures below via an increased number of delay cycles and a reduced minimum crack growth rate following an overload/underload application.

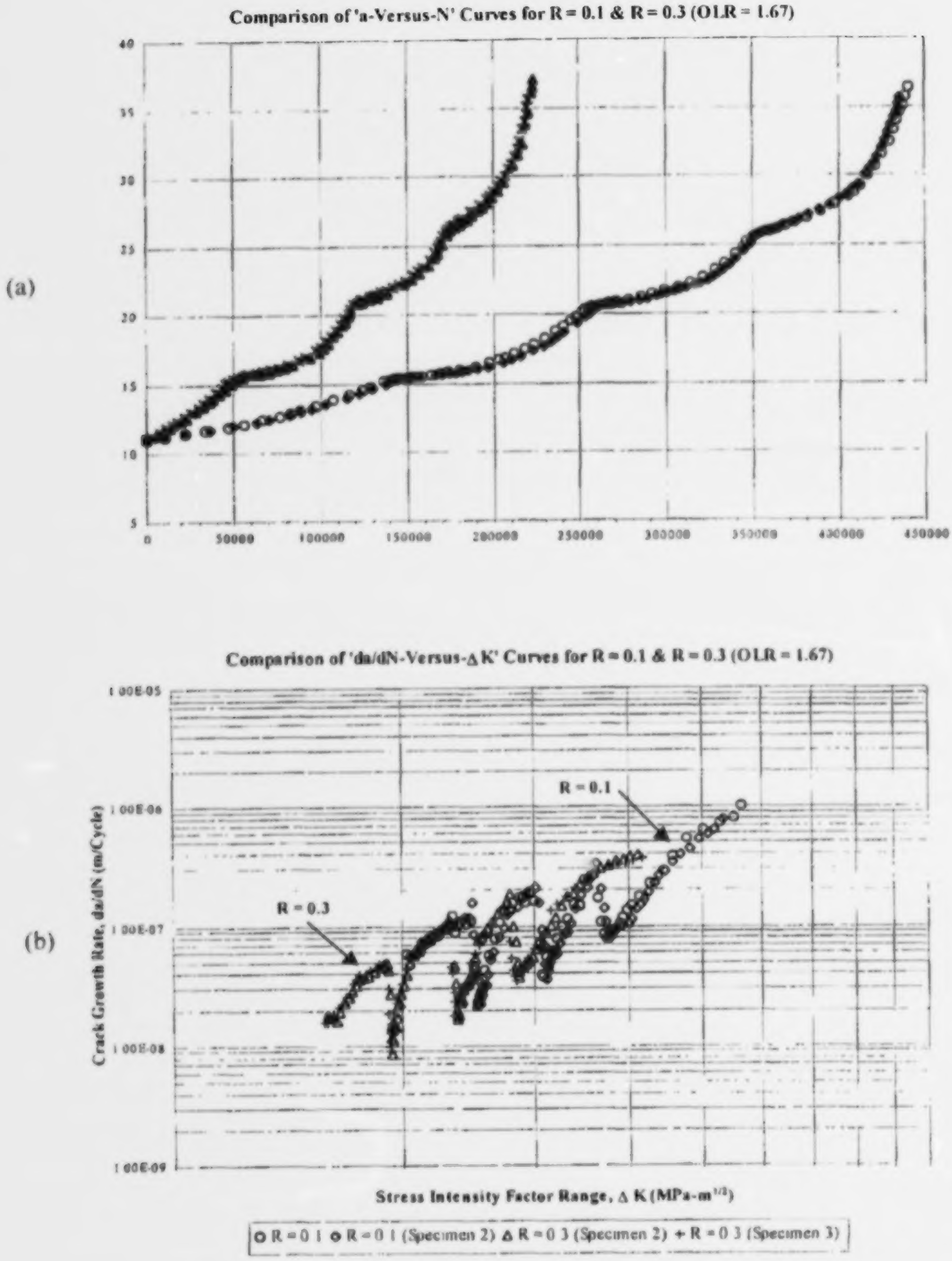

Figure 7.3 – Effect of stress ratio (R) on the (a) a-versus-N, and (b) da/dN-versus-ΔK curves

Recall the experimental investigation by Trask (1998), whose major focus was on crack growth retardation following a tensile overload. Trask compared the crack growth of a tensile overloaded specimen to one which had been subjected to a tensile overload followed by an accidentally applied compressive underload. The comparison illustrated that the minimum crack growth rate reached following an overload could be increased dramatically due to the application of a compressive underload. For the OLR and OL/UL ratio considered by Trask (OLR = 1.675 and OL/UL = 0.496), this reduction in crack growth retardation was near one order of magnitude (i.e., approximately 10 times). The degree of reduction in crack growth retardation can be expected to reduce with increasing OL/UL ratio. For the data presented in the above figures, the OL/UL ratio was held equal to unity.

Trask (1998) found that for the specimens used here, Walker's model could not adequately describe the effects of stress ratio (R) on crack growth, and instead, based on the observation of an 'inflection point' in the experimental data, he proposed a 'two-curve' Paris model for each individual stress ratio. As noticed by Trask (1998), all specimens displayed a pseudo 'inflection point' at a stress intensity factor range (ΔK) of approximately 23 $\mathrm{MPa}\sqrt{\mathrm{m}}$, where the slope of the fatigue rate curve changed considerably. Therefore, the 'two-curve' Paris model proposed by Trask (1998) was first used to characterize the fatigue rate data corresponding to the constant amplitude (CAL) portion of each test. However, as one can see from Figure 7.4b and Figure 7.5b, the fatigue rate curves so obtained appear to have the same slope as the experimental data, but lie slightly above them. In addition, the a-versus-N curves for any overload ratio (at a given R) should be almost indistinguishable prior to the application of an overload. However, the a-versus-N curves predicted using the 'original' Paris parameters suggested by Trask (1998) exhibit similar curvature to those of the experimental data, but lie above them by an appreciable amount. This would indicate that while the value of 'm_P' is correct, the value of 'C_P' might require minor adjustment. Therefore the original 'C_P' values proposed by Trask (1998) were modified slightly for each experiment in order to give a much closer approximation of the experimental data, as shown in Figures 7.4 and 7.5 below.

(a)

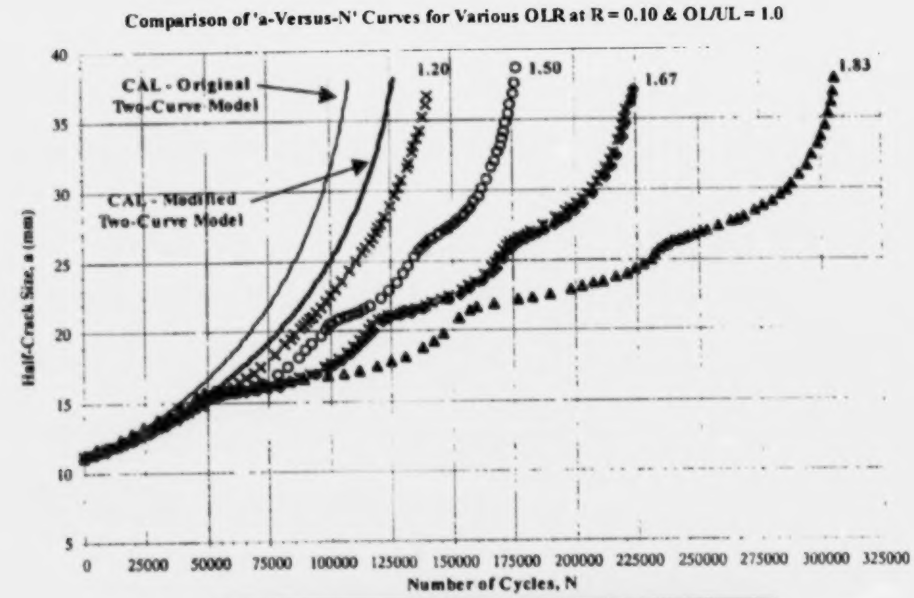

[redacted]

(b)

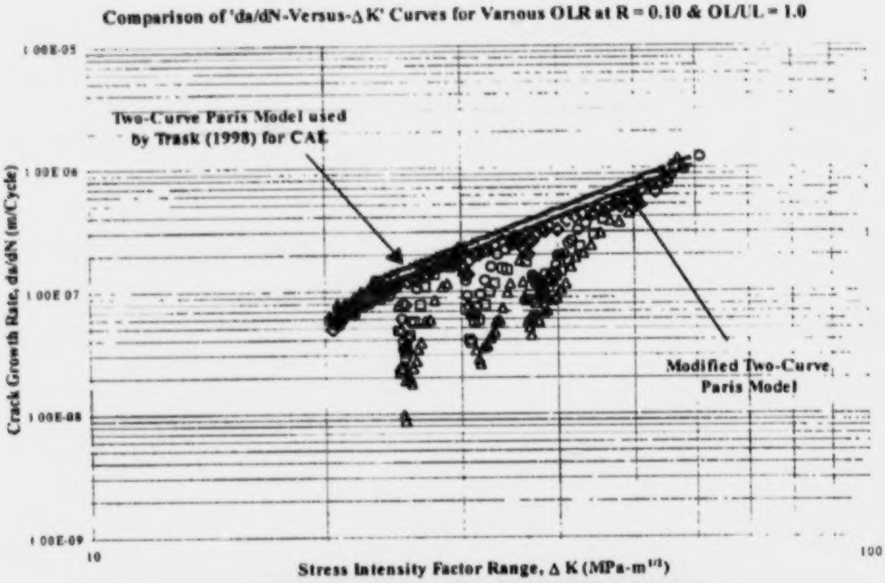

[redacted]

Figure 7.4 – Effects of OLR on the (a) a-versus-N, and (b) da/dN-versus-ΔK curves at R=0.1

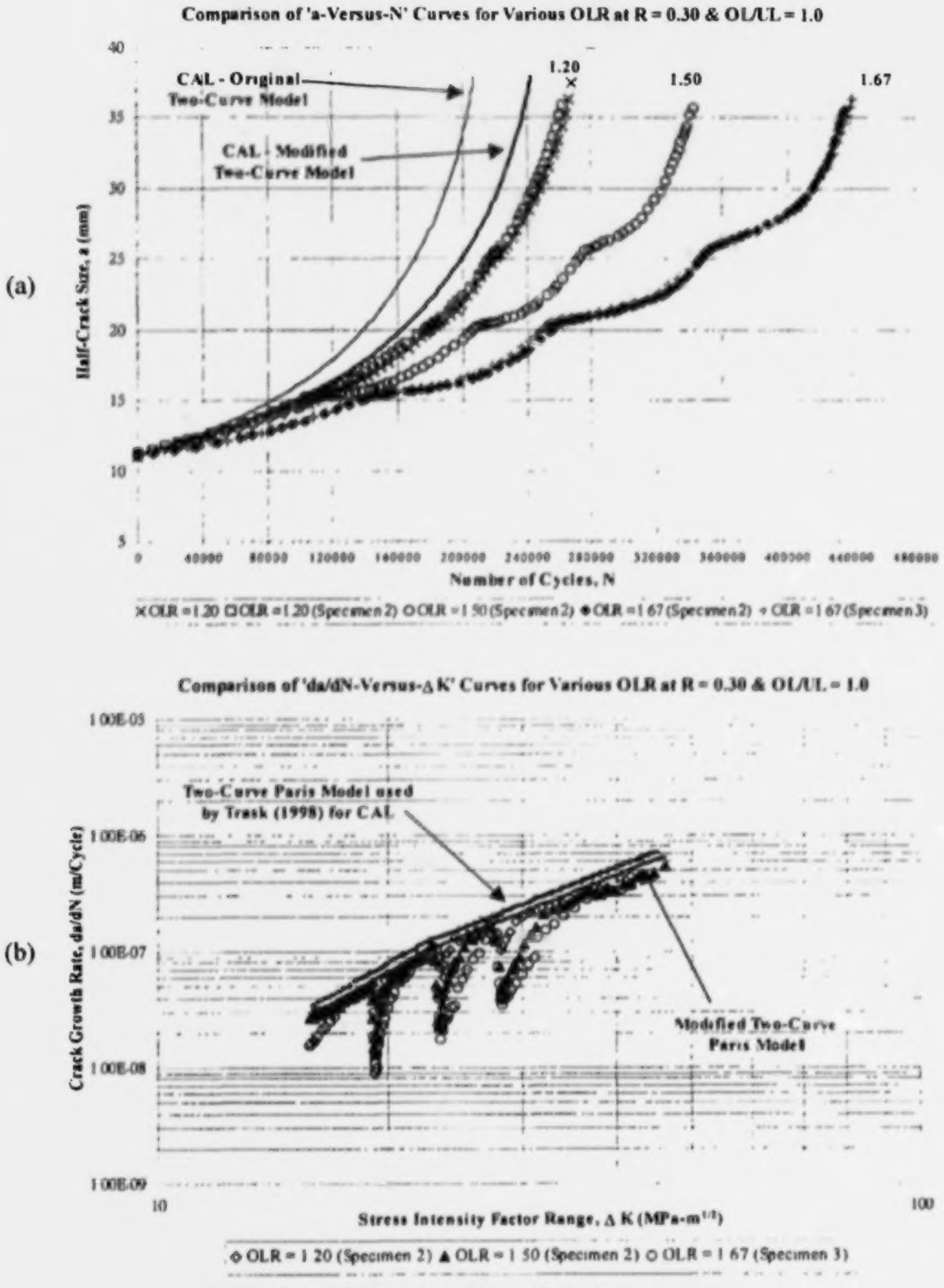

Figure 7.5 – Effects of OLR on the (a) a-versus-N, and (b) da/dN-versus-ΔK curves at R=0.3

P318665.PDF (Page [illegible] of 314)

The original and modified Paris parameters used to describe the 'upper' and 'lower' sections of the two-curve models illustrated in the above figures are given in Table 7.5.

Table 7.5 – Paris parameters for 'two-curve' model proposed by Trask (1998)

Stress Ratio (R)	C_{Lower}	m_{Lower}	C_{Upper}	m_{Upper}
0.10 (Original)	**2.04E-13**	**4.22**	**6.35E-11**	**2.41**
0.10 (Modified)	***1.74E-13***	**4.22**	***5.43E-11***	**2.41**
0.30 (Original)	**1.17E-12**	**3.71**	**3.79E-11**	**2.59**
0.30 (Modified)	***10.00E-13***	**3.71**	***3.24E-11***	**2.59**

Note. ΔK given in $MPa\sqrt{m}$. Corresponding da/dN will be given in m/cycle

It is well accepted that the application of a compressive underload following a tensile overload can significantly reduce the amount of retardation caused by the tensile overload. Furthermore, this reduction in fatigue crack growth retardation can be quantified by varying the ratio of the tensile overload to the compressive underload (OL/UL). Figure 7.6 and Figure 7.7, respectively, illustrate how a typical a-versus-N curve and the corresponding fatigue rate curve are affected by a variable OL/UL ratio. As intuitively expected, the amount of retardation is typically greater for higher OL/UL ratios. This is simply due to the fact that for a higher OL/UL ratio, there is a smaller compressive underload, which is the factor responsible for crack growth acceleration. At some OL/UL ratio, say between 2 and 3, it can be expected that crack growth retardation is relatively unaffected due to the presence of a very small compressive underload. The notion of a compressive plastic zone is somewhat questionable in much of the literature, as it is generally thought that upon closure of a propagating crack, the applied stress is distributed uniformly across the crack faces (as if there were no crack) and no additional crack growth occurs until the crack re-opens once again. However, as illustrated in Figure 7.6 below, it is interesting to note that at a given OLR, variations in the magnitude of the applied compressive underload (i.e., the OL/UL ratio) have a significant effect on the degree of crack growth retardation caused by the preceding tensile overloads. This observation appears to validate the existence of some type of 'compressive plastic zone', and will be discussed later in the report.

The original and modified Paris parameters used to describe the 'upper' and 'lower' sections of the two-curve models illustrated in the above figures are given in Table 7.5.

Table 7.5 – Paris parameters for 'two-curve' model proposed by Trask (1998)

Stress Ratio (R)	C_{Lower}	m_{Lower}	C_{Upper}	m_{Upper}
0.10 (Original)	**2.04E-13**	**4.22**	**6.35E-11**	**2.41**
0.10 (Modified)	***1.74E-13***	**4.22**	***5.43E-11***	**2.41**
0.30 (Original)	**1.17E-12**	**3.71**	**3.79E-11**	**2.59**
0.30 (Modified)	***10.00E-13***	**3.71**	***3.24E-11***	**2.59**

Note. ΔK given in $MPa\sqrt{m}$. Corresponding da/dN will be given in m/cycle

It is well accepted that the application of a compressive underload following a tensile overload can significantly reduce the amount of retardation caused by the tensile overload. Furthermore, this reduction in fatigue crack growth retardation can be quantified by varying the ratio of the tensile overload to the compressive underload (OL/UL). Figure 7.6 and Figure 7.7, respectively, illustrate how a typical a-versus-N curve and the corresponding fatigue rate curve are affected by a variable OL/UL ratio. As intuitively expected, the amount of retardation is typically greater for higher OL/UL ratios. This is simply due to the fact that for a higher OL/UL ratio, there is a smaller compressive underload, which is the factor responsible for crack growth acceleration. At some OL/UL ratio, say between 2 and 3, it can be expected that crack growth retardation is relatively unaffected due to the presence of a very small compressive underload. The notion of a compressive plastic zone is somewhat questionable in much of the literature, as it is generally thought that upon closure of a propagating crack, the applied stress is distributed uniformly across the crack faces (as if there were no crack) and no additional crack growth occurs until the crack re-opens once again. However, as illustrated in Figure 7.6 below, it is interesting to note that at a given OLR, variations in the magnitude of the applied compressive underload (i.e., the OL/UL ratio) have a significant effect on the degree of crack growth retardation caused by the preceding tensile overloads. This observation appears to validate the existence of some type of 'compressive plastic zone', and will be discussed later in the report.

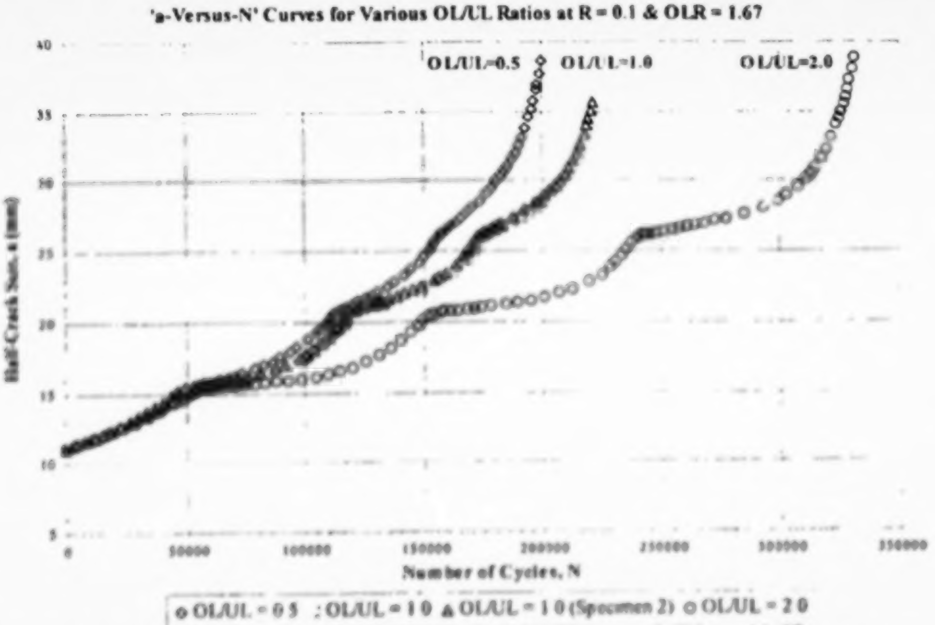

Figure 7.6 – Effect of varying the OL/UL ratio on the a-versus-N curve

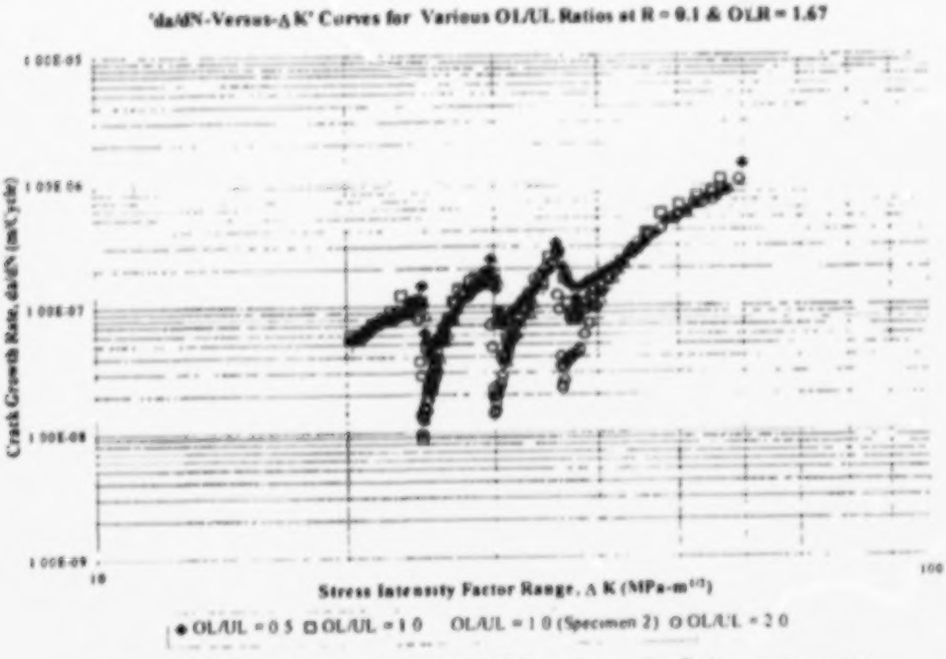

Figure 7.7 – Effect of varying the OL/UL ratio on the fatigue rate curve

The beneficial effects on fatigue life corresponding to increases in both the overload ratio (OLR) and the overload-to-underload (OL/UL) ratio are summarized in Figure 7.8 for R = 0.1. Considering a variation in overload ratio (OLR) only, Figure 7.9 illustrates a similar trend, as expected, for an OL/UL = 1.0 at R = 0.3. Due to the fact that the 'final' crack length (a_f) varied considerably from test to test (Table 7.4), the less variable 'yield' crack length (a_{yld}) was used to provide the fatigue life comparisons made in Figure 7.8 and Figure 7.9.

As previously mentioned, failure of a cracked component may occur by either yielding (collapse) of the remaining uncracked area, or by fracture, whichever condition is satisfied first. The fracture toughness of the specimens used in this investigation was large; therefore failure by yielding was anticipated and, in fact, found to be the prevailing failure mode. The axial stress in a specimen with a central crack of length '2a' is given by

$$\sigma_{axial} = \frac{P}{A} = \frac{P_{max}}{(W-2a)\cdot t} \qquad (7.5)$$

where 'W' and 't' represent the specimen width and thickness, respectively. By substituting σ_{yld} for σ_{axial} in Equation 7.5, one can derive the expression for the crack length at which the remaining uncracked area can be expected to yield.

$$a_{yld} = \frac{1}{2}\left[W - \left(\frac{P_{max}}{\sigma_{yld} t}\right)\right] \qquad (7.6)$$

Using values of P_{max} = 60 kN, W_{avg} = 101.1 mm, and t_{avg} = 5.02 mm (Table 7.2), along with the corresponding 'theoretical' static tensile yield strength for the 350WT steel used in this investigation (i.e., 450 MPa), Equation 7.6 predicts a half-crack length of 37.27 mm at yielding. From Table 7.4, the average half-crack length at yielding is 37.93 mm, representing less than 2 % error. However, using Equation 7.5 to back-calculate an 'experimental' yield stress ($\sigma_{yld,exp}$), one obtains a value of 474 MPa (representing approximately 5.33 % error), which is very close to the value of 480 MPa previously obtained by Trask (1998). This observation confirms the potential of material strain hardening due to cyclic loading.

The constant amplitude loading (CAL) fatigue life predictions for each stress ratio were made by numerically integrating the appropriate two-curve Paris model between the average 'initial' crack length (a_i) and average 'yield' crack length (a_{yld}) for a specimen of average thickness (t) and width (W). A simple Excel spreadsheet was used to perform the numerical integration. In order to obtain as accurate a prediction as possible, crack growth increments of one percent of the current crack length were selected. A sample calculation illustrating the numerical integration technique is described thoroughly in both Barsom et al (1987) and Broek (1989). It should be noted that some small percent error is inherent in these CAL predictions due to the fact that the fatigue life comparisons were based on average values of a_i, a_{yld}, t, and W for all the specimens, as opposed to the observed values for each individual specimen. The selection of a_i has a much more pronounced effect on the predicted life than does the selection of a_{yld}. This is due to the fact that very little life remains between a_{yld} and total failure. Similarly, variation in specimen thickness has a more pronounced effect than an equivalent variation in specimen width, for the obvious reason that the increase in cross-sectional area is greater for the former. Nevertheless, for illustrative purposes, the use of average values was considered adequate.

Predictions corresponding to the application of a tensile overload only (denoted 'OL Only' in Figure 7.8 and Figure 7.9) were made using a numerically integrated modified two-curve Paris model, as previously discussed, in conjunction with the delay models proposed by Trask (1998) and Kumar et al (1996). The delay model proposed by Rosenberg (1999) was not investigated.

The delay model proposed by Trask (1998) was briefly mentioned in Chapter 4. It was developed to predict the crack growth retardation caused by intermittent tensile overloads. The model was calibrated using data for R = 0.1 and assumes that each tensile overload produces the same number of delay cycles (N_D), given by Equation 7.7.

$$N_D = 10^{1.8115(OLR)+1.6497} \tag{7.7}$$

In order to facilitate such delay predictions, it was necessary to first convert the overload ratio (OLR), as defined in the present investigation, to an equivalent overload ratio (OLR_{EQ}) expressed in terms of the definition employed by Trask (1998). In the present study, the overload ratio is simply defined as

$$OLR = \frac{P_{max,OL}}{P_{max,CAL}} \tag{7.8}$$

However, Trask (1998) used an overload ratio (OLR_{EQ}) defined by

$$OLR_{EQ} = \frac{\Delta P_{OL}}{\Delta P_{CAL}} = \frac{P_{max,OL} - P_{min,CAL}}{P_{max,CAL} - P_{min,CAL}} \tag{7.9}$$

Using Equation 7.9, each overload ratio was converted into the corresponding OLR_{EQ}. The converted overload ratios are presented in Table 7.6.

Table 7.6 – Conversion of OLR into equivalent OLR_{EQ} used by Trask (1998)

OLR	R	$P_{max,CAL}$ (kN)	$P_{min,CAL}$ (kN)	$P_{max,OL}$ (kN)	ΔP_{OL} (kN)	ΔP_{CAL} (kN)	OLR_{EQ}
1.20	0.10	60	6	72	66	54	1.22
1.50	0.10	60	6	90	84	54	1.56
1.67	0.10	60	6	100	94	54	1.74
1.83	0.10	60	6	110	104	54	1.93
1.20	0.30	60	18	72	54	42	1.29
1.50	0.30	60	18	90	72	42	1.71
1.67	0.30	60	18	100	82	42	1.95

The delay model proposed by Kumar et al (1996), previously mentioned in Chapter 4, was also developed to predict the extent to which fatigue crack growth is retarded by periodic tensile overloads. The model was calibrated with fatigue crack growth data corresponding to R = 0, and incorporates an overload ratio defined in the same fashion as the current study; that is, $OLR = \frac{P_{max,OL}}{P_{max,CAL}}$. Similar to the model proposed by Trask (1998), In order to facilitate such delay predictions, it was necessary to first convert the overload ratio (OLR), as defined in the present investigation, to an equivalent overload ratio (OLR_{EQ}) expressed in terms of the definition employed by Trask (1998). In the present study, the overload ratio is simply defined as

$$OLR = \frac{P_{max,OL}}{P_{max,CAL}} \tag{7.8}$$

However, Trask (1998) used an overload ratio (OLR_{EQ}) defined by

$$OLR_{EQ} = \frac{\Delta P_{OL}}{\Delta P_{CAL}} = \frac{P_{max,OL} - P_{min,CAL}}{P_{max,CAL} - P_{min,CAL}} \tag{7.9}$$

Using Equation 7.9, each overload ratio was converted into the corresponding OLR_{EQ}. The converted overload ratios are presented in Table 7.6.

Table 7.6 – Conversion of OLR into equivalent OLR_{EQ} used by Trask (1998)

OLR	R	$P_{max,CAL}$ (kN)	$P_{min,CAL}$ (kN)	$P_{max,OL}$ (kN)	ΔP_{OL} (kN)	ΔP_{CAL} (kN)	OLR_{EQ}
1.20	0.10	60	6	72	66	54	1.22
1.50	0.10	60	6	90	84	54	1.56
1.67	0.10	60	6	100	94	54	1.74
1.83	0.10	60	6	110	104	54	1.93
1.20	0.30	60	18	72	54	42	1.29
1.50	0.30	60	18	90	72	42	1.71
1.67	0.30	60	18	100	82	42	1.95

The delay model proposed by Kumar et al (1996), previously mentioned in Chapter 4, was also developed to predict the extent to which fatigue crack growth is retarded by periodic tensile overloads. The model was calibrated with fatigue crack growth data corresponding to R = 0, and incorporates an overload ratio defined in the same fashion as the current study; that is, $OLR = \frac{P_{max,OL}}{P_{max,CAL}}$. Similar to the model proposed by Trask (1998), it is assumed that each overload produces the same number of delay cycles (N_D), given by Equation 7.10.

$$N_D = 2149.34\,(OLR)^{6.84} \tag{7.10}$$

It was anticipated that incorporating a delay model based on tensile overloads only (which can be thought of as very large OL/UL ratios) would predict longer fatigue lives than observed for an OL/UL = 2.0. However, the success of both models in predicting this expected trend was only marginal. The greatest inaccuracy was observed for an overload ratio of 1.20. It was found that both of these delay models provided similar results for R = 0.1, however, at R = 0.3, the model proposed by Kumar et al (1996) severely underpredicted the anticipated N_D.

The numbers shown in brackets in Figure 7.8 and Figure 7.9 represent the ratio of the actual fatigue life for each semi-random test to that for an 'average' specimen tested under constant amplitude loading (i e., N_{VAL}/N_{CAL}). At each overload ratio investigated, the ratio N_{VAL}/N_{CAL} is almost identical for both R = 0.1 and R = 0.3 at an OL/UL =1.0 It was anticipated that this ratio would be smaller for specimens tested at OL/UL = 0.5 than for those tested at OL/UL = 1.0. Therefore, the data for specimens VAL Ia, VAL VIIa, and VAL VIIIa, corresponding to an OLR = 1 20 at R = 0.1, were investigated further The corresponding fatigue rate curves appear to be very similar, as illustrated in Figure 7.10. However, a closer examination of the corresponding a-versus-N curves reveals subtle differences, as illustrated in Figure 7.11. For comparison, the a-versus-N curve for OLR = 1.50 and OL/UL = 1.0 has been included. Prior to the application of the first overload, one can see that the two a-versus-N curves for OL/UL = 1.0 (OLR = 1 20 and 1.50) are almost indistinguishable. However, these two curves lie slightly above those corresponding to OL/UL = 0.5 and OL/UL = 2.0, which is thought to be somewhat questionable. Furthermore, the a-versus-N curves for OLR = 1.20 (OL/UL = 0.5) and OLR = 1.50 (OL/UL = 1.0) appear to coincide near the second overload, which is also intuitively incorrect.

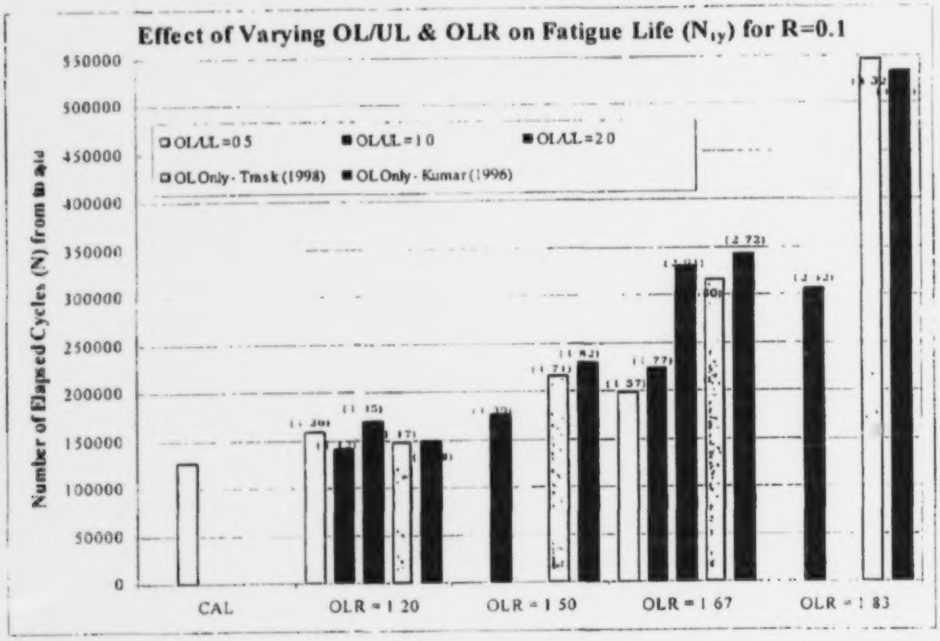

Figure 7.8 – Effect of varying the OLR and OL/UL on fatigue life (R = 0.1)

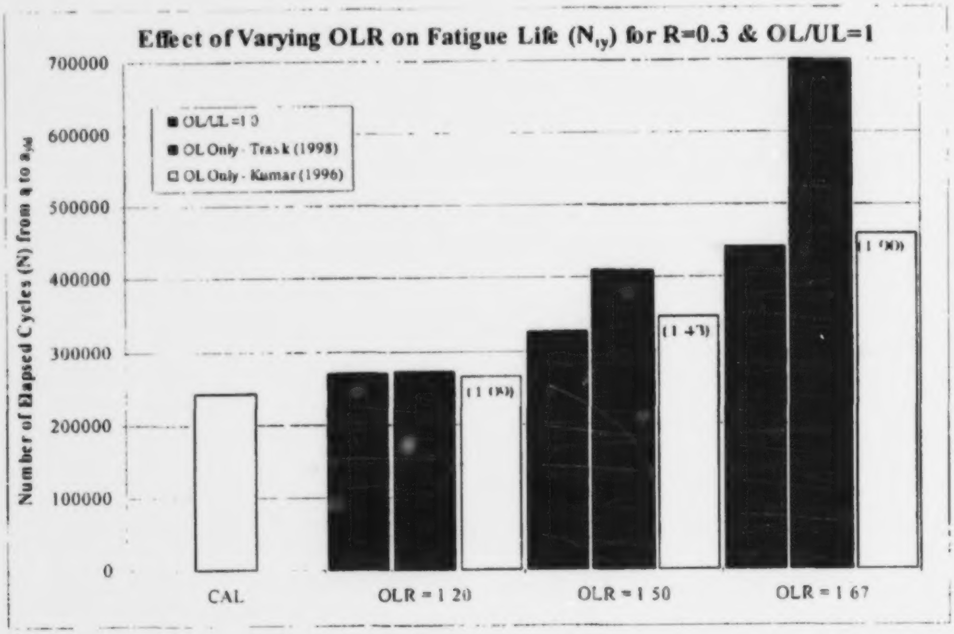

Figure 7.9 – Effect of varying OLR on fatigue life (R = 0.3 and OL/UL = 1.0)

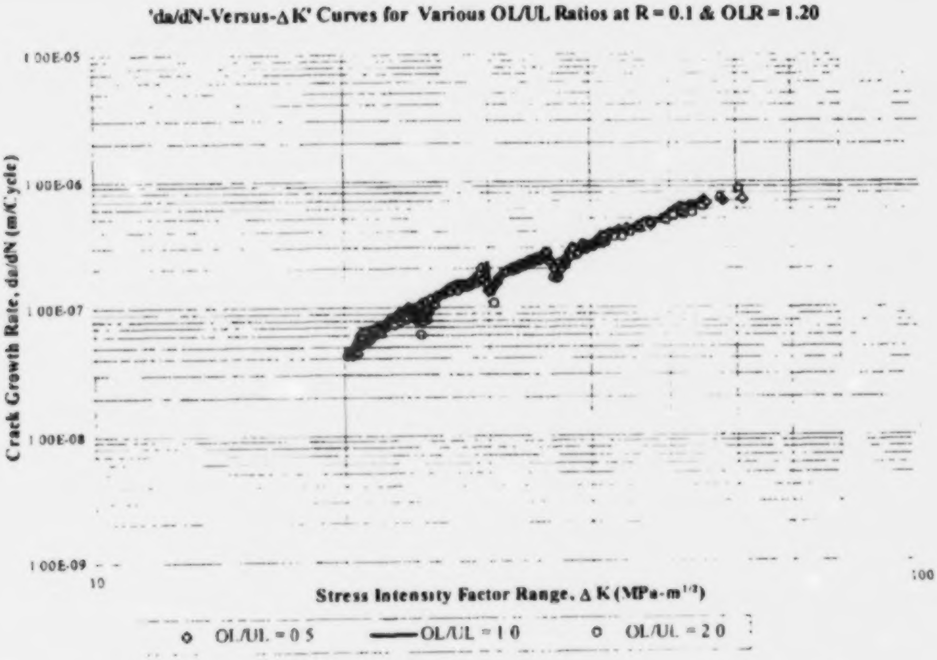

Figure 7.10 – Variation in fatigue rate curves for OLR = 1.20 (R = 0.1)

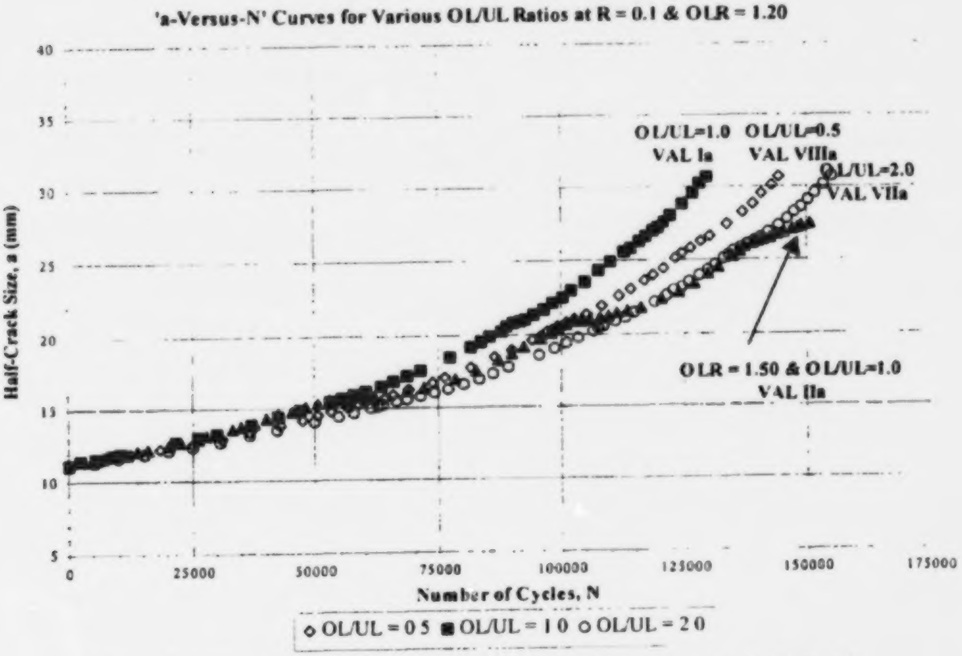

Figure 7.11 – Variation in a-versus-N curves for OLR = 1.20 (R = 0.1)

For example, one can see from Table 7.3 that specimen VAL IIa (R = 0.1, OLR = 1.50, and OL/UL = 1.0) was subjected to both a larger tensile overload and a smaller compressive underload than was specimen VAL VIIIa (R = 0.1, OLR = 1.20, and OL/UL = 0.5). One would therefore expect much more significant crack growth retardation in the former (i.e., specimen VAL IIa). Prior to the application of any overloads, the differences in the a-versus-N curves for all specimens can be attributed to minor variations in the proper values of C_P required to accurately describe the crack growth. It can thus be argued that aside from the error induced due to the initial 'offset' of the a-versus-N curve for specimen VAL VIIa (R = 0.1, OLR = 1.20, OL/UL = 2.0), the data for this specimen are acceptable. Therefore, it was decided that the data for specimen VAL VIIIa (R = 0.1, OLR = 1.20, OL/UL = 0.5) was the most controversial and will be used with some caution for the remainder of this report. It is conceivable that the error could be the result of a number of factors, including incorrect measurements, slight variations in the applied overloads and underloads. Perhaps the presence of significant residual stresses in the specimen arising from inconsistent surface machining (i.e., removal of more material from one surface of the specimen than the other) may have been the cause of some discrepancy.

To better understand how the results of the current analysis might compare with those for load sequences comprised of tensile overloads only, recall the experimental investigation by Trask (1998), whose major focus was on crack growth retardation following a tensile overload. Trask compared a specimen that had been subjected to a tensile overload only (VAL6: R=0.1, $P_{max,CAL}$=57kN, OLR=1.675) to one which had been subjected to a tensile overload followed by compressive underload (VAL5: R=0.1, $P_{max,CAL}$=57kN, OLR=1.675, OL/UL=0.496). The corresponding CAL growth rate was approximately $35\text{x}10^{-8}$ m/cycle. The crack growth rate for the specimen subjected to a tensile overload only reached a minimum of approximately $1.9\text{x}10^{-8}$ m/cycle, whereas the minimum growth rate for the specimen subjected the same OLR in conjunction with an OL/UL = 0.496 was much higher, approximately $15\text{x}10^{-8}$ m/cycle. In this case, the reduction in crack growth retardation due to the compressive underload was very close to one order of magnitude (i.e., nearly 10 times). Figure 7.12 expresses the variation in minimum crack growth rate (i.e., $(da/dN)_{min,VAL}$) following an overload application as a function of OLR and OL/UL for R=0.10. Note the minimum crack growth rates have been normalized with respect to the constant amplitude crack growth rates (i.e., $(da/dN)_{CAL}$) corresponding to the same stress intensity factor range.

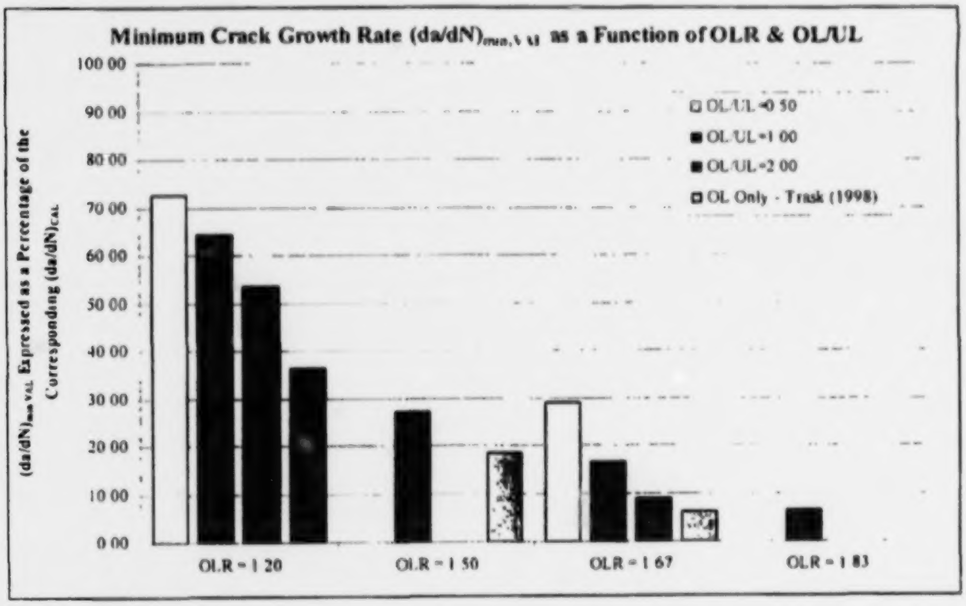

Figure 7.12 – Effect of OLR & OL/UL on (normalized) minimum crack growth rate

Although not presented here, the values corresponding to R=0.30 are almost identical. It should also be noted that the comparison illustrated in Figure 7.12 is based only upon the first overload application (at a crack length of a = 15mm). However, from the fatigue rate curves of Appendix B, one can see that for all R, OLR, and OL/UL investigated in the current study, the ratio $\left(\frac{da}{dN}\right)_{min,VAL} \Big/ \left(\frac{da}{dN}\right)_{CAL}$ remained relatively constant for all three overload applications. This is further evidenced by the fact that for each specimen, a line drawn through the points of minimum crack growth rate lies approximately parallel to that representing the constant amplitude Paris approximation. The re-establishment of 'steady state' crack growth between overload applications is an important requirement for the validity of this observation to hold.

7.5 Data Analysis

This section will analyze the significance of the results reported in the previous two sections. The effect of the threshold stress intensity factor (K_{th}) on predictions made using the Zheng and Hirt model for constant amplitude loading will be examined briefly. However, the majority of this section will focus on the investigation into crack growth behavior of specimens subjected to tensile overloads followed immediately by compressive underloads. This section of the report will also discuss the effect of varying the ratio of the applied tensile overload to the applied compressive underload (i.e., the OL/UL ratio) on the ensuing crack growth.

Some modifications to the well known and commonly used Wheeler model (for variable amplitude loading) have been proposed to facilitate the handling of not only tensile overloads, but also tensile overloads followed by compressive underloads, and single compressive underloads. In addition, an exponential delay model (similar to that proposed by Trask (1998)) has been proposed to consider the combined effects of stress ratio (R), overload ratio (OLR), and overload-to-underload ratio (OL/UL) on the number of delay cycles (N_D) produced.

A number of the variable amplitude loading models discussed in Chapter 4 were considered, but will not be included here due to the numerous parameters required for their calibration. For example, although a fatigue crack growth model such as Johnson's Multi-Parameter Yield Zone model may appear 'all-encompassing', the time and computational effort required to use such a model is believed to offset any advantages it may offer. The commonly used Willenborg model was also considered, but owing to the difficulties and inconsistencies encountered by Trask (1998) in using this model, it was decided that the model would provide somewhat unreliable fatigue life predictions for the current investigation. Finally, due to the nature of the load history investigated in the current study, neither of the root mean square models proposed by Barsom et al (1987) and Hudson (1981) was considered. As previously discussed, these models are best suited to more random load histories comprised of frequently applied overloads and underloads, as opposed to those consisting of intermittent tensile and compressive overloads, as was the case for the current investigation.

7.5.1 Constant Amplitude Predictions Using the Zheng and Hirt Model

One of the recommendations made by Trask (1998) involved the evaluation of an accurate threshold stress intensity factor (K_{th}) for use in the Zheng and Hirt model discussed in Chapter 4. Recall that the major advantage of this model lies in the fact that it requires no empirical parameters, but instead can be calibrated based on a number of material properties. In addition to having some physical significance, the parameters used in this model can be easily determined from a simple tensile test. Trask (1998) found that this model was capable of predicting the fatigue life of specimens subjected to constant amplitude loading (CAL) with incredible accuracy. However, by the same token, Trask (1998) also demonstrated that the accuracy of the Zheng and Hirt predictions were very sensitive to the selected value of K_{th}. In fact, modest variations in the threshold stress intensity were shown to yield significant errors in the fatigue life predictions. Trask (1998) based his results on a threshold value obtained from experimental data extrapolated to a crack growth rate of 1×10^{-8} m/cycle. For the current investigation, all threshold testing was using the decreasing-K test suggested in ASTM E647, which denotes an operational value of K_{th} as the value of ΔK corresponding to a growth rate of 1×10^{-10} m/cycle.

Recall from section 7.3 that the average threshold stress intensity factor for R = 0 was calculated as 5.56 $\text{MPa}\sqrt{\text{m}}$. This compares quite well with the value of 6.00 $\text{MPa}\sqrt{\text{m}}$ suggested by Barsom et al (1987) for a stress ratio of zero. Using Equation 4.2b (also suggested by Barsom et al (1987)), one can estimate the value of K_{th} for R = 0.1 to be approximately 6.41 $\text{MPa}\sqrt{\text{m}}$. The Zheng predictions may now be compared with those obtained using the two-curve Paris model suggested by Trask (1998) in conjunction with the Paris coefficients corresponding to a stress ratio R = 0.1. Figure 7.13 illustrates the difference between the Zheng predictions (using all three of the aforementioned K_{th} values) and that made using Trask's two-curve Paris model. Although there appears to be little difference between the three Zheng predictions (all using relatively similar K_{th} values), one can see that there is considerable error between the Zheng predictions and that made using the two-curve Paris model. In fact, the value of K_{th} required to reduce this error to an acceptable level is approximately 11 MPa$\sqrt{m}$, almost twice the value obtained using Equation 4.2b (suggested by Barsom et al (1987)). Figure 7.14 further illustrates how the predicted a-versus-N curves compare to one another.

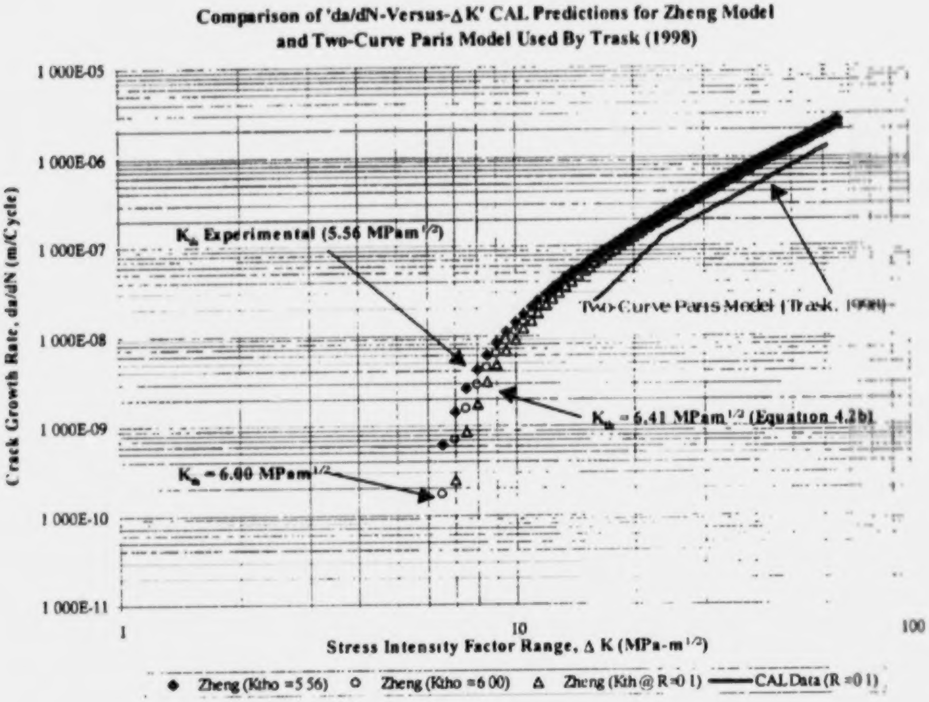

Figure 7.13 – da/dN-versus-ΔK curve predictions using Zheng & Hirt model in conjunction with the two-curve Paris model

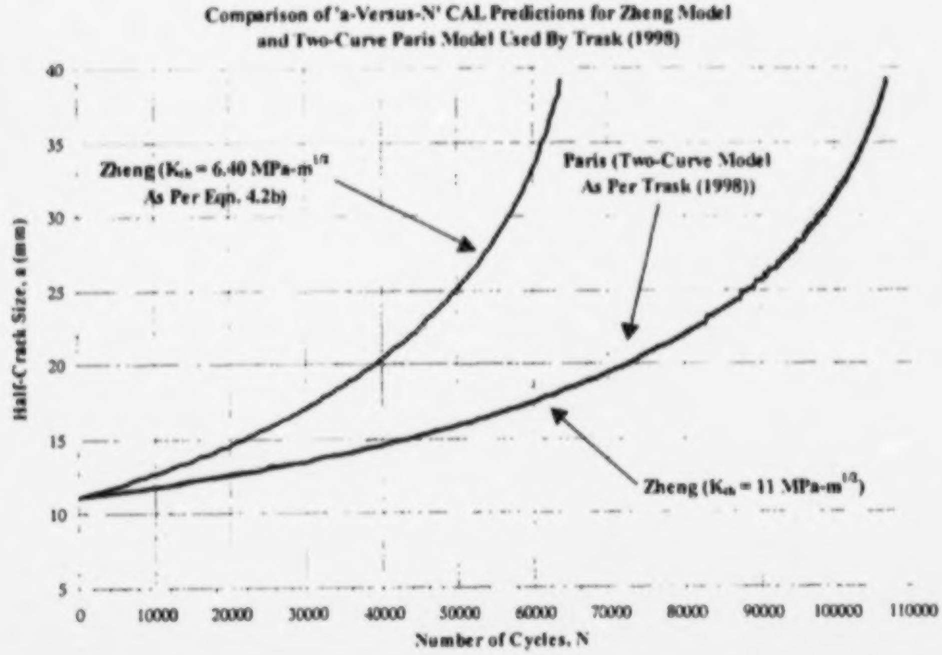

Figure 7.14 – Comparison of a-versus-N predictions: Zheng versus two-curve Paris

Based on the experimentally determined threshold value (5.56 MPa$\sqrt{\text{m}}$), and the results of Figures 7.13 and 7.14, one could deduce that the value of the stress intensity factor threshold used in the Zheng model should be modified in some fashion. Otherwise, the Zheng model appears to be inadequate in predicting the crack growth behavior of the specimens investigated here. Since the values of K_{th} used by Trask (1998) produced excellent results, it would make sense that the value of K_{th} should be redefined as 'K_{th}*'. This redefined 'K_{th}*' could then either be extrapolated from the CAL fatigue rate data at some crack growth rate (as done by Trask (1998)), or specified as some multiple of the threshold stress intensity factor for R = 0, such as $K_{th}^* = \chi\, K_{th0}$. In this case the value of χ required to accurately characterize the crack growth behavior was approximately 1.98 (based on K_{th} for R = 0). Equation 4.24 could then be revised as follows:

$$\frac{da}{dN} = \frac{(\Delta K - \Delta K_{th}{*})^2}{2\pi E\sigma_{ult}(1+RA)(-\ln(1-RA))} = \frac{(\Delta K - \chi \cdot \Delta K_{th})^2}{2\pi E\sigma_{ult}(1+RA)(-\ln(1-RA))} \qquad [7.11]$$

The reliability of this revision to the Zheng and Hirt model could be assessed using two identical specimens similar to those tested in the current investigation, perhaps made of a weaker, less expensive material such as aluminum. The first specimen would be subjected to a constant amplitude loading history, from which an 'extrapolated' threshold stress intensity factor can be determined. The second specimen would be subjected to the K-decreasing test of ASTM E647 in order to determine an 'actual' stress intensity factor threshold for $R = 0$. The value of χ required to accurately describe the experimental fatigue crack growth data of the first specimen (as per Equation 7.11) can then be determined. Finally, comparison of the crack growth predictions obtained using the extrapolated value of K_{th}^* and also $K_{th}^* = \chi K_{th}$ will dictate whether or not the use of Equation 7.11 is acceptable.

7.5.2 Variable Amplitude Predictions Using the Wheeler Model

In 1972, O.E. Wheeler proposed an empirical crack growth model for variable amplitude loading in order to account for the retardation in fatigue crack growth following a tensile overload. The model introduces a retardation parameter, ϕ_R, which may be applied to any fatigue crack growth model for constant amplitude loading such that the corresponding crack growth rate may be described by $da/dN = \phi_R \cdot f(\Delta K, R)$. For example, using Paris' law in conjunction with Wheeler's retardation parameter yields a fatigue crack growth rate described by Equation 7.12.

$$\left(\frac{da}{dN}\right)_{retarded} = \phi_R\left[C_P(\Delta K)^{m_P}\right] \tag{7.12}$$

Wheeler's retardation parameter, ϕ_R (previously described by Equation 4.43, Figure 4.15 and Figure 4.16) is essentially a function of the ratio of the current plastic zone size to the plastic zone created by a previous overload. It is based on the premise that if the boundary of the current plastic zone lies within the boundary of that induced by a previously applied tensile overload, crack growth retardation will ensue. Recall from

Equation 4.43 (below) that the Wheeler 'shaping exponent', bears little physical significance, its value determined simply as that which provides the best fit to the experimental data.

$$\phi_R = \begin{cases} \left[\dfrac{r_{pi}}{(a_{OL} + r_{p,OL} - a_i)}\right]^m & , a_i + r_{pi} \le a_{OL} + r_{p,OL} \\ 1 & , a_i + r_{pi} \ge a_{OL} + r_{p,OL} \end{cases} \tag{4.43}$$

Where a_i = the current crack length corresponding to the i^{th} cycle

r_{pi} = the current plastic zone size corresponding to the i^{th} cycle

a_{OL} = the crack length at which the overload was applied

$r_{p,OL}$ = the plastic zone created by the tensile overload

m = an empirically adjustable parameter referred to as the shaping exponent

Although any suitable equation may be used to obtain the plastic zone sizes, Irwin's estimates are often used. Moreover, some researchers have reported plastic zone sizes in terms of Irwin's estimate for plastic zone radius; however, Irwin's estimate for plastic zone diameter is typically the preferred form. The plastic zone diameter, which was employed for the current investigation, may be calculated using the following relationship

$$r_{pi} = \frac{1}{\alpha\pi}\left(\frac{K_{max,i} \text{ or } K_{max,OL}}{\sigma_{yld}}\right)^2 \tag{7.13}$$

in which $\alpha = 1$ for plane stress and $\alpha = 3$ for plane strain conditions.

For the current investigation (recall specimen $t_{avg} \sim 5$mm), plane stress conditions were expected to prevail and thus $\alpha = 1$ was used. For completeness, a simple finite element model of a typical specimen's configuration and loading was generated using the NISA (Numerically Integrated Structural Analysis) finite element package, and the resulting plastic zone was used to back-calculate the corresponding value of α and justify the use of $\alpha = 1$ throughout the analysis.

For each specimen, life predictions were obtained by combining the Wheeler retardation parameter with a two-curve Paris model similar to that suggested by Trask (1998). It was anticipated that the initial portion of each a-versus-N curve (i.e., prior to the application of any tensile overloads) would remain almost identical from one specimen to another; however, there was in fact considerable variation. Since the initial curvature (i.e., m_P) of each was similar, it was decided that the parameter C_P used in the modified two-curve Paris model of Table 7.5 should be modified accordingly for each specimen in order to provide the best fit to the experimental data. A typical a-versus-N curve comparing the experimental crack growth data for specimen VAL IIIb and the corresponding Wheeler prediction is illustrated by Figure 7.15.

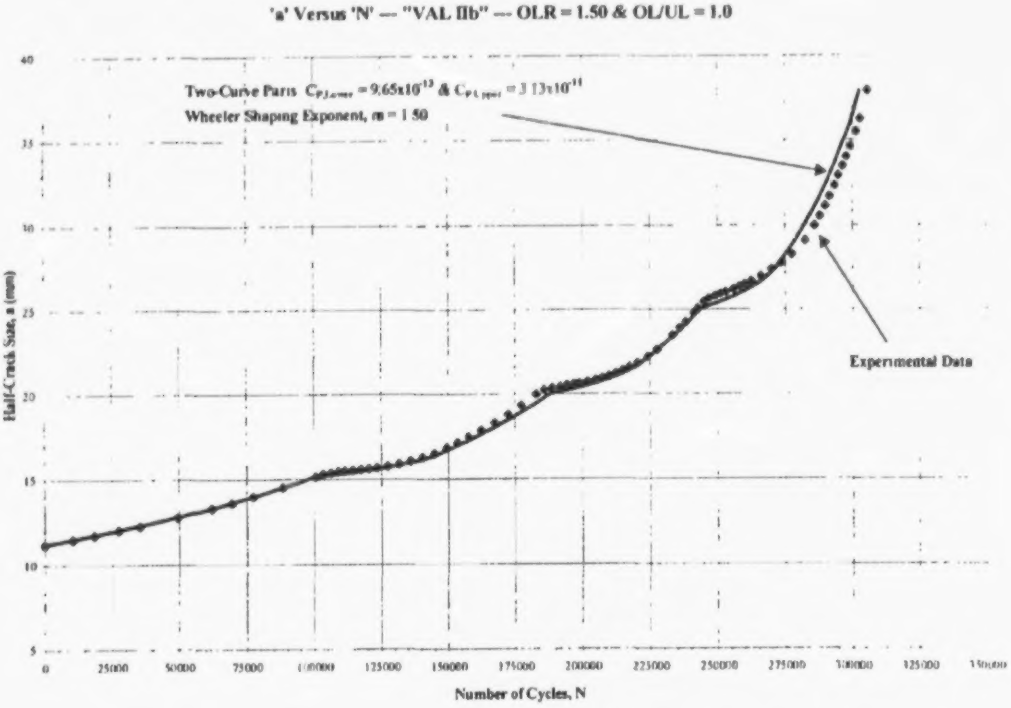

Figure 7.15 – Typical a-versus-N prediction obtained using the Wheeler model

Although the Wheeler prediction is quite accurate for this specimen, it would seem that the best results, in terms of both predicted curvature of the a-versus-N curve and predicted fatigue life, could be obtained through the use of a slightly different shaping exponent at each overload. However, for obvious reasons, this is not a practical or justifiable solution. The Wheeler crack growth predictions (i.e., a-versus-N curves) for all specimens, along with the corresponding Paris parameters used in each case, are included in Appendix C of this report. The Wheeler predictions for both crack length intervals a_i to a_f and a_i to a_{yld} are summarized in Table 7.7 (note the average error represents the average of the errors for N_{if} and N_{yld}).

Table 7.7 – Summary of Wheeler model fatigue life predictions

Specimen ID	Stress Ratio	OLR	OL/UL	Shaping Exponent	Interval a_i to a_f		Interval a_i to a_{yld}		Avg. % Error
					N_{Expt}	N_{Pred}	N_{Expt}	N_{Pred}	
VAL 8a	0.1	1.20	0.50	2.25	158,000	**158,316**	159,500	**159,587**	-0.13
VAL 1a	0.1	1.20	1.00	2.70	140,700	**141,032**	142,000	**141,991**	-0.11
VAL 7a	0.1	1.20	2.00	2.70	168,200	**168,343**	170,500	**170,505**	0.00
VAL 2a	0.1	1.50	1.00	1.92	174,400	**174,591**	176,000	**176,303**	-0.14
VAL 6a	0.1	1.67	0.50	1.38	198,000	**197,986**	199,000	**199,000**	0.00
VAL 3a	0.1	1.67	1.00	1.85	224,100	**221,636**	224,300	**221,964**	1.07
VAL 3a-2	0.1	1.67	1.00	1.88	221,300	**219,248**	223,800	**221,786**	0.92
VAL 5a	0.1	1.67	2.00	2.30	328,200	**296,718**	330,100	**298,532**	9.58
VAL 4a	0.1	1.83	1.00	1.98	304,700	**301,779**	306,400	**303,735**	0.92
VAL 1b	0.3	1.20	1.00	2.20	268,500	**269,378**	270,500	**271,379**	-0.33
VAL 1b-2	0.3	1.20	1.00	2.20	262,300	**263,970**	266,500	**267,967**	-0.60
VAL 2b	0.3	1.50	1.00	1.50	302,900	**299,838**	305,700	**302,719**	1.00
VAL 2b-2	0.3	1.50	1.00	1.58	347,200	**334,835**	348,800	**336,345**	3.57
VAL 3b	0.3	1.67	1.00	1.40	370,800	**361,274**	372,400	**363,231**	2.52
VAL 3b-2	0.3	1.67	1.00	1.55	436,000	**419,177**	440,500	**423,753**	3.83
VAL 3b-3	0.3	1.67	1.00	1.50	441,000	**405,147**	443,800	**408,276**	8.07

As illustrated in Appendix B, the fatigue rate curves for specimens VAL IIIb-2 and VAL IIIb-3 exhibit an additional pseudo 'inflection point' at a stress intensity factor range of approximately 17 $\text{MPa}\sqrt{\text{m}}$. For this reason, using the parameters indicated in Appendix C, the two-curve Paris model was extended to a three-curve Paris approximation for these two specimens only. The transition between region I and region predicted fatigue life, could be obtained through the use of a slightly different shaping exponent at each overload. However, for obvious reasons, this is not a practical or justifiable solution. The Wheeler crack growth predictions (i.e., a-versus-N curves) for all specimens, along with the corresponding Paris parameters used in each case, are included in Appendix C of this report. The Wheeler predictions for both crack length intervals a_i to a_f and a_i to a_{yld} are summarized in Table 7.7 (note the average error represents the average of the errors for N_{if} and N_{yld}).

Table 7.7 – Summary of Wheeler model fatigue life predictions

Specimen ID	Stress Ratio	OLR	OL/UL	Shaping Exponent	Interval a_i to a_f		Interval a_i to a_{yld}		Avg. % Error
					N_{Expt}	N_{Pred}	N_{Expt}	N_{Pred}	
VAL 8a	0.1	1.20	0.50	2.25	158,000	**158,316**	159,500	**159,587**	-0.13
VAL 1a	0.1	1.20	1.00	2.70	140,700	**141,032**	142,000	**141,991**	-0.11
VAL 7a	0.1	1.20	2.00	2.70	168,200	**168,343**	170,500	**170,505**	0.00
VAL 2a	0.1	1.50	1.00	1.92	174,400	**174,591**	176,000	**176,303**	-0.14
VAL 6a	0.1	1.67	0.50	1.38	198,000	**197,986**	199,000	**199,000**	0.00
VAL 3a	0.1	1.67	1.00	1.85	224,100	**221,636**	224,300	**221,964**	1.07
VAL 3a-2	0.1	1.67	1.00	1.88	221,300	**219,248**	223,800	**221,786**	0.92
VAL 5a	0.1	1.67	2.00	2.30	328,200	**296,718**	330,100	**298,532**	9.58
VAL 4a	0.1	1.83	1.00	1.98	304,700	**301,779**	306,400	**303,735**	0.92
VAL 1b	0.3	1.20	1.00	2.20	268,500	**269,378**	270,500	**271,379**	-0.33
VAL 1b-2	0.3	1.20	1.00	2.20	262,300	**263,970**	266,500	**267,967**	-0.60
VAL 2b	0.3	1.50	1.00	1.50	302,900	**299,838**	305,700	**302,719**	1.00
VAL 2b-2	0.3	1.50	1.00	1.58	347,200	**334,835**	348,800	**336,345**	3.57
VAL 3b	0.3	1.67	1.00	1.40	370,800	**361,274**	372,400	**363,231**	2.52
VAL 3b-2	0.3	1.67	1.00	1.55	436,000	**419,177**	440,500	**423,753**	3.83
VAL 3b-3	0.3	1.67	1.00	1.50	441,000	**405,147**	443,800	**408,276**	8.07

As illustrated in Appendix B, the fatigue rate curves for specimens VAL IIIb-2 and VAL IIIb-3 exhibit an additional pseudo 'inflection point' at a stress intensity factor range of approximately 17 $\mathrm{MPa}\sqrt{\mathrm{m}}$. For this reason, using the parameters indicated in Appendix C, the two-curve Paris model was extended to a three-curve Paris approximation for these two specimens only. The transition between region I and region

II crack growth was initially cited as a possible cause of this unexpected crack growth behavior. However, it was concluded that such a transition should be expected to occur at a much lower stress intensity factor range than was observed (approximately 17 MPa$\sqrt{m}$). It was also thought that EDM notch effects were possibly influencing early crack growth for these two specimens. However, the experimental data for the precracking phase (for both specimens) were verified against the precracking requirements of ASTM E647, and deemed adequate. It is therefore unclear as to the origin of this uncharacteristic crack growth behavior for these two specimens.

As shown in Table 7.7 above, the Wheeler model generally yields excellent fatigue life predictions. However, one of the major disadvantages of this model lies in the empirical nature of the shaping exponent. As previously mentioned, the parameter bears no physical significance, and is typically evaluated, based on a trial-and-error approach, as the value that 'best fits' the experimental data. While one value of 'm' might predict the crack growth retardation following one or more overload- or overload-underload sequences with incredible accuracy, oftentimes another value is required to provide a more accurate prediction of total fatigue life, as was the case for many of the specimens in the current investigation. Although pre-determined values of Wheeler's shaping exponent, previously evaluated for similar loading sequences, are often employed in practice, minor variations may warrant re-calibration. The Wheeler model therefore has the potential for requiring a large database of shaping exponents, each corresponding to a particular loading history, thereby inhibiting its usefulness somewhat.

For the stress ratios and overloads of a given loading sequence, the seemingly 'random' manner in which the Wheeler shaping exponent (m) is selected could be remedied somewhat if it were in some way a function of R, OLR, or OL/UL ratio. Figure 7.16 and Figure 7.17 illustrate the potential of describing Wheeler's shaping exponent as a function of OLR for the stress ratios and OL/UL ratios investigated here. Least squares regression analyses were not performed for those cases involving OL/UL=0.50 and OL/UL=2.0 (shown by dashed lines in the figures below), as only two data points were available for each. On the other hand, a least squares (second order) polynomial regression for data corresponding to OL/UL = 1.0 predicted very high R^2 values for both R=0.10 and R=0.30 (0.997 and 0.979, respectively), illustrating that such a method of evaluating the Wheeler shaping exponent may show some promise. The corresponding relationships for R=0.10 and R=0.30 (at OL/UL=1.0) are given by Equations 7.14 and 7.15, respectively.

$$m_{0.1} = 4.2348(OLR)^2 - 13.951(OLR) + 13.339 \tag{7.14}$$

$$m_{0.3} = 3.9716(OLR)^2 - 12.923(OLR) + 11.989 \tag{7.15}$$

However, the availability of more data points for use in regression analyses such as those performed here is of utmost importance in assessing the potential usefulness of this technique.

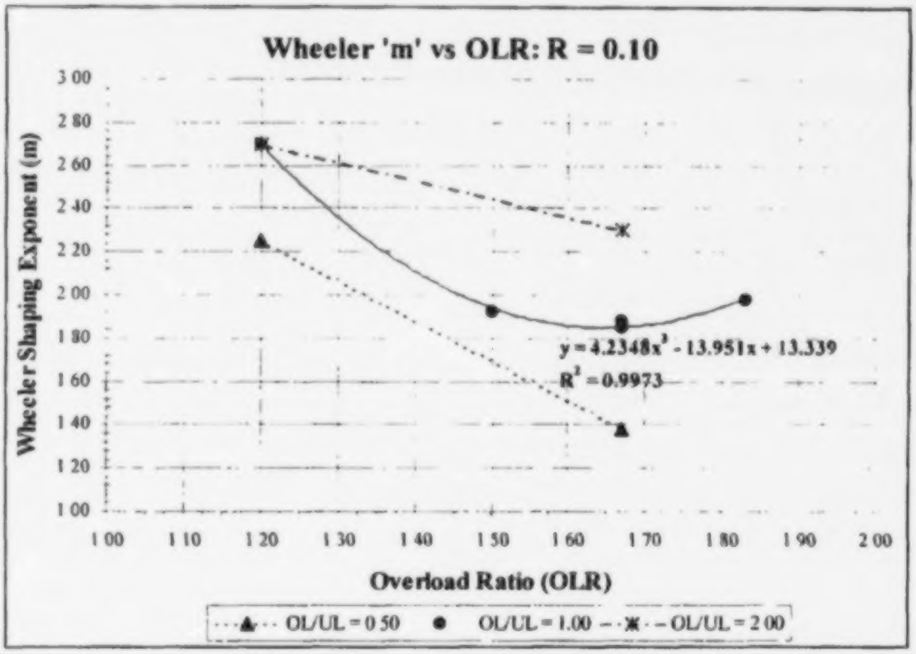

Figure 7.16 – Wheeler shaping exponent (m) expressed as a function of OLR

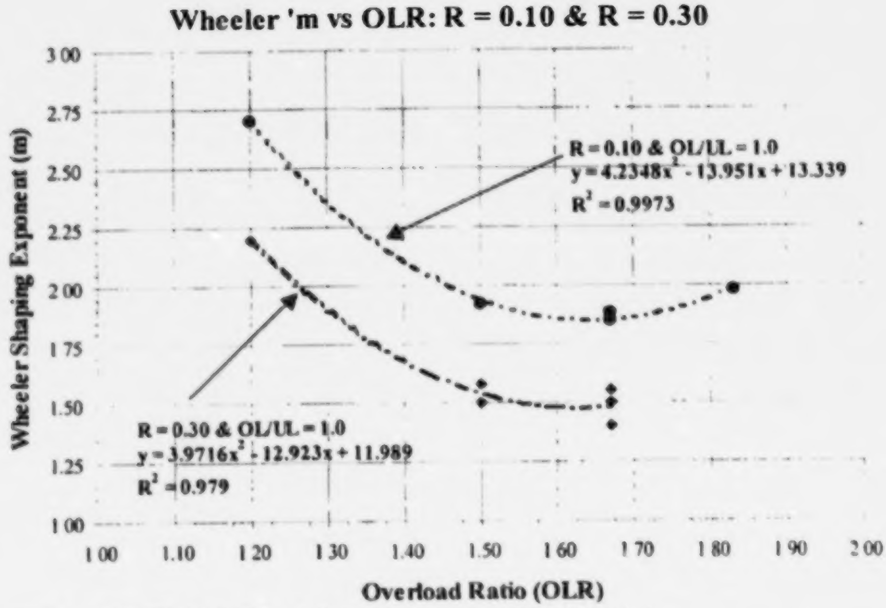

Figure 7.17 – Comparison of Wheeler 'm'-versus-OLR relationship for R=0.10 & R=0.30

Common to all curves is the general trend of a lower required value of 'm' with increasing OLR. The curvature of the predicted relationships is very similar for both R=0.10 and R=0.30. In general, however, lower values of 'm' are required for R=0.30 than are required for R=0.10, suggesting the possibility of a family of curves existing at any stress ratio, which can describe 'm' as a function of OLR for a given OL/UL ratio. Similarly, it is plausible that a family of curves exists at a given OL/UL ratio, which is capable of describing this 'm' versus OLR correlation for any stress ratio, as supported by Figure 7.17 above. Unfortunately, the limited availability of data from the current investigation (i.e., an 'm' for all OLR and OL/UL ratios considered) renders it extremely difficult to discern whether the predicted curves for OL/UL=0.50 and OL/UL=2.00 follow those corresponding to OL/UL=1.00. Therefore, any conclusions regarding the usefulness of evaluating Wheeler's shaping exponent in this manner are of somewhat limited significance. Similar testing should be carried out to ascertain some much-needed intermediate data points for OL/UL=0.50 and OL/UL=2.0, which could then be used to confirm these 'preliminary' hypotheses.

7.5.3 VAL Predictions Based on a Modified Wheeler Model

Thus far, much of the literature dismisses entirely the notion of a 'compressive plastic zone' at the crack tip when considering the crack growth acceleration or reduction in crack growth retardation induced by compressive loading. This neglect is based on the most obvious presumption that upon closure of a fatigue crack, the applied compressive stress becomes distributed evenly across the section, as if the component were uncracked. Other crack growth models try to account for this phenomenon by modifying the stress ratio (R). The concept of such a technique being to 'adjust' R (to R^* say) such that the 'equivalent' constant amplitude crack growth rate (i.e., at the same ΔK) for a stress ratio of R^* corresponds approximately to the minimum crack growth rate reached following an overload/underload sequence at stress ratio R. Moreover, for some models, this adjustment of the stress ratio is limited to $R \geq 0$. In any event, this appears to be somewhat of an empirical approach to handling the phenomena actually taking place at the tip of a fatigue crack under compressive loading.

However, as previously illustrated in Figure 7.6, neglecting the effects of compressive loading, which is rather common in practice, may in some cases have dire consequences. As noted earlier, increasing the magnitude of the applied compressive underload (i.e., decreasing the OL/UL ratio) may significantly reduce crack growth retardation, depending on the overload ratio. In light of this observation, it is evident that there is some type of 'compressive plastic zone' at the crack tip, which is responsible for such crack growth behavior.

In order to facilitate the inclusion of compressive loading effects into the Wheeler retardation model, slight modifications have been proposed by the author. Wheeler's original retardation parameter (ϕ_R) was based on the premise that crack growth retardation should cease when the boundary of the current plastic zone has extended to or beyond the outermost boundary of any previous tensile overload. That is, $\phi_R = 1$ when $a_i + r_{pi} \geq a_{OL} + r_{p,OL}$ for any cycle 'i'. Denoting the size of this alleged 'compressive plastic zone' by the symbol r_{cp} (to be defined later), one can extend Wheeler's logic to include an 'effective' overload plastic zone such that $\phi_R^{T-C} = 1$ for

$$a_i + (r_{pi} - r_{cpi}) \geq a_{OL} + (r_{p,OL} - r_{cp,UL}) \tag{7.16}$$

Figure 7.18 below summarizes the basic concept and terms describing the Modified Wheeler model.

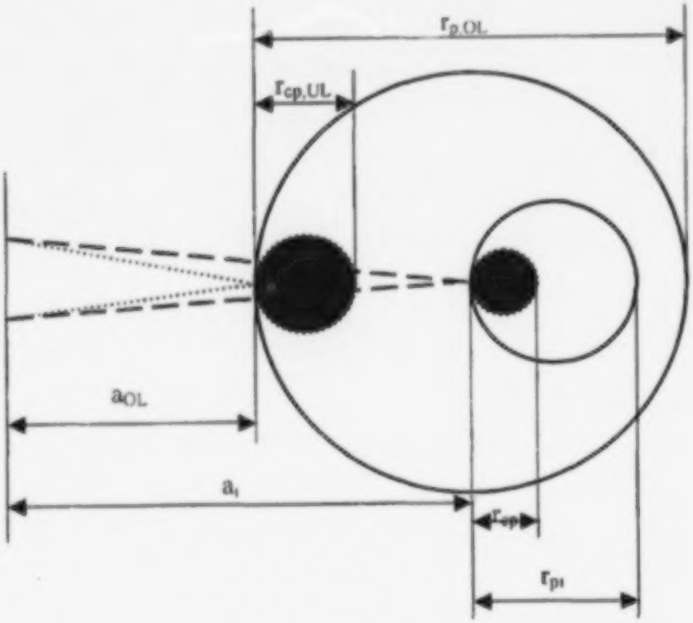

Figure 7 18 – Description of the modified Wheeler model

Further denoting the effective plastic zone by

$$r_{eff} = r_p - r_{cp} \tag{7.17}$$

and rearranging the relation given in Equation 7.16 in a manner similar to that done for Wheeler's original retardation parameter, one arrives at the following equation that describes the modified Wheeler retardation parameter

$$\phi_R^{T-C} = \begin{cases} \left[\dfrac{r_{eff,i}}{(a_{OL} + r_{eff,OL} - a_i)}\right]^m & , a_i + (r_{pi} - r_{cpi}) < a_{OL} + (r_{p,OL} - r_{cp,UL}) \\ 1 & , a_i + (r_{pi} - r_{cpi}) \geq a_{OL} + (r_{p,OL} - r_{cp,UL}) \end{cases} \quad (7.18)$$

Where a_i = the current crack length corresponding to the i^{th} cycle

r_{pi} = the current plastic zone size corresponding to the i^{th} cycle

r_{cpi} = the current compressive plastic zone size corresponding to the i^{th} cycle

a_{OL} = the crack length at which the overload was applied

$r_{p,OL}$ = the plastic zone created by the tensile overload

$r_{cp,UL}$ = the compressive plastic zone created by the compressive underload

m = an empirically adjustable parameter referred to as the shaping exponent

The tensile plastic zone diameter was calculated using Irwin's estimate, as before. However, evaluation of the compressive plastic zone diameter presented some uncertainties. Based on the concept of a cyclic plastic zone, previously presented in section 2.2.3 of this report, Equation 7.19 was used as an estimate of the compressive plastic zone diameter.

$$r_{cp} = \frac{1}{\alpha \cdot \pi}\left(\frac{\Delta K_{UL}}{2 \cdot \sigma_{yld}}\right)^2 \quad (7.19)$$

Where α = factor accounting for state of stress: 1 for plane stress, 3 for plane strain

σ_{yld} = material yield stress (assumed equal in tension and compression)

ΔK_{UL} = estimated as 'K^* - $K_{min,UL}$', for which K^* was taken as the minimum of $K_{min,CAL}$, K_{th}, or K_{open}

The results of the fatigue life predictions made using the modified Wheeler model are summarized in Table 7.8 below. The complete a-versus-N curves for all the specimens are included in Appendix D. Figure 7.19 illustrates that the expressions obtained for 'm' as a function of OLR are similar for both the original and modified Wheeler models. In general, however, slightly higher shaping exponents were required for the modified Wheeler predictions. The 'm'-versus-OLR functions for R=0.10 and R=0.30 (at OL/UL=1.0), corresponding to the modified Wheeler predictions, are given by the following expressions.

$$m_{0.1} = 4.0030(OLR)^2 - 13.036(OLR) + 12.624 \qquad (7.20)$$

$$m_{0.3} = 3.3187(OLR)^2 - 10.844(OLR) + 10.434 \qquad (7.21)$$

Table 7.8 - Summary of fatigue life predictions based on modified Wheeler model

Specimen ID	Stress Ratio	OLR	OL/UL	Shaping Exponent	Interval a_i to a_f		Interval a_i to a_{cr}		Avg. % Error
					N_{Exp}	N_{Pred}	N_{Exp}	N_{Pred}	
VAL 8a	0.1	**1.20**	0.50	5.00	158,000	**157,941**	159,500	**159,211**	0.11
VAL 1a	0.1	**1.20**	1.00	2.75	140,700	**140,802**	142,000	**141,761**	0.05
VAL 7a	0.1	**1.20**	2.00	2.70	168,200	**168,343**	170,500	**170,505**	0.04
VAL 2a	0.1	**1.50**	1.00	2.05	174,400	**174,615**	176,000	**176,327**	-0.16
VAL 6a	0.1	**1.67**	0.50	2.87	198,000	**198,106**	199,000	**199,120**	-0.06
VAL 3a	0.1	**1.67**	1.00	2.02	224,100	**224,185**	224,300	**224,514**	-0.07
VAL 3a-2	0.1	**1.67**	1.00	2.05	221,300	**221,692**	223,800	**224,227**	-0.18
VAL 5a	0.1	**1.67**	2.00	2.31	328,200	**296,815**	330,100	**298,629**	9.55
VAL 4a	0.1	**1.83**	1.00	2.16	304,700	**305,005**	306,400	**306,961**	-0.14
VAL 1b	0.3	**1.20**	1.00	2.20	268,500	**269,291**	270,500	**271,292**	-0.29
VAL 1b-2	0.3	**1.20**	1.00	2.20	262,300	**263,910**	266,500	**267,907**	-0.57
VAL 2b	0.3	**1.50**	1.00	1.58	302,900	**300,891**	305,700	**303,772**	0.65
VAL 2b-2	0.3	**1.50**	1.00	1.69	347,200	**337,738**	348,800	**339,249**	2.74
VAL 3b	0.3	**1.67**	1.00	1.50	370,800	**364,204**	372,400	**366,161**	1.73
VAL 3b-2	0.3	**1.67**	1.00	1.64	436,000	**420,151**	440,500	**424,726**	3.61
VAL 3b-3	0.3	**1.67**	1.00	1.60	441,000	**407,602**	443,800	**410,732**	7.51

The results of the fatigue life predictions made using the modified Wheeler model are summarized in Table 7.8 below. The complete a-versus-N curves for all the specimens are included in Appendix D. Figure 7.19 illustrates that the expressions obtained for 'm' as a function of OLR are similar for both the original and modified Wheeler models. In general, however, slightly higher shaping exponents were required for the modified Wheeler predictions. The 'm'-versus-OLR functions for R=0.10 and R=0.30 (at OL/UL=1.0), corresponding to the modified Wheeler predictions, are given by the following expressions.

$$m_{0.1} = 4.0030(OLR)^2 - 13.036(OLR) + 12.624 \tag{7.20}$$

$$m_{0.3} = 3.3187(OLR)^2 - 10.844(OLR) + 10.434 \tag{7.21}$$

Table 7.8 – Summary of fatigue life predictions based on modified Wheeler model

Specimen ID	Stress Ratio	OLR	OL/UL	Shaping Exponent	Interval a_i to a_f		Interval a_i to a_{cr}		Avg. % Error
					N_{Expt}	N_{Pred}	N_{Expt}	N_{Pred}	
VAL 8a	0.1	**1.20**	0.50	5.00	158,000	**157,941**	159,500	**159,211**	0.11
VAL 1a	0.1	**1.20**	1.00	2.75	140,700	**140,802**	142,000	**141,761**	0.05
VAL 7a	0.1	**1.20**	2.00	2.70	168,200	**168,343**	170,500	**170,505**	0.04
VAL 2a	0.1	**1.50**	1.00	2.05	174,400	**174,615**	176,000	**176,327**	-0.16
VAL 6a	0.1	**1.67**	0.50	2.87	198,000	**198,106**	199,000	**199,120**	-0.06
VAL 3a	0.1	**1.67**	1.00	2.02	224,100	**224,185**	224,300	**224,514**	-0.07
VAL 3a-2	0.1	**1.67**	1.00	2.05	221,300	**221,692**	223,800	**224,227**	-0.18
VAL 5a	0.1	**1.67**	2.00	2.31	328,200	**296,815**	330,100	**298,629**	9.55
VAL 4a	0.1	**1.83**	1.00	2.16	304,700	**305,005**	306,400	**306,961**	-0.14
VAL 1b	[illegible]	**1.20**	[illegible]	2.20	268,500	**269,291**	270,500	**271,292**	-0.29
VAL 1[illegible]	[illegible]	[illegible]	1.00	[illegible]	262,300	**263,[illegible]**	266,500	**267,907**	-0.57
VAL 2b	0.3	**1.50**	1.00	1.58	302,900	**300,891**	305,700	**303,772**	0.65
VAL 2b-2	0.3	**1.50**	1.00	1.69	347,200	**337,738**	348,800	**339,249**	2.74
VAL 3b	0.3	**1.67**	1.00	1.50	370,800	**364,204**	372,400	**366,161**	1.73
VAL 3b-2	0.3	**[illegible]**	1.00	1.54	436,000	**420,151**	440,500	**424,726**	3.61
VAL 3b-3	0.3	**1.67**	1.00	1.60	441,000	**407,602**	443,800	**410,732**	7.51

The most dramatic differences in shaping exponent being for the two specimens for which OL/UL=0.50 (i.e., relatively high compressive underload compared to the preceding tensile overload). This may be explained by taking a closer look at the ratio inside the brackets of Equation 7.18. The use of an 'effective' plastic zone versus a tensile plastic zone only yields a reduced denominator in this bracketed term, which yields a larger term overall. Moreover, since this ratio is always less than unity, it must be raised to a larger shaping exponent to numerically predict the same degree of crack growth retardation as was predicted using the retardation parameter of the original model. As a simple illustrative example, $(0.25)^3 = 0.015625$, while a larger value, 0.50 say, must be raised to the sixth power to give the same result.

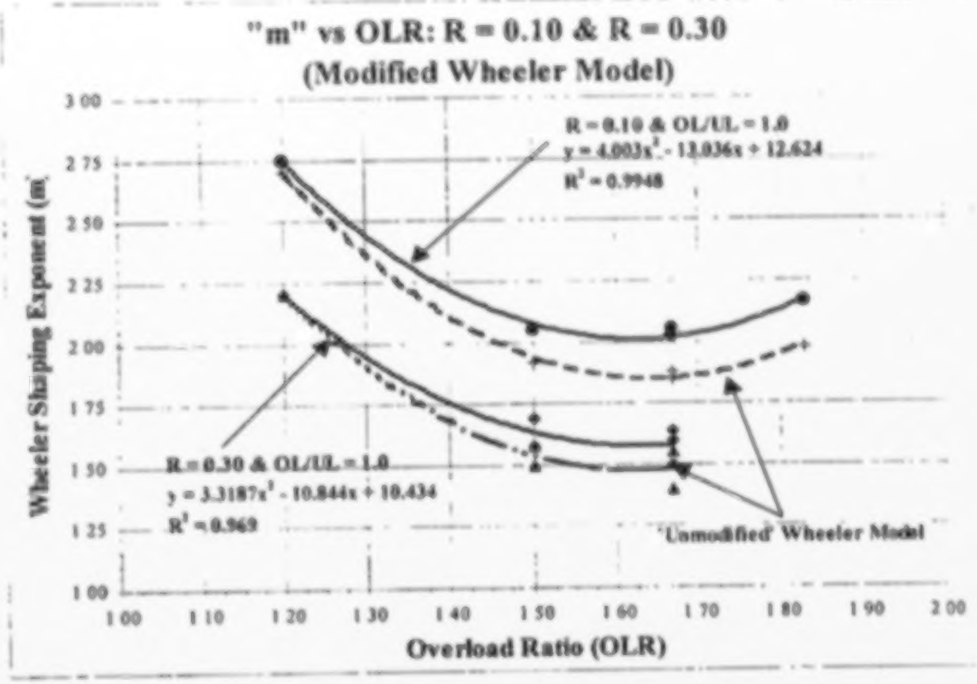

Figure 7.19 – 'm'-versus-OLR for R=0.10 & R=0.30: modified Wheeler model

It should be noted that, as is the case with many crack growth models, no attempt has been made here to consider the Bauschinger effect via one of several hardening rules. However, for load histories comprised mainly of tensile cyclic loads, neglecting the Bauschinger effect is generally considered conservative. Furthermore, the improved accuracy afforded by such an addition to an existing model would, in all probability, not warrant resulting complexity and additional effort required.

The proposed modification appears to provide an adequate means of predicting sequence effects on the fatigue crack growth of specimens subjected to intermittent tensile and compressive overloads. Although the proposed modification appears to only marginally improve the overall accuracy of the fatigue life predictions, the use of an 'effective' plastic zone does add an element of physical significance to a semi-empirical model such as this one.

7.5.4 Compressive Loading and Crack Growth Acceleration Revisited

For the sake of completeness, an attempt was made to modify the Wheeler model a second time, but in this case for the purposes of modeling the observed acceleration in crack growth following a compressive underload only. Based on the presumed existence of a compressive plastic zone, one could postulate that following a compressive underload (UL), crack growth acceleration will continue until such time as the boundary of the current plastic zone (due to tensile loading) reaches that of the largest previous compressive plastic enclave. That is, incorporating the logic behind Wheeler's original retardation parameter, crack growth acceleration following a compressive underload will continue until

$$a_i + r_{pi} \geq a_{UL} + r_{cp,UL} \tag{7.22}$$

Equation 7.23 represents the modified Wheeler acceleration parameter.

$$\phi_R^C = \begin{cases} \left[\dfrac{a_{UL} + r_{c,UL}}{(a_i + r_{pi})} \right]^m & , a_i + r_{pi} < a_{UL} + r_{cp,UL} \\ 1 & , a_i + r_{pi} \geq a_{UL} + r_{cp,UL} \end{cases} \tag{7.23}$$

Unfortunately, the current investigation did not consider intermittent compressive underloads only. The validity of this 'acceleration' parameter should therefore be confirmed through future experimental testing.

As previously mentioned, the common practice of neglecting the effects of compressive loading is based on the presumption that fatigue crack closure is accompanied by a uniform redistribution of the applied compressive stress across the entire section. However, if one considers the crack closure phenomena proposed by Elber (as discussed in section 4.2 of this report), it is quite possible that the crack path may not be perfectly linear, but instead may appear somewhat jagged when viewed on a microscopic scale. Furthermore, the corresponding faces of such jagged cracks may not match exactly upon crack closure. For example, if the crack path were jagged, with mismatched crack faces, as depicted in Figure 7.20, a compressive underload could induce a prying effect at the crack tip, thus presenting a mechanism capable of accelerating the subsequent crack growth. In addition, small-scale mixed-mode loading (a combination of shear and tensile modes) would occur under such conditions. In realization of the microscopic scale on which this phenomenon is viewed, it is expected that the resulting compressive plastic zone will be much smaller than the tensile plastic zone produced by the same ΔK. To confirm the aforementioned theory, a more detailed finite element analysis should be performed to simulate the existence of mis-matched crack faces and investigate their effect on the plastic zone at the crack tip.

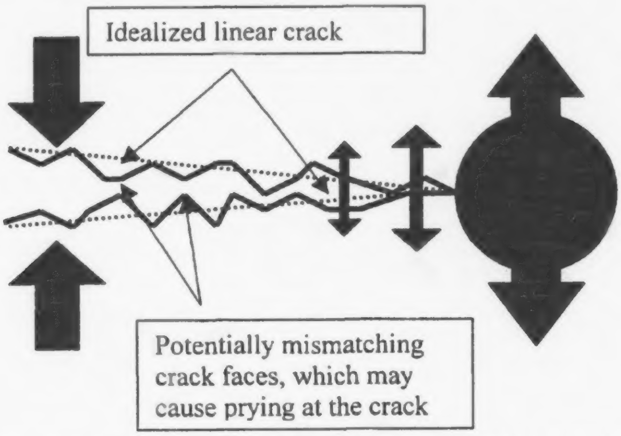
Idealized linear crack
Potentially mismatching crack faces, which may cause prying at the crack

Figure 7.20 –Schematic representation of potential crack tip prying under compressive overloads due to mis-matched crack faces

7.5.5 Finite Element Investigation Into Crack Tip Plasticity Under Compressive Loading

As a preliminary investigation into the potential creation of a compressive plastic zone following a tensile overload-compressive underload sequence, a nonlinear static analysis was performed on a typical specimen. The NISA (Numerically Integrated System Analysis) finite element package was employed for this investigation. The relevant model dimensions and material properties (350WT steel) are summarized as follows

- Plate Width, $W = 100$ mm
- Plate Thickness, $t = 5$ mm
- Crack Length, $2a = 40$ mm
- Initial Crack Face Separation, $\delta_o = 0.054$ mm
- Mass Density, $\rho = 7.850\text{x}10^{-9}\ \text{Ns}^2/\text{mm}^4$
- Modulus of Elasticity, $E = 205{,}000$ MPa
- Poisson's Ratio, $\nu = 0.30$
- Shear Modulus, $G = 77{,}000$ MPa
- Yield Strength, $\sigma_{yld} = 450$ MPa
- Applied Pressure, $p_{max} = 240$ psi (120 kN)

Although the ultimate strength for this material was known, the corresponding ultimate strain was not, thus a nonlinear material formulation was incorporated into the analysis using the vonMises yield criteria Furthermore, as material rupture was not the focus of the analysis, an assumption of elastic-perfectly plastic material behavior was thought to be adequate.

In order to include the effects of both a tensile overload and a compressive underload, the loading function was specified as follows:

- Start at zero load and ramp to a maximum tensile stress of 240 psi, which corresponds to a load of 120 kN;
- Ramp from this maximum tensile stress to an equal 'minimum' compressive stress of –240 psi (i.e., -120 kN);
- Finally, ramp from minimum compressive stress back to zero.

The entire loading function was divided into a sufficient number of equal load increments such that stability could be maintained throughout and convergence achieved within a minimal number of iterations. The nonlinear formulation incorporated the Newton-Raphson iterative technique, specifying that an equilibrium check be performed at every iteration required to achieve convergence within a given load step. Default tolerances (0.001) were selected for the allowable residuals (i.e., energy, force, and displacement) during each equilibrium check.

First-order plane stress elements (NKTP #1) were chosen to model the center-cracked plate. As illustrated in Figure 7.21, fixed boundary conditions were imposed at one end of the specimen, while the maximum load (120 kN) was applied as an edge pressure (240 psi) at the opposite end of the specimen. Accordingly, values of the loading function at each increment were specified as a fraction of the maximum applied edge pressure.

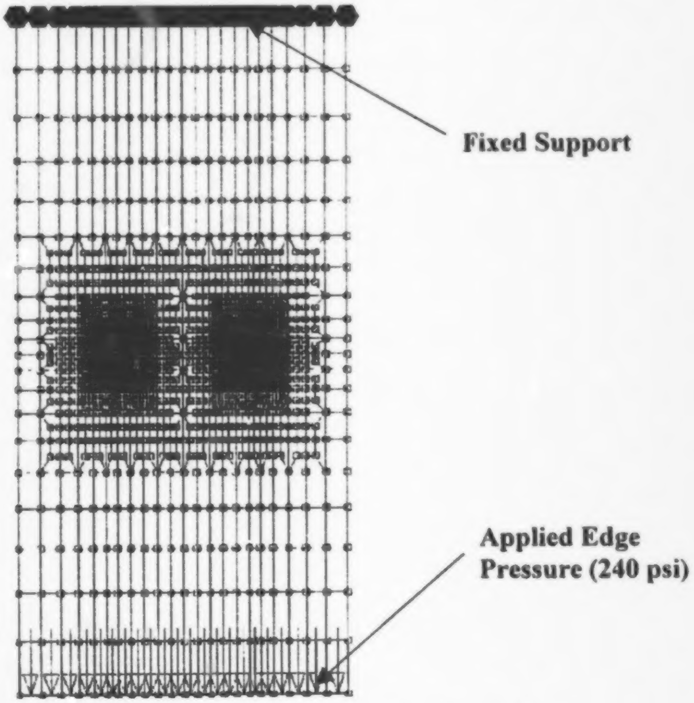

Figure 7.21- Application of boundary conditions to the FE model

Initially, the finite element model was analyzed allowing nodes on either side of the center crack to deform without any restraint whatsoever. However, the resulting nodal displacements indicated that the crack faces were overlapping upon application of a compressive load, which is physically impossible. It was therefore necessary to incorporate a suitable type of gap element capable of modeling the crack closure behavior under compressive loading. It was found that for the case of a nonlinear static analysis, this could be best accomplished through the incorporation of NISA's 2D Gap/Friction elements (NKTP #49), which were subsequently inserted across the crack faces to prevent them from overlapping, as noted in Salpekar et al (1988). For the sake of this preliminary model, frictionless contact was specified, thereby assuming smooth crack faces. For such cases, NISA requires that an axial stiffness be specified for each gap element, under both tension and compression. The compressive stiffness of each gap element was specified as approximately 10 times the axial stiffness of the adjacent elements (i.e., AE/L of the plate itself), which is within the range of values suggested in the NISA User's Manual, (EMRC, 1998) To force the tensile stiffness of the gap elements to zero (since the crack offers no tensile resistance), NISA allows the use of a 'small stiffness' (much smaller than the specified compressive stiffness, specified as unity in the current model), which is required only to prevent rigid body motion. "The effect of such 'soft springs' on solution accuracy is negligible" (EMRC, 1998). NISA further allows the gap width to be specified (and updated for each converged load increment) based on the coordinates of its corresponding nodes. The gap elements were verified to be working properly by observing the relative vertical displacement of two nodes at the center of the plate: one located on the top crack face, the other on the bottom crack face During any loadstep of compressive loading, it was verified (via NISA's output file) that the displacement of these two nodes did at no time differ more that the original gap width (δ_o) specified above, thereby confirming that although the crack faces did, in fact, close during compressive loading, they did not 'overlap'. Moreover, observation of the axial forces in the gap elements confirmed that the loadstep during which non-zero compressive gap forces first appeared was the same loadstep during which gap closure first occurred.

While most of the FE model could be discretized using a relatively coarse mesh, the region around each crack tip required considerable refinement in order to handle the stress singularities there. A convergence study was performed to determine the level of mesh refinement required to provide a reasonably smooth stress distribution in these regions of extremely high stress gradients. The FE model meshes were first refined in orthogonal direction and then refined in the radial direction to reduce the skewedness in some elements. During mesh refinement, acceptable mesh gradation, in terms of the relative size difference between adjacent elements, was an important consideration. Figure 7.22 shows the coarseness of the original unrefined mesh surrounding the crack tip, while Figure 7.23 illustrates the successive orthogonal and radial refinement of the crack tip mesh.

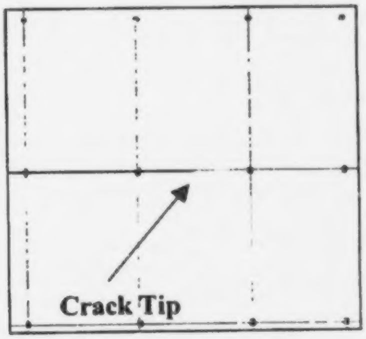

Figure 7.22 – Original crack tip mesh discretization: 449 elements (total)

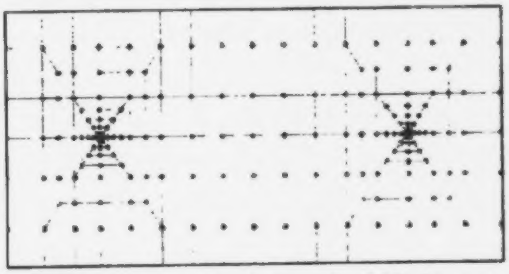

(a) Refinement #1 (orthogonal): 555 elements

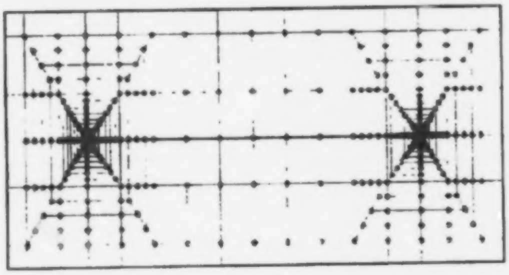

(b) Refinement #2 (orthogonal): 713 elements

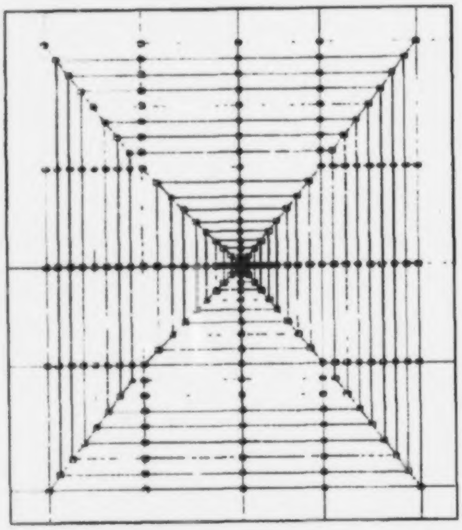

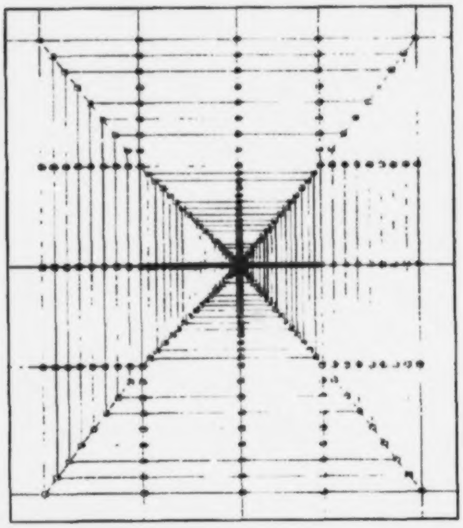

(c) Refinement #3 (orthogonal): 848 ele's (d) Refinement #4 (orthogonal): 1029 ele's

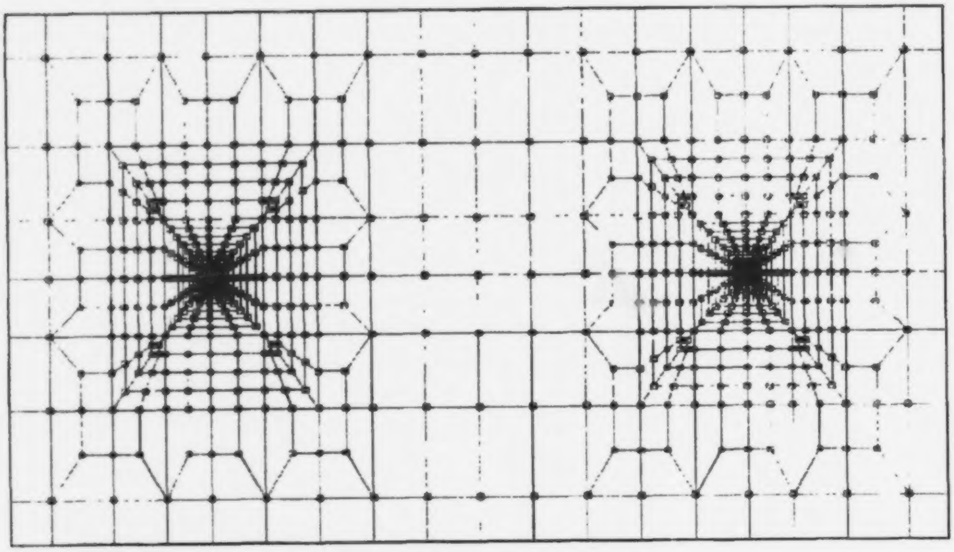

(e) Refinement #5 (radial): 1091 elements

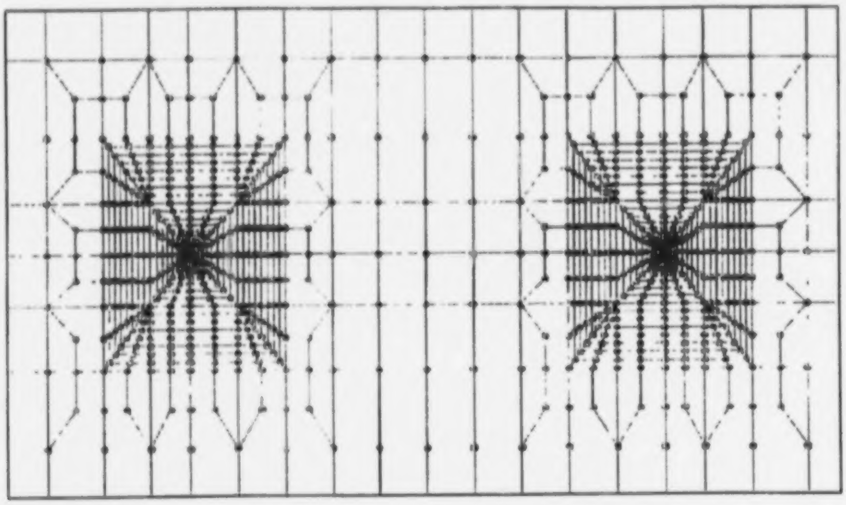

(f) Refinement #6 (radial)· 1353 elements

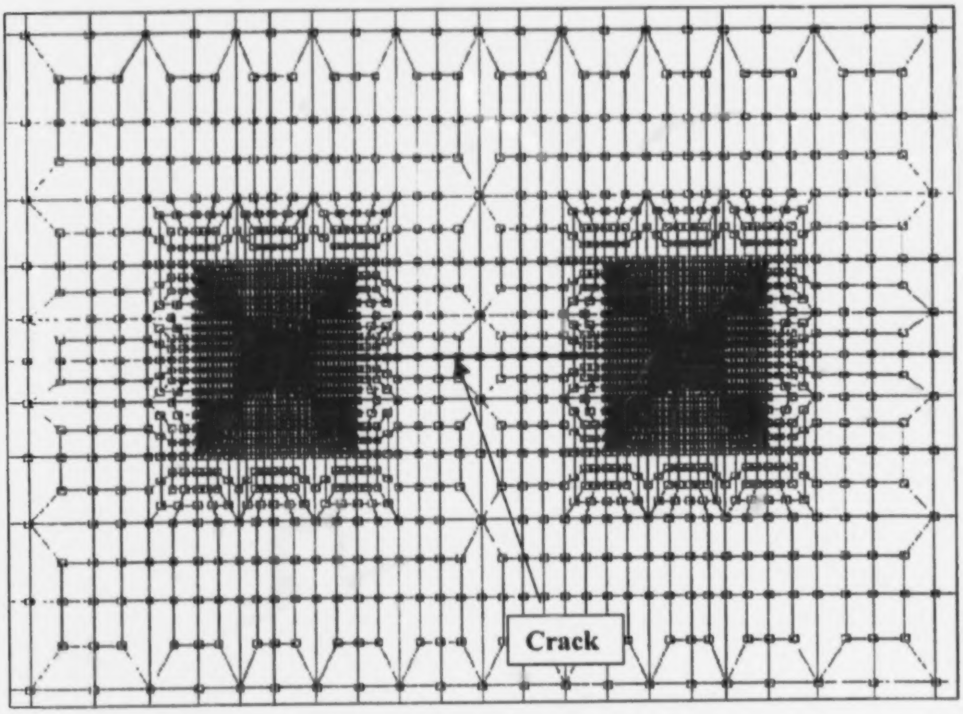

(g) Refinement #7 (radial): 4547 elements

Figure 7.23 – Orthogonal and radial refinements of FE model crack tip mesh

During one analysis, the first-order (i.e., 4-noded) elements of the original unrefined model were replaced by second order (i.e., 8-noded) quadrilateral elements, and for those elements surrounding the crack tip, the midside nodes closest to the crack tip were moved to their quarter points in order to better predict the crack tip stress distribution. The predictions from this model were much improved over those of the original unrefined model, but were not nearly as good as those for which the crack tips were reasonably refined. The results of the convergence study, based on convergence of the plastic zone stresses and crack tip displacements under maximum tension, are summarized in Table 7.9 below. The final crack tip mesh (Figure 7.23g), which incorporated 160 load increments and crack tip elements on the order of 10/1000ths of the specimen thickness), gave a largely converged displacement, as well as a very smooth crack tip plastic zone stress distribution, in the anticipated bean-shape, and will therefore be the model referred to for the remainder of this discussion.

Table 7.9 – Summary of FE model convergence study

Model Refin't. ID	# Elements/ # Loadsteps	Avg. Elem. Size @ Tip	Required CPU Time	Far-Field Δ_{ff} (mm)	Crack-Tip Δ_{tip} (mm)	Crack Tip Stresses	
						σ_{yy} (MPa)	σ_{VM} (MPa)
Original	**449/20**	**0.3333 mm**	**24.66 s**	**0.2941**	**0.14855**	**510.40**	**451.30**
8-Noded	**449/20**	**0.3333 mm**	**44.27 s**	**0.3046**	**0.15480**	**530.15**	**477.05**
Refin't. #1	**555/20**	**0.3333 mm**	**31.41 s**	**0.3041**	**0.15340**	**542.00**	**471.00**
Refin't. #2	**713/20**	**0.1670 mm**	**43.55 s**	**0.3050**	**0.15385**	**544.00**	**475.50**
Refin't. #3	**848/20**	**0.1670 mm**	**47.35 s**	**0.3053**	**0.15390**	**544.00**	**475.60**
Refin't. #4	**1029/40**	**0.0833 mm**	**106.28 s**	**0.3054**	**0.15405**	**545.30**	**477.30**
Refin't. #5	**1091/40**	**0.0833 mm**	**155.60 s**	**0.3056**	**0.15410**	**519.50**	**458.00**
Refin't. #6	**1353/40**	**0.0833 mm**	**212.40 s**	**0.3059**	**0.15410**	**519.80**	**459.00**
Refin't. #7	**4547/160**	**0.0417 mm**	**5832.31 s**	**0.3070**	**0.15465**	**525.80**	**455.30**

Having refined the FE model to a sufficient extent, the investigation proceeded with an examination of the stress distributions at the major loading points of interest. maximum tensile load, zero load following the maximum tensile load, maximum compressive load, and finally the zero load following the maximum compressive load. Figure 7.24 below illustrates the NISA output for the y-displacement contours of loadstep 40, during which the applied load was a maximum (120 kN). Figure 7.25 illustrates the corresponding distribution of axial stresses.

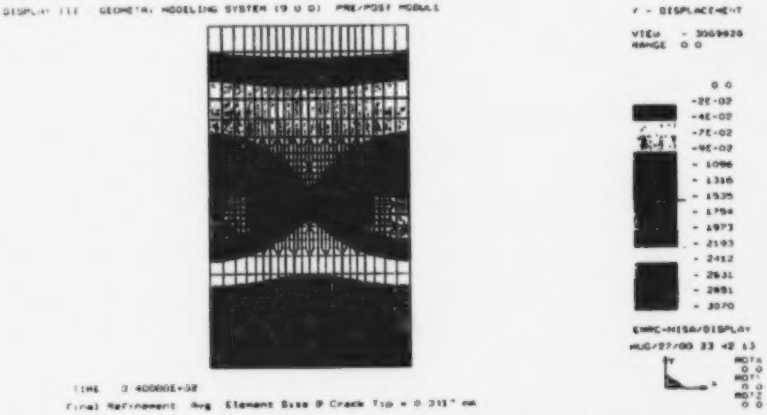

Figure 7.24 – Y-Displacement contours of loadstep 40

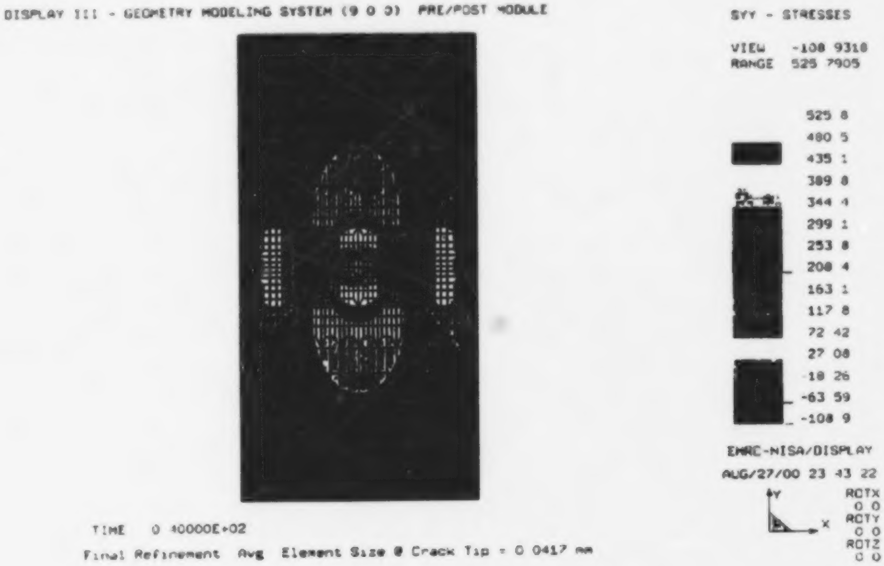

(a) Entire model

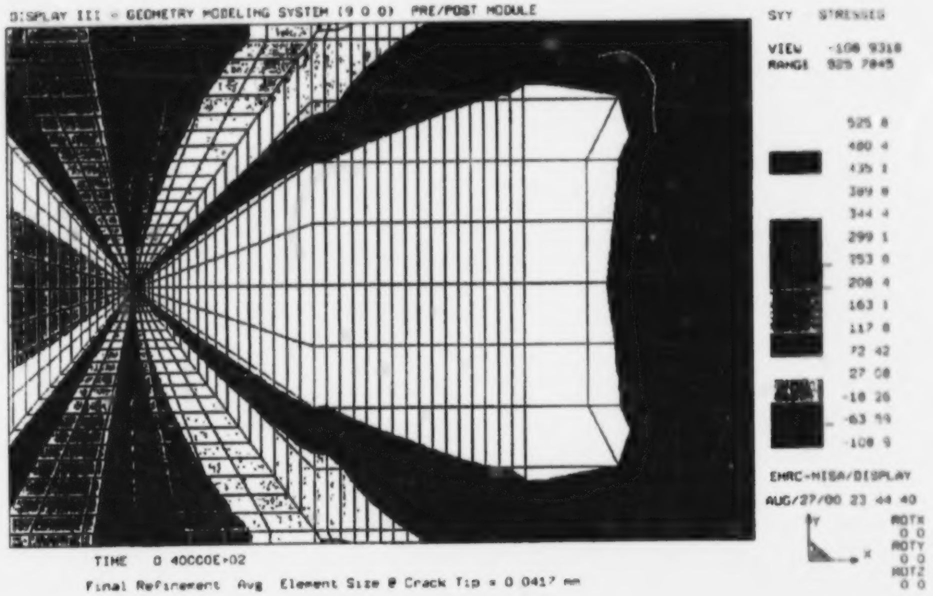
DISPLAY III - GEOMETRY MODELING SYSTEM (9 0 0) PRE/POST MODULE
SYY STRESSES
VIEW -108 9318
RANGE 525 7845
525 8
480 4
435 1
389 8
344 4
299 1
253 8
208 4
163 1
117 8
72 42
27 08
-18 26
-63 59
-108 9
EMRC-NISA/DISPLAY
AUG/27/00 23 44 40
Y
X
ROTX
0 0
ROTY
0 0
ROTZ
0 0
TIME 0 40CCOE+02
Final Refinement Avg Element Size @ Crack Tip = 0 0417 mm

(b) Right crack tip region

Figure 7.25 – Axial (Syy) stresses during loadstep 40 ($p_{max} \approx 240$ psi, $P_{max} \approx 120$ kN)

Figure 7.26 illustrates that upon return to zero load (loadstep 80), a large zone of residual compressive stresses (within which lies a smaller compressive 'yield zone' (see inset)) has developed at the crack tip, along with a zone of residual tensile stresses further from the crack tip. The far-field stresses during this loadstep are almost zero. It is interesting to note that similar, yet smaller, stress distributions were observed during the few load increments prior to reaching loadstep 80. The development of this zone of compressive stresses most certainly explains the observed phenomenon of crack growth retardation following a tensile overload.

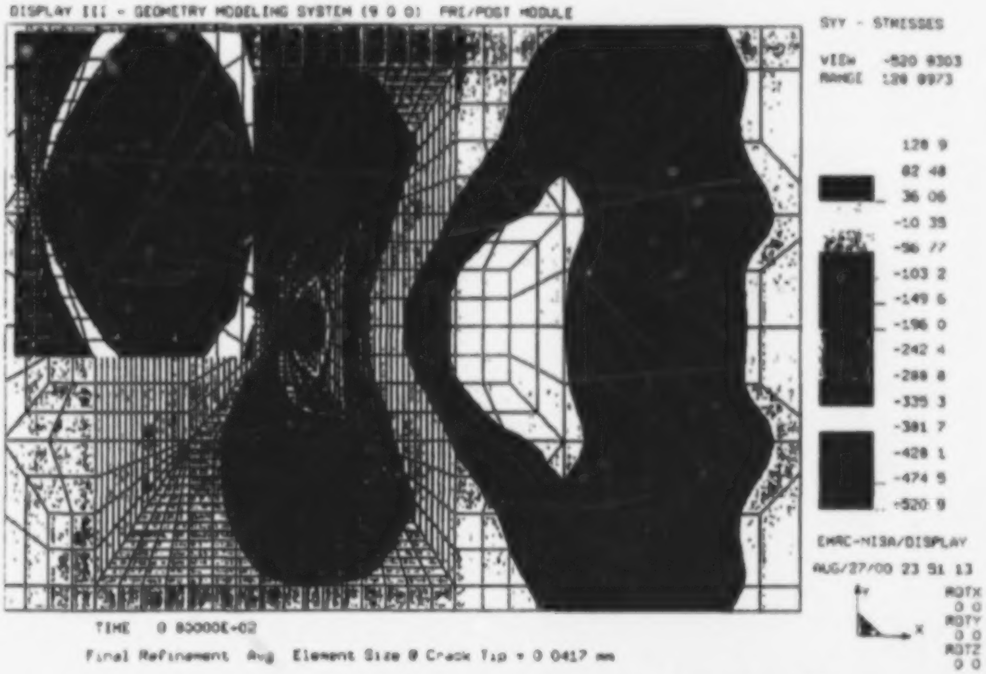

Figure 7.26 – Axial (Syy) stress distribution for loadstep 80: compressive residual stresses upon return to zero load form P_{max}

As previously mentioned, much of the literature accepts the notion that upon the application of compressive stresses, the fatigue crack simply closes and the stresses are uniformly distributed as if applied to an uncracked component. However, based on Figure 7.27 below, it appears that this may not be entirely true, and that the assumption of a compressive plastic zone, upon which the modified Wheeler model was previously based, may show some potential. Under maximum compression, there appears to be a zone in which the compressive stresses are at or above yield (recall the vonMises yield criterion was specified for the analysis). Comparison with Figure 7.25b shows that this zone is smaller than that developed under an equivalent tensile load, as previously anticipated. The vonMises stress distribution for this load increment shows the commonly observed bean-shaped plastic zone at the crack tip, but was not included due to the fact that it cannot depict the compressive nature of this stress distribution.

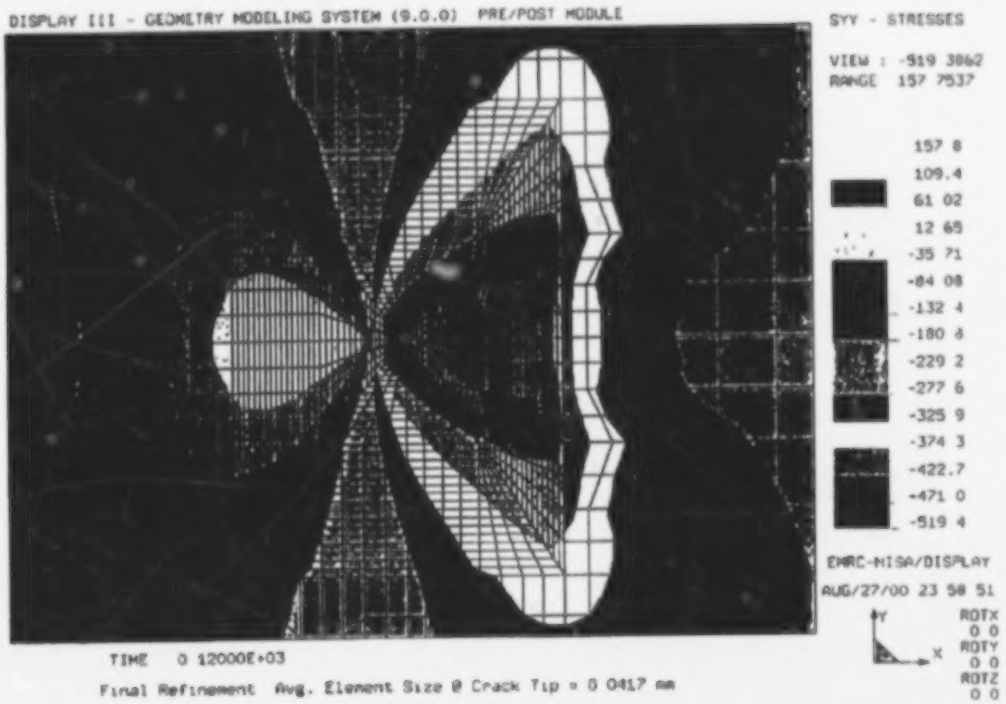
DISPLAY III - GEOMETRY MODELING SYSTEM (9.0.0) PRE/POST MODULE
SYY - STRESSES
VIEW : -519 3062
RANGE 157 7537
157 8
109.4
61 02
12 65
-35 71
-84 08
-132 4
-180 8
-229 2
-277 6
-325 9
-374 3
-422.7
-471 0
-519 4
EMRC-NISA/DISPLAY
AUG/27/00 23 58 51
Y
X
ROTX
0 0
ROTY
0 0
ROTZ
0 0
TIME 0 12000E+03
Final Refinement Avg. Element Size @ Crack Tip = 0 0417 mm

Figure 7.27 - Axial (Syy) stress distribution for loadstep 120: compressive plastic zone at minimum compressive load

Upon return to zero load (loadstep 160) from the minimum compressive load, a large zone of residual compressive stresses was observed in a portion of the uncracked ligaments. More importantly, however, is the development of a bean-shaped zone of tensile stresses at the crack tip, the center portion of which contains a type of yield zone, as illustrated in Figure 7.28 below. As previously mentioned for loadstep 80, comparable stress distributions were observed on a smaller scale during load increments just prior to reaching the final loadstep. The development of this zone of tensile stresses would tend to accelerate a propagating fatigue crack, thereby contributing to the observed reduction in crack growth retardation observed for a given tensile overload/compressive underload sequence.

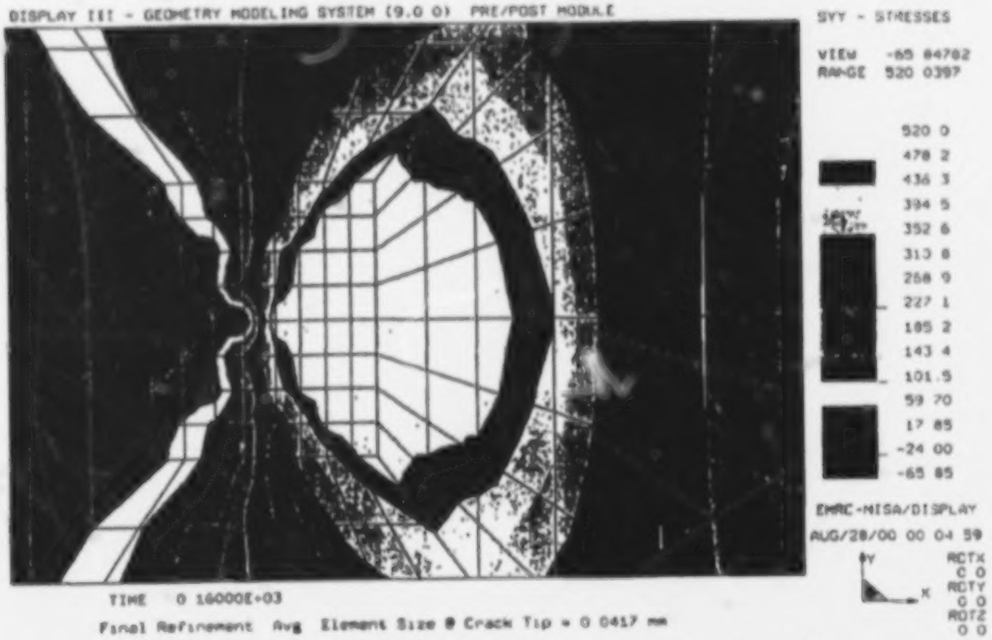

Figure 7.28 - Axial (Syy) stress distribution for loadstep 160: tensile residual stresses upon return to zero load from P_{min}

Although the above results appear to confirm the experimental observations, they are based on an initial crack separation (δ_o) of 0.054 mm, which may conceivably be much less. Therefore, to confirm the occurrence of similar trends when a much smaller crack separation is used, the 'final' refined model was further modified by reducing the initial crack separation to $\delta = 0.0054$ mm (i.e., 10X smaller than δ_o). As one would expect, the resulting stress distributions for the tensile portion of the loading function are identical to those depicted in Figures 7.25 and 7.26 above. The axial stress distribution corresponding to loadstep 120 (i.e., $p_{min} = -240$ psi and $P_{min} = -120$ kN) is illustrated in Figure 7.29 below. Comparison with Figure 7.27 above yields some subtle differences. Firstly, note that aside from those regions near the crack tip, the stresses appear to be very nearly uniformly distributed across the crack faces. Secondly, the size of the crack tip 'compressive plastic zone' is smaller than that depicted in Figure 7.27 for the larger crack face separation. One might therefore expect a reduction in the size of this plastic zone with decreasing crack face separation. However, the general trend in the distribution, that is, the existence of such a 'compressive plastic zone', should be expected to continue. Based on the use of actual values for crack face separation, a similar model could be used to correlate the size of the resulting compressive plastic zone with experimentally observed crack growth phenomena, in terms of both reductions in crack growth retardation and crack growth accelerations.

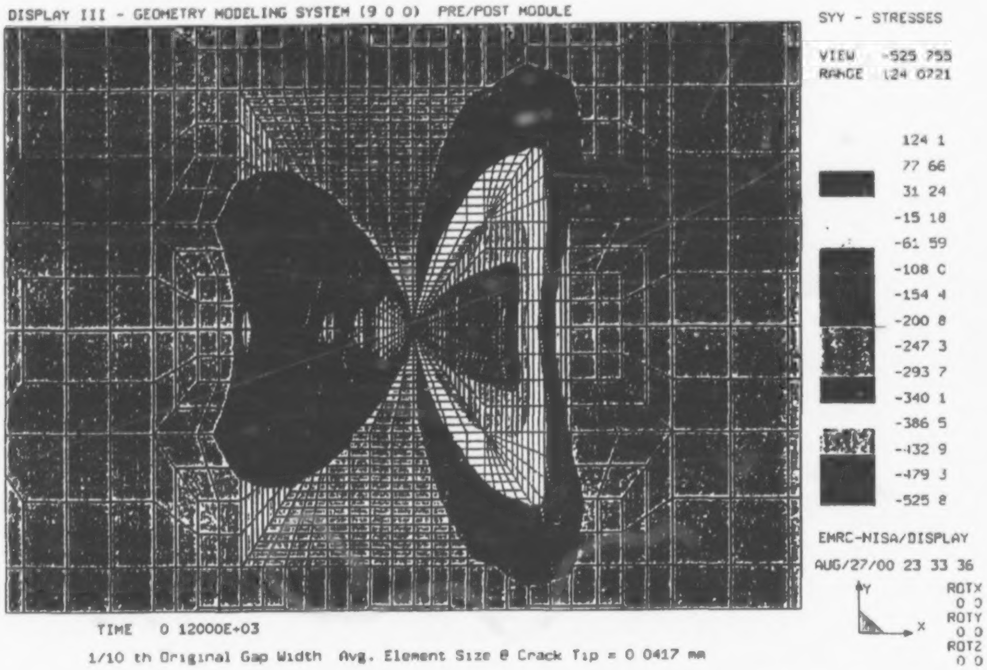

Figure 7.29 – Axial (Syy) stress distribution for loadstep 120: crack face separation reduced by 10X

Again, upon returning to zero load following the application of minimum compressive stress, a zone of residual tension (including tensile yielding) developed at the crack tip, as illustrated in Figure 7.30. Comparison with Figure 7.28 reveals that while the stress values are nearly identical, the size of the zone in which tensile yielding occurred is much smaller for a smaller crack face separation.

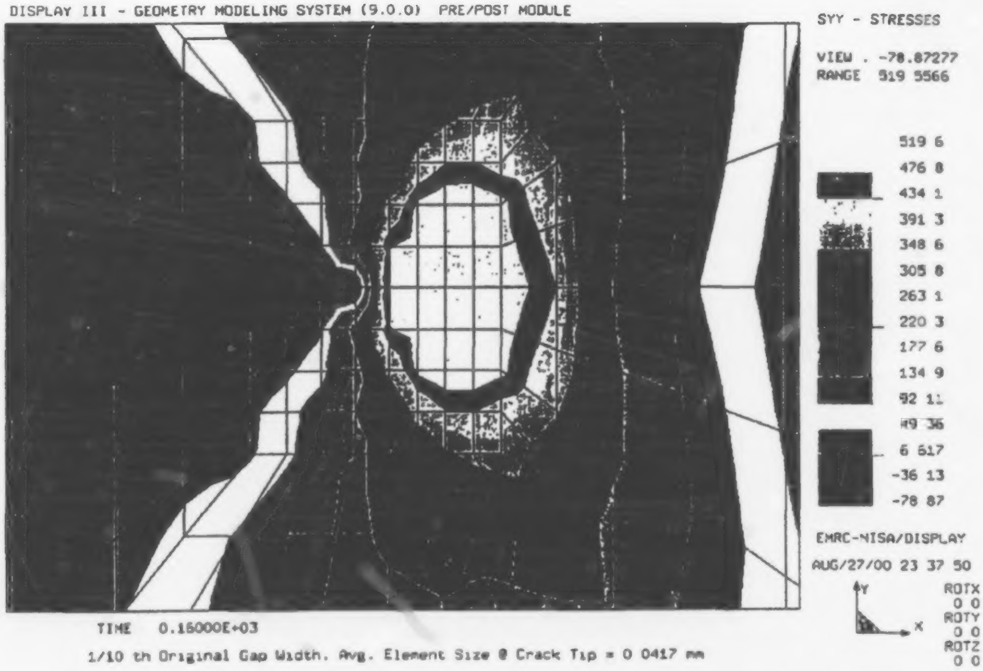

Figure 7.30 – Axial (Syy) stress distribution for loadstep 160:
crack face separation reduced by 10X

In summary, this preliminary finite element investigation appears to have confirmed the alleged existence of a crack tip compressive plastic zone under a compressive underload, the size of which is typically smaller than those produced by an equal tensile overload. The FE analysis also predicts a zone of tensile yielding at the crack tip upon removal of this compressive underload, which helps to explain the experimentally observed crack growth acceleration phenomena. In addition, it was found that the size of these 'yield zones' depends not only on the relative magnitude of the compressive underload and the preceding tensile overload, but also on the assumed crack face separation (δ). A more detailed finite element analysis could be performed to investigate the effects of varying these parameters on the size of the resulting 'yield zones', and develop a more accurate correlation function similar to Equation 7.19 for use with the modified Wheeler model. As alluded to in section 7.5.4, one could also perform an FE analysis to investigate the effects of roughened (mismatched) crack faces and mixed-mode loading on the formation of residual tensile stresses at the crack tip under compressive loading.

7.5.6 A Revised Form of Trask's Exponential Delay Model

As previously discussed in Chapter 4 of this report, the application of a tensile overload within an otherwise constant amplitude loading history induces a compressive residual crack tip stress field, thereby resulting in a period of retarded crack growth This crack growth retardation is usually quantified in terms of the number of delay cycles (N_D) required to re-establish the corresponding CAL crack growth rate. The extent to which crack growth is retarded (i.e., N_D) increases with increasing overload ratio (OLR). In addition, results of the current investigation have shown that N_D typically increases with increasing stress ratio (R).

If, on the other hand, the tensile overload were followed by a compressive underload, the amount of retardation is reduced, a phenomenon commonly referred to as 'reduction in retardation'. As the results of this experimental investigation have illustrated, at a given OLR, compressive underloads of increasing magnitude (i.e., reducing the corresponding OL/UL ratio) yields progressively smaller values of N_D on a 'per overload' basis.

Trask (1998) proposed a simple delay model capable of predicting the amount of crack growth retardation (in terms of N_D) produced by a given tensile overload (defined in terms of its corresponding OLR) at a stress ratio of R=0.10. Trask's delay model was based on the observation that the number of delay cycles were approximately equal for each overload-underload, and that the crack length interval between successive overload-underload applications were large enough to facilitate the re-establishment of 'steady state' crack growth rates. Re-evaluating Trask's delay equation (previously given by Equation 4.70), after redefining the overload ratio such that OLR is given in terms of the definition used in the current investigation, one obtains the following 'equivalent' relations.

$$\log_{10} N_D = 2.0291\ \text{OLR} + 1.4255 \tag{7.24a}$$

$$N_D = 10^{2.0291\,OLR + 1.4255} \tag{7.24b}$$

The delay model is then used in conjunction with an existing crack growth model for constant amplitude loading to predict the total fatigue life (N_{tf}) of a given component. For example, using Trask's delay model (for a given number of tensile overloads (N_{OL})) in conjunction with the Paris model yields the following prediction for N_{tf}.

$$N_{tf} = \int_{a_i}^{a_f} \frac{da}{C_P \Delta K^{m_P}} + \sum_{i=1}^{N_{OL}} (N_D)_i \tag{7.25}$$

It is quite possible that such a model can be extended to not only consider variations in OLR, but also changes in stress ratio (R) and OL/UL ratio. Table 7.10 summarizes the delay data for each of the specimens tested during the current investigation. Recall that for each sample, there were three overload-underload applications, and therefore N_D was calculated as one-third of the difference between the experimental fatigue life and the corresponding Paris prediction.

Figure 7.31 suggests that relationships similar to Equation 7.24 exist for both R=0.10 and R=0.30, at various OL/UL ratios. It appears that all the functions shown exhibit a similar slope, but depict slightly different intercepts. Note that for a tensile overload only, which may be thought of as a large OL/UL ratio, the corresponding function is described using the largest intercept. The only questionable relationship is that corresponding to OL/UL=2.0 (for R=0.10), which could easily be attributed to the fact that only two specimens were tested at this OL/UL ratio, not to mention the possibility of appreciable variation between specimens.

P51[illegible]85.PDF [Page: 249 of 314]

Table 7.10 – Summary of delay data for each specimen

Specimen ID	Stress Ratio	OLR	OL/UL	Experimental		CAL (Paris)		Average N_D (Per Overload)
				N_d	N_{od}	N_c	N_{cal}	
VAL 8a	0.1	**1.20**	0.50	**158,000**	159,500	**151,486**	152,756	**2,212**
VAL 1a	0.1	**1.20**	1.00	**140,700**	142,000	**133,104**	134,063	**2,589**
VAL 7a	0.1	**1.20**	2.00	**168,200**	170,500	**159,056**	161,220	**3,070**
VAL 2a	0.1	**1.50**	1.00	**174,400**	176,000	**128,539**	130,259	**15,267**
VAL 6a	0.1	**1.67**	0.50	**198,000**	199,000	**139,750**	140,763	**19,415**
VAL 3a	0.1	**1.67**	1.00	**224,100**	224,300	**130,016**	130,345	**31,340**
VAL 3a-2	0.1	**1.67**	1.00	**221,300**	223,800	**125,496**	128,034	**31,928**
VAL 5a	0.1	**1.67**	2.00	**328,200**	330,100	**142,662**	144,476	**61,860**
VAL 4a	0.1	**1.83**	1.00	**304,700**	306,400	**120,320**	122,276	**61,417**
VAL 1b	0.3	**1.20**	1.00	**268,500**	270,500	**256,575**	258,581	**3,975**
VAL 1b-2	0.3	**1.20**	1.00	**262,300**	266,500	**250,856**	254,852	**3,849**
VAL 2b	0.3	**1.50**	1.00	**302,900**	305,700	**243,402**	246,283	**19,819**
VAL 2b-2	0.3	**1.50**	1.00	**347,200**	348,800	**269,344**	270,843	**25,969**
VAL 3b	0.3	**1.67**	1.00	**370,800**	372,400	**252,274**	254,231	**39,449**
VAL 3b-2	0.3	**1.67**	1.00	**436,000**	440,500	**286,791**	291,366	**49,724**
VAL 3b-3	0.3	**1.67**	1.00	**441,000**	443,800	**285,134**	288,263	**51,900**

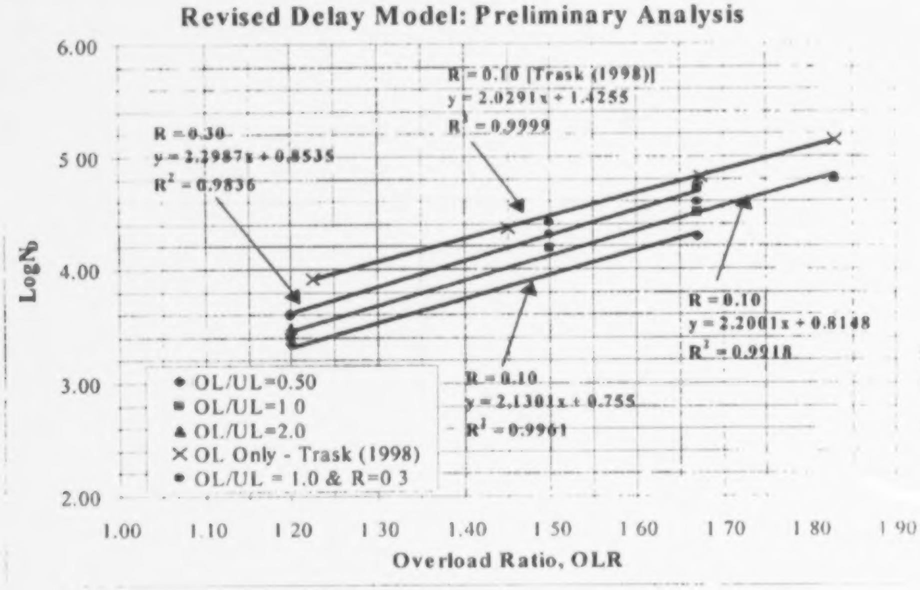

Figure 7.31 – Preliminary evaluation of revised delay model

Table 7.10 – Summary of delay data for each specimen

Specimen ID	Stress Ratio	OLR	OL/UL	Experimental		CAL (Paris)		Average N_D (Per Overload)
				N_{a1}	N_{a10}	N_{a1}	N_{a10}	
VAL 8a	0.1	**1.20**	0.50	**158,000**	159,500	**151,486**	152,756	**2,212**
VAL 1a	0.1	**1.20**	1.00	**140,700**	142,000	**133,104**	134,063	**2,589**
VAL 7a	0.1	**1.20**	2.00	**168,200**	170,500	**159,056**	161,220	**3,070**
VAL 2a	0.1	**1.50**	1.00	**174,400**	176,000	**128,539**	130,259	**15,267**
VAL 6a	0.1	**1.67**	0.50	**198,000**	199,000	**139,750**	140,763	**19,415**
VAL 3a	0.1	**1.67**	1.00	**224,100**	224,300	**130,016**	130,345	**31,340**
VAL 3a-2	0.1	**1.67**	1.00	**221,300**	223,800	**125,496**	128,034	**31,928**
VAL 5a	0.1	**1.67**	2.00	**328,200**	330,100	**142,662**	144,476	**61,860**
VAL 4a	0.1	**1.83**	1.00	**304,700**	306,400	**120,320**	122,276	**61,417**
VAL 1b	0.3	**1.20**	1.00	**268,500**	270,500	**256,575**	258,581	**3,975**
VAL 1b-2	0.3	**1.20**	1.00	**262,300**	266,500	**250,856**	254,852	**3,849**
VAL 2b	0.3	**1.50**	1.00	**302,900**	305,700	**243,402**	246,283	**19,819**
VAL 2b-2	0.3	**1.50**	1.00	**347,200**	348,800	**269,344**	270,843	**25,969**
VAL 3b	0.3	**1.67**	1.00	**370,800**	372,400	**252,274**	254,231	**39,449**
VAL 3b-2	0.3	**1.67**	1.00	**436,000**	440,500	**286,791**	291,366	**49,724**
VAL 3b-3	0.3	**1.67**	1.00	**441,000**	443,800	**285,134**	288,263	**51,900**

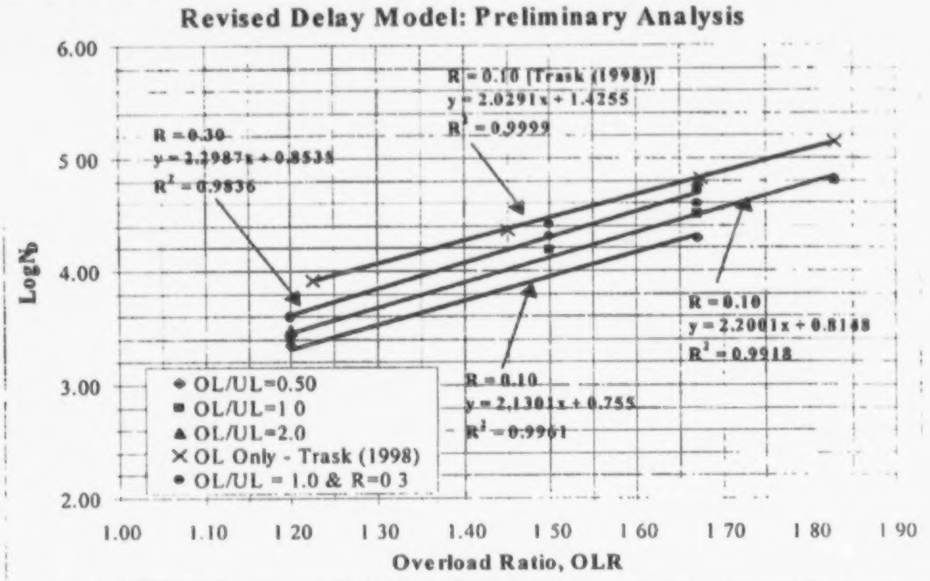

Figure 7.31 – Preliminary evaluation of revised delay model

Adopting a step-by-step approach to developing this delay model, the first task undertaken was to consider the effects of stress ratio (R) on N_D. After several attempts to include the effects of stress ratio, it was found that by plotting $\log_{10}(N_D \times (1-R)^2)$ versus OLR, the functions illustrated in Figure 7.31 for R=0.10 and R=0.30 (both at an OL/UL=1.0) could be consolidated onto a single curve, as illustrated in Figure 7.32 below. A linear regression of their combined data yields the following relation.

$$\log_{10}(N_D \cdot (1-R)^2) = 2.1917 \cdot OLR + 0.7192 \qquad 7.26a)$$

$$N_D = \frac{10^{2.1917 OLR + 0.7192}}{(1-R)^2} \qquad (7.26b)$$

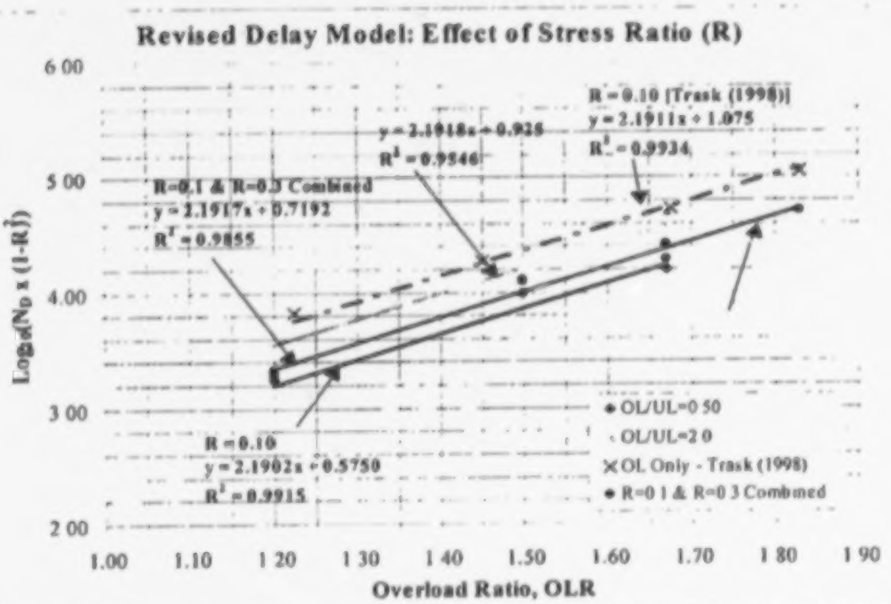

Figure 7.32 – Incorporation of stress ratio into revised delay model

Although this data consolidation for R=0.10 and R=0.30 was limited to an OL/UL ratio of 1.0, the slope of the function representing the consolidated data was found to be very close to those of the two curves corresponding to the original data. It was therefore estimated that the individual intercepts of the 'family of curves' illustrated in the figure above could be a function of the OL/UL ratio. If this were the case, Equation 7.26b could be described as

$$N_D = \frac{10^{2.1917\,OLR+\beta}}{(1-R)^2} \tag{7.26c}$$

where β may be assumed a function of OL/UL (i.e., β = *f*(OL/UL)). Unfortunately, the seemingly questionable relationship for OL/UL=2.0 (for reasons previously discussed), coupled with the uncertainty regarding the relative magnitude of OL/UL which constitutes a tensile overload only (i.e., no compressive underload), meant that only two data points were available with which to develop the function, namely those intercept values corresponding to OL/UL=0.50 and OL/UL=1.0.

In hopes of providing somewhat of a solution to the aforementioned problems, the slopes of the two curves representing OL/UL=2.0 and Trask's delay model were first adjusted to approximately equal the average slope of the remaining curves. As illustrated in Figure 7.32 above, their respective R^2 values (coefficients of determination) remained very high despite this adjustment, indicating that data correlation was still acceptable. This provided a third data point (i.e., intercept value) with which to evaluate the assumed relation, namely that corresponding to OL/UL=2.0. Secondly, in order to estimate an OL/UL ratio capable of approximating a tensile overload, and in doing so, determine a fourth data point, the following approach was taken. For a given overload ratio, there is a maximum OL/UL ratio above which $P_{min,UL} > P_{min,CAL}$. In such cases, the use of this parameter provides little information regarding the influence of compressive loading and is therefore not recommended beyond this upper limit OL/UL ratio. Imposing the requirement that $P_{min,UL}$ be approximately equal to or less than $P_{min,CAL}$, one could evaluate this upper bound OL/UL ratio via Equations 6.5 and 6.6 as follows

$$P_{min,UL} \le P_{min,CAL}$$

$$P_{max,CAL} \cdot \left[\left(\frac{1+R}{2}\right) - \frac{1}{OL/UL}\left(OLR - \left(\frac{1+R}{2}\right)\right)\right] \le R \cdot P_{max,CAL}$$

$$\left[\left(\frac{1+R}{2}\right)-\frac{1}{OL/UL}\left(OLR-\left(\frac{1+R}{2}\right)\right)\right]\leq R$$

$$\left(\frac{1+R}{2}\right)-R\leq\frac{1}{OL/UL}\left(OLR-\left(\frac{1+R}{2}\right)\right)$$

which finally yields

$$\frac{OL}{UL}\leq\frac{OLR-\left(\frac{1+R}{2}\right)}{\left(\frac{1+R}{2}\right)-R} \tag{7.27}$$

It can be shown that the upper limit described by the inequality of Equation 7.27 lies between two and three for most overload ratios. By temporarily labeling the predictions made using Trask's (1998) delay model (tensile overloads only) as those corresponding to OL/UL=3.0, a fourth data point is now available with which to evaluate the relationship between OL/UL and the corresponding intercept (β) of the curves in Figure 7.32 above. A least squares polynomial regression of β versus OL/UL ratio predicts excellent correlation between the two parameters, as illustrated in Figure 7.33 below. The relationship between β and OL/UL is summarized by Equation 7.28.

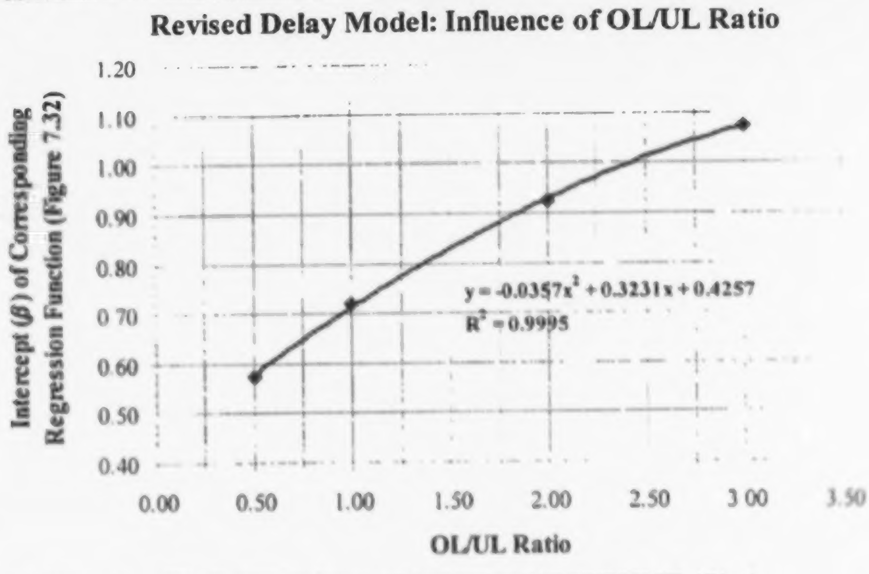

Figure 7.33 – Relationship between intercept (β) and OL/UL ratio

$$\beta = -0.0357 \cdot \left(\frac{OL}{UL}\right)^2 + 0.3231 \cdot \left(\frac{OL}{UL}\right) + 0.4257 \qquad (7.28)$$

Finally, incorporating the above relation into Equation 7.27c, one obtains the following expression for an exponential delay model similar to that proposed by Trask (1998), capable of predicting the number of delay cycles for a given overload application, while accommodating variations in not only overload ratio, but also stress ratio (R), and OL/UL ratio.

$$N_D = \frac{10^{2.1917\,OLR + \left(-0.0357\left(\frac{OL}{UL}\right)^2 + 0.3231\left(\frac{OL}{UL}\right) + 0.4257\right)}}{(1-R)^2} \qquad (7.29)$$

The results of the fatigue life predictions made using Equation 7.25 in conjunction with the delay model described by Equation 7.29 have been summarized in Table 7.11 below for a crack length interval a_i to a_f.

Table 7.11 – Fatigue life predictions based on delay model of Equation 7.29

Specimen ID	Stress Ratio	OLR	OL/UL	Experimental N_a	Delay Model Prediction (N_d)	% Error
VAL 8a	0.1	1.20	0.50	158,000	157,470	0.34
VAL 1a	0.1	1.20	1.00	140,700	141,266	-0.40
VAL 7a	0.1	1.20	2.00	168,200	172,477	-2.54
VAL 2a	0.1	1.50	1.00	174,400	165,632	5.03
VAL 6a	0.1	1.67	0.50	198,000	203,886	-2.97
VAL 3a	0.1	1.67	1.00	224,100	217,489	2.95
VAL 3a-2	0.1	1.67	1.00	221,300	212,969	3.76
VAL 5a	0.1	1.67	2.00	328,200	286,501	12.71
VAL 4a	0.1	1.83	1.00	304,700	316,451	-3.86
VAL 1b	0.3	1.20	1.00	268,500	270,067	-0.58
VAL 1b-2	0.3	1.20	1.00	262,300	264,348	-0.78
VAL 2b	0.3	1.50	1.00	302,900	304,718	-0.60
VAL 2b-2	0.3	1.50	1.00	347,200	330,660	4.76
VAL 3b	0.3	1.67	1.00	370,800	396,873	-7.03
VAL 3b-2	0.3	1.67	1.00	436,000	431,390	1.06
VAL 3b-3	0.3	1.67	1.00	441,000	429,733	2.55

Although Equation 7.29 may seem complex, the delay model is extremely easy to incorporate. Aside from a few minor variations, the model predictions are in good agreement with the experimental data. The proposed model predicts less than 8% error in all but one of the specimens tested. Moreover, a percent error of less than 4% was predicted for 12 of the 16 specimens. It should be noted that no data points were discarded in the development of this delay model, due to the fact that so few were available. Had more data been available, one could have discarded some of the potential outliers, thereby increasing the resulting accuracy of the model. Nevertheless, at each stage of model development, high coefficient of determination (R^2) values were maintained, indicating good correlation between the respective parameters. Figure 7.34 below graphically compares the experimental results with the model predictions, while Figure 7.35 further illustrates delay model predictions which have been extrapolated for several stress ratios and OL/UL ratios for which no experimental data was obtained.

PS16865.PDF (Page 254 of 314)

Table 7.11 – Fatigue life predictions based on delay model of Equation 7 29

Specimen ID	Stress Ratio	OLR	OL/UL	Experimental N_d	Delay Model Prediction (N_d)	% Error
VAL 8a	0.1	1.20	0.50	**158,000**	**157,470**	**0.34**
VAL 1a	0.1	1.20	1.00	**140,700**	**141,266**	**-0.40**
VAL 7a	0.1	1.20	2.00	**168,200**	**172,477**	**-2.54**
VAL 2a	0.1	1.50	1.00	**174,400**	**165,632**	**5.03**
VAL 6a	0.1	1.67	0.50	**198,000**	**203,886**	**-2.97**
VAL 3a	0.1	1.67	1.00	**224,100**	**217,489**	**2.95**
VAL 3a-2	0.1	1.67	1.00	**221,300**	**212,969**	**3.76**
VAL 5a	0.1	1.67	2.00	**328,200**	**286,501**	**12.71**
VAL 4a	0.1	1.83	1.00	**304,700**	**316,451**	**-3.86**
VAL 1b	0.3	1.20	1.00	**268,500**	**270,067**	**-0.58**
VAL 1b-2	0.3	1.20	1.00	**262,300**	**264,348**	**-0.78**
VAL 2b	0.3	1.50	1.00	**302,900**	**304,718**	**-0.60**
VAL 2b-2	0.3	1.50	1.00	**347,200**	**330,660**	**4.76**
VAL 3b	0.3	1.67	1.00	**370,800**	**396,873**	**-7.03**
VAL 3b-2	0.3	1.67	1.00	**436,000**	**431,390**	**1.06**
VAL 3b-3	0.3	1.67	1.00	**441,000**	**429,733**	**2.55**

Although Equation 7.29 may seem complex, the delay model is extremely easy to incorporate. Aside from a few minor variations, the model predictions are in good agreement with the experimental data. The proposed model predicts less than 8% error in all but one of the specimens tested. Moreover, a percent error of less than 4% was predicted for 12 of the 16 specimens. It should be noted that no data points were discarded in the development of this delay model, due to the fact that so few were available. Had more data been available, one could have discarded some of the potential outliers, thereby increasing the resulting accuracy of the model. Nevertheless, at each stage of model development, high coefficient of determination (R^2) values were maintained, indicating good correlation between the respective parameters. Figure 7.34 below graphically compares the experimental results with the model predictions, while Figure 7.35 further illustrates delay model predictions which have been extrapolated for several stress ratios and OL/UL ratios for which no experimental data was obtained.

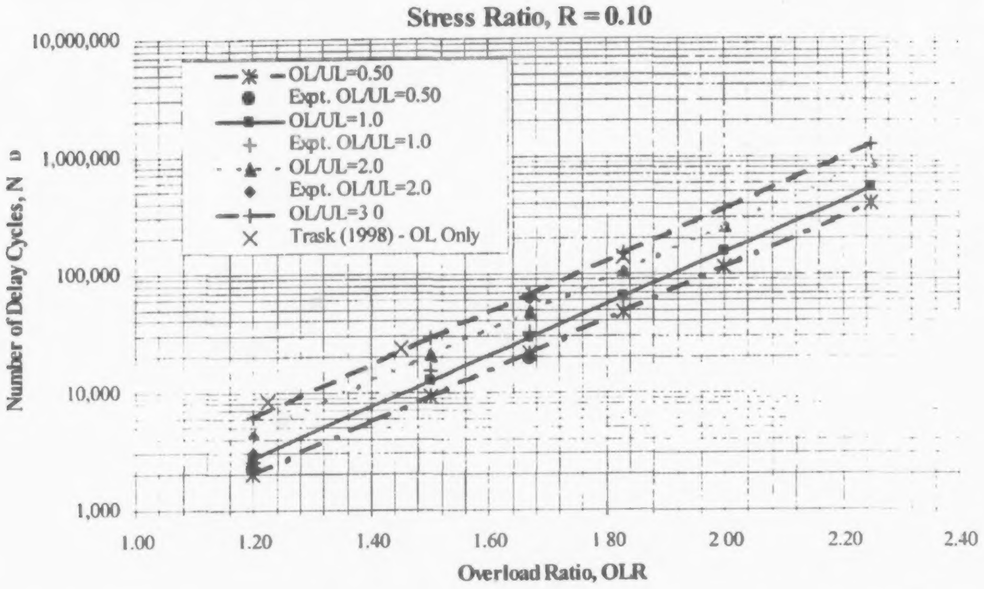

Figure 7.34 – Graphical comparison of delay model predictions and experimental data

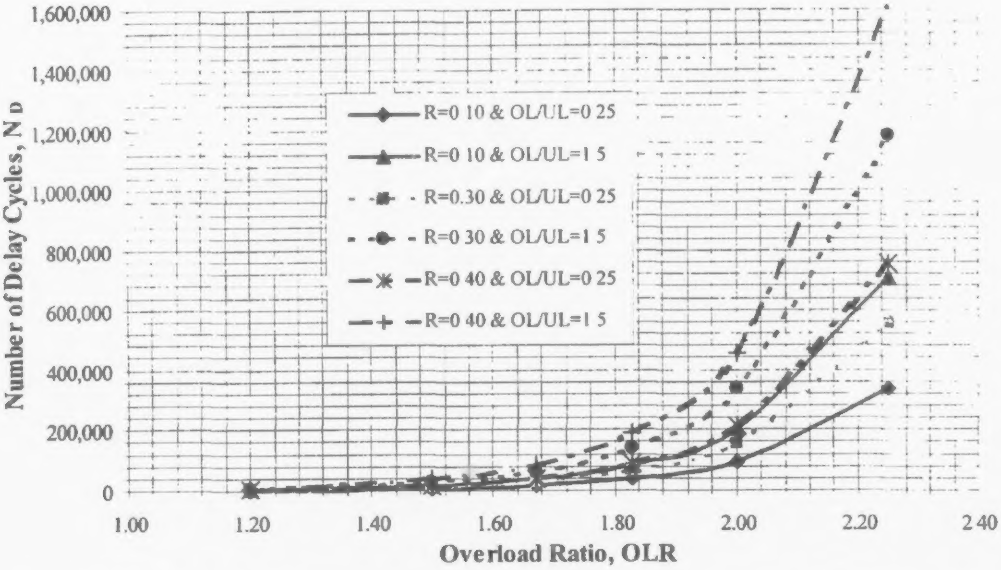

Figure 7.35 – Delay model predictions illustrating influence of R and OL/UL ratio on N_D

Although the model appears to provide adequate predictions and considers the effect of several key parameters, verification against the experimental results of future testing under similar loading sequences is nevertheless recommended. It should also be re-affirmed that the proposed delay model is based on the application of intermittent overload-underload sequences at crack length intervals between which ‘steady state’ (i.e., constant amplitude) crack growth rates may be re-established. The model is also based on the observation that N_D is approximately equal for all overload-underload applications within a single test. However, if this latter condition were not the case, a suitable proportioning technique could be employed (in conjunction with sound experience-based engineering judgement) to properly allocate the total number of delay cycles. Finally, it should be noted that although the proposed model was used in conjunction with the Paris model for CAL, any suitable constant amplitude crack growth model may be employed.

Chapter 8
Conclusions and Recommendations

8.1 Conclusions

A variety of aspects in the fields of fracture mechanics, fatigue, and fatigue crack propagation were reviewed in the first five chapters of this report, as well as a number of methodologies employed in fracture control and repair. It is hoped that the information provided in these chapters will not only educate the reader, but also provide him or her with the tools necessary to perform a variety of fatigue- and fracture-related analyses.

In Chapter 4, a number of constant amplitude and variable amplitude fatigue crack growth models were discussed. There is great variation amongst these models, with respect to modeling approach, parameters considered (i.e., stress ratio and fracture toughness, for example), the number of calibration parameters required (empirical or otherwise), relative ease of use, and the required computational effort. Unfortunately, few of these models bear any physical or practical significance and many will see only limited use due to their inherent complexity. Moreover, despite the enormous number of models currently available, a reliable all-encompassing fatigue crack growth model has yet to be developed.

Chapters 6 and 7 focused on the experimental testing program employed to investigate the fatigue crack growth of center-cracked 350WT steel specimens subjected to semi-random loading sequences comprised of a number of intermittent tensile overloads and compressive underloads. A significant amount of information has been gained regarding post-overload and post-underload fatigue crack growth behavior. Minor modifications to the Wheeler model have been proposed to facilitate the incorporation of fatigue crack acceleration phenomena into the model's fatigue life predictions. A revised delay model was also proposed to consider the effects of a number of parameters on the crack growth retardation produced by a given tensile overload or tensile overload/compressive underload sequence. Finally, a preliminary finite element analysis was performed to investigate the extent to which crack tip plasticity develops when a tensile overload is followed by a compressive underload of equal magnitude. In addition to the aforementioned investigation, the fatigue crack growth threshold behavior of 350WT steel was also examined.

Based on the findings of this report, the following conclusions may be made:

1. The resulting threshold stress intensity factors from all tests (average value of K_{th}=5.56 MPa$\sqrt{m}$) compared relatively well with the limiting value of 6.00 MPa$\sqrt{m}$ (for R=0) suggested by Barsom et al (1987). Although K_{th} is an important parameter in the Zheng and Hirt model, Trask (1998) demonstrated that the accuracy the model's predictions very sensitive to the selected value of K_{th}, with modest variations in the threshold stress intensity typically yielding significant errors in the fatigue life predictions. Results of the current investigation have shown that the Zheng and Hirt predictions using the experimentally determined threshold stress intensity factor grossly underestimate those made using the two-curve Paris model. In fact, the value of K_{th} required to reduce this error to an acceptable level is almost twice the value obtained experimentally. Alternatively, as discussed in section 7.5.1, it may be feasible to scale the experimental threshold stress intensity by some factor prior to incorporating it into the Zheng and Hirt model. A second alternative may involve extrapolation of the fatigue rate curve to determine a 'pseudo threshold stress intensity factor' which can be used to improve the accuracy of the Zheng and Hirt predictions.

2. Based on the crack length at which yielding occurred, a 'cyclic' yield stress was calculated and found to be some 5.33% greater than the specified static yield stress, similar to that observed by Trask (1998). This observation suggests the potential of material strain hardening due to cyclic loading, which although small, is a factor not considered by most fatigue crack growth laws.

3. The minimum fatigue crack growth rate reached following a tensile overload reduces with increasing overload ratio, which translates into a corresponding increase in the amount of crack growth retardation that results. Moreover, when a compressive underload follows a tensile overload, the corresponding reduction in fatigue crack

growth retardation can be quantified by varying the ratio of the tensile overload to the compressive underload (OL/UL). As intuitively expected, the amount of retardation is typically greater for higher OL/UL ratios, simply due to the fact that for a higher OL/UL ratio, there is a smaller compressive underload, which is the factor responsible for crack growth acceleration.

4. The notion of a compressive plastic zone is somewhat questionable in much of the literature, as it is generally thought that upon closure of a propagating crack, the applied stress is distributed uniformly across the crack faces (as if there were no crack) and no additional crack growth occurs until the crack re-opens once again. However, it was found that for a given OLR, variations in the magnitude of the applied compressive underload (i.e., the OL/UL ratio) have a significant effect on the degree of crack growth retardation caused by the preceding tensile overloads. This observation suggests the existence of some type of 'compressive plastic zone'.

5 The modified Wheeler model appears to provide accurate fatigue life predictions and considers the sequence effects on the fatigue crack growth of specimens subjected to intermittent tensile and compressive overloads via the use of an 'effective' plastic zone. While the modified Wheeler provides no improvement in predictive accuracy over the original Wheeler model, it does give some physical significance to an otherwise empirical approach to modeling the reduction in crack growth retardation due to a compressive underload.

6. Regression of the test parameters for the Wheeler model predictions revealed that a family of curves may exist, at any stress ratio, which can describe the Wheeler shaping exponent 'm' as a function of OLR for a given OL/UL ratio. Similarly, it is possible that a family of curves exists at a given OL/UL ratio, which is capable of describing this 'm' versus OLR correlation for any stress ratio.

7. It is quite likely that when viewed on a microscopic scale, the path of a propagating fatigue crack may not be perfectly linear, but instead may exhibit a somewhat jagged

nature. Moreover, the faces of such jagged cracks may not match exactly upon crack closure, thereby potentially inducing a 'prying effect' at the crack tip, thus presenting a mechanism capable of accelerating the subsequent crack growth. In addition, small-scale mixed-mode loading (a combination of shear and tensile modes) would occur under such conditions. In realization of the microscopic scale on which this phenomenon is viewed, it is expected that the resulting compressive plastic zone will be much smaller than the tensile plastic zone produced by the same ΔK. To confirm the aforementioned theory regarding 'prying effects' at the crack tip, a more detailed finite element analysis should be performed to simulate the existence of mis-matched crack faces and investigate their effect on the crack tip plastic zone and mixed mode crack growth.

8. A nonlinear finite element analysis was performed on a typical specimen (using the NISA finite element package) to investigate the crack tip plasticity under a typical overload/underload sequence. Gap elements were used to bridge the crack faces and ensure that fictitious overlapping did not occur under compressive loading. Elements surrounding the crack tip were refined to an approximate size on the order of 10/1000ths of the specimen thickness. During the FE analysis, the following observations were made:
    - Upon returning to zero load from a maximum tensile load, it was found that a large zone of residual compressive stresses, including a smaller compressive 'yield zone' had developed at the crack tip, along with a zone of residual tensile stresses further from the crack tip. It was noted that similar, yet smaller stress distributions were observed during the few load increments prior to reaching zero load. The development of this zone of crack tip compressive stresses helps to explain the observed phenomenon of crack growth retardation following a tensile overload.
    - Under maximum compression, the material within a small region ahead of the crack tip had yielded in compression. It was found that this zone is smaller than that developed under an equivalent tensile load, as previously anticipated.

- Upon return to zero load from the minimum compressive load, a large zone of residual compressive stresses was observed in a portion of the uncracked ligaments. More importantly, however, is the development of a bean-shaped zone of tensile stresses at the crack tip, the center portion of which depicted a small yield zone. This zone of crack tip tensile stresses would tend to accelerate a propagating fatigue crack somewhat, thereby contributing to the observed reduction in crack growth retardation observed for a given tensile overload/compressive underload sequence.
- Similar trends were observed when the crack face separation was reduced to one-tenth of its original value, the main difference being a significant reduction in the relative size of the plastic zones created under the compressive portion of the loading sequence.

9. At each overload ratio investigated, it was noticed that the ratio of fatigue lives N_{VAL}/N_{CAL} was nearly identical for both $R = 0.1$ and $R = 0.3$ at an OL/UL =1.0. This observation led to the development of a delay model with the capacity to include the effects of not only overload ratio, but also stress ratio and overload/underload ratio, as described by Equation 7.29. Although seemingly complex, the proposed delay model is extremely easy to incorporate and provided fatigue life predictions which were generally in good agreement with the experimental data.

8.2 Recommendations for Future Investigations

The experimental testing program described herein was the second phase of a multi-phase, systematic investigation into fatigue crack growth behavior of specimens (center-cracked in this case) to a variety of commonly occurring loading sequences. This second phase accomplished a number of objectives previously suggested from the initial phase of this investigation, including:

1. Fatigue crack growth threshold testing to evaluate a suitable value of ΔK_{th} for use in the Zheng and Hirt model for fatigue crack growth under constant amplitude loading.

2. An investigation into the reduction in tensile overload–induced crack growth retardation when a tensile overload is immediately followed by a compressive underload.

3. The effects of varying both OLR and OL/UL ratio were investigated in order to help quantify the extent to which this 'reduction in retardation' occurs.

4. The crack growth retardation predictions (i.e., in terms of N_D) made using the delay model previously proposed by Trask (1998) were compared with the results of the current investigation. The results were then collectively used to facilitate the development of a 'revised' delay model, which shows potential capabilities of accounting for the effects of stress ratio (R), overload ratio (OLR), and tensile overload-to-compressive underload ratio (OL/UL) on post-overload crack growth behavior.

Recommendations for future experimental work include:

1. Verification of the threshold stress intensity factor (K_{th}) for this 350WT steel and compare with the average value obtained for the current investigation (5.56 MPa$\sqrt{m}$).

2. Briefly investigate the possibility of using a 'scaling factor' or suitable extrapolation of fatigue rate data to determine a K_{th} which will reduce the error in the Zheng and Hirt model predictions. Perhaps there is a correlation between the experimental threshold stress intensity factor (K_{th}) and the one that accurately predicts the crack growth behavior. For example, the Zheng and Hirt model may require a slight modification as follows

$$\frac{da}{dN} = \frac{1}{2\pi E \sigma_f \varepsilon_f} \cdot \left(K_{max} - \alpha \cdot K_{th}\right) \tag{8.1}$$

where: $\alpha = f\left(\frac{K_{th,extrapolated}}{K_{th,experimental}}\right)$

As an alternative, the fatigue rate data may be extrapolated to the y-axis, and the y-intercept taken as an extrapolated K_{th}. The fact that the actual K_{th} would no longer be employed in the model is really of no importance if the modification described by Equation 8.1 were to provide a means of consistently predicting the crack growth behavior with reasonable accuracy. Performing both a threshold test and a CAL fatigue test on two aluminum specimens, for example, could assess the acceptability of this modification. The extrapolated threshold stress intensity factor could then be compared to that obtained experimentally and subsequently correlated to similar tests on steel to see if there is, in fact, a consistent relation.

3. As indicated by the da/dN-versus-ΔK curve for OLR=1.83 (Appendix B), the re-establishment of 'steady-state' (i.e., CAL) crack growth rates between successive overload applications is somewhat questionable for such high overload ratios. Therefore, it is theoretically possible to 'optimize' the amount of crack growth retardation (i.e., maximize N_D), thereby maximizing the potential for extended service life of a cracked structural component (say, a piping system containing part-through fatigue cracks). For example, consider the plastic zones produced by two overloads, as illustrated in Figure 8.1 below.

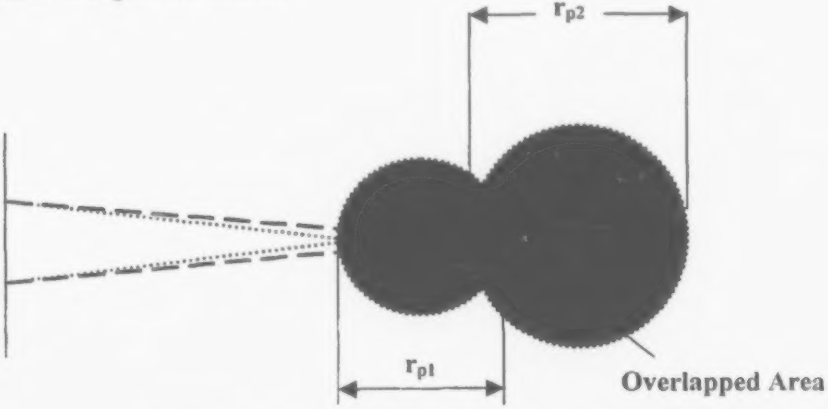

Figure 8.1 – Overlapping plastic zones

By applying multiple overloads at intervals such that the overlapped area between their plastic zone boundaries is minimized, one should obtain the maximum amount of retardation in the ensuing crack growth. One could investigate this by applying the same overload ratio to a set of test specimens, while varying the crack growth interval (Δa) between which the overloads are applied.

4. Investigate the relative reduction in crack growth retardation produced by a compressive underload when it is applied prior to applying a tensile overload. In a realistic sense, consider two elements on the hull of a ship: one near the deck and a second near the keel. As a ship sails through stormy weather, its hull will be subjected to a loading sequence comprised of both hogging and sagging moments. For a ship hull subjected to a hogging moment followed by a sagging moment, an element closer to the deck will experience a tensile stress followed by a compressive stress, whereas an element near the keel will experience the opposite; that is, a compressive stress followed by a tensile stress.

5. Based on the use of actual values for crack face separation, an FE investigation similar to that performed herein could be undertaken to correlate the size of the resulting compressive plastic zone with experimentally observed crack growth phenomena, in terms of both reductions in crack growth retardation and crack growth accelerations. Such an investigation could be used in conjunction with experimental results to improve the 'effective' plastic zone definition upon which the modified Wheeler model is based. In addition, one could also perform a finite element analysis to investigate the effects of mismatched crack faces and mixed-mode loading on the formation of residual tensile stresses at the crack tip under compressive loading.

6. Further testing based on the application of both overload/underload and underload-only loading sequences to verify the proposed modifications to the Wheeler retardation parameter.

7. Although the revised delay model appears to provide reasonably accurate fatigue life predictions and considers the effect of several key parameters, verification against the experimental results of future testing under similar loading sequences is recommended. For example, testing should be done to obtain more data from those OL/UL ratios investigated in the current study, as well as at intermediate values of OL/UL which were not considered.

8. If feasible, an investigation should be undertaken to evaluate the fatigue crack growth behavior of 350WT steel under more realistic, random loading sequences. The selection of crack growth models best capable of characterizing such crack growth should also be reported.

References

1. Anderson, T.L., *Fracture Mechanics. Fundamentals and Applications.* Second Edition, CPR Press, Inc., Florida, 1995.

2. Barsom, John M. and Rolfe, Stanley T., *Fracture and Fatigue Control in Structures Applications of Fracture Mechanics.* Second Edition, Prentice Hall, Englewood Cliffs, New Jersey, 1987.

3. Broek, David, *Elementary Engineering Fracture Mechanics.* Third Edition, Kluwer Academic Publishers, Netherlands, 1982.

4. Broek, David, *The Practical Use of Fracture Mechanics.* Kluwer Academic Publishers, Netherlands, 1989.

5. Chang, J.B., "Round-Robin Crack Growth Predictions on Center-Cracked Tension Specimens under Random Spectrum Loading," *Methods and Models for Predicting Fatigue Crack Growth under Random Loading*, ASTM STP 748, J.B. Chang and C.M. Hudson, Eds., American Society for Testing and Materials, 1981. pp. 3-40.

6. Cheng, X., Okuhara, Y., Kondo, A., and Yamada, K., "Fatigue Crack Growth Rate Measurement of Structural Steel Under Overload Conditions," *Journal of Structural Engineering and Earthquake Engineering*, Vol. 11, No. 1, April 1994, pp. 71-78.

7. Collins, Jack A., *Failure of Materials in Mechanincal Design Analysis, Prediction, Prevention.* Second Edition, John Wiley & Sons, New York, 1993.

8. Domazet, Z., "Comparison of Fatigue Crack Retardation Methods," *Engineering Failure Analysis*, Vol. 3, No. 2, 1996, pp. 137-147.

9. Dowling, Norman E., *Mechanical Behavior of Materials EngineeringMethods for Deformation, Fracture, and Fatigue.* Prentice Hall, Englewood Cliffs, New Jersey, 1993.

10. Engineering Mechanics Research Corporation, *NISA II/DISPLAY III User's Manual.* EMRC, Michigan, 1998.

11. Etube, L.S., Brennan, F.P., and Dover, W.D., "Prediction of Fatigue Crack Growth in Offshore Structures Using a Sea State Equivalent Stress Concept," *Proceedings of the 8th (1998) International Offshore and Polar Engineering Conference*, 1998, pp. 95-101.

12. Hammouda, M., Ahmad, S., Seleem, M., and Sallam, H., "Fatigue Crack Growth Due To Two Successive Single Overloads," *Fatigue and Fracture of Engineering Materials and Structures*, Vol. 21, 1998, pp. 1537-1547.

13. Hudson, C.M., "A Root-Mean-Square Approach for Predicting Fatigue Crack Growth under Random Loading," *Methods and Models for Predicting Fatigue Crack Growth under Random Loading*, ASTM STP 748, J.B. Chang and C.M. Hudson, Eds., American Society for Testing and Materials, 1981, pp. 41-52.

14. Johnson, W.S., "Multi-Parameter Yield Zone Model for Predicting Spectrum Crack Growth," *Methods and Models for Predicting Fatigue Crack Growth under Random Loading*, ASTM STP 748, J.B. Chang and C.M. Hudson, Eds., American Society for Testing and Materials, 1981, pp. 85-102.

15. Kim, C.Y. and Song, J.H., "Fatigue Crack Closure and Growth Behavior under Random Loading," *Engineering Fracture Mechanics*, Vol. 49, No. 1, 1994, pp. 105-120.

16. Kulak, G.L., Adams, P.F., and Gilmor, M.I., *Limit States Design in Structural Steel*. Fifth Edition, Canadian Institute of Steel Construction, Universal Offset Limited, Ontario, 1995.

17. Kumar, R., Kumar, A, and Kumar, S., "Delay Effects in Fatigue Crack Propagation," *International Journal of Pressure Vessels and Piping*, Vol. 67, 1996, pp. 1-5.

18. Lampman, Steven R., Ed. *ASM Handbook, Volume 19· Fatigue and Fracture*. ASM International, USA, 1996.

19. Lang, M. and Marci, G., "The Influence of Single and Multiple Overloads on Fatigue Crack Propagation," *Fatigue and Fracture of Engineering Materials and Structures*, Vol. 22, 1999, pp. 257-271.

20. Lui, A.F., *Structural Life Assessment Methods*. ASM International, USA, 1998.

21. Rice, Richard C., *Fatigue Design Handbook*. Second Edition, Society of Automotive Engineers, PA, 1988.

22. Rosenberg, G., "The Influence of Yield Strength on Overload Affected Crack Growth Rate Behavior in Steels," *Metalurgija*, Vol. 38, No. 2, 1999, pp. 81-85.

23. Rudd, J.L. and Engle, R.M., Jr., "Crack Growth Behavior of Center-Cracked Panels under Random Spectrum Loading," *Methods and Models for Predicting Fatigue Crack Growth under Random Loading*, ASTM STP 748, J.B. Chang and C.M. Hudson, Eds., American Society for Testing and Materials, 1981, pp. 103-114.

24. Salpekar, S.A., Raju, I.S., and O'Brien, T.K., "Strain Energy Release Rate Analysis of the End-Notched Flexure Specimen Using the Finite-Element Method," *Journal of Composite Technology and Research*, Vol. 10, No. 4, 1988, pp.133-139.

25. Schijve, J., Skorupa, A., Skorupa, M., and Zachwieja, A., "Experimental Results and Predictions on Crack Growth In a Structural Steel Under Periodically Applied Single and Multiple Overloads," *17th International Conference on Offshore Mechanics and Arctic Engineering*, ASME, 1998.

26. Sheu, B.C., Song, P.S., and Hwang, S., "Shaping Exponent in Wheeler Model under a Single Overload," *Engineering Fracture Mechanics*, Vol.51, No. 1, 1995, pp.135-143.

27. Suresh, S., *Fatigue of Materials*. Second Edition, Cambridge University Press, UK, 1998.

28. Szamossi, M., Lui, K.W., and Chang, J.B., "Random Spectrum Fatigue Crack Life Predictions With or Without Considering Load Interactions," *Methods and Models for Predicting Fatigue Crack Growth under Random Loading*, ASTM STP 748, J.B. Chang and C.M. Hudson, Eds., American Society for Testing and Materials, 1981, pp. 115-132.

29. Trask, D., *Review of Fracture Mechanics and Fatigue Crack Propagation Analysis*. MASc Report, Technical University of Nova Scotia, 1997.

30. Trask, D., *Experimental and Numerical Investigation Into Fatigue Crack Propagation Models for 350WT Steel*. MASc. Thesis, Technical University of Nova Scotia, 1998.

31. Tur, Y.K. and Vardar, O., "Periodic Tensile Overloads in 2024-T3 Al-Alloy," *Engineering Fracture Mechanics*, Vol. 53, No. 1, 1996, pp. 69-77.

32. Wasen, J. and Heier, E., "Fatigue Crack Growth Thresholds – The Influence of Young's Modulus and Fracture Surface Roughness," *International Journal of Fatigue*, Vol. 20, No. 10, 1998, pp. 737-742.

33. Wang, Wei and Hsu, Cheng Tsu Thomas, "Fatigue Crack Growth Rate of Metal by Plastic Energy Damage Accumulation Theory," *Journal of Engineering Mechanics*, Vol. 120, No. 4, April 1994, pp. 776-795.

34. Willenborg, J.D., Engle, R.M., and Wood, H.A., "A Crack Growth Retardation Model Using an Effective Stress Concept," Report AFFDL-TM-71-1-FBR, Air Force Flight Dynamics Laboratory, Wright-Patterson Air Force Base, Dayton, Ohio, January 1971.

35. Zheng, Xiulin and Hirt, M.A., "Fatigue Crack Propagation in Steels," *Engineering Fracture Mechanics*, Vol. 48, No. 3, June 1994, pp. 965-973.

Appendix A

Fatigue Crack Growth Data for Threshold Testing

SAMPLE DATA SHEET

PRECRACKING DATA --- K_{th} - #4

[redacted]

da/dN	Crack Tip Position (mm)			da/dN	Average	ΔK
(LT)	Left	Cycles	Right	(RT)	"2a/W"	(MPa-m$^{0.5}$)
N/A	12.83	0	13.07	N/A	N/A	N/A
1.07E-08	12.91	7500	13.11	5.33E-09	0.257	20.36
2.55E-08	13.05	13000	13.13	3.64E-09	0.258	20.43
1.29E-08	13.14	20000	13.19	8.57E-09	0.260	20.50
1.80E-08	13.23	25000	13.22	6.00E-09	0.261	20.56
1.20E-08	13.29	30000	13.28	1.20E-08	0.262	20.61
2.20E-08	13.40	35000	13.39	2.20E-08	0.264	20.69

THRESHOLD DATA (Load Shedding Technique) --- K_{th} - #4

[redacted]

	da/dN	Crack Tip Position (mm)			da/dN	Average	ΔK
P_{max} (N)	(LT)	Left	Cycles	Right	(RT)	"2a/W"	(MPa-m$^{0.5}$)
50000	5.00E-08	13.75	42000	13.73	4.86E-08	0.269	20.90
50000	4.67E-08	13.89	45000	13.86	4.33E-08	0.273	21.12
45000	2.57E-08	14.07	52000	14.00	2.00E-08	0.276	19.13
45000	2.50E-08	14.20	57200	14.16	3.08E-08	0.279	19.25
45000	2.50E-08	14.28	60400	14.24	2.50E-08	0.282	19.35
40600	1.82E-08	14.32	62600	14.28	1.82E-08	0.283	17.50
40600	1.22E-08	14.35	65063	14.32	1.62E-08	0.284	17.53
40600	1.22E-08	14.41	70000	14.37	1.01E-08	0.284	17.56
40600	2.17E-08	14.66	81500	14.63	2.26E-08	0.287	17.68
36600	1.00E-08	14.70	85500	14.67	1.00E-08	0.290	16.03
36600	1.36E-08	14.87	98010	14.83	1.28E-08	0.292	16.10
33000	3.24E-09	14.88	101100	14.84	3.24E-09	0.294	14.57
33000	4.39E-09	14.93	112500	14.88	3.51E-09	0.295	14.59
33000	1.31E-08	15.43	150800	15.35	1.23E-08	0.300	14.75
29800	8.10E-09	15.60	171800	15.50	7.14E-09	0.306	13.49
29800	7.50E-09	15.63	175800	15.52	5.00E-09	0.308	13.54
29800	4.76E-09	15.65	180000	15.55	7.14E-09	0.309	13.56
26800	6.00E-09	15.68	185000	15.59	8.00E-09	0.309	12.21
26800	3.75E-09	15.71	193000	15.60	1.25E-09	0.310	12.22
26800	7.14E-09	15.76	200000	15.64	5.71E-09	0.310	12.24
24200	1.43E-09	15.77	207000	15.65	1.43E-09	0.311	11.06
24200	3.75E-09	15.80	215000	15.67	2.50E-09	0.311	11.07
24200	5.33E-09	15.88	230000	15.76	6.00E-09	0.312	11.09
24200	2.00E-09	15.89	235000	15.77	2.00E-09	0.313	11.12
21800	2.86E-09	15.93	249000	15.80	2.14E-09	0.314	10.02
21800	2.31E-09	15.96	262000	15.84	3.08E-09	0.315	10.04
21800	1.67E-09	15.97	268000	15.85	1.67E-09	0.315	10.04

Figure A.1 – Sample data sheet for threshold testing

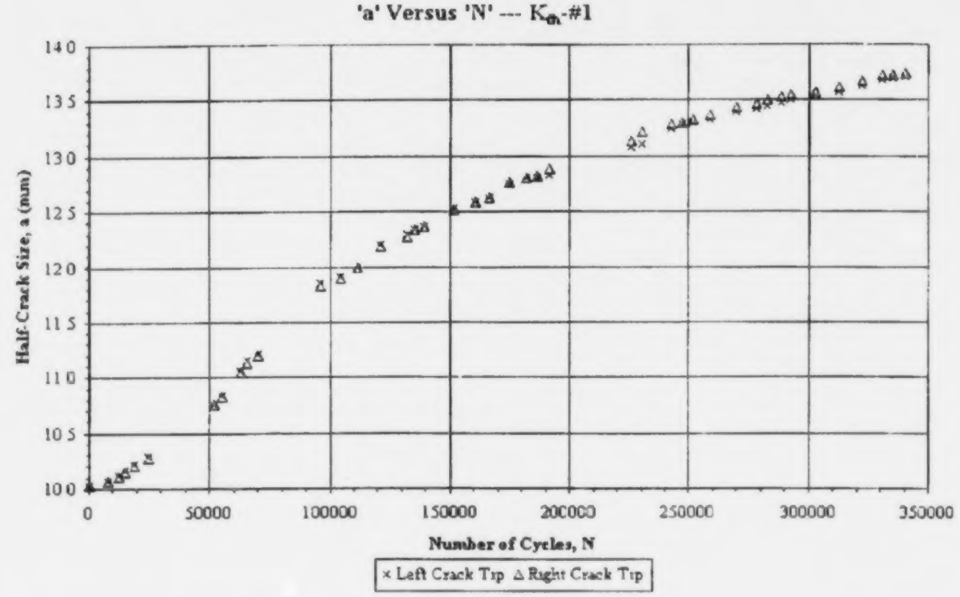

'a' Versus 'N' --- K_{th}-#1

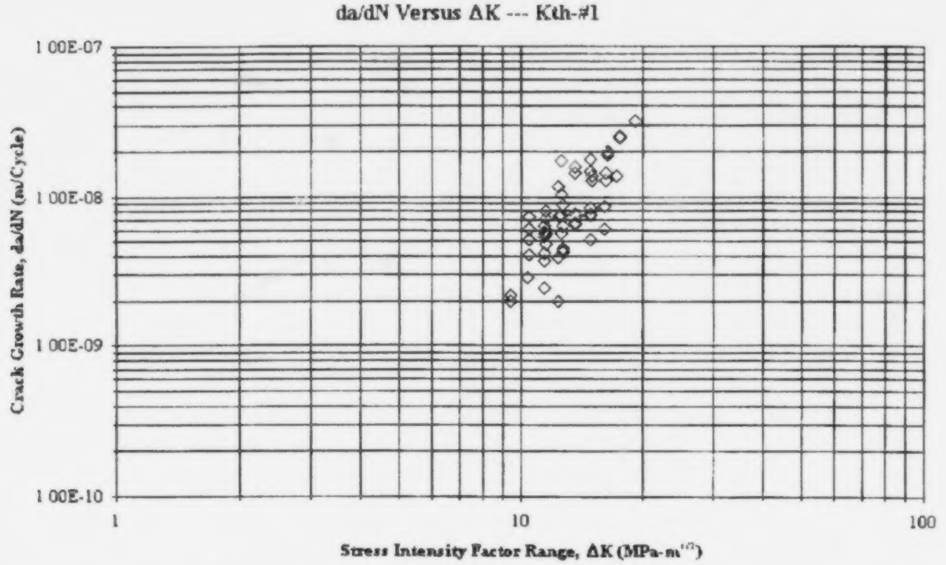

da/dN Versus ΔK --- Kth-#1

Figure A 2 – 'a-versus-N' data and fatigue rate data for specimen K_{th}#1

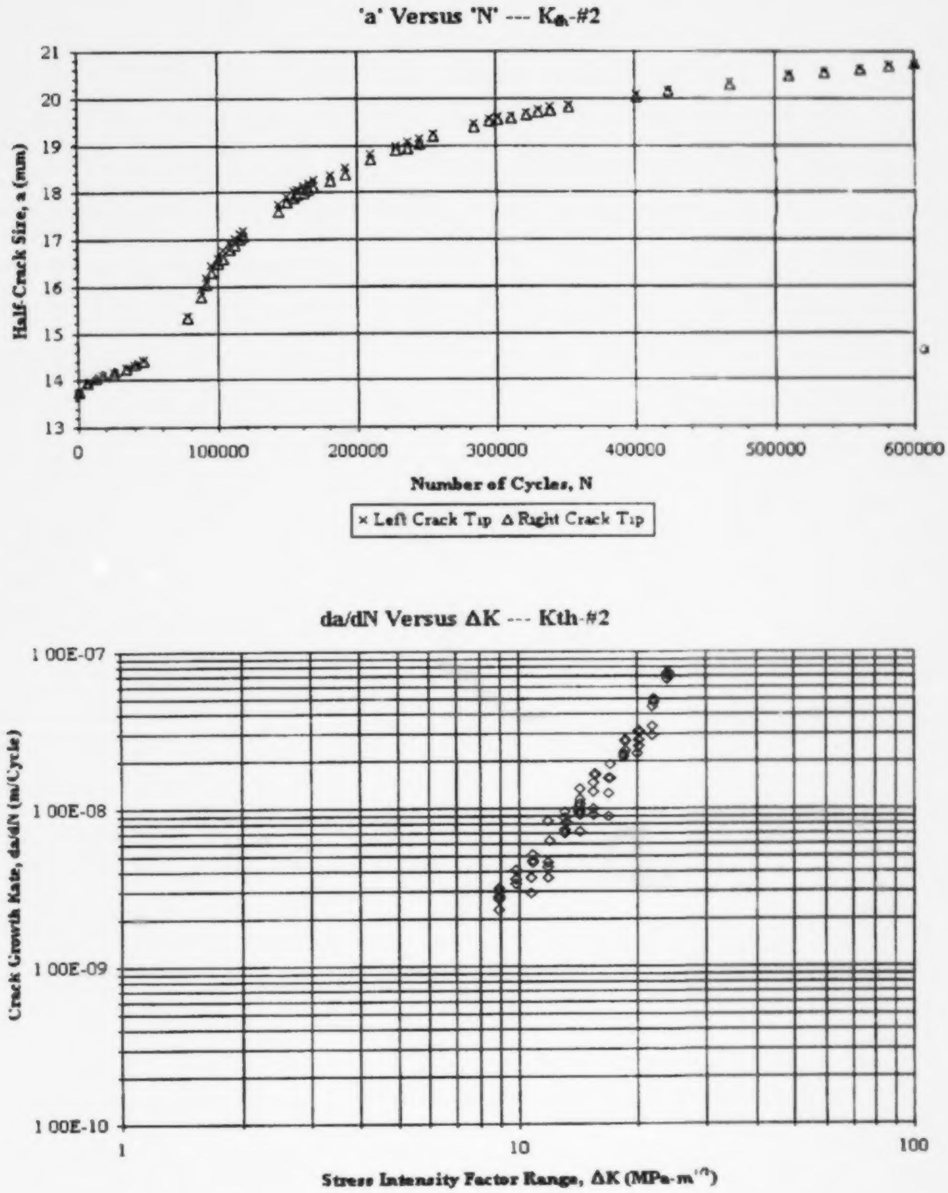

Figure A.3 – 'a-versus-N' data and fatigue rate data for specimen K_{th}#2

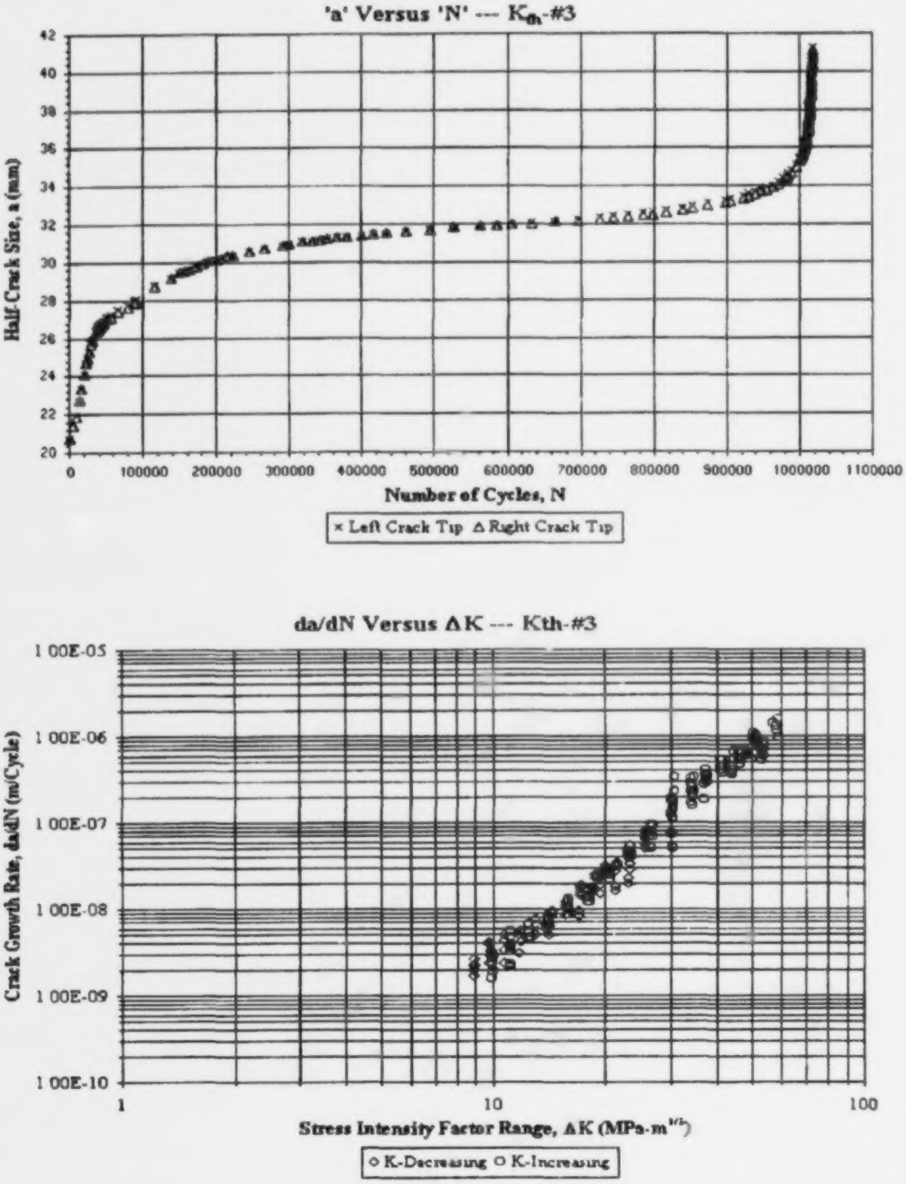

Figure A.4 – 'a-versus-N' data and fatigue rate data for specimen K_{th}#3

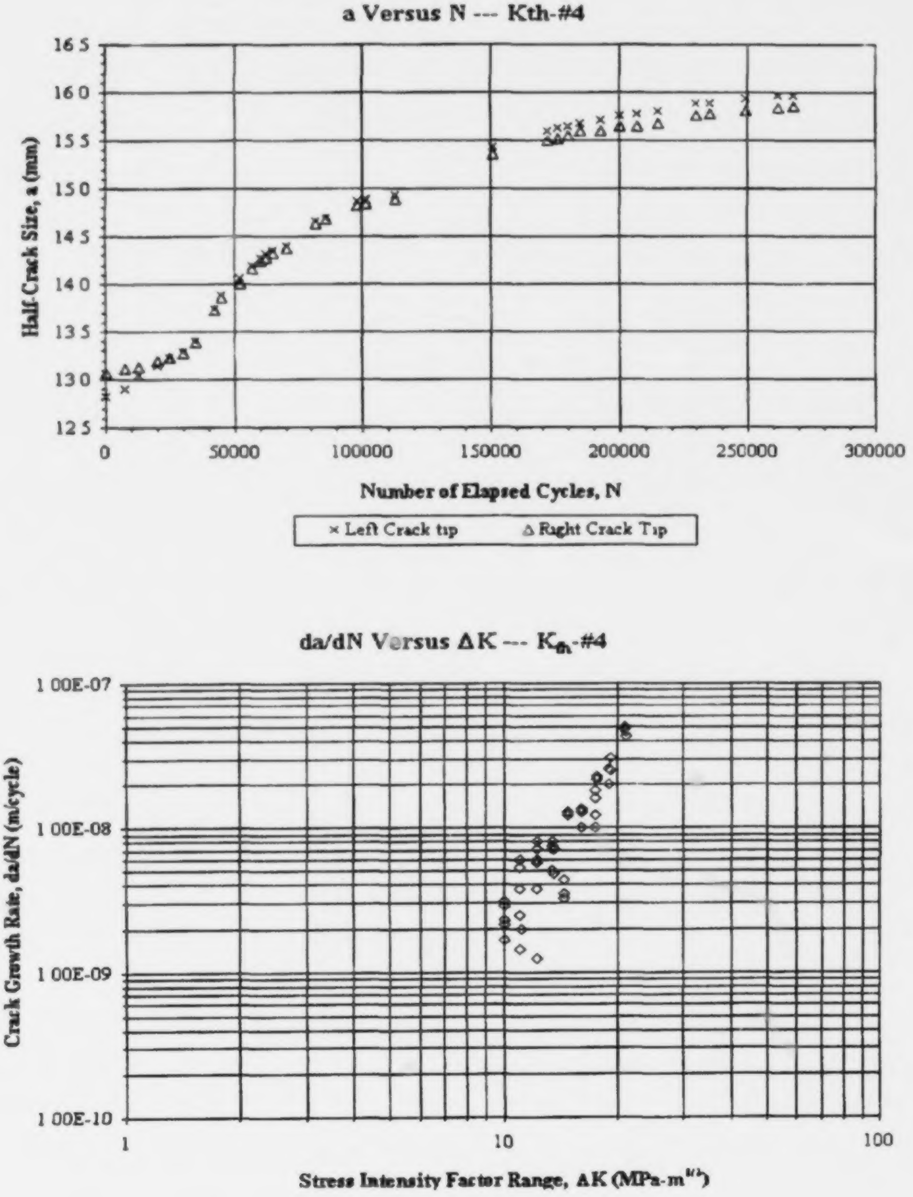

Figure A.5 – ‘a-versus-N’ data and fatigue rate data for specimen K_{th}#4

Appendix B

Fatigue Crack Growth Data for Semi-Random Loading Tests

SAMPLE DATA SHEET

CRACK GROWTH ANALYSIS DATA --- VAL IIIa (OLR = 1.67 & R = 0.10)

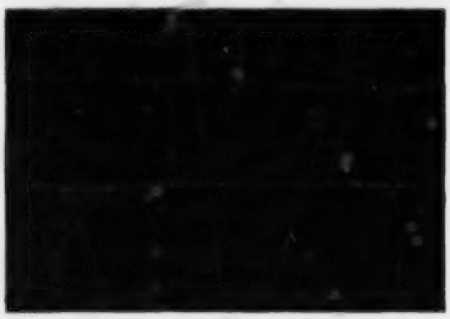

	da/dN (LT) (m/cycle)	Crack Tip Position (mm) Left	Cycles	Right	da/dN (RT) (m/cycle)	Average "2a/W"	ΔK (MPa-m$^{1/2}$)
	N/A	10.05	0	10.05	N/A	N/A	N/A
	1.13E-08	10.17	10600	10.18	1.23E-08	0.201	19.42
	2.95E-08	10.30	15000	10.31	2.95E-08	0.204	19.56
	3.18E-08	10.51	21600	10.53	3.33E-08	0.207	19.74
	5.00E-08	10.69	25200	10.70	4.72E-08	0.211	19.95
START >	5.97E-08	11.09	31900	11.09	5.82E-08	0.217	20.24
	5.88E-08	11.39	37000	11.38	5.69E-08	0.224	20.60
	6.00E-08	11.66	41500	11.64	5.78E-08	0.229	20.89
	6.57E-08	11.89	45000	11.85	6.00E-08	0.234	21.14
	6.87E-08	12.33	51400	12.32	7.34E-08	0.241	21.49
	7.57E-08	12.61	55100	12.60	7.57E-08	0.248	21.86
	8.07E-08	13.07	60800	13.08	8.42E-08	0.256	22.24
	9.25E-08	13.44	64800	13.45	9.25E-08	0.264	22.67
	1.00E-07	13.81	68500	13.76	8.38E-08	0.271	23.02
	1.13E-07	13.99	70100	13.97	1.31E-07	0.276	23.29
	8.65E-08	14.31	73800	14.30	8.92E-08	0.282	23.56
	1.09E-07	14.68	77200	14.67	1.09E-07	0.289	23.91

Figure B.1 – Sample data sheet for semi-random testing

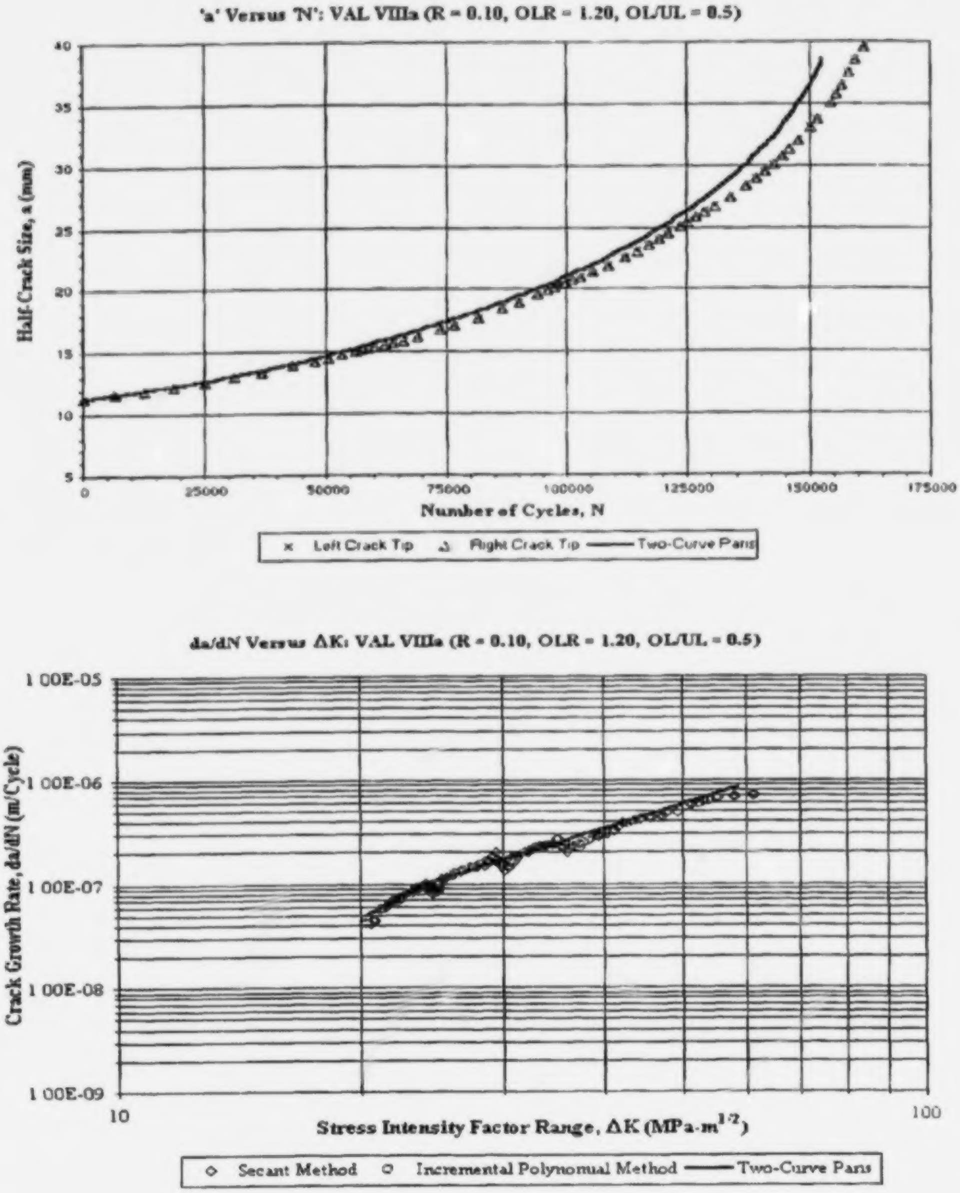

Figure B.2 – 'a-versus-N' data and fatigue rate data for specimen VAL VIIIa

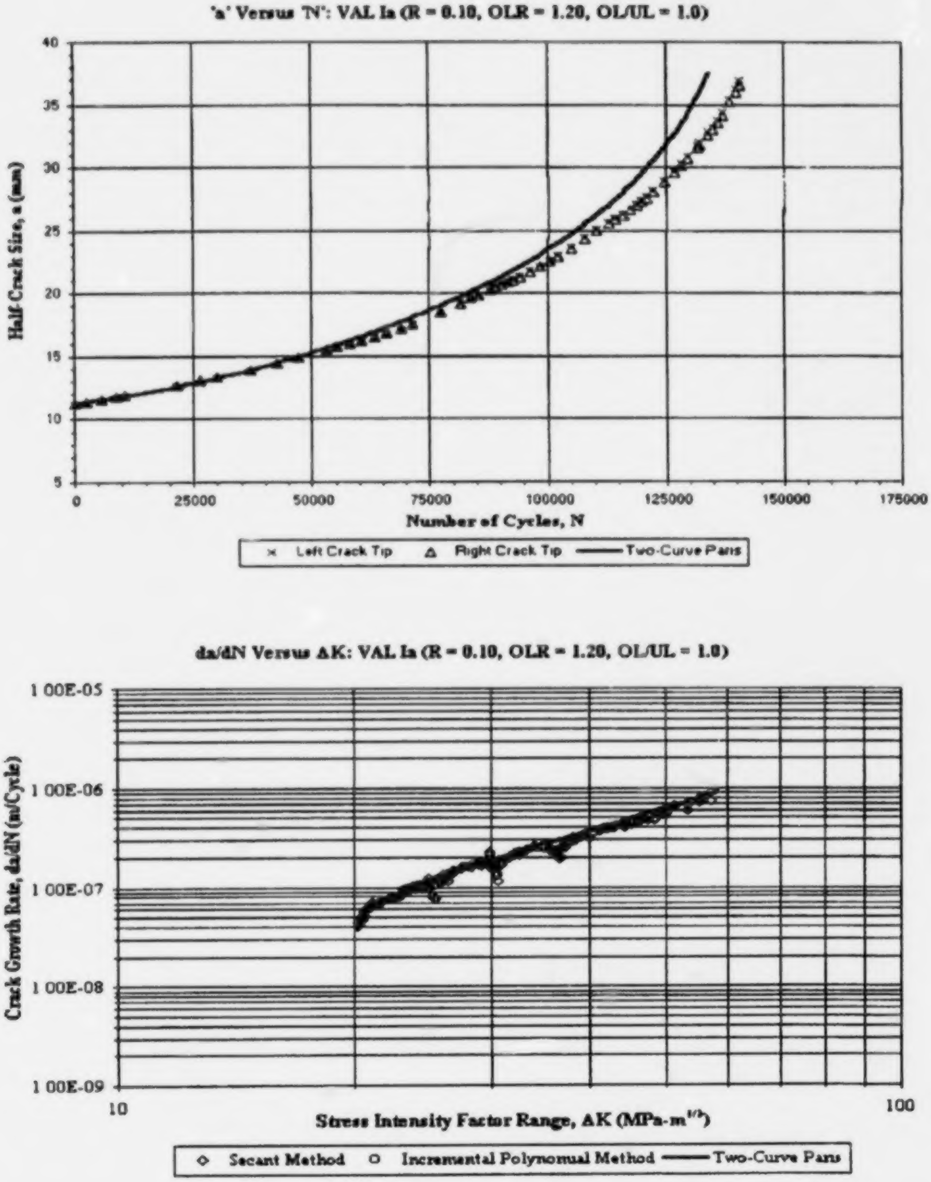

Figure B.3 – 'a-versus-N' data and fatigue rate data for specimen VAL Ia

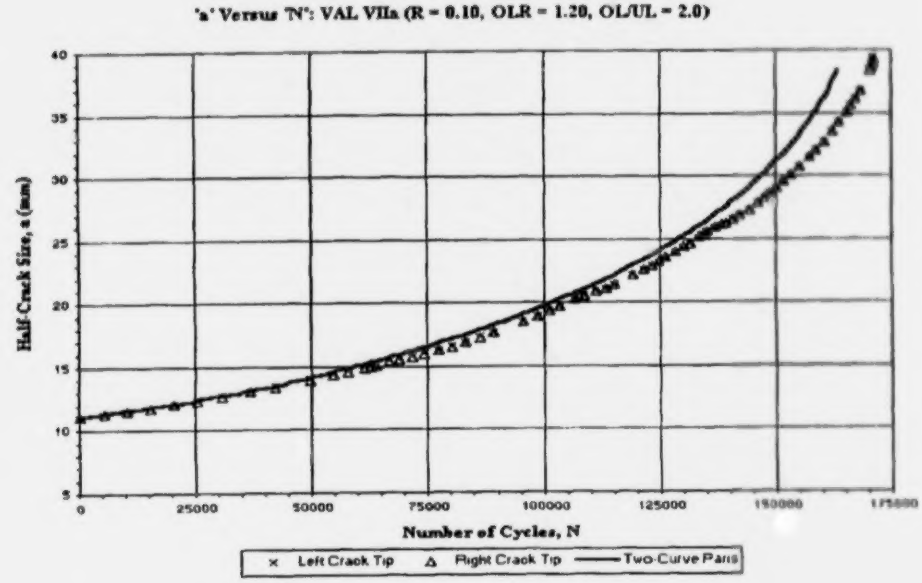

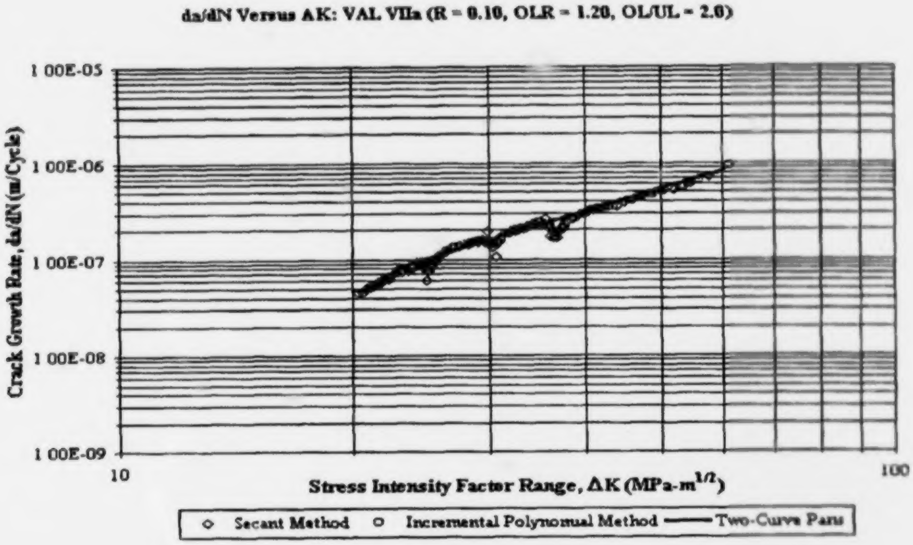

Figure B.4 – 'a-versus-N' data and fatigue rate data for specimen VAL VIIa

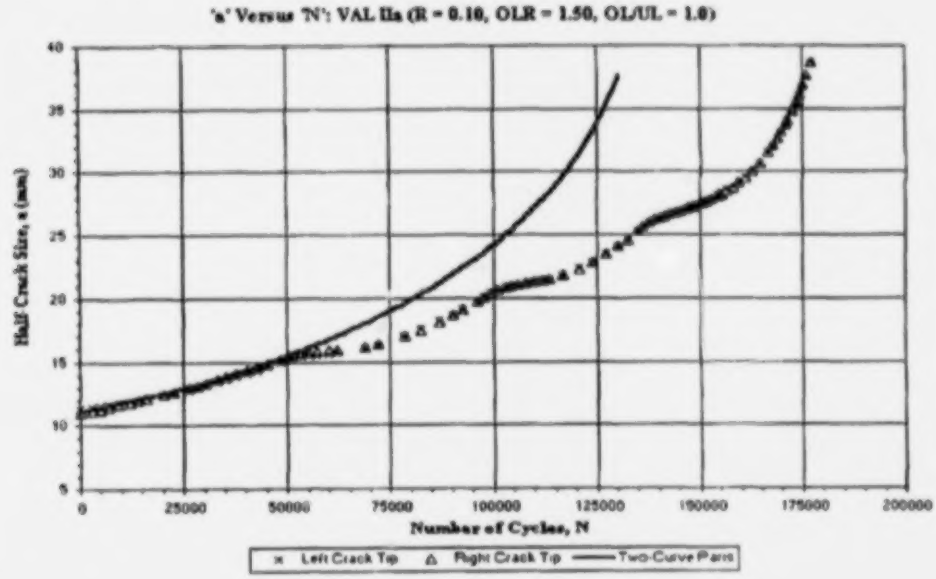

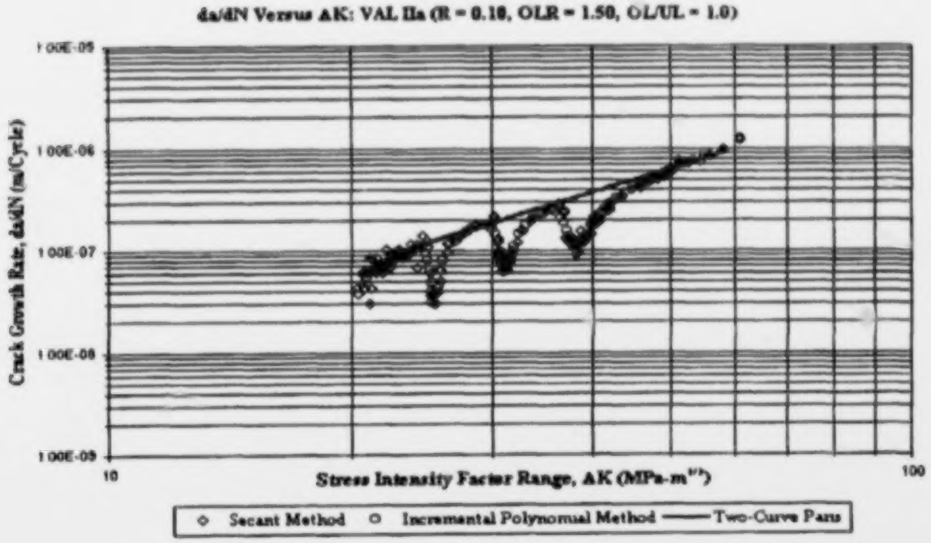

Figure B.5 – 'a-versus-N' data and fatigue rate data for specimen VAL IIa

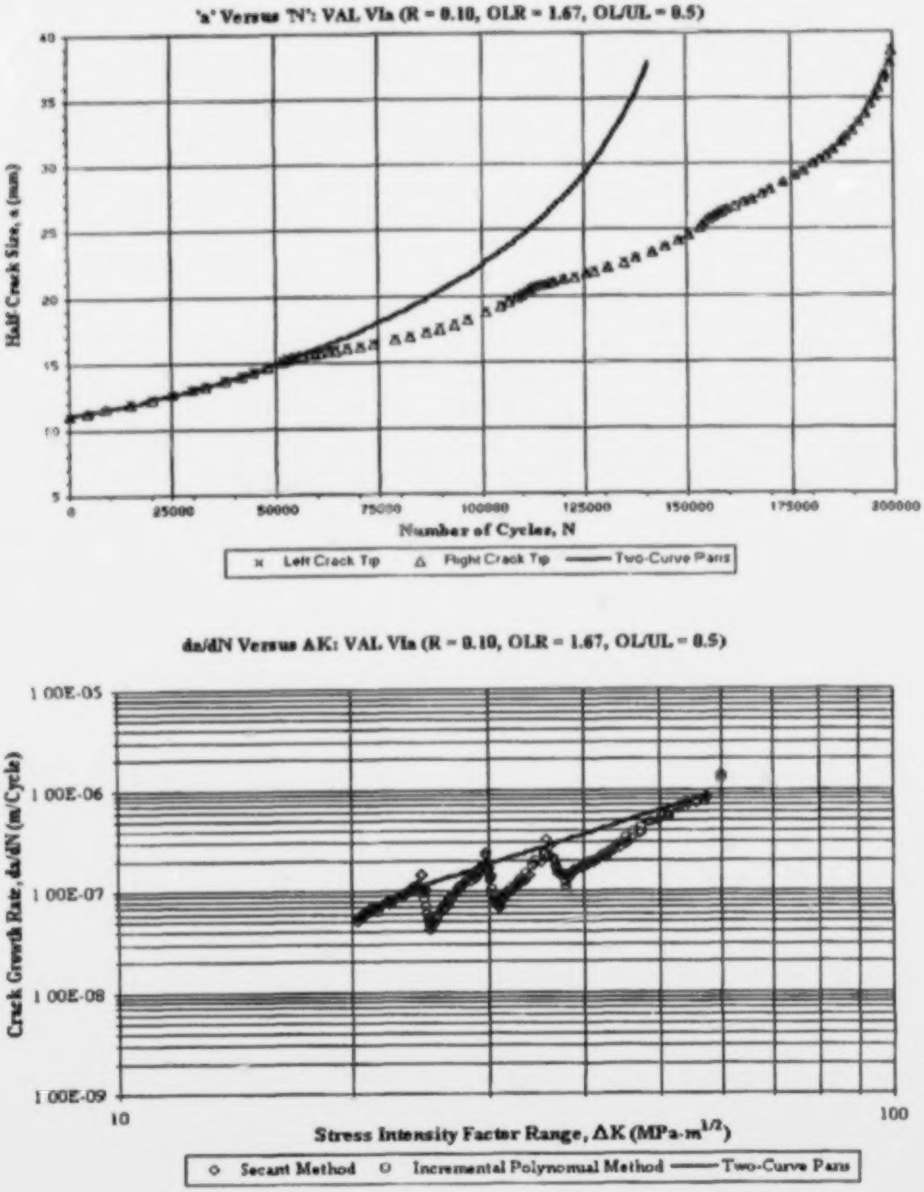

Figure B.6 – 'a-versus-N' data and fatigue rate data for specimen VAL VIa

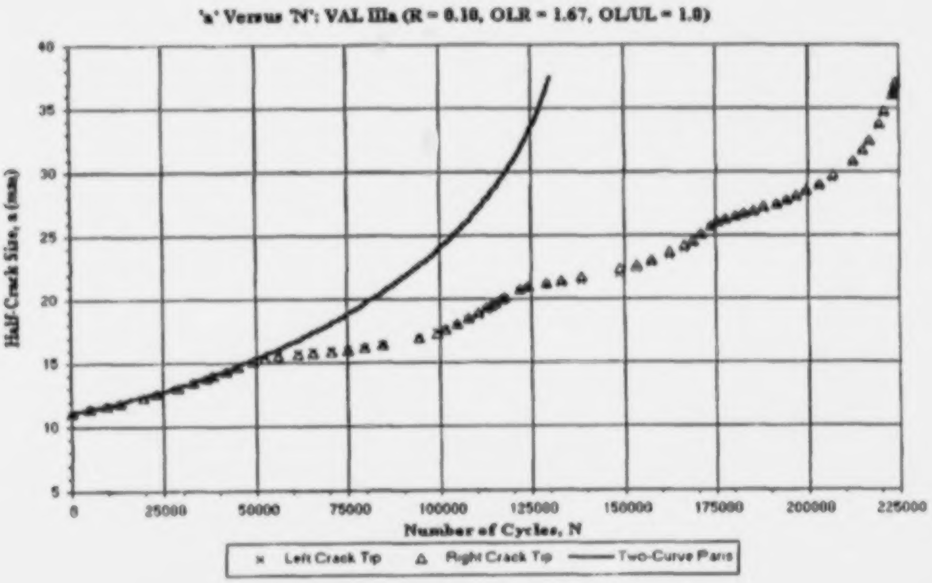

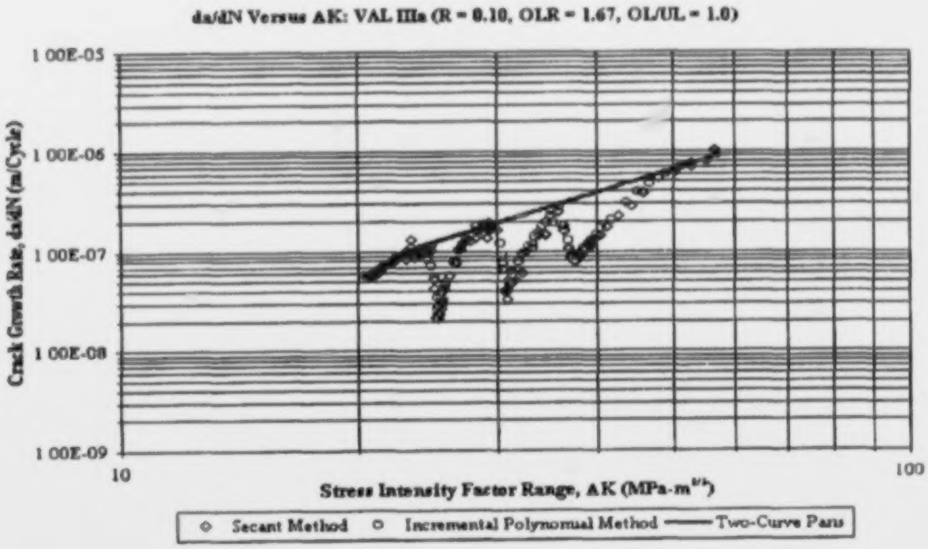

Figure B.7 – 'a-versus-N' data and fatigue rate data for specimen VAL IIIa

SAMPLE PARIS CAL FATIGUE LIFE PREDICTION

Modified Cp Values: VAL IIIa

2-Curve Paris Model CAL Data, R=0.10 (Trask, 1998)

$C_{P,\ Lower}$ =	1.70E-13	$m_{P,\ Lower}$ =	4.22	P_{max} (N) =	60000
$C_{P,\ Upper}$ =	5.29E-11	$m_{P,\ Upper}$ =	2.41	P_{min} (N) =	6000
				t_{avg} (mm) =	5.06
R =	0.1			W_{avg} (mm) =	100.45

a (mm)	Δa (1%) (mm)	2a/W	Geom Fact Y	ΔK (MPa-m$^{1/2}$)	$(da/dN)_{Paris}$ $=C\Delta K^m$ (m/cycle)	ΔN	Cumulative N (Paris)
11.09	0.111	0.221	1.0312	20.45	5.774E-08	1921	0
11.20	0.112	0.223	1.0318	20.56	5.912E-08	1895	1921
11.31	0.113	0.225	1.0325	20.68	6.054E-08	1869	3815
11.43	0.114	0.227	1.0332	20.80	6.199E-08	1843	5684
11.54	0.115	0.230	1.0339	20.91	6.349E-08	1818	7527
11.66	0.117	0.232	1.0346	21.03	6.502E-08	1793	9345
11.77	0.118	0.234	1.0353	21.15	6.660E-08	1768	11137
11.89	0.119	0.237	1.0360	21.27	6.822E-08	1743	12905
12.01	0.120	0.239	1.0368	21.39	6.988E-08	1718	14648
12.13	0.121	0.241	1.0376	21.52	7.159E-08	1694	16366
12.25	0.123	0.244	1.0383	21.64	7.334E-08	1670	18061
12.37	0.124	0.246	1.0392	21.77	7.514E-08	1647	19731
12.50	0.125	0.249	1.0400	21.89	7.699E-08	1623	21378
12.62	0.126	0.251	1.0408	22.02	7.8[illegible]E-08	1600	23001
12.75	0.127	0.254	1.0417	22.15	8.085E-08	1577	24600
12.88	0.129	0.256	1.0426	22.28	8.286E-08	1554	26177
13.00	0.130	0.259	1.0435	22.41	8.493E-08	1531	27731
13.13	0.131	0.262	1.0444	22.54	8.705E-08	1509	29262
13.27	0.133	0.264	1.0453	22.67	8.924E-08	1486	30771
13.40	0.134	0.267	1.0463	22.81	9.149E-08	1464	32257
13.53	0.135	0.269	1.0473	22.94	9.380E-08	1443	33722
13.67	0.137	0.272	1.0483	23.08	1.020E-07	1340	35164
13.80	0.138	0.275	1.0493	23.21	1.035E-07	1334	36504
13.94	0.139	0.278	1.0503	23.35	1.050E-07	1328	37837
14.08	0.141	0.280	1.0514	23.49	1.065E-07	1322	39165
14.22	0.142	0.283	1.0525	23.64	1.081E-07	1316	40487
14.36	0.144	0.286	1.0536	23.78	1.097E-07	1310	41803
14.51	0.145	0.289	1.0548	23.92	1.113E-07	1304	43112
14.65	0.147	0.292	1.0560	24.07	1.129E-07	1297	44416
14.80	0.148	0.295	1.0572	24.22	1.146E-07	1291	45714
14.95	0.149	0.298	1.0584	24.37	1.163E-07	1285	47005
15.10	0.151	0.301	1.0596	24.52	1.181E-07	1279	48290
15.25	0.152	0.304	1.0609	24.67	1.198E-07	1272	49569
15.40	0.154	0.307	1.0623	24.82	1.216E-07	1266	50841
15.55	0.156	0.310	1.0636	24.98	1.235E-07	1260	52107
15.71	0.157	0.313	1.0650	25.14	1.254E-07	1253	53367
15.87	0.159	0.316	1.0664	25.29	1.273E-07	1247	54620
16.03	0.160	0.319	1.0678	25.46	1.292E-07	1240	55867
16.19	0.162	0.322	1.0693	25.62	1.312E-07	1233	57107
16.35	0.163	0.325	1.0708	25.78	1.333E-07	1227	58340
16.51	0.165	0.329	1.0724	25.95	1.353E-07	1220	59567
16.68	0.167	0.332	1.0739	26.12	1.375E-07	1213	60787
16.84	0.168	0.335	1.0756	26.29	1.396E-07	1206	62000

Figure B.8 – Sample data sheet for Paris fatigue life prediction

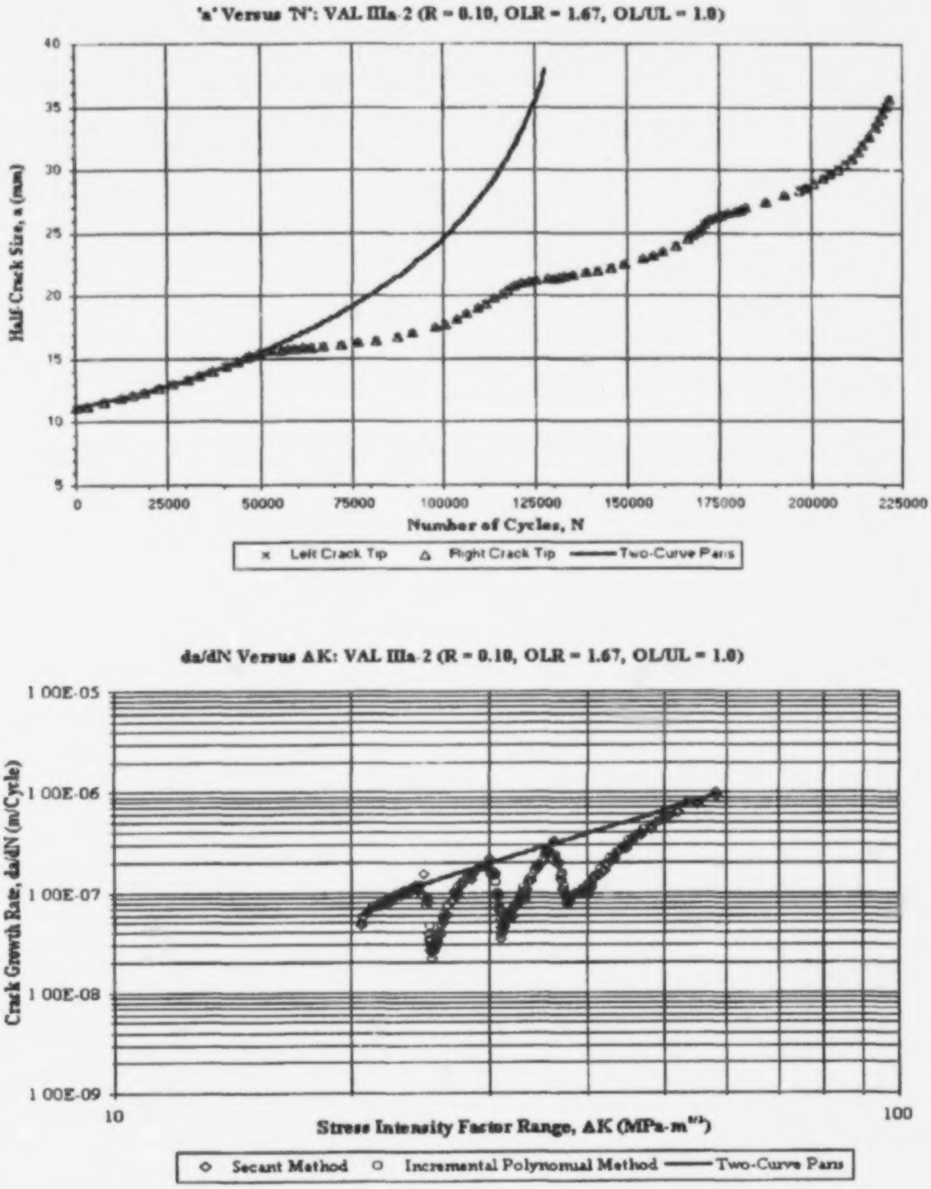

Figure B.9 – 'a-versus-N' data and fatigue rate data for specimen VAL IIIa-2

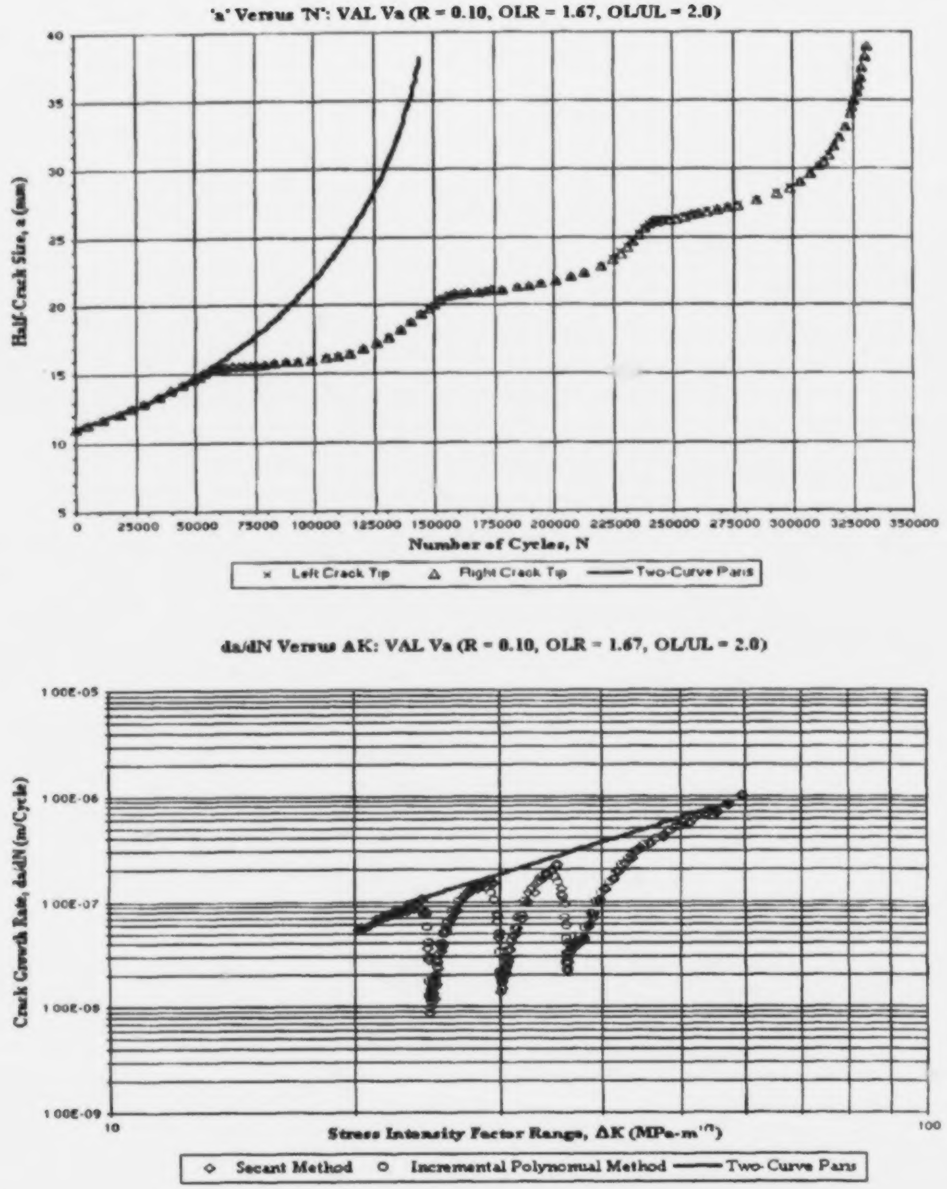

Figure B.10 – 'a-versus-N' data and fatigue rate data for specimen VAL Va

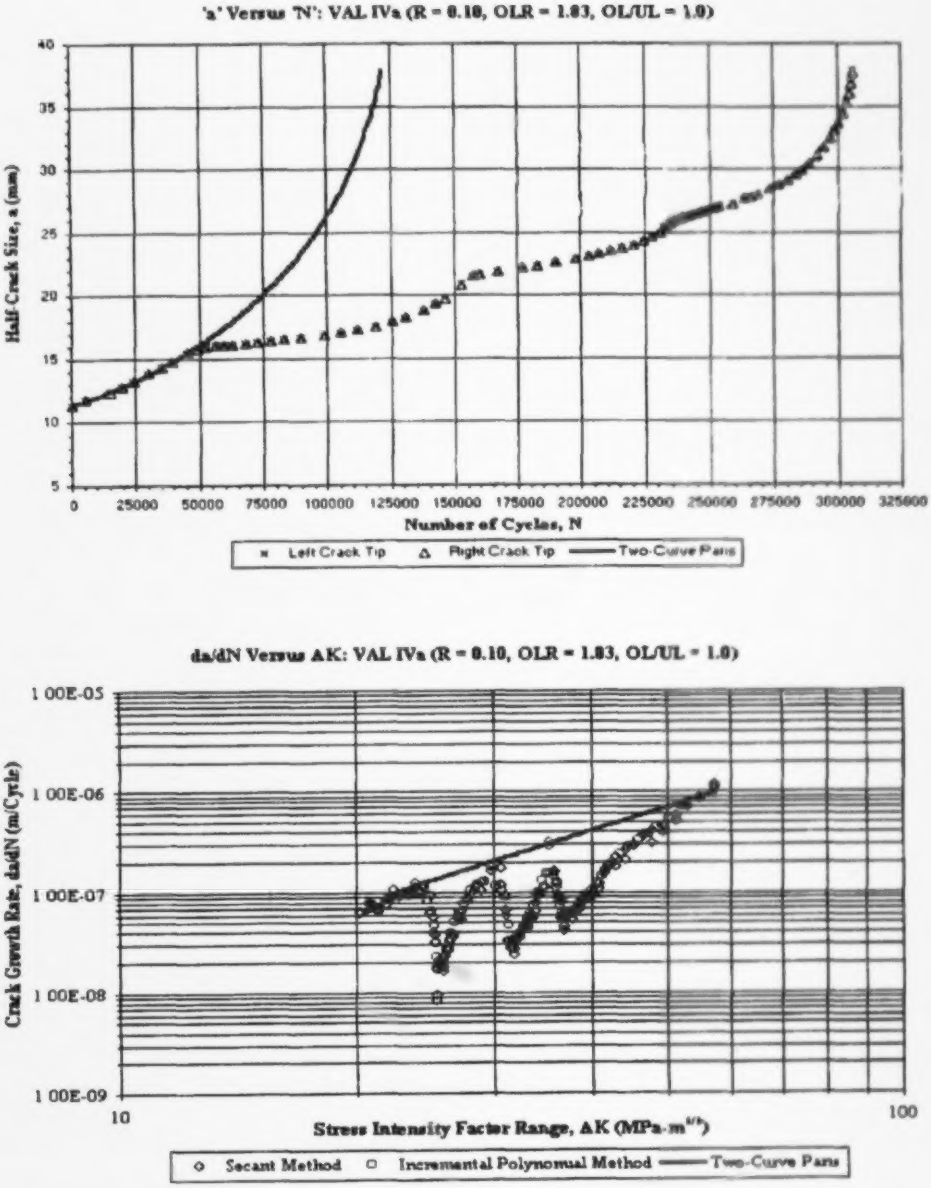

Figure B.11 – 'a-versus-N' data and fatigue rate data for specimen VAL IVa

'a' Versus 'N': VAL Ib (R = 0.30, OLR = 1.20, OL/UL = 1.0)

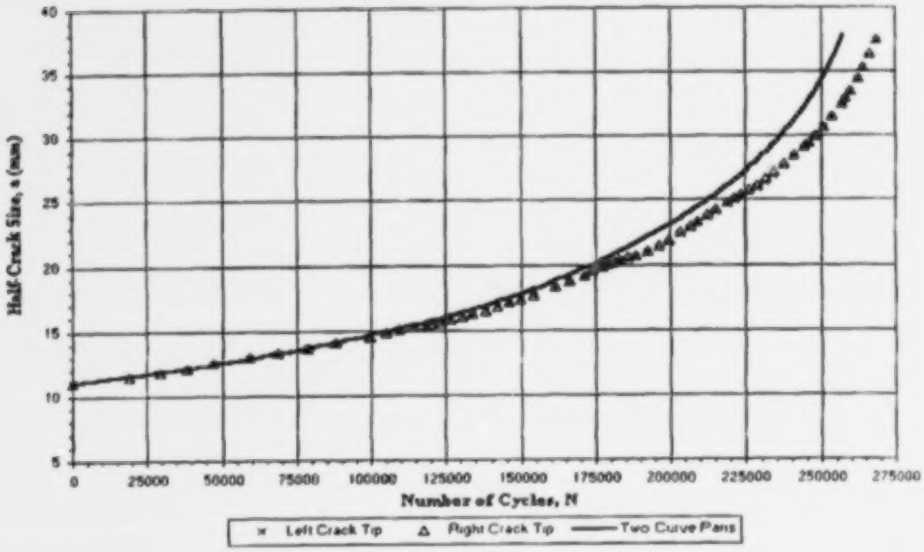

da/dN Versus ΔK: VAL Ib (R = 0.30, OLR = 1.20, OL/UL = 1.0)

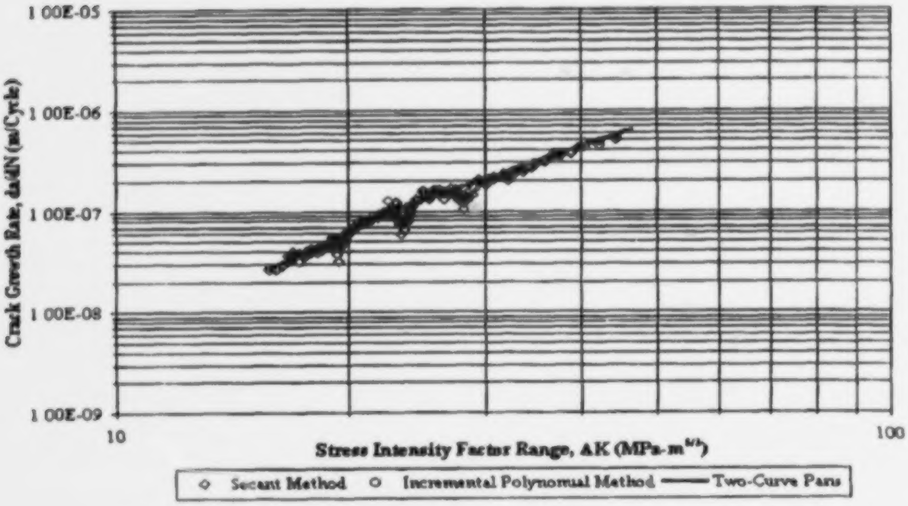

Figure B.12 – 'a-versus-N' data and fatigue rate data for specimen VAL Ib

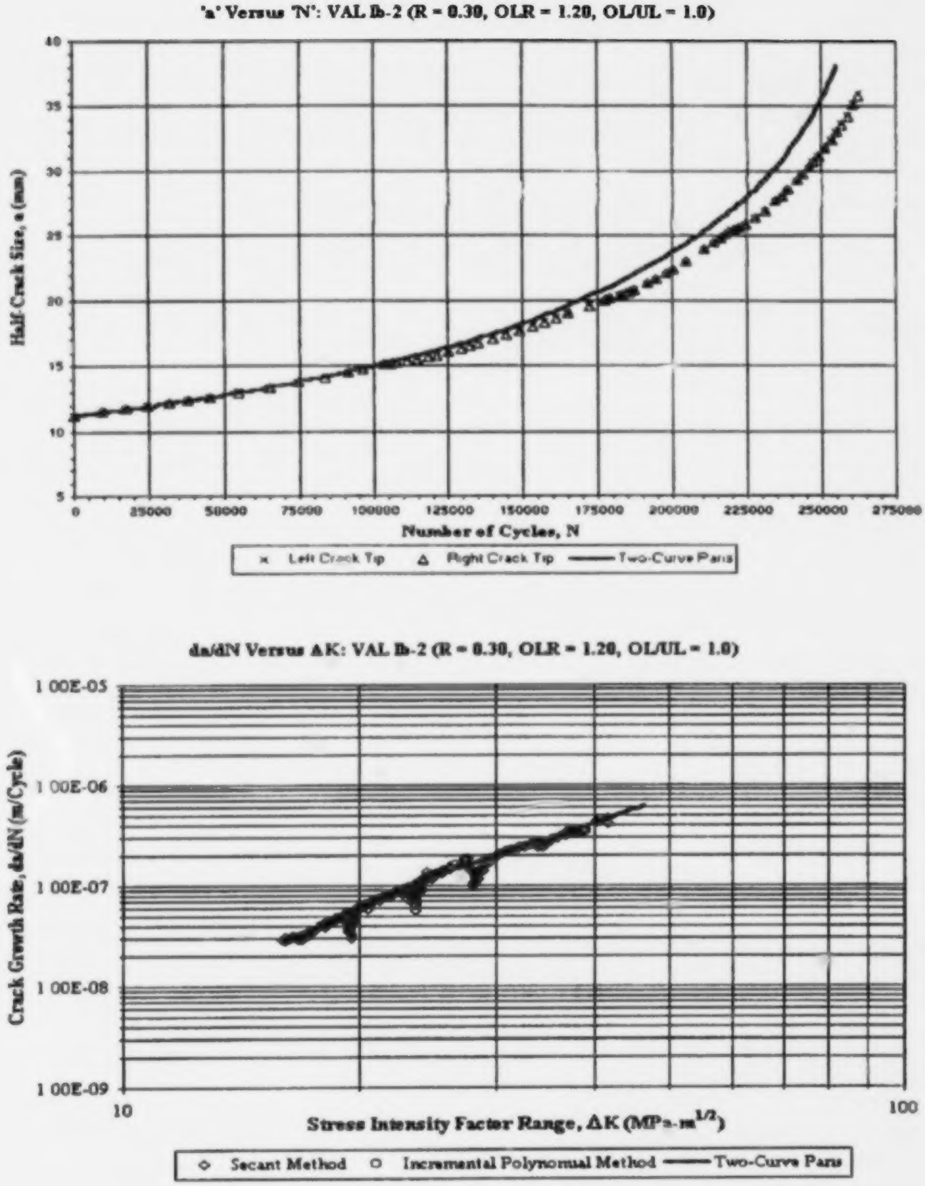

'a' Versus 'N': VAL Ib-2 (R = 0.30, OLR = 1.20, OL/UL = 1.0)

da/dN Versus ΔK: VAL Ib-2 (R = 0.30, OLR = 1.20, OL/UL = 1.0)

Figure B.13 – 'a-versus-N' data and fatigue rate data for specimen VAL Ib-2

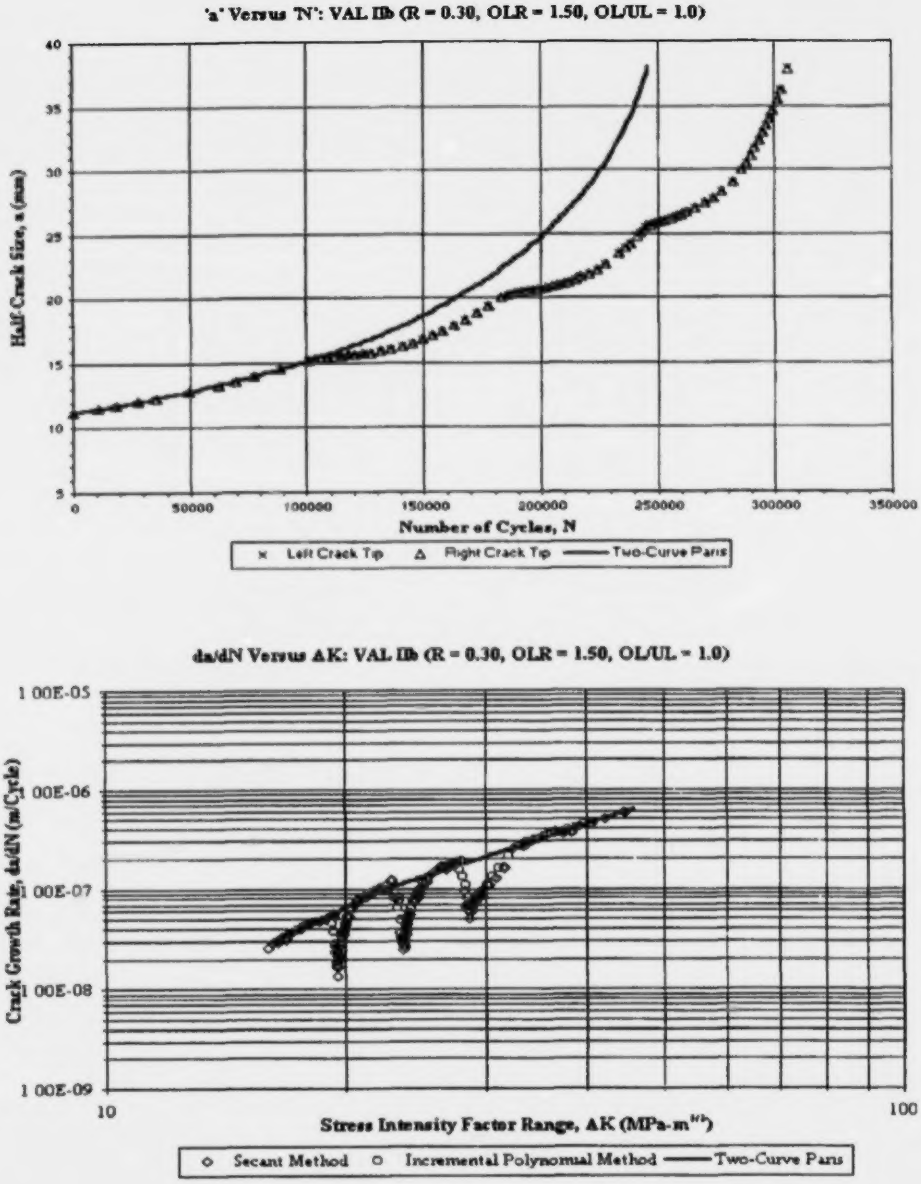

Figure B.14 – 'a-versus-N' data and fatigue rate data for specimen VAL IIb

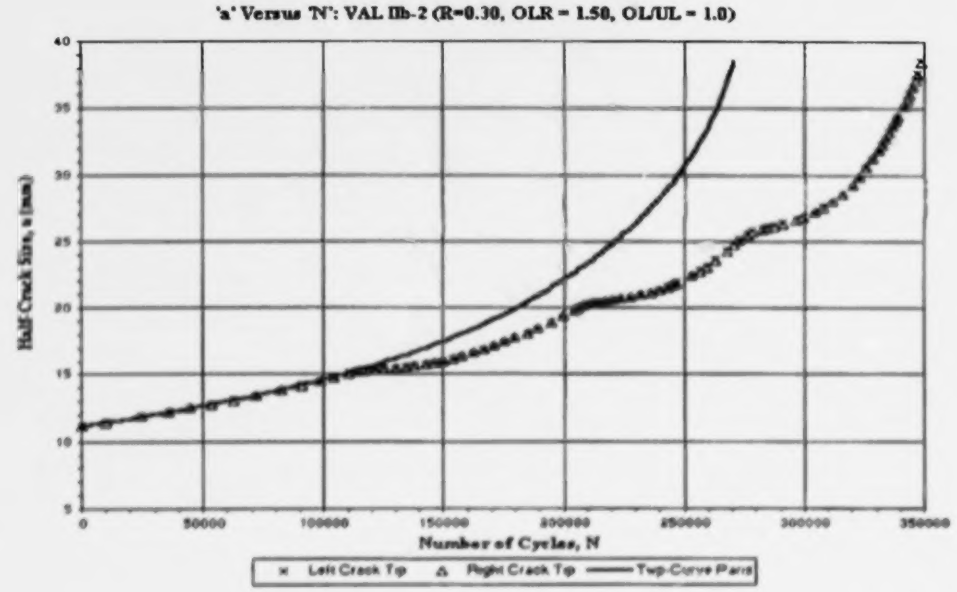
'a' Versus 'N': VAL IIb-2 (R=0.30, OLR = 1.50, OL/UL = 1.0)

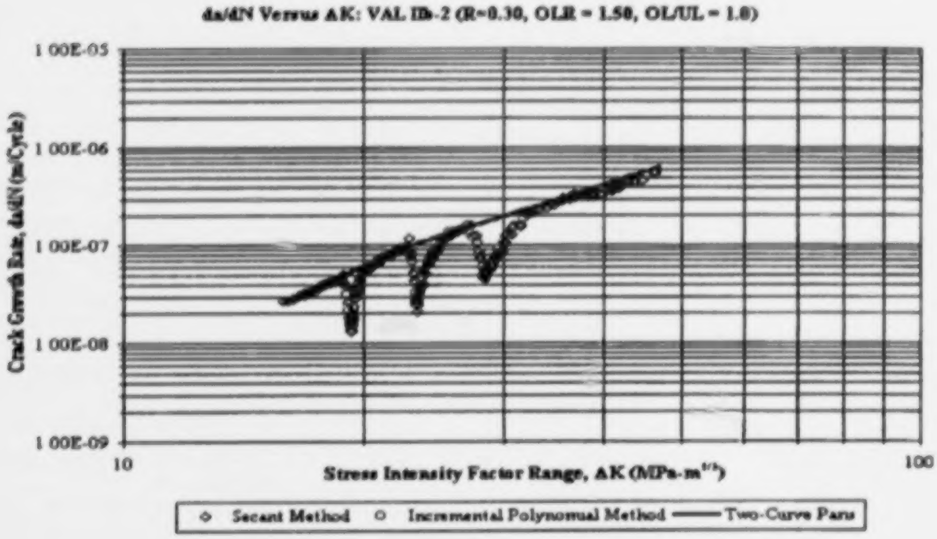
da/dN Versus ΔK: VAL IIb-2 (R=0.30, OLR = 1.50, OL/UL = 1.0)

Figure B.15 – 'a-versus-N' data and fatigue rate data for specimen VAL IIb-2

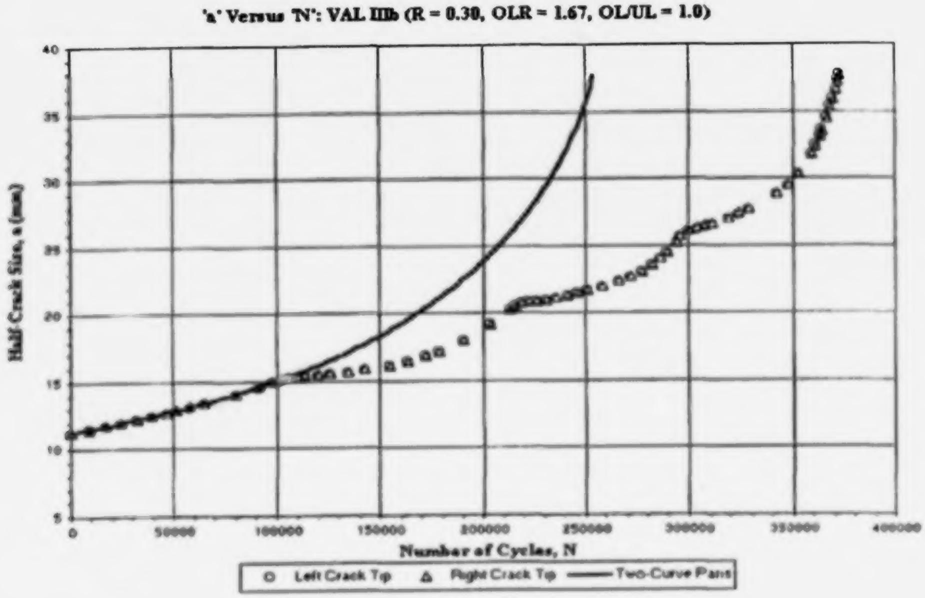

'a' Versus 'N': VAL IIIb (R = 0.30, OLR = 1.67, OL/UL = 1.0)

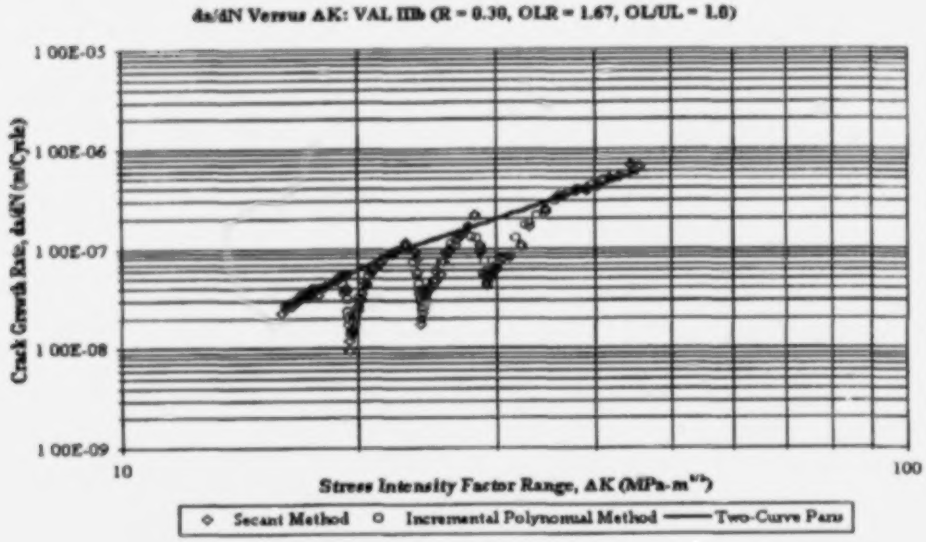

da/dN Versus ΔK: VAL IIIb (R = 0.30, OLR = 1.67, OL/UL = 1.0)

Figure B.16 – 'a-versus-N' data and fatigue rate data for specimen VAL IIIb

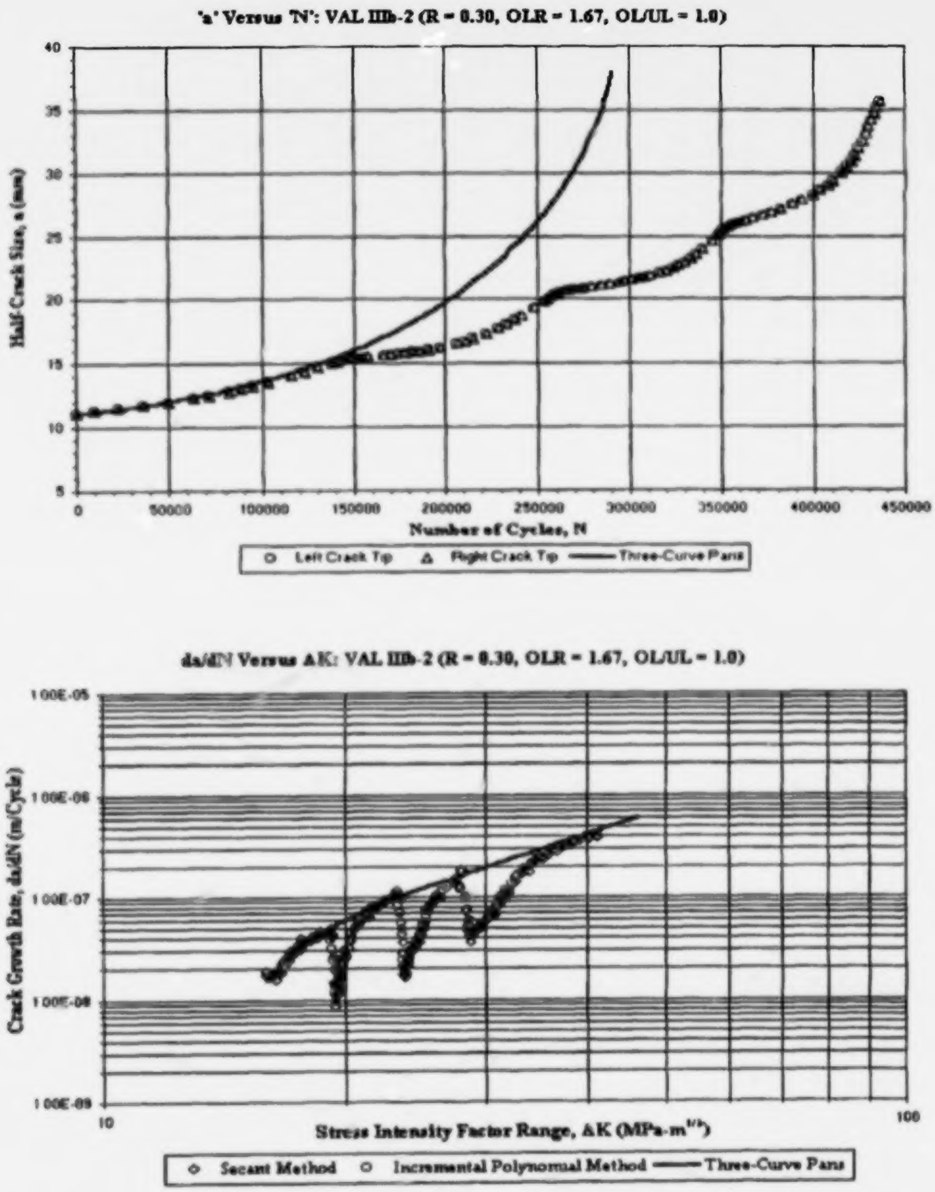

Figure B.17 – 'a-versus-N' data and fatigue rate data for specimen VAL IIIb-2

'a' Versus 'N': VAL IIIb-3 (R = 0.30, OLR = 1.67, OL/UL = 1.0)

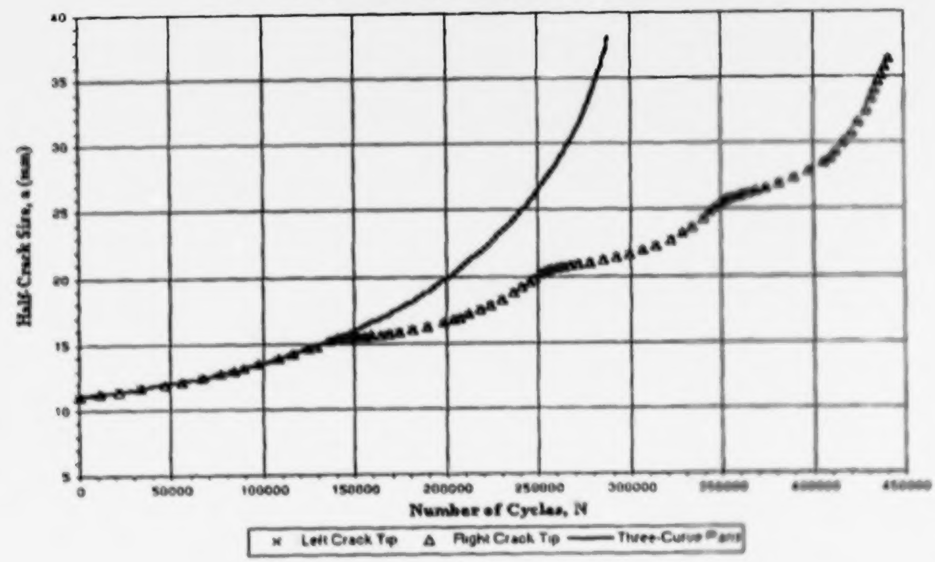

da/dN Versus ΔK: VAL IIIb-3 (R = 0.30, OLR = 1.67, OL/UL = 1.0)

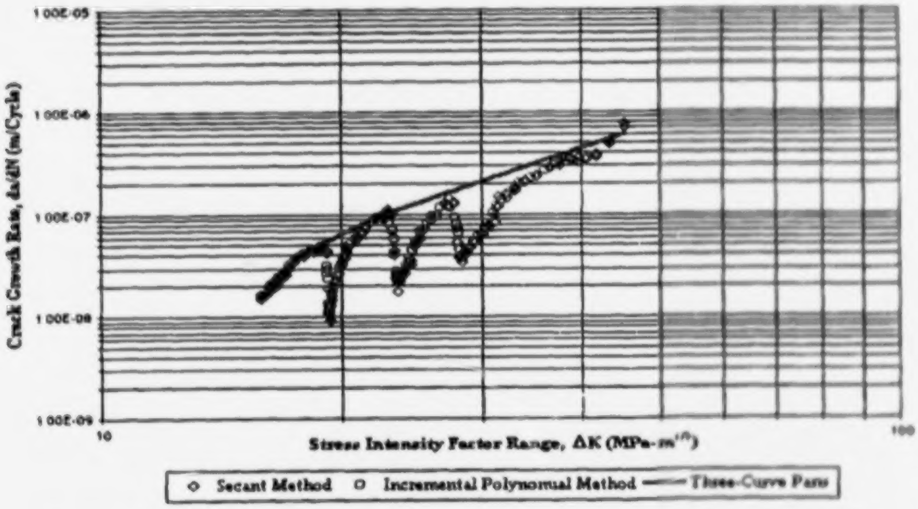

Figure B.18 – 'a-versus-N' data and fatigue rate data for specimen VAL IIIb-3

Appendix C

Fatigue Life Predictions Using the Wheeler Model

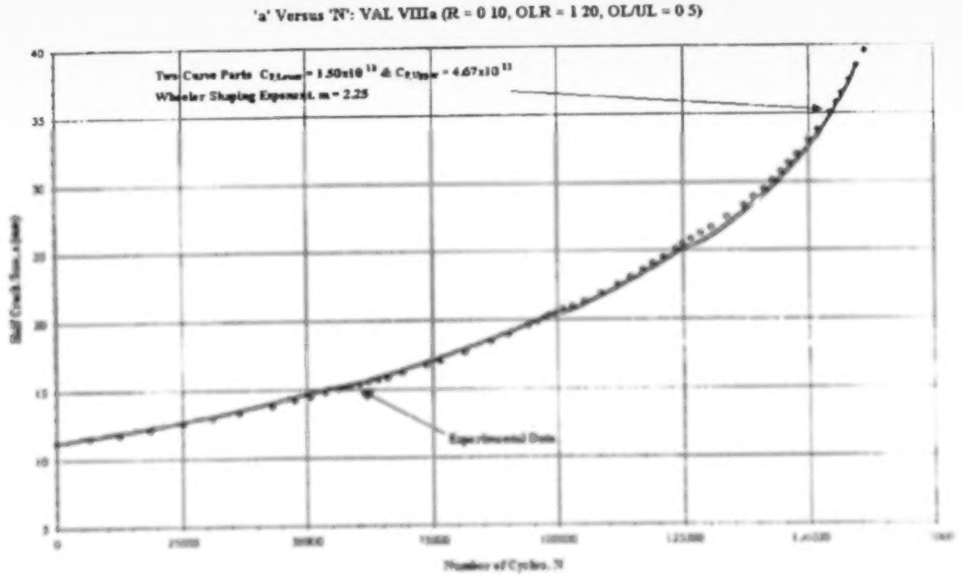

Figure C.1 – Wheeler prediction for specimen VAL VIIIa

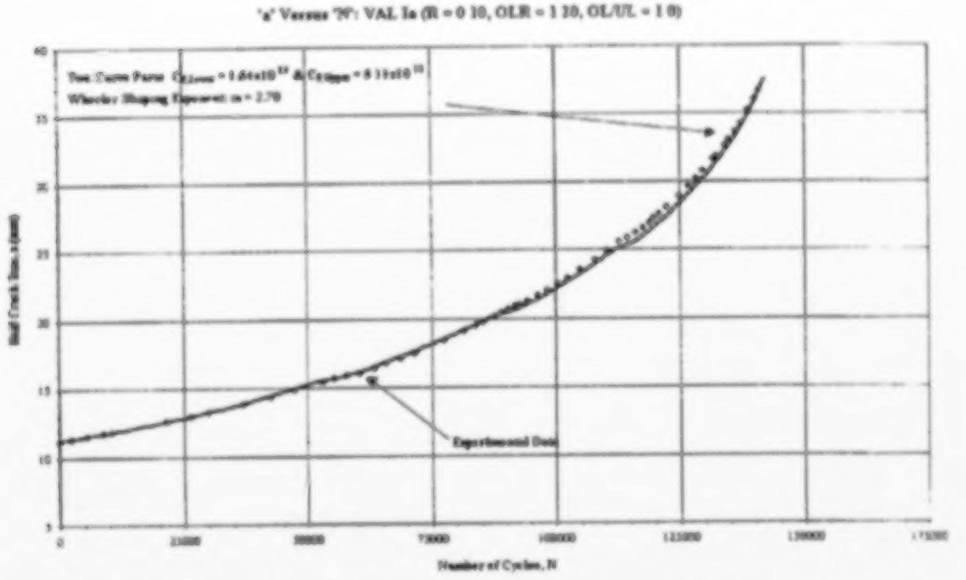

Figure C.2 – Wheeler prediction for specimen VAL Ia

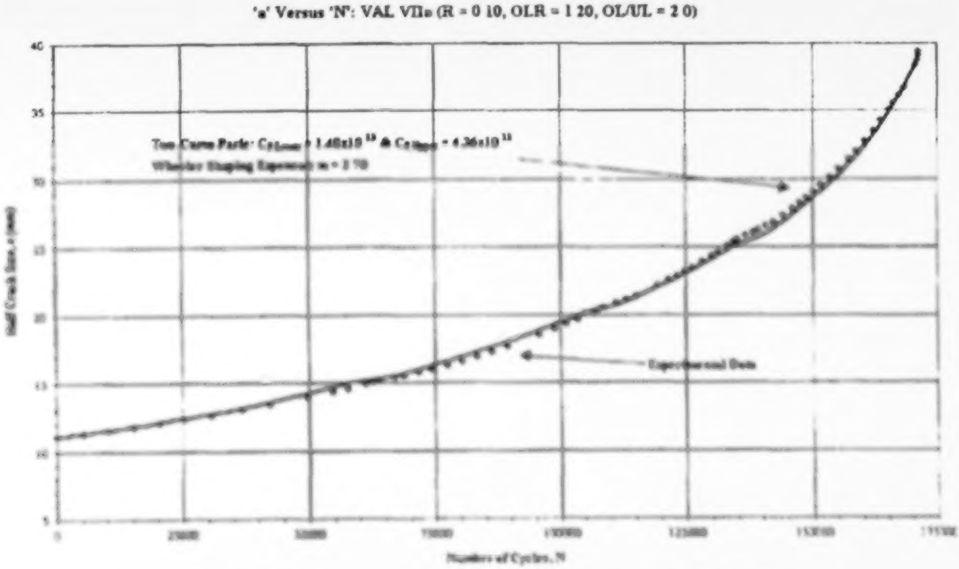

Figure C.3 – Wheeler prediction for specimen VAL VIIa

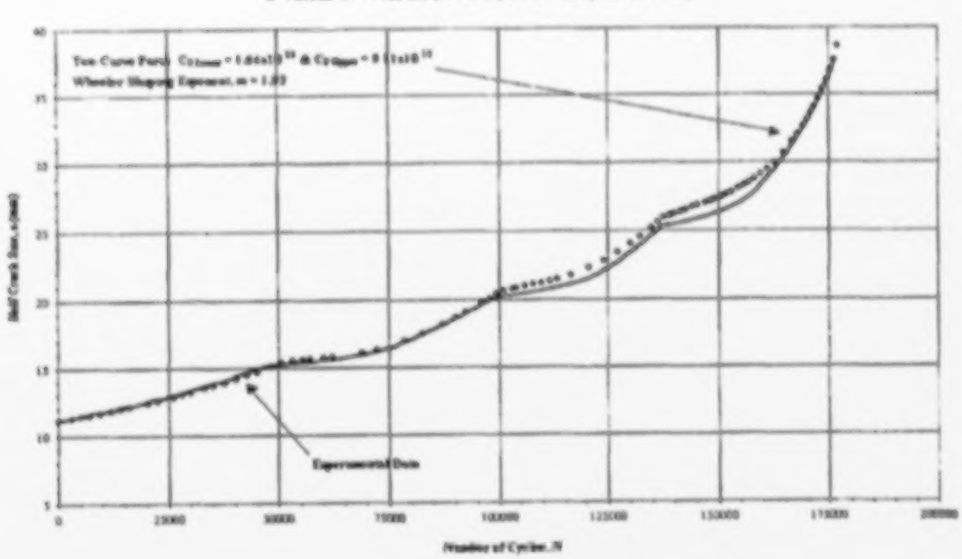

Figure C.4 – Wheeler prediction for specimen VAL IIa

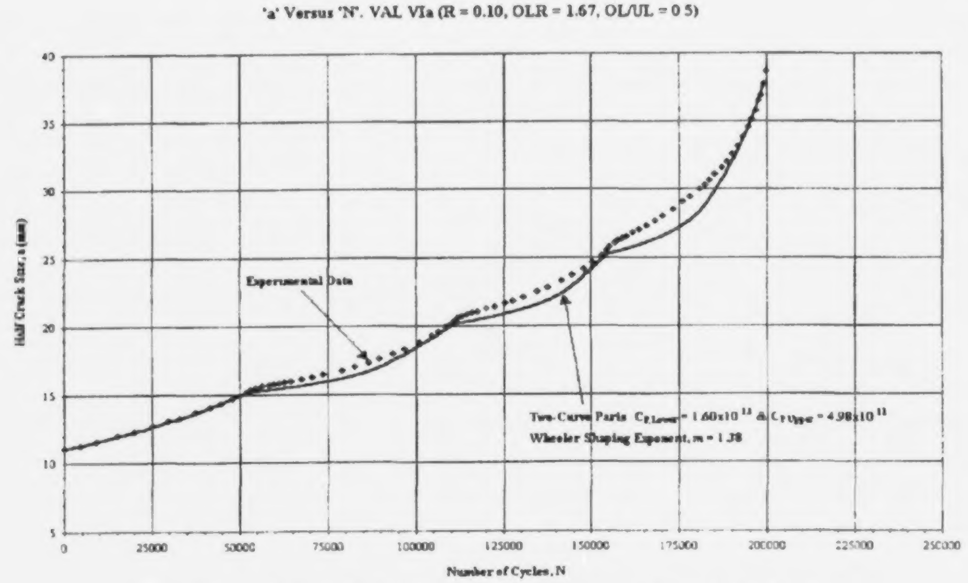

Figure C.5 – Wheeler prediction for specimen VAL VIa

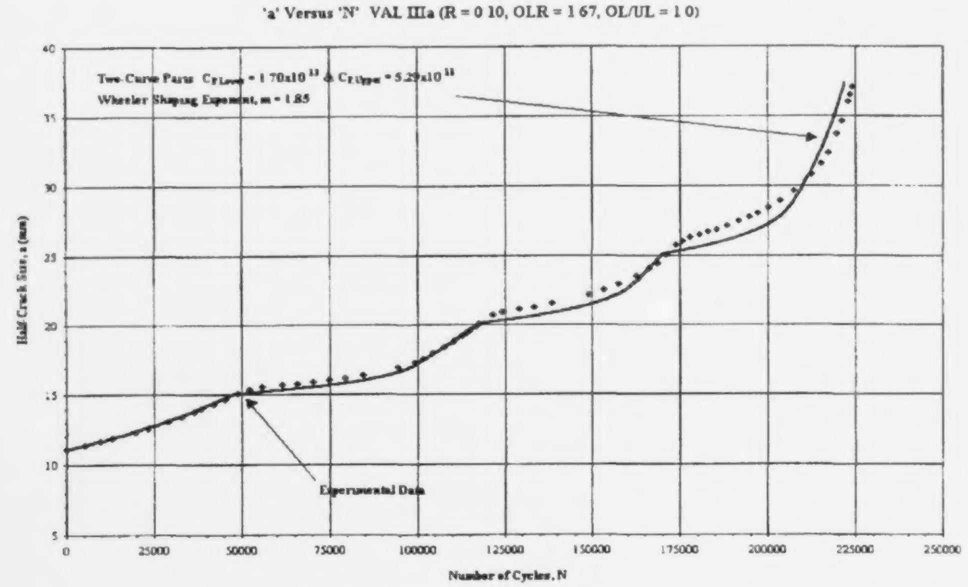

Figure C.6 – Wheeler prediction for specimen VAL IIIa

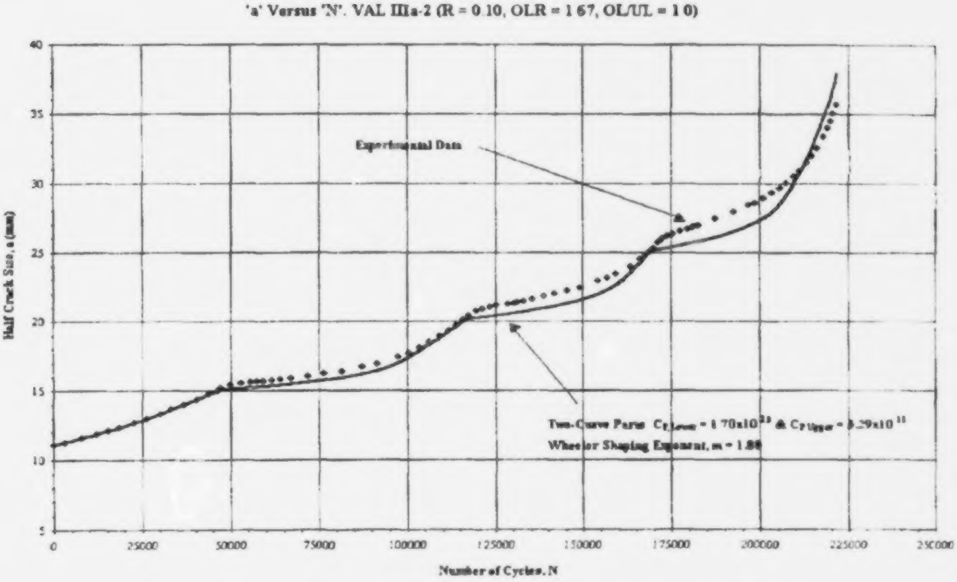

Figure C.7 – Wheeler prediction for specimen VAL IIIa-2

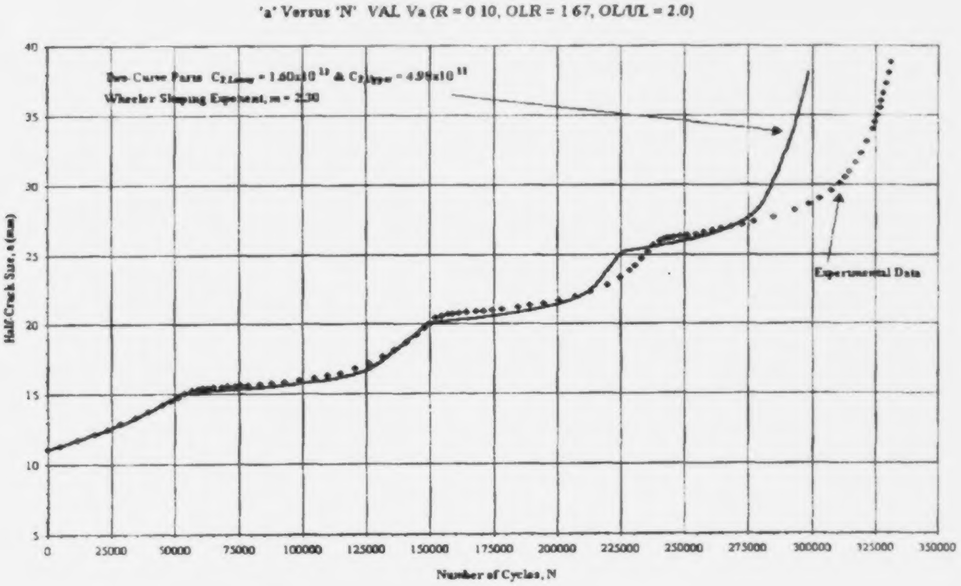

Figure C.8 – Wheeler prediction for specimen VAL Va

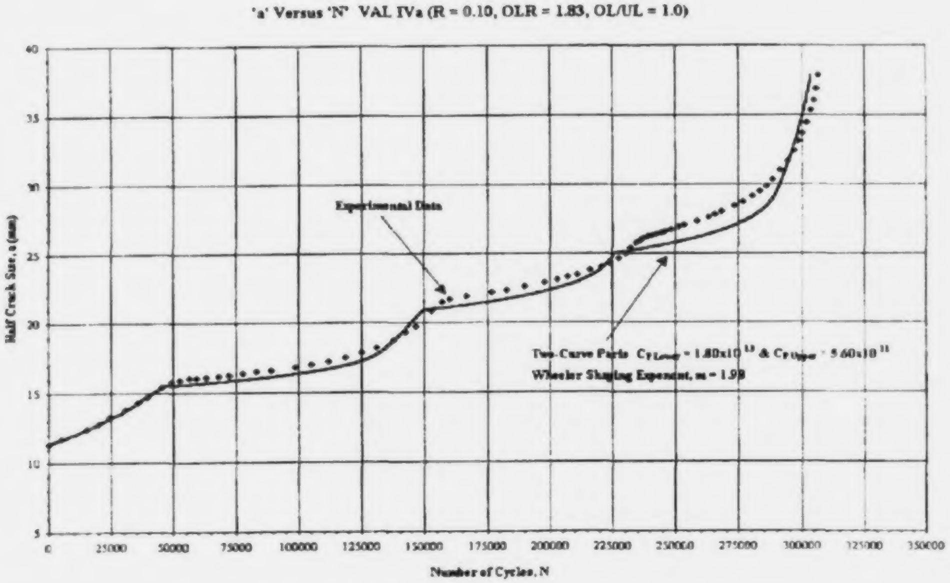

Figure C.9 – Wheeler prediction for specimen VAL IVa

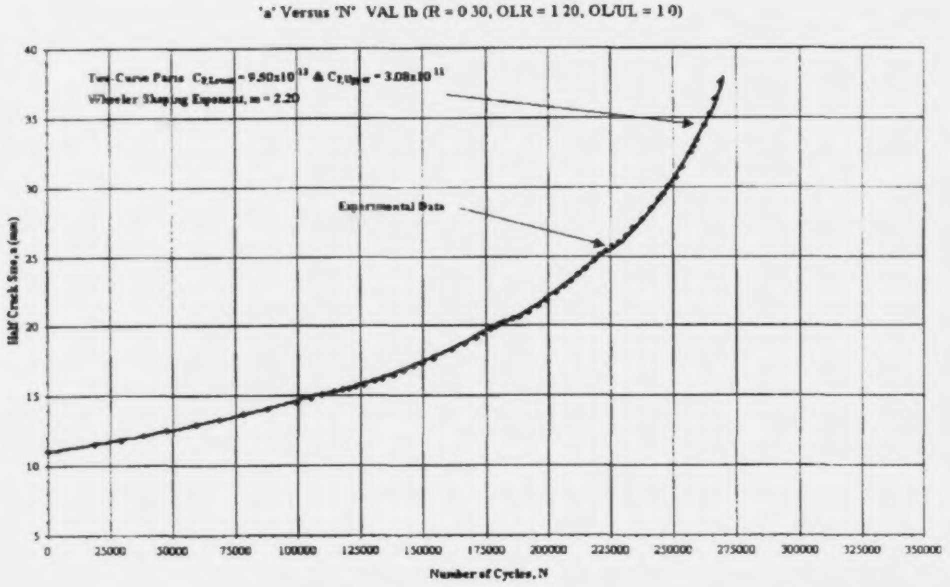

Figure C.10 – Wheeler prediction for specimen VAL Ib

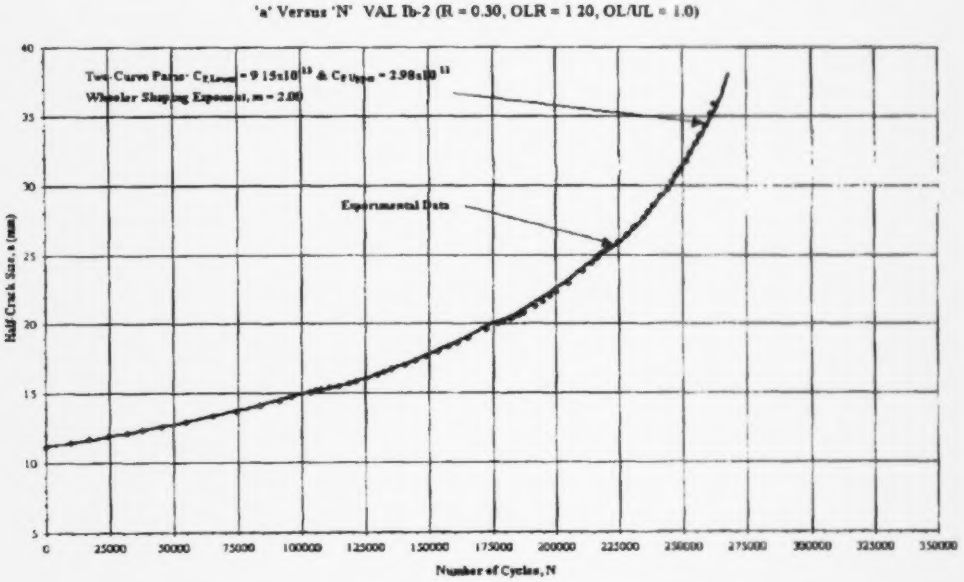

Figure C.11 – Wheeler prediction for specimen VAL Ib-2

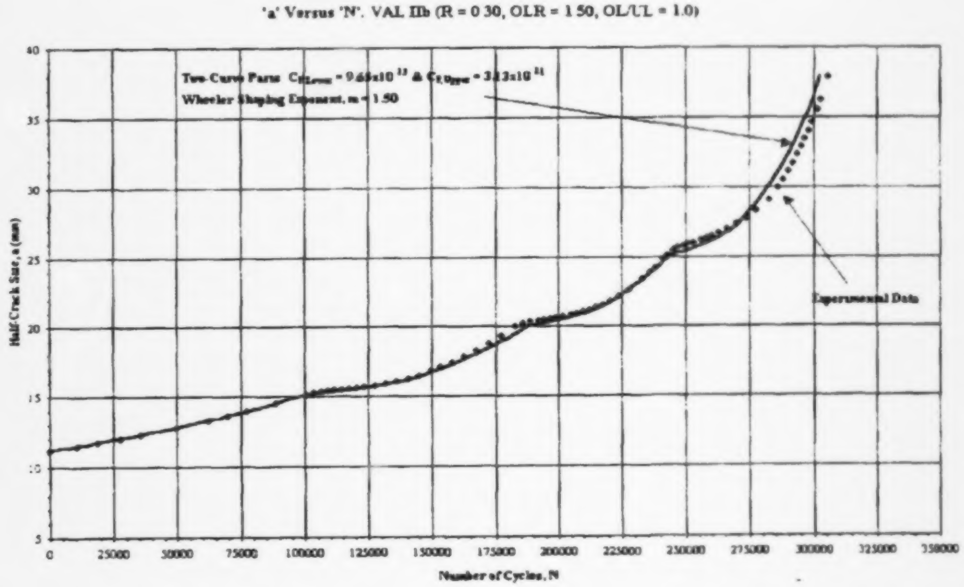

Figure C.12 – Wheeler prediction for specimen VAL IIb

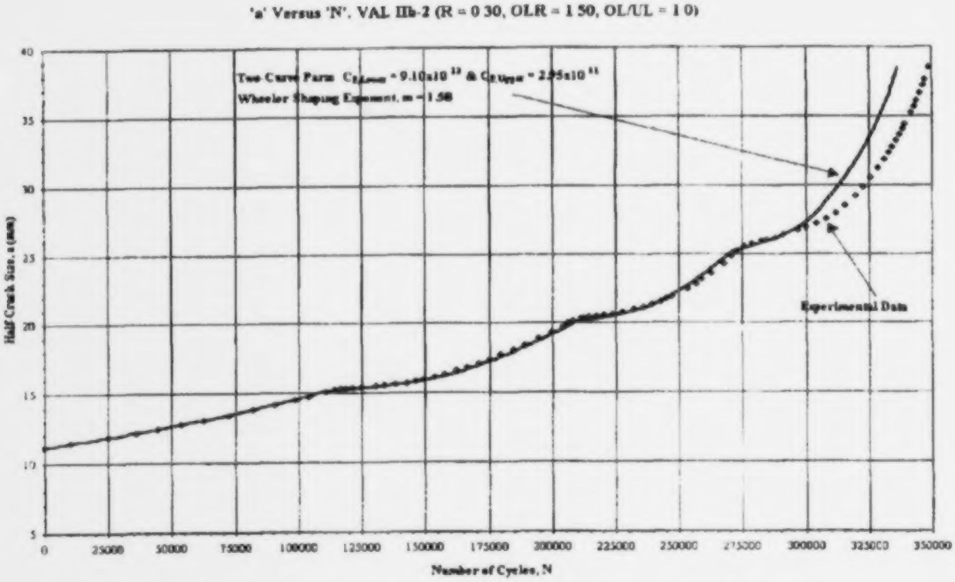

Figure C.13 – Wheeler prediction for specimen VAL IIb-2

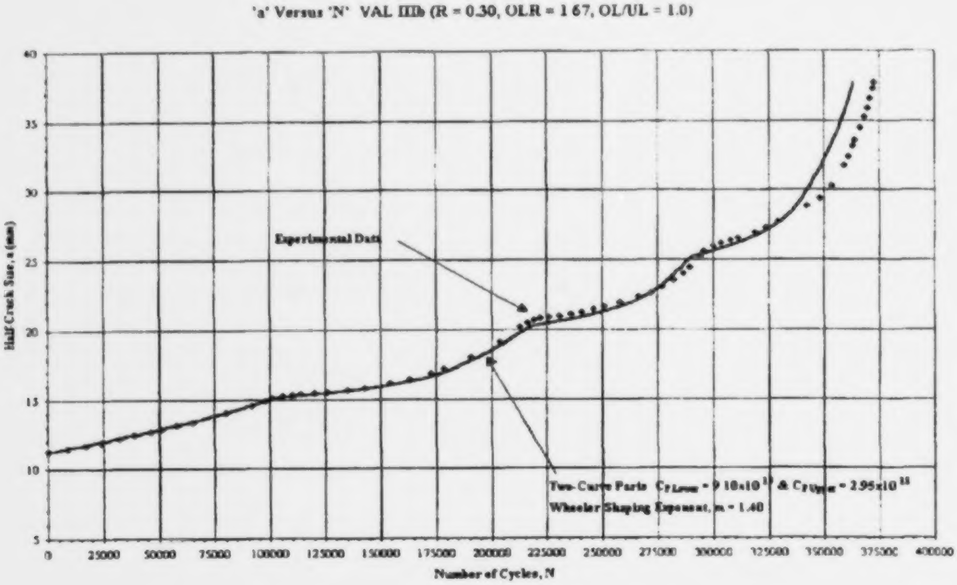

Figure C.14 – Wheeler prediction for specimen VAL IIIb

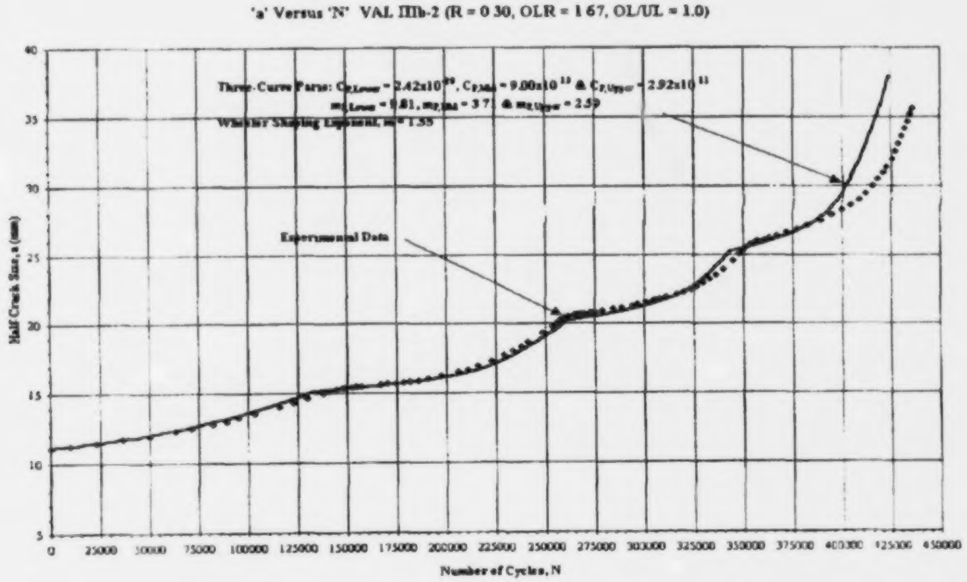

Figure C.15 – Wheeler prediction for specimen VAL IIIb-2

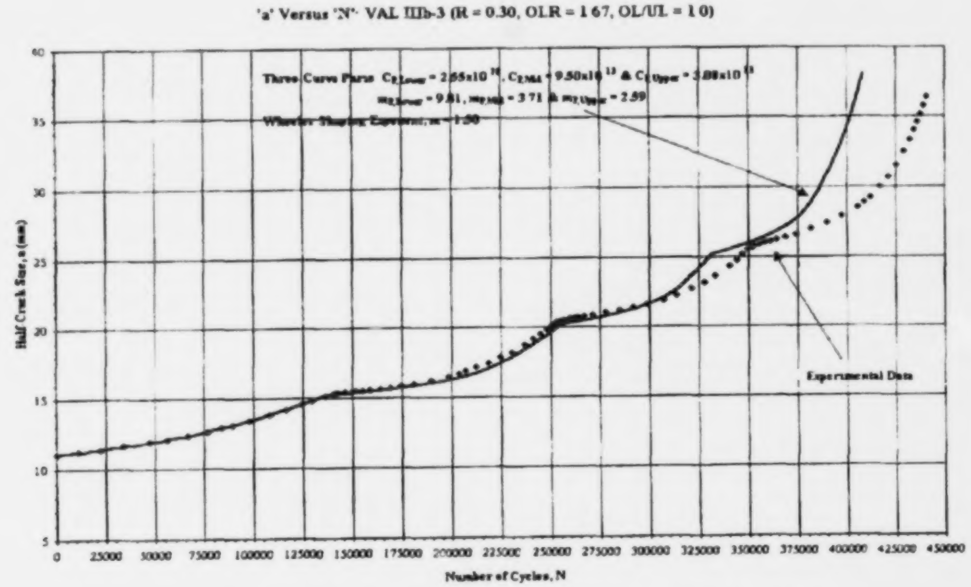

Figure C.16 – Wheeler prediction for specimen VAL IIIb-3

Appendix D

Fatigue Life Predictions Using the Modified Wheeler Model

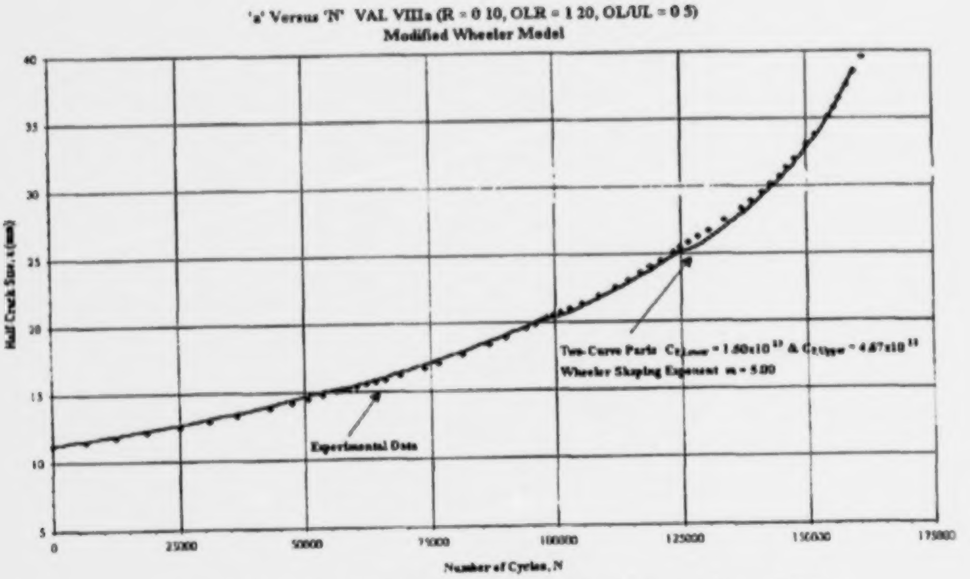

Figure D.1 – Modified Wheeler prediction for specimen VIIIa

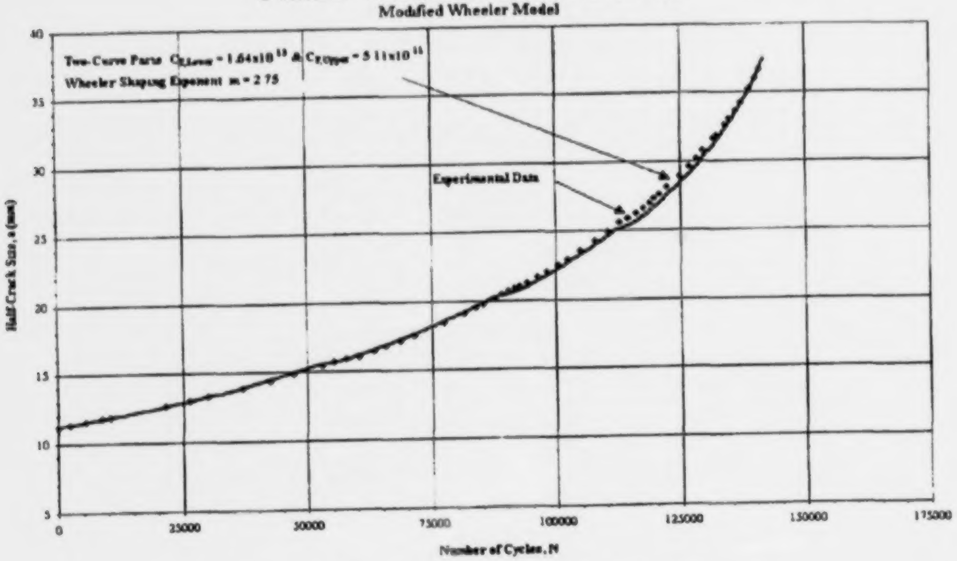

Figure D.2 – Modified Wheeler prediction for specimen Ia

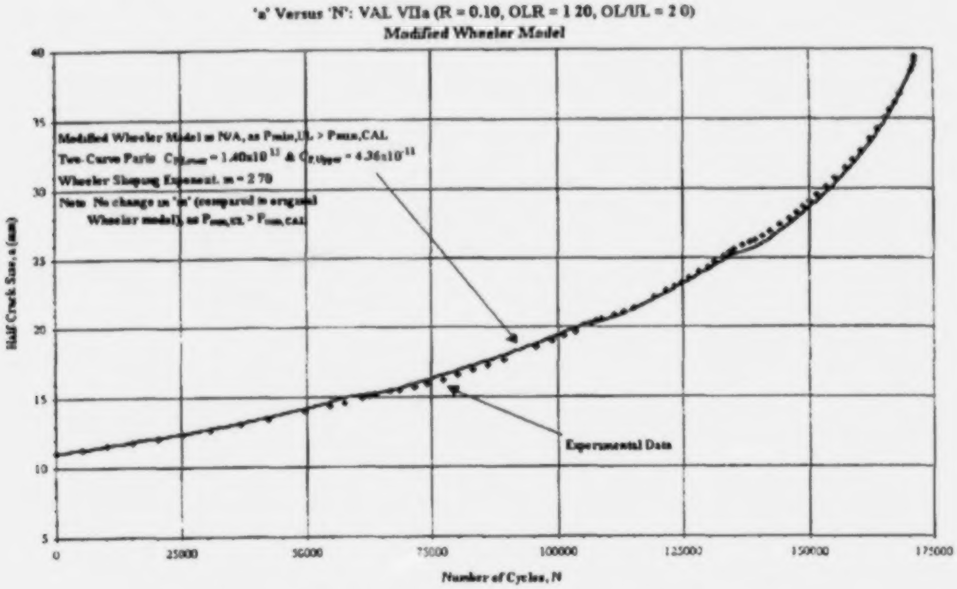

Figure D.3 – Modified Wheeler prediction for specimen VIIa

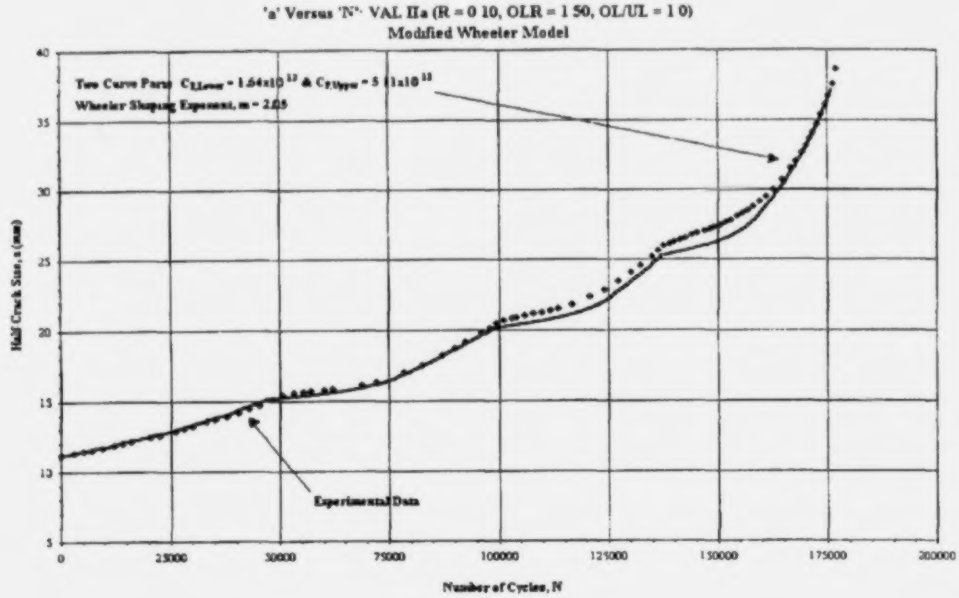

Figure D.4 – Modified Wheeler prediction for specimen IIa

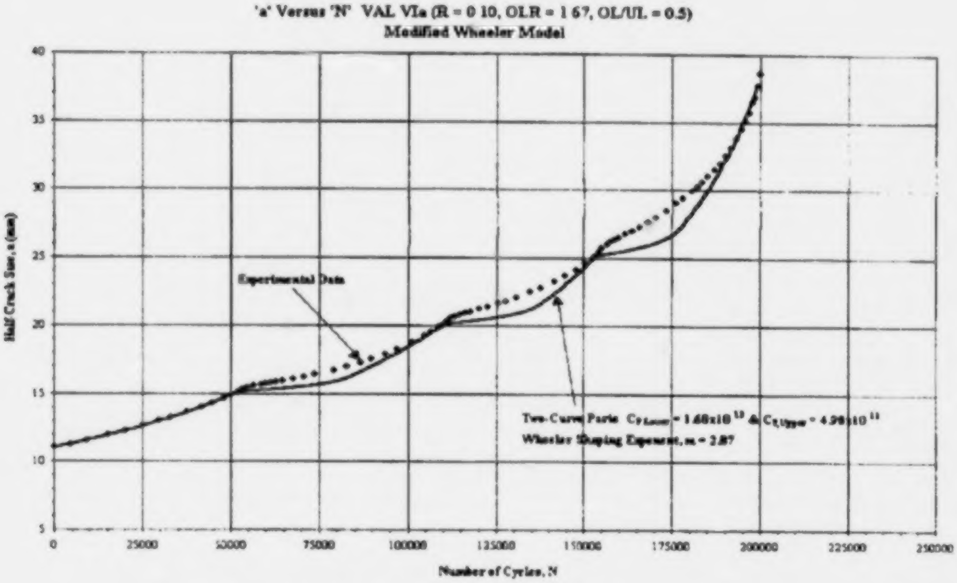

Figure D.5 – Modified Wheeler prediction for specimen VIa

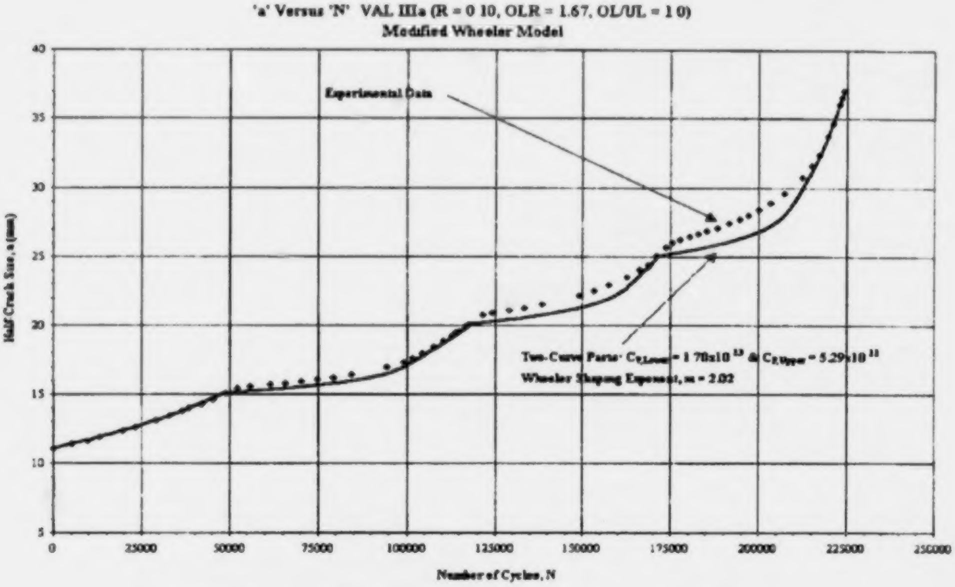

Figure D.6 – Modified Wheeler prediction for specimen IIIa

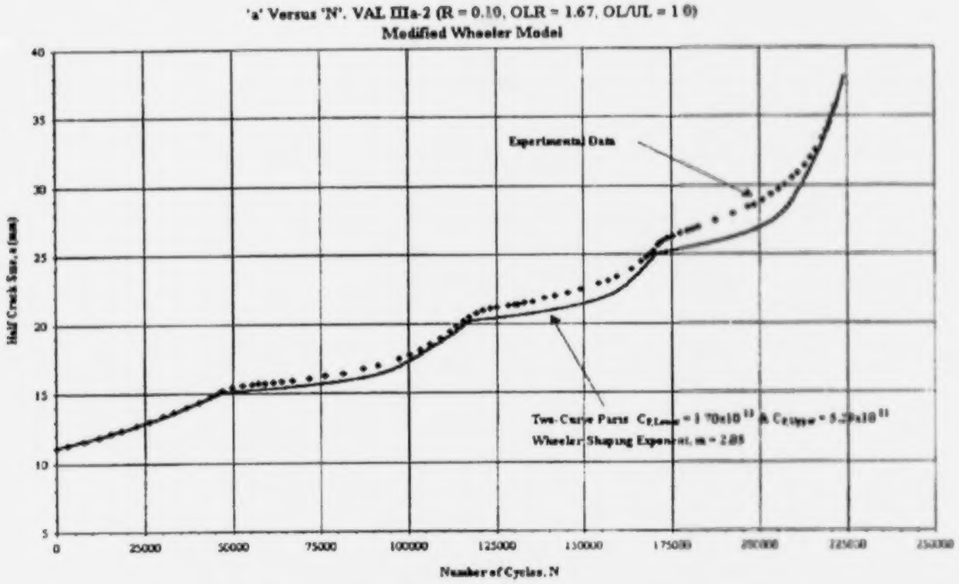

Figure D.7 – Modified Wheeler prediction for specimen IIIa-2

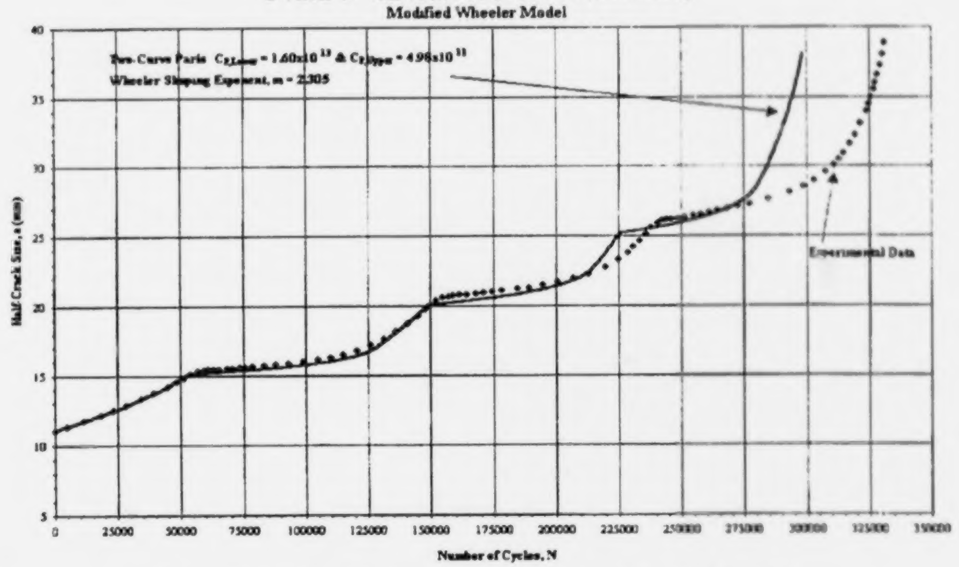

Figure D.8 – Modified Wheeler prediction for specimen Va

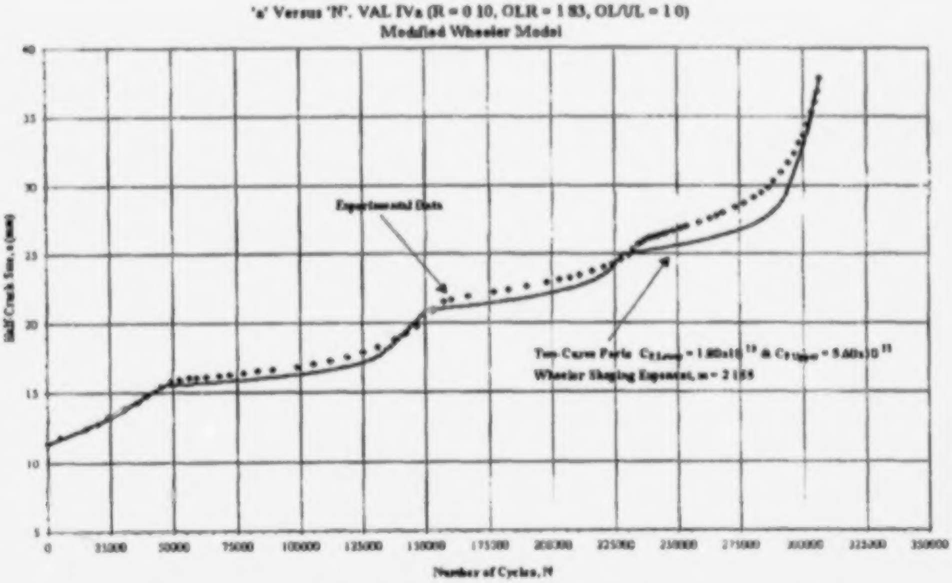

Figure D.9 – Modified Wheeler prediction for specimen IVa

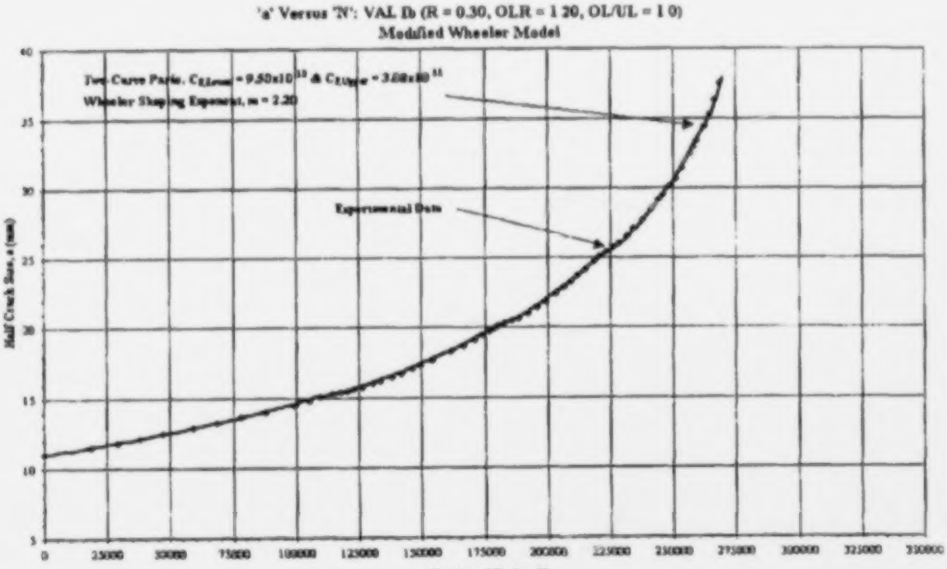

Figure D.10 – Modified Wheeler prediction for specimen Ib

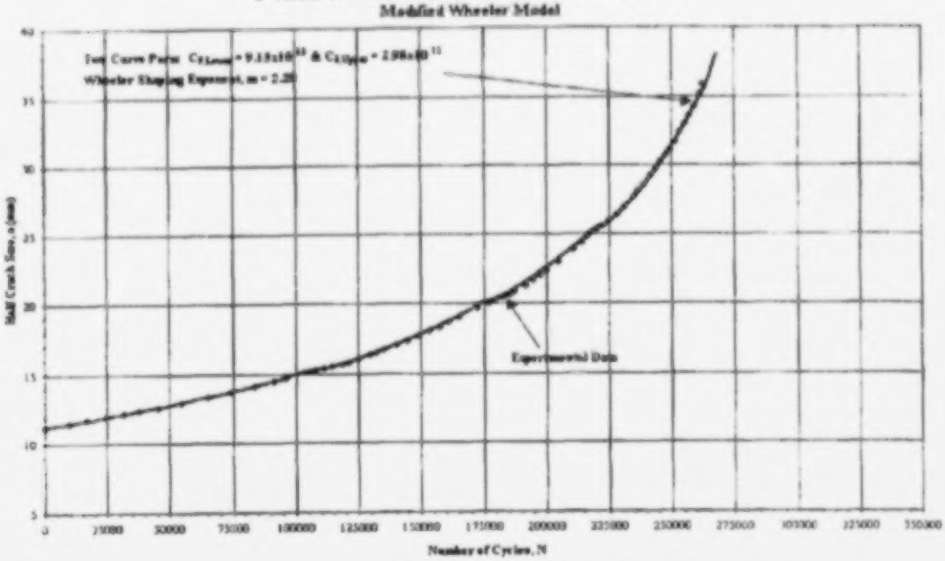

Figure D.11 – Modified Wheeler prediction for specimen Ib -2

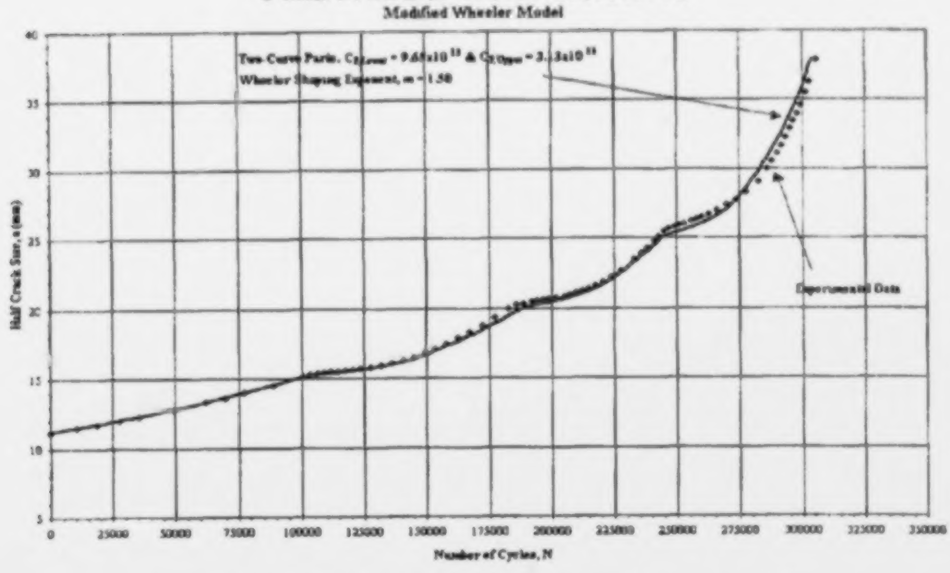

Figure D.12 – Modified Wheeler prediction for specimen IIb

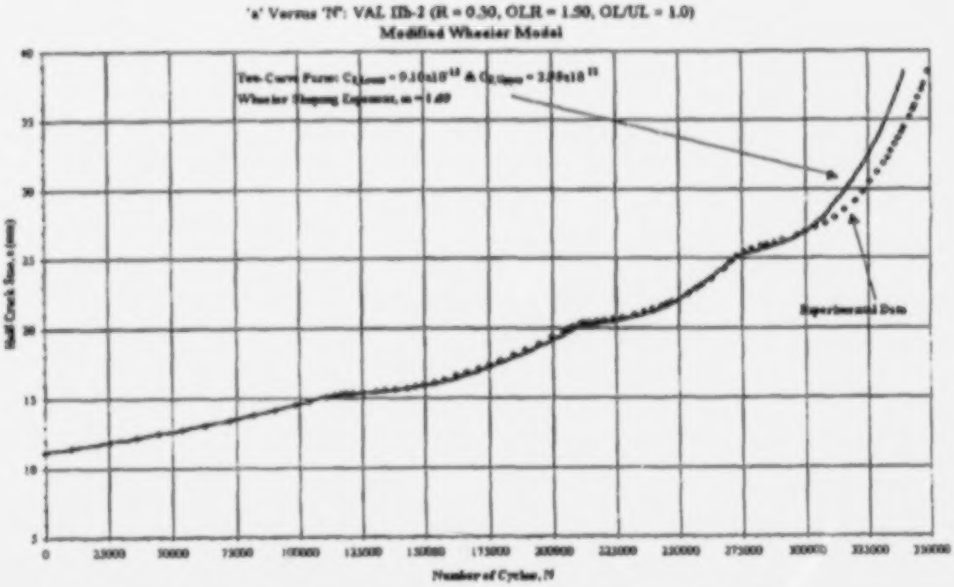

Figure D.13 – Modified Wheeler prediction for specimen IIb-2

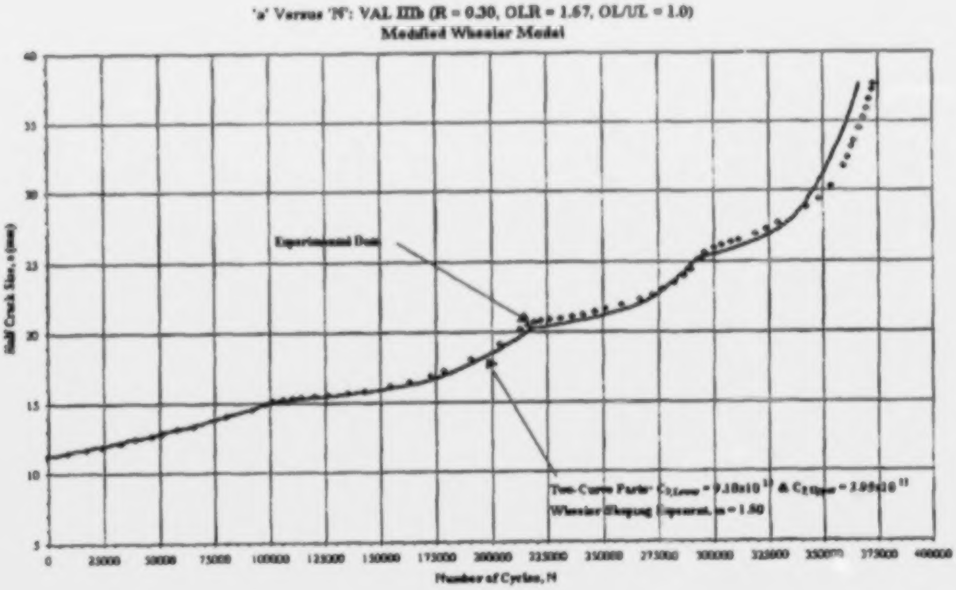

Figure D.14 – Modified Wheeler prediction for specimen IIIb

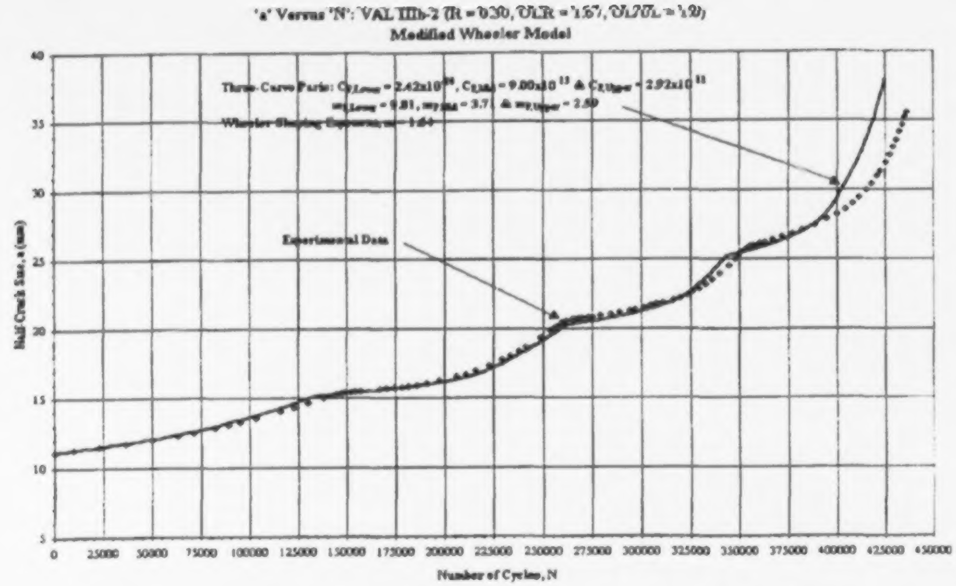

Figure D.15 – Modified Wheeler prediction for specimen IIIb-2

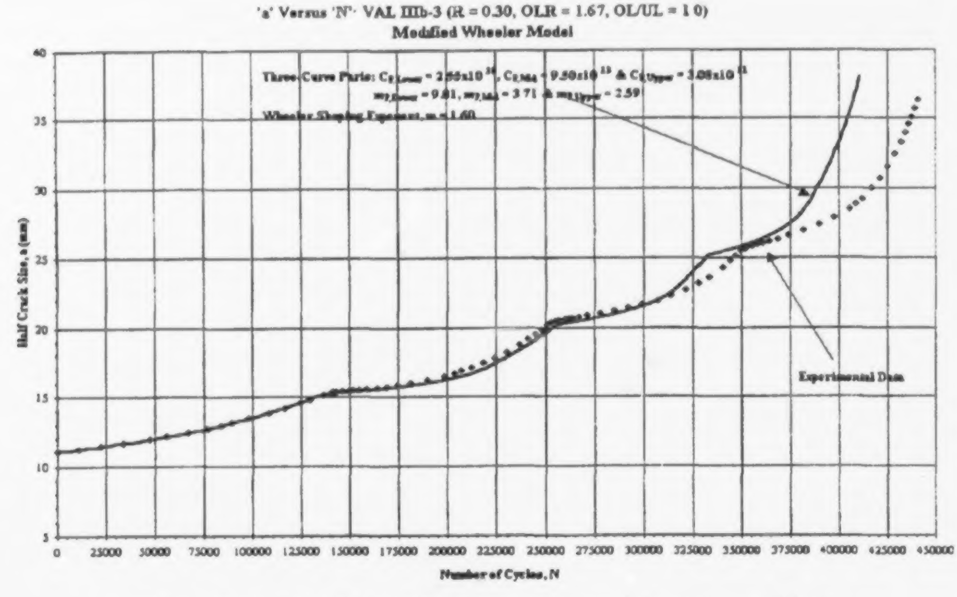

Figure D.16 – Modified Wheeler prediction for specimen IIIb-3

UNCLASSIFIED
SECURITY CLASSIFICATION OF FORM
(highest classification of Title, Abstract Keywords)

DOCUMENT CONTROL DATA

(Security classification of title, body of abstract and indexing annotation must be entered when the overall document is classified)

1 **ORIGINATOR** (the name and address of the organization preparing the document Organizations for whom the document was prepared e g Establishment sponsoring a contractor's report, or tasking agency, are entered in section 8)

Department of Civil Engineering, Dalhousie University
PO Box 1000, Halifax, Nova Scotia, Canada, B3J 2X4

2 **SECURITY CLASSIFICATION** (overall security classification of the document including special warning terms if applicable)

UNCLASSIFIED

3 **TITLE** (the complete document title as indicated on the title page Its classification should be indicated by the appropriate abbreviation (S,C,R or U) in parentheses after the title)

AN EXPERIMENTAL AND NUMERICAL INVESTIGATION INTO FATIGUE CRACK PROPAGATION OF 350WT STEEL SUBJECTED TO SEMI-RANDOM CYCLIC LOADING

4 **AUTHORS** (Last name, first name middle initial If military show rank, e g Doe, Maj John E)

Rushton, Philip A

5 **DATE OF PUBLICATION** (month and year of publication of document)

March 2001

6a **NO OF PAGES** (total containing information Include Annexes, Appendices etc)

302

6b **NO OF REFS** (total cited in document)

35

7 **DESCRIPTIVE NOTES** (the category of the document, e g technical report, technical note or memorandum It appropriate enter the type of report, e g interim, progress, summary, annual or final Give the inclusive dates when a specific reporting period is covered)

CONTRACTOR REPORT

8 **SPONSORING ACTIVITY** (the name of the department project office or laboratory sponsoring the research and development Include address)
Defence Research Establishment Atlantic
PO Box 1012
Dartmouth, NS, Canada B2Y 3Z7

9a **PROJECT OR GRANT NO** (if appropriate, the applicable research and development project or grant number under which the document was written Please specify whether project or grant)

Project 1gc11

9b **CONTRACT NO** (if appropriate, the applicable number under which the document was written)

W7707-8-5687/001/HAL

10a **ORIGINATOR'S DOCUMENT NUMBER** (the official document number by which the document is identified by the originating activity This number must be unique to this document)

none

10b **OTHER DOCUMENT NOs** (Any other numbers which may be assigned this document either by the originator or by the sponsor)

DREA CR 2000-154

11 **DOCUMENT AVAILABILITY** (any limitations on further dissemination of the document, other than those imposed by security classification)
(X) Unlimited distribution
(   ) Defence departments and defence contractors, further distribution only as approved
(   ) Defence departments and Canadian defence contractors, further distribution only as approved
(   ) Government departments and agencies, further distribution only as approved
(   ) Defence departments, further distribution only as approved
(   ) Other (please specify).

12 **DOCUMENT ANNOUNCEMENT** (any limitation to the bibliographic announcement of this document This will normally correspond to the Document Availability (11) However, where further distribution (beyond the audience specified in (11) is possible, a wider announcement audience may be selected)

Unlimited

UNCLASSIFIED
SECURITY CLASSIFICATION OF FORM

UNCLASSIFIED
SECURITY CLASSIFICATION OF FORM

13. ABSTRACT (a brief and factual summary of the document It may also appear elsewhere in the body of the document itself It is highly desirable that the abstract of classified documents be unclassified Each paragraph of the abstract shall begin with an indication of the security classification of the information in the paragraph (unless the document itself is unclassified) represented as (S), (C), (R), or (U) It is not necessary to include here abstracts in both official languages unless the text is bilingual)

A variety of aspects in the fields of fracture mechanics, fatigue, and fatigue crack propagation are reviewed in the first five chapters of this report, as well as a number of concepts and methodologies employed in fracture control and repair. The information provided in these chapters will not only educate the reader, but also provide him or her with the tools necessary to perform a variety of fatigue- and fracture-related analyses. Chapter 4 contains a comprehensive review of a number of constant amplitude and variable amplitude fatigue crack growth models. There is inherently great variation amongst these models, with respect to modeling approach, parameters considered, the number of calibration parameters required (empirical or otherwise), relative ease of use, and the level of computational effort required. Unfortunately, few of these models bear any physical or practical significance and many will see only limited use due to their inherent complexity Moreover, an all-encompassing fatigue crack growth model has yet to be developed, despite the enormous number of models currently available.Chapters 6 and 7 focus on the experimental testing program employed to investigate the fatigue crack growth of center-cracked 350WT steel specimens subjected to semi- random loading comprised of various combinations of intermittent tensile overloads and compressive underloads. A significant amount of information is presented regarding post-overload and post-underload crack growth behavior.Modifications to the commonly used Wheeler model have been proposed, which allow the effects of compressive loading to be considered. The modified Wheeler model appears to provide reasonably accurate fatigue life predictions by using an 'effective' plastic zone to incorporate sequence effects. While the modified Wheeler model does not significantly improve the predictive accuracy of the original Wheeler model, it does give some physical significance to an otherwise empirical approach to modeling such sequence effects In addition, it is shown that the Wheeler shaping exponent may potentially be expressed as a function of the overload ratio and the overload/underload ratio for a given stress ratio.A finite element investigation (using the NISA finite element package) was performed on a typical specimen, the results of which appear to validate the proposed existence of a crack tip 'compressive plastic zone' under compressive loading. The size of this plastic zone is typically smaller than that produced by an equivalent tensile overload. The nonlinear finite element analysis also predicts a zone of tensile yielding at the crack tip upon removal of this compressive underload, further substantiating the observed phenomenon of crack growth acceleration. The size of these compression-induced 'yield zones' were found to depend not only on the relative magnitude of the compressive underload and preceding tensile overload, but also on the assumed crack face separation.The exponential delay model proposed by Trask (1998) has been revised to include the effects of not only overload ratio, but also stress ratio and overload/underload ratio Although seemingly complex, the resulting delay model may be easily incorporated into any existing crack growth model for constant amplitude loading, and has been shown to yield fatigue life predictions which are in good agreement with the experimental data.Fatigue crack growth threshold behavior of 350WT steel was also examined. The resulting K_{th} was similar to that suggested by Barsom et al (1987), but yielded poor life predictions when used in conjunction with the Zheng and Hirt model.

14. KEYWORDS, DESCRIPTORS or IDENTIFIERS (technically meaningful terms or short phrases that characterize a document and could be helpful in cataloguing the document They should be selected so that no security classification is required Identifiers, such as equipment model designation, trade name, military project code name, geographic location may also be included If possible keywords should be selected from a published thesaurus e g Thesaurus of Engineering and Scientific Terms (TEST) and that thesaurus-identified If it not possible to select indexing terms which are Unclassified, the classification of each should be indicated as with the title)

Ship
Structures
Fracture
Fatigue
Materials
Experimental testing